Nanoparticles for tumour diagnostics

Kate P.M. Ricketts

Submitted for the Degree of
Doctor of Philosophy
From
University College London

RADIATION PHYSICS GROUP
DEPARTMENT OF MEDICAL PHYSICS AND BIOENGINEERING
FACULTY OF ENGINEERING SCIENCES
UNIVERSITY COLLEGE LONDON

December 2011

I, Kate Ricketts, confirm that the work presented in this thesis is my own. Where information has been derived from other sources, I confirm that this has been indicated in the thesis.

Signed...

Acknowledgements

I would sincerely like to thank my supervisors, Professor Gary Royle and Dr Adam Gibson for their guidance, time, humour and friendship over the course of this work. They were always there to offer support and encouragement when I needed it. I am grateful to Dr Marilena Loizidou, for being a great teacher and for her unending enthusiasm in this project. I am indebted to Dr Umber Cheema, Ms Agata Nyga, Dr Hazel Welch and Ms Maria Menikou for their encouragement and patience during my work at the Royal Free Hospital and the Royal National Orthopaedic Hospital. Special thanks go to Professors Chiara Guazzoni and Andrea Castoldi, and their PhD students, for their hard work and all of the time we shared in late night synchrotron measurements. I owe thanks to Dr Catherine Holt of the Chemistry Department, UCL, for her help in making the nanoparticle solutions; Ms Jackie Lewin for her time in producing TEM images; and Denzil Booth and Joe Evans for their workshop assistance in making phantoms. I would like to thank my colleague and friend Christiana Christodoulou for her great help throughout the project; Dr Konstantin Ignatyev for his discussions and ideas; Dr Jennifer Griffiths for her guidance and experience, Dr Ben Price for his advice and laughter; and all from the Radiation Physics Department at UCL. I owe a great deal of thanks to my teacher and friend Mr Patrick Robbins for opening up the world of physics to me. I am also very grateful to Mr Andrew Doggart for sharing his enthusiasm for radiotherapy with me. Finally, I would like to mention the constant presence of my family and friends through these eventful three years; in particular John, Astrid, Mossie, James, Emma, and Massey, with special thanks to Joe as without his support this work would not have been possible.

Dedicated to my Mother, Mary

Abstract

X-ray fluorescence techniques have proven beneficial for identifying and quantifying trace elements in biological tissues. A novel approach has been developed that employs x-ray fluorescence with an aim to locate the presence of nanoparticles, such as gold, which are embedded into tissues. The nanoparticles can be functionalised to act as markers for tumour characteristics to map the disease state, and then imaged to inform cancer therapy regimes. The uptake of nanoparticles by cancer cells could also enable detection of small clusters of infiltrating cancer cells which are currently missed by commonly used imaging modalities. The novel system, consisting of an energy resolving silicon drift detector with high spectral resolution, and a synchrotron source, showed potential in both quantification of and sensitivity to nanoparticle concentrations typically found in tumours. A linear relationship between fluorescence intensity and nanoparticle concentration was found down to 0.001 mgAu/ml, the detection limit of the system. A successful translation using a more clinically available bench-top x-ray tube was demonstrated, and found not to degrade the linearity or detection limit. The achieved system sensitivity suggests clinical usefulness in measuring tumour uptake *in vivo*. A set of bio-phantoms consisting of collagen type 1 gel, populated with colorectal cancer cells (HT29) and healthy murine fibroblast cells (3T3) that have been incubated with gold nanoparticles (GNPs), were created. The bio-samples were successfully used to (i) demonstrate GNP uptake in cells, and (ii) demonstrate the use of the novel bench-top system in measuring GNP uptake in cells. Translation to a 2D imaging technique was undertaken, using polycapillary optic technology to acquire positional information of gold XRF emissions, and energy resolving single channel and pixellated detectors. The GNP-imaging capabilities of the XRF technique were demonstrated using Perspex phantoms incorporating different GNP concentrations. Details of phantoms with concentrations as low as 0.025 mgAu/ml have been successfully imaged, with potential to image lower concentrations. It can be inferred from feasibility data collected that the x-ray fluorescence technique can be combined with x-ray diffraction methods to form a novel multi-modality system that is sensitive to GNP distribution and can discriminate biological tissue. Future work will develop this combined system to locate tumours and provide information on tumour characteristics.

Table of Contents

List of figures

List of tables

List of abbreviations

3T3	Mouse embryonic fibroblast cell line
ACM	Artificial cancer mass
ATSM	Diacetyl-bis(N^4-methylthiosemicarbazone)
BOLD-MRI	Blood oxygenation level dependent
CCD	Charge-coupled device
CDD	Controlled Drift Detector
CMOS	Complementary metal-oxide-semiconductor
CTAB	Cetyltrimethylammonium bromide
dHb	De-oxyhaemoglobin
DIW	De-ionised water
DL	Detection limit
DMEM	Dulbecco’s Modified Eagle Medium
ECM	Extra cellular matrix
EDTA	Ethylenediaminetetraacetic acid
EPR	Enhanced permeability and retention effect
FCS	Foetal Calf Serum
FMISO	Fluoromisonidazole
FWHM	Full width at half maximum
GNPs	Gold nanoparticles
GNRs	Gold nano-rods
HA	Hyaluronic acid
Her2	Human epidermal growth factor receptor 2
HIF-1	Hypoxia inducible factor 1
HPGe	High purity germanium detector
HT29	Human colon adenocarcinoma cell line
ICP-AES	Inductively coupled plasma atomic emission spectroscopy
IMRT	Intensity modulated radiotherapy
K-XRF	X-ray fluorescence resulting from electron transitions to the K-shells
L-XRF	X-ray fluorescence resulting from electron transitions to the L-shells
MCS	Multicellular spheroids

MEM	Minimum Essential Medium
MPV	Mean pixel value
OHb	Oxyhaemoglobin
PBS	Phosphate buffered saline
PEG	Polyethylene glycol
RME	Receptor mediated endocytosis
SDD	Silicon drift detector
SERS	Surface-enhanced Raman spectroscopy
SNR	Signal to noise ratio
TEM	Transmission electron microscopy
TER	Total external reflection
VEGF	Vascular endothelial growth factor
XFCT	X-ray fluorescence computed tomography
XRD	X-ray diffraction
XRES	X-ray edge subtraction
XRF	X-ray fluorescence

Outputs

Journal publications

Ricketts, K., Castoldi, A., Guazzoni, C., Ozkan, C., Christodoulou, C., Gibson, A., Royle, G. (2011) A quantitative x-ray imaging system for gold nanoparticle tumour biomarkers. *Physics in medicine and biology – in print*.

Ricketts, K., Loizidou, M., Cheema, U., Nyga, A., Castoldi, A., Guazzoni, C., Gibson, A., Royle G. (2011) 3D biological phantom production of cells with nanoparticle inclusions -*in preparation.*

Castoldi, A., Guazzoni, C., Ricketts, K., Ozkan, C., Gibson, A., Royle, G. (2012) Application of silicon drift detectors in x-ray fluorescence imaging of gold nanoparticles *Nuclear Instruments and Methods in Physics Research – in preparation*.

Conference publications

Castoldi, A., Guazzoni, C., Ricketts, K., Gibson, A., Griffiths, J., Royle, G., & Bjeoumikhov, A. (2011) 2-D energy-resolved imaging of gold nanoparticle distribution at concentrations relevant for in-vitro studies. *IEEE Transactions on Nuclear Science*.

Ricketts, K., Christodoulou, C., Guazzoni, C., Castoldi, A., Ozkan, C., Sodini, N., Griffiths, J. A., Gibson, A., Royle, G. (2010) A system for x-ray diffraction and fluorescence imaging of nanoparticle biomarkers. *IEEE Transactions on Nuclear Science*.

Ricketts, K., Ozkan, C., Christodoulou, C., Dreossi, D., Castoldi, A., Guazzoni, C., Gibson, A., Royle, G. (2011) X-ray edge subtraction imaging of gold nanoparticle concentrations for biological imaging. *IEEE Transactions on Nuclear Science*.

Prizes

First prize: UCL Medical Physics & Bioengineering Poster Prize 2011 (Final year PhD students), Quantitative biological imaging of tumour properties using nanoparticles

First prize: UCL Medical Physics & Bioengineering Poster Prize 2010 (First and Second year PhD students), Diffraction applications in radiotherapy – imaging hypoxia

Grants

Beamtime at Diamond Light Source, Oxford, UK (December 2011)
Beamtime at Elettra Synchrotron Source, Trieste, Italy (June 2011)
Beamtime at Diamond Light Source, Oxford, UK (February 2011)
Beamtime at Elettra Synchrotron Source, Trieste, Italy (October 2010)

UCL Graduate School travel grant to enable experiments at Politecnico di Milano, Italy

Chapter One

1 Introduction

1.1 The clinical problem

Current radiotherapy techniques prescribe a homogeneous dose to the target volume. However, tumours are heterogeneous tissues that encompass a variety of cell types of differing radiosensitivities. The distribution of cells is also heterogeneous throughout the tumour volume, with infiltrating cancer cells lying on the periphery of the bulk tumour. Such infiltrating cells may lie outside the treatment volume and survive therapy, thereby reducing treatment efficacy. The microenvironment of the tumour also dictates treatment success (for example, cells under hypoxic conditions will be less radiosensitive than their normoxic counterparts).

Modern intensity modulated radiotherapy (IMRT) techniques can be used to deliver heterogeneous dose distributions across the tumour, boosting the dose to less radiosensitive regions. In order to make use of this technology, there is now a clinical need for a functional imaging technique sensitive to tumour characteristics that gives radiosensitivity information (such as oxygen concentration, proliferative ability and angiogenesis [1]). An equally important need is the development of a technique with high enough tumour specificity and sensitivity to detect the presence of peripheral infiltrating cancer cells.

In order to fully understand the clinical problem in radiotherapy, an understanding of the biology of the tumour microenvironment is required.

1.1.1 Biology of the tumour microenvironment

The tumour microenvironment consists of the following: (i) cancer cells; (ii) non-cancer cells (including endothelial cells that line the inner surface of blood vessels, and immune system cells e.g. lymphocytes and macrophages); (iii) secreted soluble factors (growth factors and cytokines which are signalling molecules used in cellular communication); and (iv) non-cellular solid material e.g. extra cellular matrix (ECM) consisting of collagen which provides structural support. The tumour and its stroma (the layer of tissue surrounding it) are multi-regional as illustrated in Figure 1.

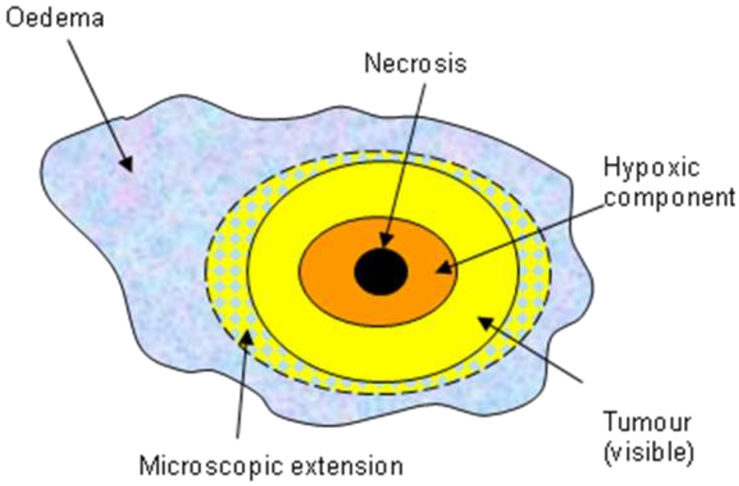

Figure 1 The tumour and its environment (the hypoxic component is spatially and temporally heterogeneous throughout the tumour).

The tumour stroma environment may be hypoxic, with low pH and low glucose levels. As a result normal cells surrounding the tumour exhibit altered characteristics compared with cells in normal conditions. They can develop mutations in response to soluble products released by the tumour altering genes, and tissue and vasculature structure becomes more disorganised [2]. There may therefore be a need to target both cancer cells and stromal components to be more effective. Radiotherapy treatment volumes aim to target the bulk tumour and region of microscopic extension with the aim of killing the proliferative cancerous cells.

Tumour characteristics play a role in determining radiotherapy treatment success. For example, cell density should be considered when prescribing dose; a greater number of cells per unit volume will require a greater dose to achieve tumour control. Also, the effect of other concurrent treatments will impact on the treatment outcome of radiotherapy, e.g. a good tumour blood supply is required for chemotherapy agents to reach cancer cells. The heterogeneity of the tumour and its environment will impact on the radiosensitivity of the cells within the cancer mass. Hypoxia will be used as a case study to demonstrate how cell biology affects radiosensitivity.

1.1.2 Hypoxia: a case study in radiotherapy

Nearly 50% of locally advanced breast cancers exhibit hypoxic and/or anoxic tissue areas within the tumour mass [2]. Hypoxia has three main causes: (i) abnormalities in the structure and function of tumour microvessels result in **perfusion related (acute)** hypoxia which is transient and affects cells up to the vessel wall; (ii) increased diffusion distances between blood vessels and an expanding tumour cell mass competing for oxygen results in **diffusion related (chronic)** hypoxia, which affects cells greater than 70-100 μm from the nearest capillary (the maximum oxygen diffusion distance); (iii) **anaemic** hypoxia due to the reduced oxygen carrying capacity of blood as a result of disease or treatment related anaemia [2], [3].

O_2 has a role as the terminal electron acceptor in oxidative phosphorylation; the electron transferral releases energy which is used to form ATP, the energy source of cells. When O_2 is absent the hypoxia inducible factor 1 (HIF-1), a transcription factor, promotes hypoxic cells to up-regulate more than 100 proteins that promote survival and increase aggressiveness of hypoxic tumour cells [4]. The functions of the proteins include stimulating angiogenesis, switching the mitochondria to glycolysis (a source of energy that does not require O_2), and inhibiting apoptosis by inducing mutations in the p53 gene (the gene that controls apoptosis) [5]. Metastatic spread is also promoted by upgrading enzymes that degrade the ECM, allowing cells to break away from the primary tumour [6], and producing molecules that down-regulate the immune surveillance system [7].

As a result of the proteome (complete set of proteins in a cell at a given time) changes, the effectiveness of certain cancer therapies becomes impaired below the values of oxygen tensions (pO_2) displayed in Table 1. Loss of apoptosis and chaotic angiogenesis results in decreased blood flow which in turn results in decreased delivery of chemotherapy drugs. It is the aim of radiotherapy to kill cancer cells, but poor oxygen availability results in a lower radiation cell kill. Ionising radiation produces free radicals that cause DNA double strand breaks which act to cause cell death; if the primary free radical reacts with oxygen to form a secondary radical, damage to the DNA is permanent. However, if the primary radical reacts with smaller molecules such as thiols the damage is repairable [1]. The radiosensitivity of cells is dependent on the phase of the cell cycle, with cells in the G1 phase being more radiosensitive than cells in the S-phase [3]. Cells exposed to hypoxia are generally arrested at the G1/S-phase boundary of the cell cycle [8]. This results in a decreased rate of proliferation, and so cells have reduced radiosensitivity resulting in reduced cell kill.

Sustained hypoxia also plays an important role in malignant progression of solid tumours by increasing the genomic instability and number of genetic variants. New variants that can survive the hypoxic conditions are selected through clonal expansion, leading to the emergence of more aggressive clones that are resistant to therapy, able to overcome nutrient deprivation and able to escape the hostile environment resulting in metastases [2], [8].

Table 1 pO_2 values below which outcome of therapy is impaired and proteome and genome changes are apparent [8]. *Oxygen tensions measured in head and neck cancers revealed a median range pO_2 of 10 - 30 mmHg compared with a median range value of pO_2 of 24 - 66 mmHg in normal tissue* [9].

Effect	**pO_2 range (mmHg)**
Effectiveness of immunotherapy becomes impaired	$\leq 30 – 35$
Cell death with photodynamic therapy	$\leq 15 – 35$
Cell death on exposure to radiation	$\leq 25 – 30$
Binding of hypoxia markers	$\leq 10 – 20$
Proteome changes	$\leq 1 – 15$
Genome changes	$\leq 0.2 – 1$

Hypoxia imaging will assist the selection of patients requiring more aggressive treatment or individualised therapy. Hypoxia should be used as a biometric parameter to assist dose prescription in radiotherapy, and can also be used as an independent prognostic factor for overall and disease-free survival, resulting from the association of tumour hypoxia with treatment failure and malignant progression [2], [5].

A hypoxia imaging technique is necessary as hypoxia is difficult to predict or model; hypoxia is not static and changes in response to irradiation and chemotherapy [2], [9].

1.1.3 Current hypoxia measurement techniques

An ideal hypoxia imaging technique would: (i) reflect cellular instead of vascular pO_2; (ii) be sensitive to pO_2 levels relevant to tumour therapy (<25 – 30 mmHg); (iii) be simple to perform, non-toxic, and allow repeated measurements; and (iv) have the ability to be performed during treatment once the patient has been positioned for treatment [3]. For particular use as a radiotherapy imaging technique, the following points must be considered: (i) hypoxia is not static; levels of oxygenation change in response to irradiation and chemotherapy; and (ii) it is important to know when and if re-oxygenation occurs after fractions as this changes the distribution of hypoxic regions [1]. The extent and rapidity of re-oxygenation is difficult to predict for individual tumours, and so it may be useful to map perfusion as well as hypoxia. These factors highlight the need for repeated imaging throughout the treatment course.

A variety of methods have been used to measure cellular oxygenation in tumours, including invasive intra-tumoural measurement with pO_2 electrodes. Technical limitations of this direct measurement have encouraged the use of alternate markers for tumour hypoxia [10]. *Ex vivo* techniques include immunohistochemical detection of endogenous proteins overexpressed as a result of the cells' hypoxic condition (such as HIF-1α) and exogenous injected drugs that are bound intracellularly only in areas of hypoxia. Clinically used exogenous markers are the 2-nitroimidazoles and pimonidazole which are injected intravenously prior to a tumour biopsy. Clinical studies have reported that such markers become detectable at a pO_2 below 10 mmHg [11], whereas radiotherapy becomes impaired at higher pO_2 values (Table 1). Necrotic cells do not metabolise the marker and so do not stain positive for hypoxia. Staining is also mainly observed at a distance greater than 100 µm from the nearest perfused vessel, suggesting that these exogenous markers indicate chronic, diffusion limited hypoxia [12]. Histology studies may only be performed on thin slices due to the low penetration of radiation wavelengths used in optical imaging techniques, rendering it not useful as an *in vivo* technique.

A number of biological parameters may be used to image hypoxia. De-oxyhaemoglobin (dHb) concentrations can be directly measured by blood oxygenation level dependent (BOLD) MRI techniques. dHb in red blood cells is paramagnetic whereas oxyhaemoglobin (OHb) is not paramagnetic. dHb increases the MR transverse relaxation time (R2*) of water in blood and surrounding tissues; thus T2* weighted imaging reveals changes in vascular oxygenation [5]. BOLD-MRI is sensitive to pO_2 within and in tissues adjacent to perfused vessels [3]. BOLD-MRI images are more likely to reflect perfusion related hypoxia rather than chronic diffusion related hypoxia;

red blood cells in vessels are too distant from chronically hypoxic regions. Also, for BOLD-MRI to measure tissue oxygenation status, red blood cells must be delivered to the tissue of interest, and so good blood flow is a requirement. Furthermore, it is sensitive to changes in Hb concentration, which may result from vascular volume and flow alterations. BOLD-MRI can therefore only provide qualitative rather than quantitative measurement of oxygenation change [5].

Nuclear medicine techniques make use of the change in chemistry at low oxygen tensions enabling the reduction and retention of certain radiopharmaceuticals at hypoxic sites. ^{18}F-fluoromisonidazole [1-(2-nitroimidazolyl)-2-hydroxy-3-fluoropropane; ^{18}F-FMISO] is the most widely used PET agent for mapping regional hypoxia. Estimated total body absorbed dose for a 70 kg man injected with 3.7 MBq/kg is 0.013 mSv/MBq; for a woman it is 0.014 mSv/MBq. The limitations of FMISO include the dependency of early tumour uptake on blood flow to the region, making late phase imaging preferable [13]. Whole body clearance of ^{18}F-FMISO is slow resulting in a poor contrast in raw images [5]. An alternative PET imaging technique for hypoxia is based on a metal complex of radioactive copper with ATSM, diacetyl-bis(N^4-methylthiosemicarbazone). Cu-ATSM uptake is more rapid than 18F-FMISO uptake, and the reported hypoxic-to-normoxic ratio is greater. However the early uptake and washout of Cu-ATSM may be influenced by regional blood flow [5].

The degree of angiogenesis can also be determined using microCT techniques. However measurement of angiogenesis does not directly determine oxygenation levels as it does not consider the possible presence of acutely hypoxic regions resulting from random temporary occlusions of the blood vessels [3].

The presence of lactate/lipids in the tumour region is linked to hypoxia; they are the result of cell membrane breakdown caused by the hypoxia induced proteome changes. Lactate/lipid levels can be detected using optical techniques [14]. ^{1}H MRI can also be used to image lactate [5].

The advantages and disadvantages of current hypoxia measurement techniques are summarised in Table 2.

Table 2 Summary of advantages and disadvantages of current hypoxia imaging techniques.

Modality	**Advantages**	**Disadvantages**
BOLD-MRI **(Paramagnetic dHb increases transverse relaxation rate R2*)**	Monitors changes in pO_2 Also measures cell density	Requires good blood flow Takes long time Not available during treatment Not quantitative method
PET 1. **^{18}F-MISO** 2. **Cu-ATSM**	Can see metastases of 1° cancer	Requires injection Does not monitor changes in pO_2 Not available during treatment
Optical Imaging	Quantitative information on OHb and dHb concentration	Current availability in clinic
Micro-CT **(Images angiogenesis)**	Angiogenesis: perfusion info	Indirect measure of hypoxia (does not account for acute hypoxia)

1.2 Requirements of an imaging technique to answer the clinical problem

In order to improve treatment response to radiotherapy, and inform dose prescription by considering radiosensitivity of the tumour, a technique is required that has the following capabilities:

1. A technique that provides a metric of the biology of the target volume is required. Bio-parameters that affect radiosensitivity (such as the case study of hypoxia presented in this thesis) should be identified.
2. A technique that can measure the distribution of such bio-parameters will provide a map of radiosensitivity.
3. It would be advantageous if more than one bio-parameter could be imaged concurrently (such as hypoxia and proliferative ability), as radiosensitivity is not only attributed to just one bio-parameter. Also, some bio-parameters are related such as hypoxia and perfusion, and gaining information on both parameters would increase the sensitivity of the technique.
4. A quantitative technique rather than a qualitative imaging method is needed to better inform radiotherapy dose prescription.
5. A system that is sensitive to low numbers of infiltrating cells on the tumour periphery. Current techniques do not provide the required sensitivity.
6. A technique that could image the distribution of bio-parameters *in vivo* or in thick *ex vivo* tissue samples as opposed to currently available *ex vivo* histopathology techniques would have a big impact on cancer treatment. Current histopathology techniques are limited to thin slices due to the poor penetrating power of optical fluorescence light that produces the images.

1.3 Aims

The overarching aim of this project is to develop a technique for guiding the planning and maximising the treatment objectives of radiotherapy. In order to strive towards this grand aim, the following specific aims were set for this work:

1. Identification of a suitable contrast agent that can be used to image bio-parameters in cancer. This work proposes the use of gold nanoparticles (GNPs) to image bio-parameters in tumours.
2. To design, build and evaluate a new system for quantitative x-ray detection of GNPs *in vivo* or in thick *ex vivo* tissue / research samples, taking advantage of the penetration of x-rays at depth.
3. Assessment of feasibility and collection of proof of principle data on x-ray based diagnostic imaging of GNP distribution.
4. Establishment of novel 3D *in vitro* cancer models with GNP inclusions in order to test the x-ray based system, and demonstrate GNP uptake in cells.

1.4 Technical objectives

To achieve these aims, the following technical objectives are required:

1. Development of a quantitative technique based on x-ray fluorescence (XRF) that is sensitive to GNP concentrations typically delivered to tumours.
2. Feasibility measurements for assessment of a quantitative imaging technique. This system will be capable of high resolution (better than 1 mm), high sensitivity to GNP concentration (provided by XRF techniques), and with the ability to discriminate tissue type (through use of x-ray diffraction (XRD) techniques) within a bulk 3D volume.
3. Development of a procedure to produce 3D tumour models with GNP inclusions, in order to facilitate system testing. This objective is broken down into the following:
    a. Procedural development to achieve GNP uptake in cell lines.
    b. Production of 3D cellular models with GNP inclusions.

c. Development of methods to reliably distribute GNP uptake within the cellular models.

1.5 Justification of technical objectives

It is believed that the technical objectives outlined above work towards providing a solution to the clinical need for imaging bio-parameters to better inform radiotherapy. Each suggested component to the proposed project will be discussed in turn in order to provide evidence for its use and role in solving the clinical problem.

1.5.1 Use of GNPs as a contrast agent for radiotherapy

GNPs are increasingly used in *in vivo* cancer models to act as a contrast agent for x-ray based imaging techniques [15]. Nanoparticles (NPs) can target tumours passively or actively. Passive targeting relies on the unique characteristics of the tumour microenvironment, mainly: (i) leaky tumour vasculature; the size of nanoparticles (1-100 nm) is smaller than the tumour vasculature pores (up to 400 nm) and so may be leaked into the tumour interstitium via surrounding blood vessels [16], and (ii) a dysfunctional lymphatic drainage system which increases retention of particles in the tumour tissue. This is referred to as the enhanced permeability and retention (EPR) effect. Tumour specificity may be further increased through active targeting; antibodies attached to the nanoparticle can be taken up by specific cellular receptors, thus acting as markers for bio-parameters that provide information about cell radiosensitivity. Linking to cancer specific antibodies to enhance targeting and detection has been reported in *in vivo* models [17]. The uptake of nanoparticles by cancer cells could also enable detection of small clusters of infiltrating cancer cells which are currently missed by commonly used imaging modalities.

GNPs present a realistic potential for clinical use; they are biocompatible (gold is biologically inert and stable), and have readily modifiable surfaces to increase solubility (in order to travel through the bloodstream) and enhance cell-specific uptake [18]. GNP coating with polyethylene glycol (PEG), sodium citrate or heparin lowers acute toxicity and sufficiently evades both host immune reactions and irreversible binding to circulating serum proteins [19].

GNPs are an ideal contrast medium for use in x-ray imaging techniques. GNPs are more effective than previous iodinated contrast techniques as gold has a higher atomic number (Au:79 compared to I:53) and therefore is more absorptive, providing better contrast with lower dose. Molecular imaging is also possible due to the greater number of atoms delivered to the receptor site (~250 Au atoms per 1.9 nm nanoparticle compared with 3 (monomer) or 6 (dimer) I atoms per molecule when using iodinated contrast agents [15]), thereby increasing the signal per cell

A great advantage of using GNPs as an imaging contrast agent for radiotherapy is that GNPs have been shown to enhance local dose deposition for both x-ray radiotherapy [20], [21], [22] and proton radiotherapy [23]. Their high Z leads to increased photoelectric absorption and production of secondary ionising species. Therefore, as well as a novel approach to defining sub-clinical tumour infiltration, GNPs may also allow tumour-specific local dose enhancement if they can be located and retained in tumour cells. This relies on ionisation occurring close enough to DNA; this can be achieved either through targeting the NP to the cell nucleus, or inducing an energetic ionising species that can reach DNA from elsewhere in the cell.

The literature was searched for typical GNP concentrations found in tumours. Hainfeld *et al* studied the uptake of 15 nm GNPs coated with PEG and covalently coupled to Herceptin using a mouse model [24]. Herceptin is a humanised monoclonal antibody currently used to treat human breast cancers with upregulated Her2 (human epidermal growth factor receptor 2) expression, namely Her2+ tumours. The resulting GNP concentrations found in the whole tumour, periphery and muscle for a 15 nm GNP injection of 1.1 gAu / kg mouse are displayed in Table 3.

Coupling the GNPs to Herceptin demonstrated the ability to functionalise GNP uptake; an increased uptake of the GNPs in Her2+ tumours compared with Her2- tumours was found. A high dose of GNPs (1.1 mgAu/g) was injected into the mouse, but other studies presented in the literature administer a much lower dose of typically 0.01 mgAu/g [25]. Our system was therefore designed to be sensitive to concentrations 100 times lower than those reported in Table 3. The tumour/muscle contrast values were also used in the development of imaging phantoms in Section 4.2.

Table 3 Quantification results from microCT measurements of mice intravenously injected with Herceptin-GNPs. The Her2+/Her2- ratio is the Her2+ % injected dose/g divided by the corresponding Her2- % injected dose/g. Muscle value is from atomic absorption measurements [24].

	GNP concentration (mgAu/ml)*	**Her2+/Her2-**	**Tumour/muscle**
Her2+ (whole tumour)	1.82	1.3 (whole tumour)	11.4
Her2- (whole tumour)	1.36		8.5
Her2+ (periphery)	3.48	1.6 (periphery)	21.8
Her2- (periphery)	2.22		13.9
Her2+ (centre)	0.34	2.2 (centre)	2.1
Her2- (centre)	0.16		1.0
Muscle	0.16	1.0 (muscle)	

*Calculated for a 20 g mouse injected with 1.1 mgAu/g (i.e. a 22 mgAu injection) from percentage uptake of initial GNP dose values presented in [24].

1.5.2 Current techniques used to image GNPs

Non invasive *in vivo* techniques are being developed. Hainfeld *et al* are the first group to image gold nanoparticles (GNPs) *in vivo* in mice using microCT; the mice were injected intravenously with 1.9 nm GNPs at a concentration of 2.7 mgAu/g [15]. Deliberately high amounts of gold were used to investigate x-ray contrast given by the NPs. No signs of toxicity resulting from the gold were found, with low retention in the liver and spleen, and elimination by the kidneys. Another group have demonstrated that good contrast to noise CT images can be obtained at gold concentrations of 0.1 mgAu/ml [26]. A more recent study by Hainfeld *et al* reports that microCT enables quantification of GNPs within various regions of a murine tumour; a calibrated relationship between radiodensity and gold concentration was demonstrated down to 0.05 mgAu/ml [24].

Techniques based on optical spectroscopy were found to be satisfactory for the quantification of GNP concentration *in vivo* [27], [28]; it has been demonstrated that a diffuse optical spectroscopy technique can measure down to 15.4 x 10^8 gold nanoshells/ml to within 12.6% of the known concentration. The literature also reports photoacoustic imaging techniques that use GNPs as a contrast agent [29]. Photoacoustic imaging involves delivering non-ionising laser pulses to tissue; some of the delivered energy is absorbed and converted to heat, leading to transient thermoelastic expansion followed by ultrasonic emission which is detected to form high spatial resolution images. GNPs have unique optical absorption properties and are therefore useful in this field. Surface-enhanced Raman spectroscopy (SERS) techniques have also been used to image GNPs; GNPs consisting of a gold core, a Raman-active molecular layer (a fluorescence dye) and a silica coating were used for Raman imaging *in vivo* [30]. However, the aforementioned optical techniques are limited to shallow sites (~ 5 mm deep)

There is currently a need for an *in vivo* system sensitive to even lower GNP concentrations than the techniques presented in the literature in order to meet the aims of this project.

1.5.3 Requirements for GNP imaging

There is a clinical need for imaging GNP distribution, particularly for GNPs located (i) *in vivo*, and (ii) in *ex vivo* samples or *in vitro* research samples.

In vivo imaging will require a high energy radiation technique (such as x-rays) in order to penetrate through thicknesses of tissue, and will require a high intensity source in order to keep acquisition time to a minimum to avoid motion artefacts and increase patient throughput. The system will have to be optimised to keep absorbed dose to a minimum. The scope of this project is to assess the feasibility of a novel GNP imaging technique, and dose considerations have not been considered at this stage.

The imaging of *in vitro* research samples or *ex vivo* tissue poses a different set of requirements. Lower energy x-rays are sufficient to penetrate the lower thicknesses involved, and acquisition time is not an issue as the sample is not moving (although an optimum system is preferred to keep sample throughput times at a minimum). Dose is not an issue for fixed research samples or *ex vivo* tissue; however, if the project is developed to include live 3D cultures, sample dose must be considered.

1.5.4 X-ray fluorescence techniques

Current imaging technologies for GNPs lack the ability to measure sufficiently low concentrations (the lowest measurable concentration was 0.05 mgAu/ml using microCT [24]). Mentioned techniques are also incapable of mapping two or more biomarkers simultaneously (refer to Section 1.2 for details of why this capability is useful).

This project proposes the use of XRF as a technique that can be used to improve on sensitivity and multi-biomarker capability lacking in current systems. XRF employs x-rays to generate a fluorescence signal from the GNPs that can be detected and mapped to provide quantitative information about the sample. Figure 2 illustrates the XRF process. The energy of the emitted XRF x-ray is determined by the energy transition made by the electron lowering in energy which is characteristic to the element that was fluoresced.

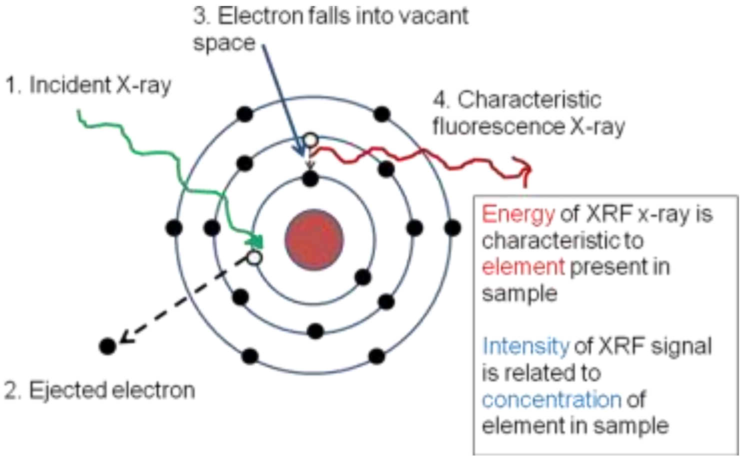

Figure 2 Illustration of x-ray fluorescence process.

A range of transitions are possible, resulting in a range of possible XRF emission energies. The energy level transitions corresponding to each of the fluorescence lines are illustrated in Figure 3. K-XRF and L-XRF correspond to energy transitions involving electrons falling down to K and L shells respectively.

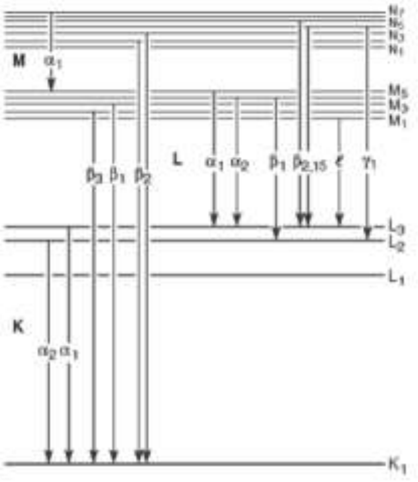

Figure 3 Transitions that give rise to the various emission lines [31].

XRF is a technique that can be used to provide concentration information; the energy of the fluorescence x-ray gives information about the element present, and the magnitude of the XRF signal is proportional to the concentration of that element. XRF is now a well established technique for the detection and quantification of trace amounts of heavy metals *in vivo*. The technique has been used to measure metals in organs near the skin surface such as lead in bone, first reported in 1976 [32]. K-XRF has been successfully used to determine low levels of gold in the kidney following chrysotherapy [33], [34]. *In vivo* XRF in cancer and rheumatology patients has helped to understand how platinum and gold are retained in the target sites (tumour and bone joints for platinum and gold respectively) and other organs (with particular attention to the kidneys) [35]. Techniques using a number of different sources and geometries have been reviewed, including systems that excite both L-XRF and K-XRF [36].

The benefit of this approach in comparison with conventional optical biofluorescent markers is that the XRF signal can penetrate centimetres of tissue and is therefore appropriate to bulk tissue volumes and potentially *in vivo* studies. XRF also has the benefit that two or more biomarkers can be imaged simultaneously; different molecular targeting biomarkers can be tagged to different element NPs each of which will give a different energy signal.

A feasibility study of an x-ray fluorescence computed tomography (XFCT) system using an x-ray tube that can produce quasi-monochromatic x-rays for *in vivo* measurement of high Z contrast media was undertaken [37]. Drawing from simulations and experiment of K-XRF production from gadolinium contrast medium (Z = 64), the study concluded that neither fan- nor pencil-beam XFCT is practical for *in vivo* use in terms of spatial resolution, minimum detectable concentration and scanning time.

XFCT imaging of GNP-loaded phantoms has been successfully performed using K-XRF in gold (67 and 68.8 keV) [38]. Relatively high GNP concentrations were tested by the system, the lowest being 5 mgAu/ml (greater than that expected *in vivo*). Also, this technique requires a pencil beam and therefore its speed will limit its clinical use.

This project hypothesises that an XRF system could achieve greater sensitivity and spatial resolution than XRF systems presented in the literature, and could be used for quantitative measurement of GNP concentration. In order to determine the capabilities of XRF, the performance of three different XRF systems will be compared; (i) a synchrotron based L-XRF system, (ii) a bench-top L-XRF system, and (iii) a bench-top K-XRF technique.

1.5.5 Introduction to x-ray diffraction

Whilst XRF relies on NP markers, x-ray diffraction (XRD) can discriminate between tissue types based upon differences in their elemental composition. Section 4.7.2 in Chapter Four will discuss the role of XRD in tissue discrimination. The diffraction signal stems from coherent interactions. Coherent (or Rayleigh) scatter occurs when an incident photon interacts with tightly bound atomic electrons, causing them to oscillate and emit radiation of the same wavelength as the incident photon. The probability of an x-ray coherently scattering from a single free electron into solid angle *dΩ* is written as the Thomson coefficient

$$\frac{d\sigma_o}{d\Omega} = \frac{{r_o}^2}{2}(1 + cos^2\theta)$$ Equation 1

where $d\sigma_0$ is the classical scattering coefficient per electron, θ the scattering angle and r_o is the classical electron radius. The linear differential scattering cross section is given by

$$\frac{d\sigma_{coh}}{d\Omega} = \frac{{r_0}^2}{2}\left(1 + \cos^2 \vartheta\right)\left[F(x, Z)\right]^2$$ Equation 2

where $F_m(x,Z)$ is the molecular form factor and Z is the atomic number. $F_m(x,Z)$ accounts for the interference effects by radiation scattered by electrons in the material, and is the Fourier transform of the electron charge distribution in the scattering atoms; it is therefore a property of the material only [39]. $F_m(x,Z)$ is presented in terms of momentum transferred to the photon (x) which accounts for the dependence of scatter distribution on scatter angle and energy:

$$x = \frac{E}{hc}\sin\frac{\theta}{2}$$ Equation 3

Photons coherently scattered by electrons in the same atom, molecule or neighbouring molecule can interfere with each other [40]. The condition for constructive interference is described by the Bragg law; the difference in path length must be equal to an integer number of wavelengths:

$$n\lambda = 2d\sin\theta$$ Equation 4

where n is the order of diffraction, λ is the photon wavelength, d is the spacing between the scattering planes and θ is the photon scatter angle.

It has been demonstrated that tissue discrimination is possible using XRD techniques [41], [42], [43], [44]. The extent to which the XRD signal will be of use in combination with XRF measurement will be assessed in this project. A further discussion of the role of XRD will be undertaken in Chapter Four.

1.5.6 Justification of bio-phantom production

In order to test and demonstrate the use of the novel developed x-ray imaging technique, a range of bio-phantoms will be made. The aim of this section of the project will be to demonstrate GNP-uptake in both healthy and cancer cells, and to attain GNP concentrations similar to that expected in literature (refer to Section 1.5.1 for typical concentration values).

It is important to use a range of phantoms that resemble *in vivo* tumour conditions; *in vivo* cancers incorporate densely packed cancer cells surrounded by ECM and other non-cancerous cells. Tissue engineering work will be carried out to develop artificial cancer masses (ACMs) to closely mimic these components. Novel ACMs will be constructed that incorporate different concentrations and distributions of GNPs. The ACM phantoms will act as challenging 3D imaging test phantoms for the XRF imaging technique.

Tissue engineering techniques are currently available that can control collagen density in scaffolds; these techniques are fully discussed in Chapter Three, Section 3.4.10. We will further develop these techniques to embed GNP-loaded cells within a collagen matrix to provide samples appropriate for measurement with the novel XRF system, and to demonstrate the ability of the XRF system in quantitative measurement of GNP uptake in cells.

1.6 Novelty of this work

A novel solution is required to meet the clinical need for a quantitative technique to map bio-markers *in vivo*, as a complete solution does not currently exist in the literature. The following facets of the project were novel:

- The overall concept developed in this project to use GNPs as a contrast agent to map radiosensitivity in order to inform radiotherapy dose prescription (and additionally act as a dose enhancer) is novel.
- The use of the spectrometer developed by Politecnico di Milano for GNP concentration measurement is novel; the spectrometer had previously been used for XRD techniques [45], [46] and also to measure proton induced x-ray emissions [47]. The spectrometer was optimised for use to measure GNPs (in terms of source used).
- An XRF system was developed that has the highest sensitivity to GNP concentration found in literature (sensitive down to 0.005 mgAu/ml, and further improved to a detection limit of 0.001 mgAu/ml). The closest technique for quantitative measurement of GNP concentration was an order of magnitude less sensitive [24].
- A K-XRF imaging system was previously reported in the literature; however, fundamental limitations of interaction cross sections involved in K-XRF (refer to Section 2.5.1.1) means that an L-XRF technique would provide greater

sensitivity. To the author's knowledge, our system is the first quantitative L-XRF GNP measurement system.

- Previous work in tissue engineering enabled production of 3D cellular phantoms, and also artificial cancer masses (refer to Section 3.4.10). I extended the established technique to make novel XRF imaging test phantoms, and also to produce cellular phantoms to demonstrate the capability of the quantitative XRF system in measuring GNP uptake in cells. The novel technique incorporated GNP inclusions in the cells in a known distribution; to the author's knowledge this is the first time that such GNP-included cellular phantoms have been made.
- The idea to combine XRF/XRD as an imaging system to measure GNP concentration and distribution and to identify tissue type for radiotherapy applications is novel. The system design put forward in this project is novel, and open to further development in the future.

1.7 My contribution to this work

An interdisciplinary approach was required to meet the aims of this project, and as such this was a collaborative effort. The following departments were involved in this collaboration, and I spent time in each department to draw the research lines together:

- Radiation Physics Section, Department of Medical Physics and Bioengineering, UCL, London
- Division of Surgery and Interventional Science, UCL, London
- Tissue Repair and Engineering Centre, UCL, London
- Department of Electrical Engineering, Politecnico di Milano, Milan

The project required the convergence of different research areas. The areas are listed below, along with my particular contribution to each aspect of the project:

1. Understanding and identification of clinical needs in radiotherapy:

   I was well placed to identify clinical needs in radiotherapy as I previously worked as a hospital physicist in a radiotherapy department. I identified gaps in the capabilities of current radiotherapy techniques through a focussed literature search. Also, attendance at the Mayneord Philips Summer School, 2009, which was focussed on modern radiotherapy techniques, broadened my awareness of the field. Discussion with clinicians from the UCL Cancer Institute, research physicists at the Royal Marsden Hospital, Surrey, and academic staff in the Radiation Physics Department, UCL (in particular my supervisors) led to the selection of this particular project.

2. Tissue engineering and tissue culture:

   I worked at the Division of Surgery and Interventional Science, UCL, London to learn tissue culture techniques. I performed all cell maintenance involved in the cellular studies. I developed a protocol to achieve GNP uptake in cells, and verified this procedure through assistance with the Electron Microscopy Service at the Royal Free Hospital, Hampstead. I spent time at the Royal National Orthopaedic Hospital, Stanmore, to learn existing tissue engineering techniques. I extended this standardised technique to produce novel 3D cultures of cells with GNP inclusions. I designed and constructed a range of 3D bio-phantoms that were appropriate to be measured by the developed XRF system. Building upon previously developed tissue engineering techniques, I extended existing procedures in making ACMs through novel addition of GNP inclusions. The 3D phantoms had optimum design for use in XRF imaging systems.

3. Handling of nanoparticles:

   I followed the recommended procedure to re-suspend the NPs in a water solution, and provided a range of GNP concentration solutions in order to test the system. I designed a range of GNP imaging phantoms to include concentrations and contrasts found *in vivo*. All but one set of samples were made by me (a collaborator made the set of samples taken to the Elettra Synchrotron source for the synchrotron L-XRF study).

4. X-ray detector development:

   The silicon drift detector and controlled drift detector were designed and made by our collaborators from the Department of Electrical Engineering, Politecnico di Milano, Milan. The high purity germanium detector was manufactured by EG&G, Ortec. I was involved in selecting the optimum settings of each detector, such as pulse shaping time, amplification etc. appropriate for use in gold XRF measurement.

5. Implementation of x-ray techniques in the development of a quantitative system sensitive to GNPs:

   I designed and optimised the K-XRF system to induce gold XRF. The design of the L-XRF already existed and had been previously used to measure proton induced x-ray emissions [47]; however I optimised it for use to induce L-XRF in gold, including selection of a source (in terms of target, energy, filtration), detector collimation and geometry. Along with collaborators (who assisted with detector operation) I performed the measurement and comparison of the different XRF systems.

   I was successful in a proposal for a grant to gain synchrotron access for the series of measurements (both at the Diamond Light Source, UK and at the Elettra Synchrotron Source, Trieste). I planned the necessary experiments for each synchrotron trip, and provided samples for this measurement campaign (biological and non-biological). I was part of a team consisting of members from UCL and Politecnico di Milano which operated in shift work to collect all the XRF and XRD data.

6. Feasibility study of XRF imaging of GNPs, and work towards a combined XRF/XRD imaging technique:

   I designed and made a set of Perspex phantoms with GNP inclusions to mimic concentrations found *in vivo* in order to test the performance of XRF imaging systems. I also extended an existing protocol to make cellular 3D bio-phantoms with GNP inclusions to test the imaging capabilities of the XRF technique.

   I devised a set of measurements necessary to direct future work in the development of a combined XRF/XRD imaging system, and performed the data acquisition of all of the investigations. I have also referred to literature to support my proposal of measurements previously undertaken. I drew conclusions as to the appropriateness of the combined modality system.

7. Data analysis of GNP measurements:

   I developed Matlab code to perform all data analysis of the measurements reported in this thesis, with the exception of the 2D image reconstruction, which was performed by colleagues at the Politecnico di Milano.

1.8 Structure of this thesis

This thesis has already outlined the clinical problem, and put forward a novel technique that meets the listed requirements. The novel system makes use of GNPs as a contrast agent combined with an XRF technique to measure tumour properties *in vivo*. Chapter Two will demonstrate the sensitivity of XRF techniques to make quantitative measurements of a range of GNP concentrations expected to be found *in vivo*. The performance of three alternative XRF systems will be compared, and conclusions made as to the suitability of the XRF technique in meeting the requirements to solve the clinical problem. Chapter Three will present the procedure that has been developed for making novel 3D GNP-loaded cellular phantoms. It will also demonstrate that GNP uptake in cells has been achieved, and will report the measured passive GNP uptake in two different cell lines (cancer and non-cancer lines were considered). A demonstration of the novel XRF technique’s ability to measure GNP uptake in cells is presented. Transmission electron microscopy was used to confirm and further understand the GNP uptake process in cells. Chapter Four presents XRF images collected of different GNP phantoms constructed to test the system imaging capabilities. These images act as a proof of concept for the envisaged XRF imaging technique. A preliminary set of measurements is finally presented to assess the feasibility of a combined XRF/XRD imaging system, and conclusions are made as to the viability of such a technique in radiotherapy.

Chapter Two

2 Quantitative measurement of gold nanoparticle concentration

2.1 X-ray fluorescence: Introduction

X-ray fluorescence (XRF) can be used to provide quantitative information about elements present in a sample, and the magnitude of the XRF signal is proportional to the concentration of that element (Section 1.5.4). This project proposes to measure GNP concentration using XRF measurement techniques. XRF involves high energy radiation and so can be a useful technique in measuring GNP distribution *in vivo*. XFCT imaging of a GNP-loaded PMMA phantom has been successfully demonstrated [38]; however this technique requires a pencil beam and therefore its speed will limit its clinical use. Relatively high GNP concentrations were tested by the system, the lowest being 5 mgAu/ml. However it is expected that much lower concentrations will typically be taken up by cells, with concentrations of the order of 0.01 mgAu/ml expected in tumours [24], [25]; refer to Section 1.5.1 for a discussion of expected concentrations from literature. The XFCT technique was designed to induce and detect K-XRF as opposed to L-XRF; this is beneficial for measurements at depth as higher energy x-rays are required to penetrate the required distance.

The XRF properties of gold are displayed in Table 4 and Figure 4.

Table 4 Theoretical energies and yields of the gold K-XRF and L-XRF emissions [31].

	$K_{\alpha1}$	$K_{\alpha2}$	$K_{\beta1}$	$L_{\alpha1}$	$L_{\alpha2}$	$L_{\beta1}$	$L_{\beta2}$	$L\gamma_1$
Energy (keV)	68.80	66.99	77.98	9.71	9.63	11.44	11.58	13.38
Emission relative to $K_{\alpha1}$ (%)	100	59	23	37	4	25	8	4
Absorption edge energy (threshold energy for fluorescence) (keV)	80.7	80.7	80.7	11.9	11.9	13.7	11.9	13.7

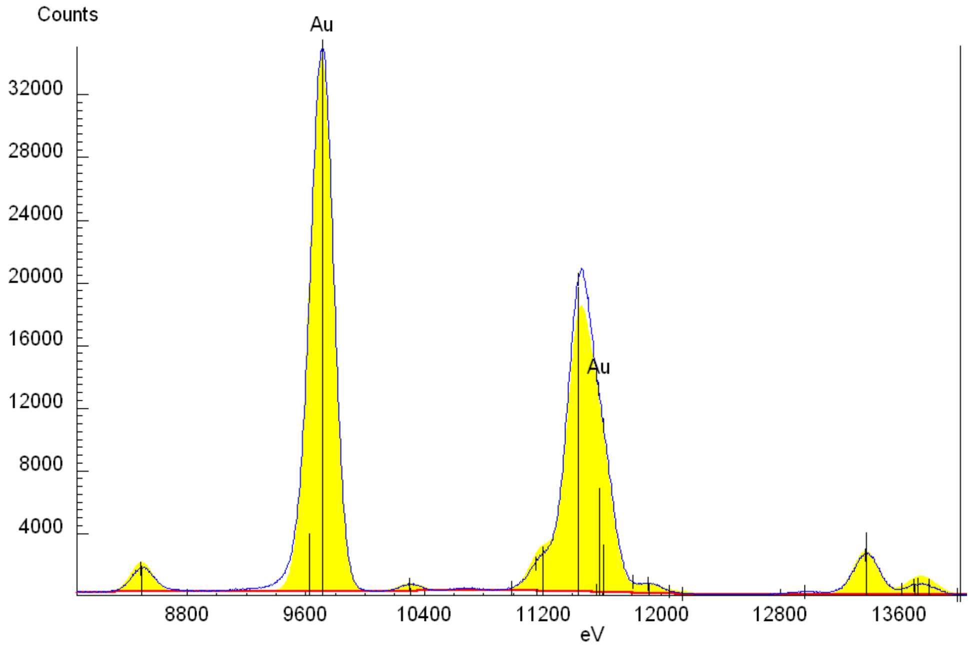

Figure 4 Theoretical Lα and Lβ gold x-ray emissions, taken from Winaxil X-ray Analysis Software are displayed.

This chapter presents the measurements made with a novel system in assessing the ability of the fluorescence signal to determine nanoparticle concentration. The sensitivity of the system was also found through measurement of the minimum detectable concentration of nanoparticles. Three different XRF systems are compared, one using synchrotron radiation, one a bench-top molybdenum target x-ray tube (both inducing gold L-XRF) and the other a higher energy tungsten target bench-top system (used to induce gold K-XRF).

2.2 Nanoparticle samples

The samples consisted of GNPs (Aurovist^{TM}, Nanoprobes Inc., USA) suspended in a 1 ml de-ionised water buffer. The nanoparticles used had a 1.9 nm gold core and water soluble organic shell. Each sample solution was held in a plastic 1.5 ml Eppendorf tube (Eppendorf, Germany). Twelve samples were made with concentrations ranging from 0.001 – 8.0 mgAu/ml (made to an accuracy of ± 1%), selected to resemble possible tumour gold concentrations *in vivo* (refer to Section 1.5.1), and to test the minimum detectable concentration. The samples are displayed in Figure 5.

Figure 5 GNP samples produced over different concentrations ranging from 0.001 – 8 mgAu/ml.

The 1.9 nm GNPs are delivered freeze dried and are stored in a plastic pot. There is a mass of 40 mg GNPs per pot. The procedure used to suspend the GNPs in de-ionised water (DIW) is as follows:

1. 0.2 ml DIW was added to 40 mgAu (using a micropipette (Eppendorf) with an accuracy of 1 µl.

2. All 40 mgAu solution was pipetted into a centrifugal tube filter (provided by Aurovist^{TM}) and centrifuged for 8 mins at 15,000 x g.

3. Another 0.2 ml DIW was added to the remnants in the original pot, transferred to the tube filter and centrifuged again for another 8 mins.

4. Step 3 was repeated. In total, 0.6 ml DIW was added to the 40 mg of GNPs.

5. The filter piece was removed, and another 0.4 ml DIW added to make the volume of DIW added up to 1ml. This gave 1 ml of 40 mgAu/ml concentration.

6. In order to minimise liquid losses when dealing with small volumes, the high concentration was diluted to produce a stock solution of 20 mgAu/ml. 0.5 ml DIW was added to a clean Eppendorf tube, followed by 0.5 ml of the 40 mgAu/ml solution. This made 1 ml of 20 mgAu/ml, and left 0.5 ml of 40 mgAu/ml for future use.

7. When not in use, all GNP solutions should be refrigerated at ~ 5 °C. It was observed that samples not refrigerated for a time period of a few days suffered from the GNPs settling out and clumping together.

Error observations:

- Not all of the 40 mg gold was successfully transferred to DIW (negligible loss): three filtrations were performed to maximise recovery of the GNPs.

- Not all of DIW measured was transferred: some liquid remained on the pipette tip (this is a negligible loss, and may counteract the loss in the recovery of GNPs).

- The volume of DIW is accurate to 1 μl (the accuracy of the micropipette).

A 1 ml DIW sample was measured for background data. The samples were held on a water-cooled cooling plate during measurement, operating at a temperature of 5 ºC, to reduce the possibility of the sample liquid evaporating. No sample evaporation was observed during the measurements.

The sample concentration error was determined by repeating the sample making process three times for the same concentration (0.03 mgAu/ml). Each sample was measured using the XRF technique and data analysis process described in the following sections. The percentage standard deviation of the measured XRF signal for the three samples was found to be 3.7% (the percentage error of each XRF measurement was 1.3%). This demonstrates the repeatability of the sample making process.

2.3 Synchrotron fluorescence system: L-fluorescence

2.3.1 System design

Measurements were made at the SYRMEP beamline at the Elettra synchrotron source, Trieste, Italy. The XRF system consists of a collimated silicon drift detector (SDD) [48], [49]. A laminar x-ray beam irradiated the sample close to the top surface to minimize self attenuation of the fluorescence signal (Figure 6). A charge-coupled device (CCD) camera located behind the sample was used to monitor the beam-sample alignment.

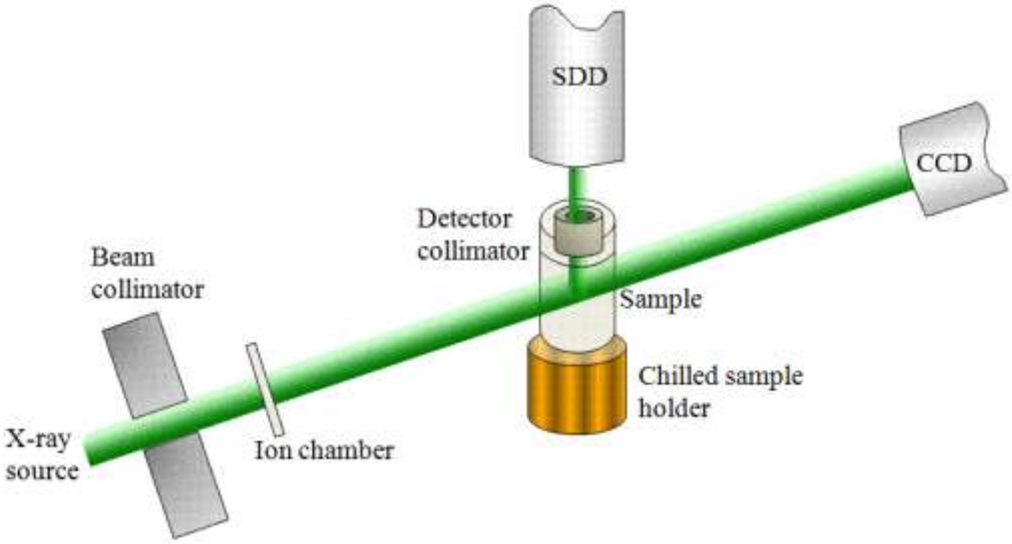

Figure 6 Experimental set-up of XRF measurement system.

2.3.2 X-ray source

The photoelectric cross section for XRF is greatest when the exciting x-ray is just above the absorption edge energy. The beamline energy was set to 15 keV (above the threshold for gold L-XRF of 11.9 keV and 13.7 keV for Lα / $L\beta_2$ and $L\beta_1$ fluorescence respectively). The energy set was 1.3 keV above the highest L-edge of gold, a compromise between optimum excitation and minimization of the impact of the Compton shoulder background on the gold fluorescence line. The beamline collimators gave a beam 13 mm wide and 2.7 mm high, covering the full width of the sample.

2.3.3 X-ray detector system

A 10 mm^2 SDD chip, produced in polysilicon technology by PNSensor GmbH and featuring an on chip JFET, was mounted in a dedicated vacuum-tight housing together with a Peltier cooler and dedicated front-end electronics in charge amplifier configuration with pulsed reset developed by Politecnico di Milano, Italy, and INFN Milano [50]. Optimum energy resolution is found at a 3 μs shaping time. However, a sub-optimal shaping time constant of 1 μs was chosen for the whole measurement as a compromise between energy resolution (still very high for this shaping time, with a measured value of 134 eV FWHM at 5.9 keV) and pulse pile-up occurrence. The detector can operate at a maximum count rate of the order of 10^5 s^{-1}. The SDD, consisting of a 450 μm thick detector-grade silicon substrate, gives a high efficiency of gold $L\alpha$ peak detection (97 %). No gold contacts are present in the detector arrangement, and so all gold signal measured derives from the samples.

The preamplifier signal was fed to a 5th-order shaping amplifier with 1 μs shaping time constant. A multichannel analyzer (MCA-8000A, Amptek Inc., MA, USA) interfaced the detector with a personal computer for data acquisition and spectrum analysis.

2.3.4 Detector Collimator

The detected x-rays consist of: (i) the desired gold XRF signal, and (ii) the unwanted background resulting from Compton and coherently scattered x-rays and fluorescence x-rays from other elements present in the sample and the experimental set-up. For a fluorescence system to be able to detect elements present in low concentrations, the background signal must be minimised as much as possible in order for the XRF peak to be visible. Firstly, an optimum system geometry was used, involving mounting the detection module at 90° to the incident beam. This acted to minimize Compton background, profiting also from the fact that the synchrotron light was linearly polarized in a plane parallel to the detector surface. Secondly, a detector collimator consisting of a 2.9 mm hole set in a 15.4 mm long aluminium block reduced the detection of Compton scattered x-rays from the sample. The use of a collimator was a compromise between reducing the Compton scatter peak width to give a low background signal beneath the gold XRF peaks, and maintaining a high XRF count rate (and thus reducing exposure time). The detector collimation used improved the gold fluorescence signal to background ratio by 35% compared with no collimator. The detector collimator is displayed in Figure 7, alongside the sample held in measurement position.

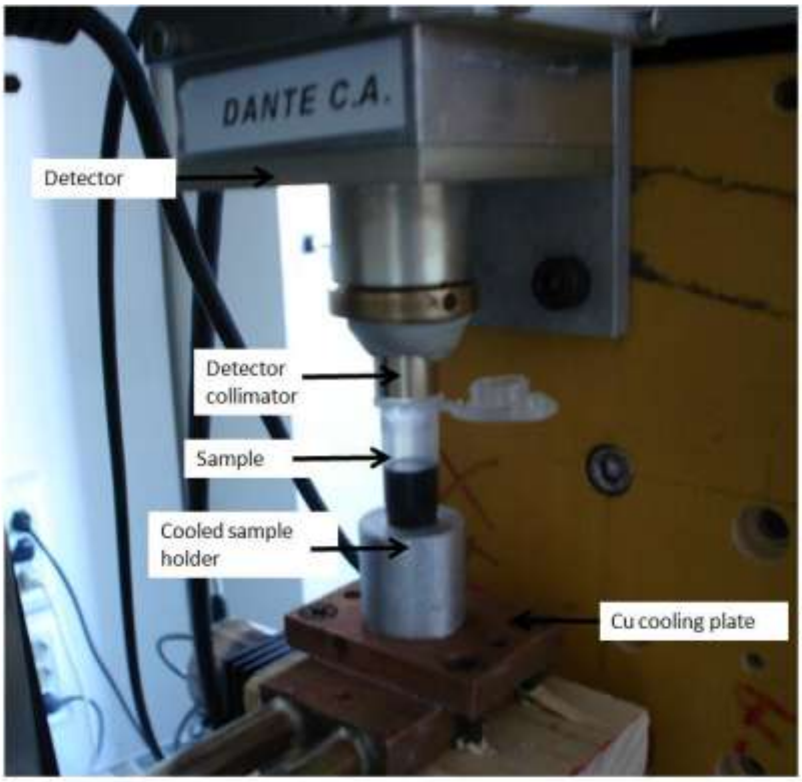

Figure 7 Experimental arrangement of sample, detector collimator and SDD.

2.3.5 Measurement procedure

The main L-XRF lines of gold are peaked at 9.7 keV and 11.4 keV corresponding to gold $L\alpha_1$ and $L\beta_1$ respectively (see Table 4). The duration of spectra collection was set to keep the uncertainty due to counting statistics of the fluorescence peak below 1% for each sample concentration measured. Typical measurement times ranged from 20 s for the 8 mgAu/ml sample to 1800 s for the very low concentrations (down to 0.0032 mgAu/ml).

2.4 Translation to a bench-top fluorescence system: L-fluorescence

The XRF GNP concentration measurements were repeated by replacing the monoenergetic synchrotron source with a commercially available bench-top molybdenum target x-ray tube to determine the clinical viability of the XRF measurement system.

2.4.1 Difficulties involved in translating from a synchrotron source to a clinical x-ray tube

2.4.1.1 Translation from a monoenergetic to polyenergetic source

As stated previously, the ideal spectral shape to induce XRF is one consisting of many x-rays of energy just above the absorption edge of the sample. Ideally there should be as few as possible below the absorption edge energy, as these do not induce XRF and only contribute to the unwanted background signal. Likewise, x-rays of energy well above the absorption edge are less likely to induce fluorescence than those just above the absorption edge; these x-rays may be Compton scattered by the samples and will also contribute to the unwanted background. For this reason, monoenergetic synchrotron radiation sources provide the optimum spectral shape if they are tuned just above the absorption edge of gold. Bench-top x-ray tubes are polyenergetic sources, and so a greater proportion of the incident spectrum will not be converted to useful XRF signal than when using a monoenergetic synchrotron source. The spectrum shape of a bench-top x-ray source may be optimised for XRF measurements by selecting an appropriate filter material, filter thickness, and tube voltage (kV_p). The combination of a filter and appropriate kV_p can re-shape the spectrum to a more optimum distribution.

The L-XRF system used a molybdenum target source, which produces a spectrum that has a major contribution from the characteristic K-lines of molybdenum. In this sense, it can be considered as a quasi-monoenergetic source (as demonstrated later in Figure 27).

2.4.1.2 Translation from high to low intensity

Synchrotron radiation sources are also ideal for XRF measurements as they are high intensity sources. Bench-top sources are approximately four orders of magnitude lower in spectral brightness (defined as photon fluence rate per solid angle per 0.1% bandwidth) [31]; however when considering spectral width the integrated intensity of a bench-top source is approximately two orders of magnitude less than a synchrotron source. Therefore, translation to a bench-top system requires longer acquisition times to achieve similar counting statistics. However, integrating the intensity across all energies above the absorption edge leads to sufficient intensities for XRF measurement. Also, use of commercially available high power bench-top sources can boost the intensity.

2.4.1.3 Translation from non-diverging to diverging source

Synchrotron sources provide a non-diverging x-ray beam, which is beneficial in XRF measurements because: (i) it is easier to achieve a 90° detection geometry to minimise the Compton background and (ii) the beam can be easily collimated to be only incident upon the sample. The latter point minimises background scatter due to interactions of x-rays with other materials present in the system. Bench-top sources produce a diverging x-ray beam, and therefore a higher scatter background which can mask the XRF signal if measuring low concentrations. Bench-top sources are quasi-parallel at a large distance from the target; however, the inverse square law decreases the x-ray intensity at distance.

Polycapillary optic technology can be used to convert the diverging beam into a parallel beam. Polycapillary lenses are monolithic structures of bundles of hollow glass capillaries. X-rays are guided along the capillaries by total external reflection (TER), and only accepted into the optic channels if the incident angle of the x-ray is below the critical angle for TER at that energy ($\theta_c(E)$). A collimating polycapillary optic works upon the following principle; if the curvature of the fibres is less than the critical angle for TER, the direction of the x-rays can be guided to exit the optic parallel to each other, as illustrated in Figure 8.

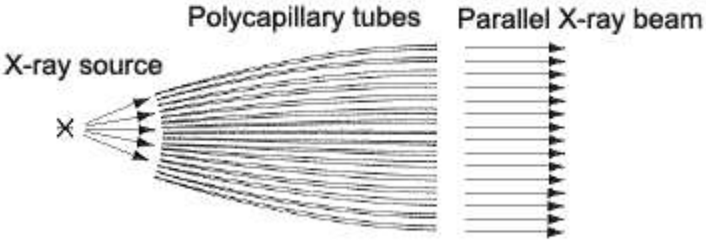

Figure 8 Concept of a collimating polycapillary optic [51]

A collimating polycapillary optic was coupled to the bench-top molybdenum source in order to give a quasi-parallel beam.

2.4.2 System design

Measurements were made at the Dipartimento di Elettronica e Informazione, Politecnico di Milano, Italy. The bench-top L-XRF system consists of the same collimated SDD used for the synchrotron measurements. The same measurement geometry was used as for the synchrotron technique, as displayed in Figure 9.

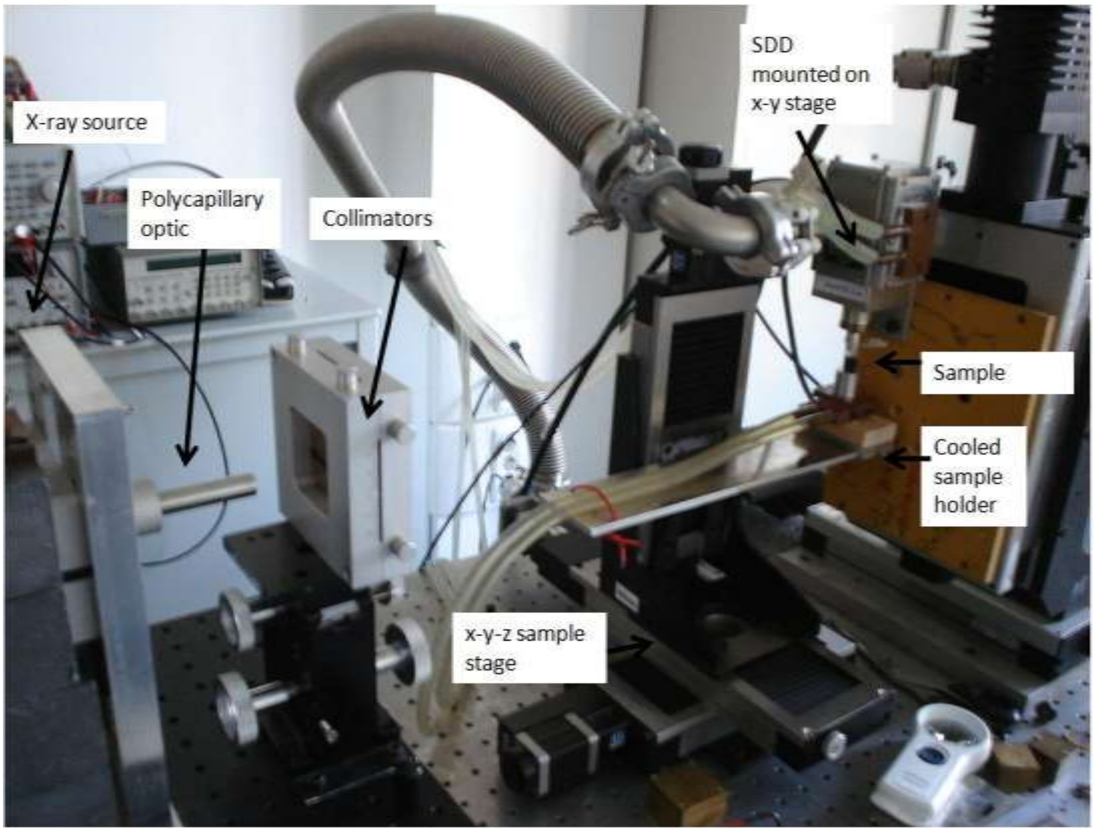

Figure 9 Experimental arrangement of bench-top L-XRF system.

2.4.3 Bench-top x-ray source

A molybdenum-anode x-ray generator (X-Beam® Powerflux PC, X-ray Optical Systems, NY, USA) operating at 50 kV_p and 1 mA was used to induce x-ray fluorescence of the GNP samples. This source makes use of a polycapillary semi-lens which acts to collect the divergent x-rays emitted by the anode and collimate them to a quasi-parallel beam. The divergence of the output beam is approximately 1.75 mrad

(0.1°) at the molybdenum $K\alpha$-line (factory data). The intensity of the molybdenum $K\alpha$-line is of the order of 10^8 photons/s at maximum anode voltage (50 kV) and beam current (1 mA) (factory data). The beam is approximately 6 mm in diameter.

2.4.4 Beam collimator

The incident beam was collimated using a Cross Slit Screen 3002.40 (Huber Diffraktionstechnik GmbH, Germany), consisting of tantalum blades and aluminium housing. The blades can be set to a precision of 0.02 mm. The slits were used to set a beam size of 1.5 mm high and 3.4 mm wide, the width covering the uniform portion of the beam.

2.4.5 X-ray detector system

The same SDD module was used as for the synchrotron measurements, with a slight modification. Zinc fluorescence lines were detected during the synchrotron measurements, which interfered with the $L\alpha$ gold line. In order to reduce the unwanted zinc contribution to the detected spectrum, the beryllium window holder of the SDD (which is made of an aluminium-zinc alloy and was the source of zinc contamination) was enlarged to avoid interaction with incident x-rays. No zinc was then seen. The same aluminium collimator and MCA were used as for the synchrotron measurements.

2.4.6 Measurement procedure

The same measurement procedure was used as outlined in Section 2.3.5.

2.5 Translation to a bench-top fluorescence system: K-XRF

In order to perform fluorescence analysis at depth, higher energy XRF x-rays are required to penetrate through overlying tissue. The K-absorption edge of gold lies at 80.7 keV, and so in order to induce K-XRF a higher energy source is required. In addition to this, a detector more suited to detecting higher energy x-rays is required. Therefore translation to a K-XRF system involved: (i) replacing the SDD with a high energy x-ray detector, and (ii) replacing the molybdenum x-ray source with a tungsten target higher energy source. Gold K-XRF characteristics are displayed in Table 4.

2.5.1 Difficulties involved in translating to a K-XRF system

2.5.1.1 Translation from L-XRF to K-XRF

In addition to the greater penetrations, another advantage of K-XRF is that the fluorescence yields for K-shells is more than a factor of three larger than for the L-shells (refer to Table 4). However, the photoelectric cross section just above the L-edge of gold (σ (11.98 keV) = 179.11 cm^2/g) is over 21 times greater than that just above the K-edge (σ (81.13 keV) = 8.2842 cm^2/g) (values taken from [52]). Also, the ratio of photoelectric cross section to total scatter cross section (corresponding to signal to noise ratio) is greater for L-XRF than K-XRF (ratios of 43.4 and 22.0 at the L-edge and K-edge energies respectively). This means that the scatter contribution to the background beneath the gold signal for the K-XRF system is double that for the L-XRF system, making it less sensitive to low concentration measurement.

2.5.1.2 Translation from low energy to high energy source

As mentioned in Section 2.4.1.3, bench-top x-ray tubes produce a diverging beam. An ideal XRF system uses a collimated parallel x-ray beam so that it is only incident on the sample (i) in order to avoid inducing fluorescence in other material present in the system, (ii) in order to minimise the background scatter contribution to the detected spectrum, and (iii) to fully benefit from Compton reduction in a 90° detection geometry. For the L-XRF bench-top system, this problem was solved through use of polycapillary x-ray technology to convert the diverging beam in to a parallel beam. However for high energy sources such as the one required to induce K-XRF, polycapillary optic techniques may not be implemented as the high energy x-rays will penetrate through the glass capillary fibres rather than being channelled between them [45]. Therefore, a high scatter background was present throughout these measurements.

The source target used in the K-XRF measurements is tungsten which at high kV_p settings produces a polyenergetic beam with tungsten characteristic lines. It is important to consider the effect of (i) the polyenergetic beam increasing the background beneath the gold signal, and (ii) the possible overlapping of the tungsten K-lines with the gold signal.

2.5.1.3 Translation from SDD to high energy detector

The SDD is an ideal detector for use in an L-XRF measurement system; its high energy resolution and low noise makes it useful for measuring very low concentrations. However, the detection module being made of a 450 µm thick silicon substrate means that it is not efficient at absorbing and detecting high energy x-rays. The SDD was replaced with a high purity germanium (HPGe) detector of active depth 7 mm which is more efficient at K-XRF energies (99.7% efficiency of detection of the gold Kα_1 68.8 keV).

2.5.2 System considerations

The diverging nature of the tungsten source beam meant that careful consideration had to be given to component materials used in the system to ensure that no fluorescence lines of other materials interfered with the K-XRF lines of gold. The K-lines of potential system materials were reviewed to identify problem materials.

It can be seen that the fluorescence lines of lead (commonly used in shielding and collimation) and tungsten (the material of the x-ray source) are very similar to the gold K-lines, and so would complicate the measured spectrum and subsequent analysis. The fluorescence characteristics of lead and tungsten are displayed in Table 5.

Table 5 Fluorescence characteristics of lead and tungsten [31].

	Pb			**W**			**Au**		
	Kα_1	***Kα_2***	***Kβ_1***	***Kα_1***	***Kα_2***	***Kβ_1***	***Kα_1***	***Kα_2***	***Kβ_1***
Energy (keV)	74.96	72.79	84.92	59.31	57.97	67.23	68.8	66.99	77.98
Emission relative to $K\alpha_1$ (%)	100	60	23	100	58	22	100	59	23
Threshold energy for fluorescence (keV)	88.01	88.01	88.01	69.53	69.53	69.53	80.7	80.7	80.7

The smallest difference between the significant K-lines of tungsten and gold is 0.24 keV (gold $K\alpha_2$ – tungsten $K\beta_1$); this difference will not be resolved by the HPGe detector (measured energy resolution of 0.7 keV at 59.5 keV). However, use of a tungsten target was acceptable as long as no primary beam was incident on the detector. This was achieved by (i) using a 90° detection geometry, and (ii) using detector shielding to minimise the amount of primary beam incident on the detector. No direct primary radiation was measured by the detector; however Compton scattered tungsten $K\alpha$-peaks were found. The Compton scattering process reduced the energy of the tungsten lines and so they did not interfere with the gold signal.

Lead XRF lines are at an energy that can be easily resolved from the gold signal using the HPGe detector, and so lead presence in the set up posed no problems.

2.5.3 System design

Measurements were made at the University College London Radiation Physics laboratory, London, UK. The K-XRF system consists of a collimated HPGe detector. An x-ray beam irradiated the sample and the HPGe detector was placed at 90° to the incident beam beside the sample (Figure 10). The detector was beside rather than above the sample due to practical problems in the detector holding module. A complementary metal-oxide-semiconductor (CMOS) sensor was located behind the sample to monitor the beam-sample alignment, and an ionisation chamber was used to correct for changes in incident beam intensity.

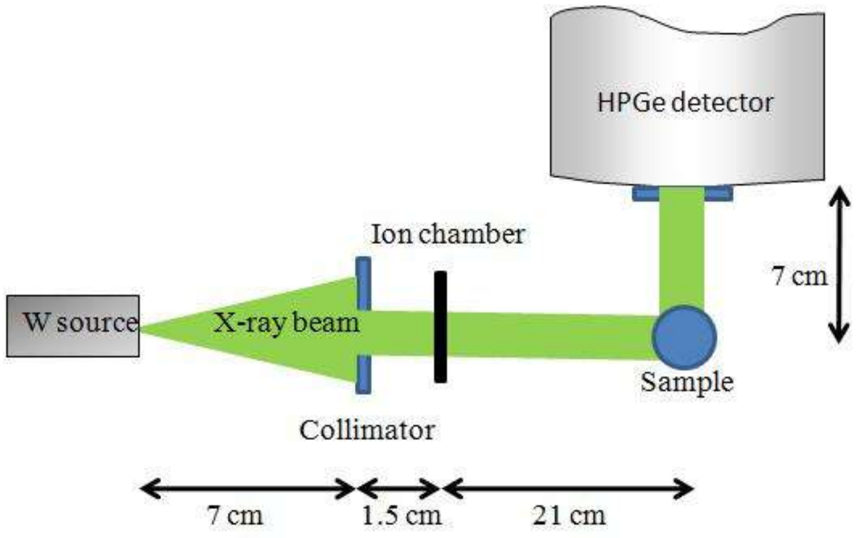

Figure 10 Experimental set-up of bench-top K-XRF measurement system, viewed from above.

2.5.4 X-ray source

The $K\alpha_1$ fluorescence at 68.8 keV is the dominant emission and so the system was designed to increase sensitivity to this energy. The choice of exciting source is governed by several factors. Firstly a photon energy that is greater than, but as close as possible to, the gold K-edge at 80.7 keV is required to overcome the binding energy of the K-electrons and thus maximise the gold XRF yield. Secondly, the source should have as narrow a spectral width as possible in order to minimise the background due to scatter in the gold fluorescence peaks region.

An industrial water-cooled x-ray tube (AGO installations, Philips) was used with a tungsten anode of nominal focal spot size 3 mm x 3 mm, and inherent filtration of 1 mmBe. It runs in continuous mode with a maximum output of 160 kV and 19 mA. A specially designed lead collimating circular window of 5 mm diameter was mounted onto the front of the x-ray tube to act as an initial coarse collimator to reduce x-ray scatter in the room.

2.5.5 X-ray filtration

The simplest method of filtration is to use a material with a K-absorption edge at an appropriate energy that selectively allows a range of wavelengths to pass through and attenuates other wavelengths. The amount of attenuation is proportional to the thickness of filter material, the thickness of which is a compromise between attenuation of unwanted wavelengths and intensity of the useful wavelengths.

Lead has a K-absorption edge at 88.2 keV and therefore provides sufficient shaping of the beam. A simple simulation was performed to assess the effect of filter thickness on spectral shape. SpekCalc [53] was used to simulate an x-ray spectrum from a tungsten source set at 120 kV_p, 30° anode angle, 1 mmBe inherent filtration (according to the specification of the x-ray unit used in these measurements). An inverse square law correction was made to calculate the spectrum at the position of the sample (70 mm from the source). An attenuation calculation was performed across the spectrum by performing a power fit to the x-ray attenuation coefficients of lead (taken from [52]). Figure 11 demonstrates the effect of using different thicknesses of lead filter upon spectral shape.

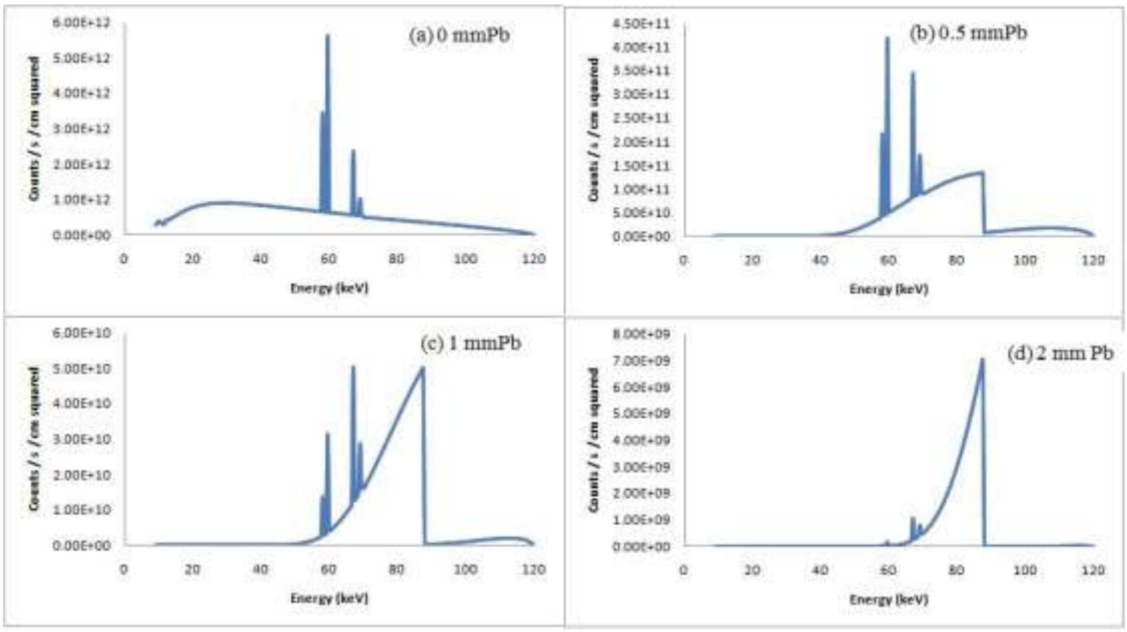

Figure 11 Simulated spectral shape of x-ray beam at tube voltage 120 kV_p with a range of lead filter thicknesses.

Figure 11 demonstrates that the characteristic tungsten lines become reduced as lead thickness increases; this is beneficial as the tungsten lines contribute to the detector dead time without contributing to the gold XRF production. It can be seen that the spectral width of the spectrum becomes narrower with increasing lead thickness.

When selecting filter thickness, a compromise must be made between achieving a high enough x-ray intensity and narrow enough spectral width. A series of measurements of spectral width and intensity were made over a range of lead filter thicknesses; results are displayed in Figure 12.

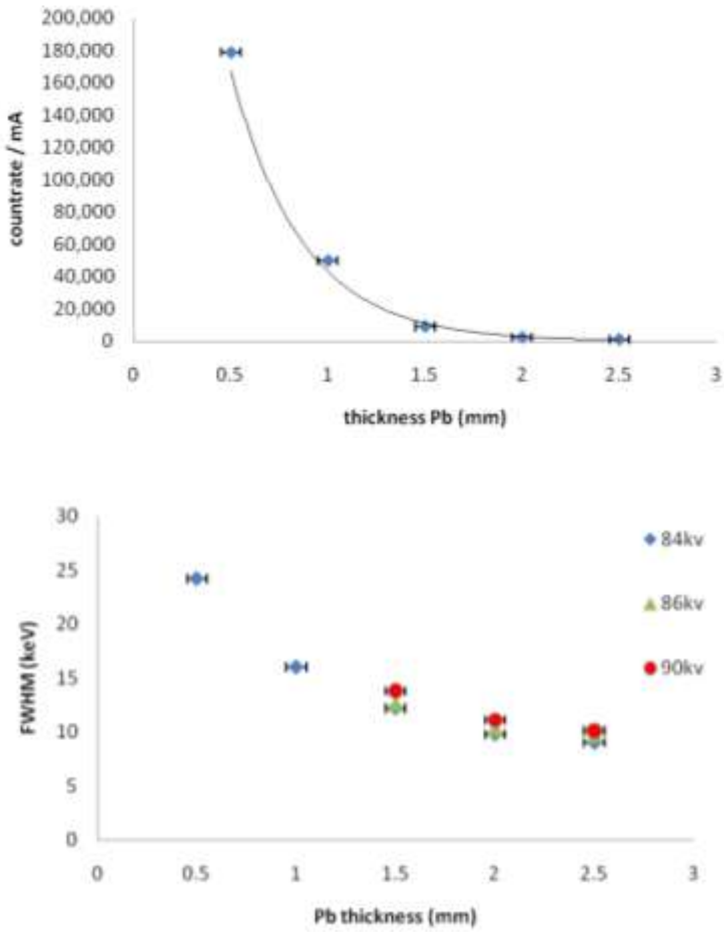

Figure 12 Measured effect of lead filter thickness on (a) x-ray intensity corrected by incident intensity measured using an ion chamber, and (b) spectral width (expressed as full width at half maximum (FWHM)).

The low energy cut-off (minimum energy of the spectrum) of the filtered beam was measured for a range of lead filter thicknesses. The low energy cut-off is related to filter thickness.

Table 6 Measured minimum energy of filtered x-ray spectrum at different lead filter thicknesses.

Filter thickness (mmPb)	Low energy cut-off (keV)
0.5	41.1
1	47.9
1.5	54.4
2	58.6

Table 6 shows that as the filter thickness increases, the minimum energy of the filtered spectrum also increases as the spectral width narrows. After consideration of all factors it was decided that use of a 0.5 mm lead filter and tube setting of 120 kV_p gave a compromise between spectral width, minimum energy of beam and x-ray intensity.

2.5.6 HPGe detector

An HPGe detector (manufactured by EG&G Ortec) was used for the detection of scattered and fluorescence photons. The HPGe detector consisted of a single planar germanium crystal of diameter 36 mm with an active depth of 7 mm enclosed in a vacuum with a 0.254 mm thick beryllium window. The HPGe operated under liquid nitrogen temperatures. Spectrum Master 92X Multi Channel Analyser (EG&G Ortec) and Maestro 32 software was used to analyse the energy spectrum. The HPGe was positioned as close as possible to the samples (at a distance of 70 mm) in order to maximise the detection of the isotropically emitted XRF signal. Closer distances were not possible due to practical limitations in the experimental set-up.

The energy resolution of the HPGe detector was measured to be always less than 0.7 keV at 59.5 keV using an Americium-241 source. This measurement was repeated before and after each measurement session. The efficiency of the 7 mm thick germanium crystal was calculated as being 99.7% over the gold $K\alpha_1$ energy (68.8 keV). The detector was encased in a purpose built lead x-ray shield with a circular aperture of diameter 10 mm on the front face of the detector, concentric with the Ge crystal. This acted to shield from unwanted multiple scatter x-rays and to minimise the detector dead time.

The HPGe detector energy to channel number calibration was found to drift over time. The XRF analysis was modified to account for the drift in the position of XRF peaks by giving a degree of freedom to the peak position of the Gaussian fit.

A tube current of 12 mA was selected to avoid over-loading the x-ray tube. The dead time of the HPGe detector was below 10% at all times; greater deadtimes can result in pulse pile-up of the x-ray counts and can warp the energy spectrum.

2.5.7 Measurement procedure

The time duration of spectra collection was set to keep the counting statistics error of the fluorescence peak below 1% for each sample concentration measured. A measurement time of 1200s provided sufficient counting statistics. Ion chamber readings were recorded for each acquisition to perform an incident x-ray intensity correction, as the tube intensity varied between measurements.

2.6 Data analysis procedure

Each measured spectrum was analysed to extract the concentration information held by the gold XRF signal.

2.6.1 Isolation of the gold L-XRF signal

Example measured spectra are displayed in Figure 13, showing the presence of *Lα, Lβ* and also *Lγ, Ll* and *Ln* peaks (the latter three only visible for high concentration samples).

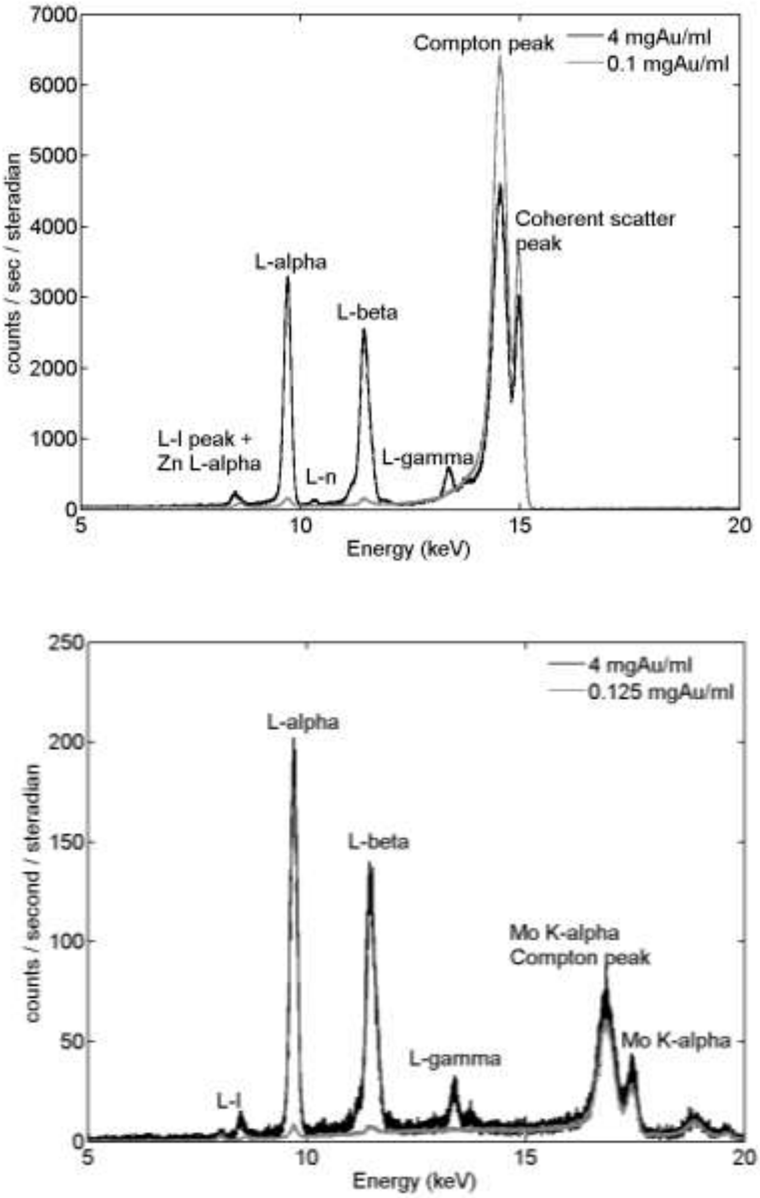

Figure 13 (top) Synchrotron measured spectra of two different GNP concentrations (4 mgAu/ml (60 s acquisition time) and 0.1 mgAu/ml (120 s)); (bottom) Laboratory measured spectra of 4 mgAu/ml (120 s) and 0.125 mgAu/ml (840 s).

A region covering the *Lα* and *Lβ* peaks was selected for analysis (those lines being the strongest present in the range of concentrations measured). A 6-order polynomial least squares fit gave the best fit to the background non-peak regions (an improvement of 11% and 58% in the standard deviation of the fit was found using a 6-order polynomial compared with a 2-order polynomial and linear fit respectively), and was interpolated to give an estimate of the background signal under each gold XRF peak (an example background fit is displayed in Figure 14).

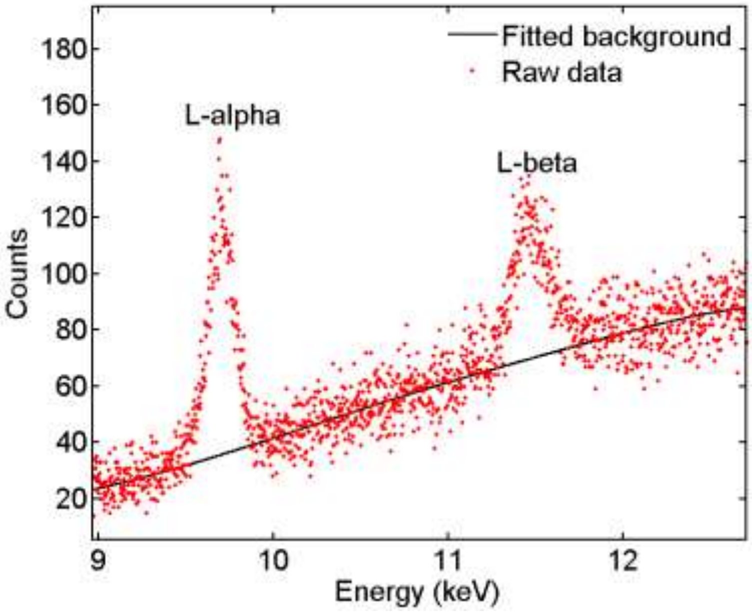

Figure 14 Data surrounding the gold Lα and Lβ peaks. A background fit (solid line) gives the background beneath each gold fluorescence peak.

The background fit (B_i) was subtracted from the measured peak counts (P_i) to isolate the gold XRF signal (F_i). A Gaussian distribution was fitted to each prominent gold L-line. This was simple for the $L\alpha$ peak where due to the intrinsic resolution of silicon detectors only one Gaussian was used to fit the two $L\alpha$ lines. The negligible contribution of the $K\beta$ zinc line caused by zinc presence in the beryllium window holder of the SDD was not included in the fit. However, a more in-depth analysis was performed for the $L\beta$ peak which contains three prominent lines ($L\beta_{1,2,3}$). Gaussians were fitted with the following constraints: (i) the measured width of the Gaussian fitted to the $L\alpha$ line (corresponding to the energy resolution of the detector) was set for all other gold L-lines, neglecting the 8% variation of the peak width due to intrinsic resolution between $L\alpha$ and $L\beta$ lines; (ii) the peak position was fixed at the energy of each gold L-line taken from Table 4 (this required a good energy calibration); (iii) the peak heights of the $L\alpha$ and $L\beta_1$ lines were fitted, and used to set the secondary peak heights using the relative contribution of the gold L-emissions (from Table 4). An example of the resulting data fits are displayed in Figure 15.

The XRF signal for each peak (I_{net}) was found by summing the Gaussian fits of each XRF line. The XRF signals were divided by acquisition time and primary beam intensity.

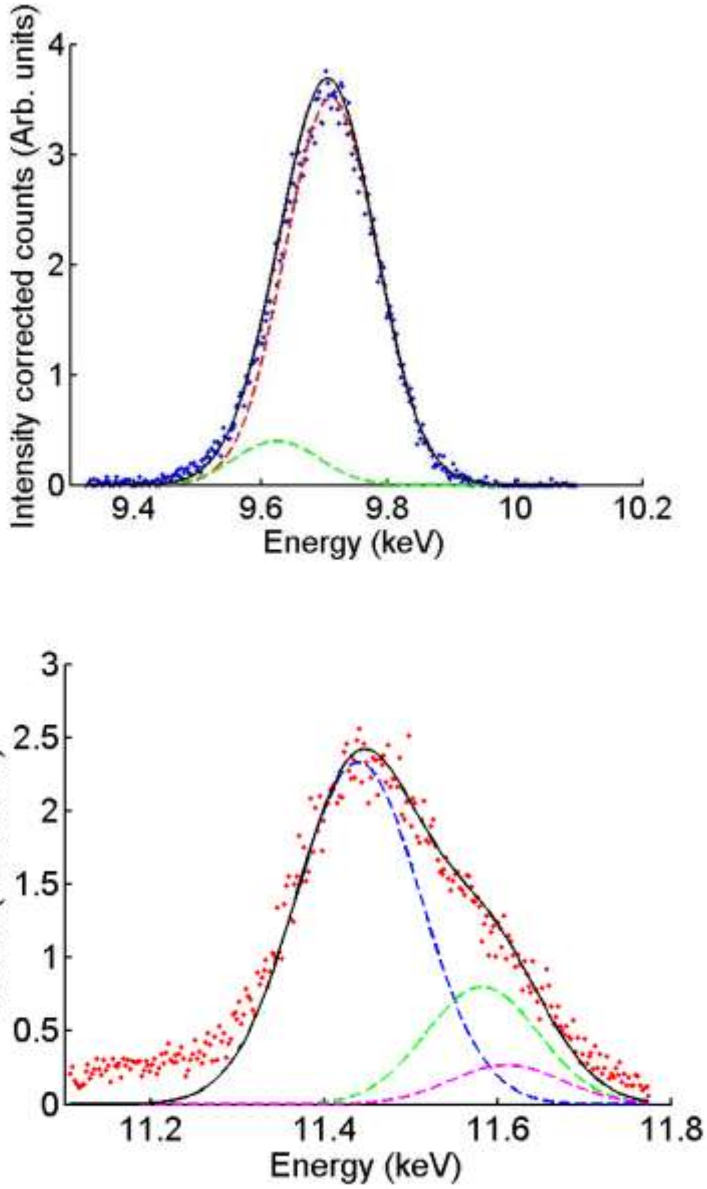

Figure 15 Gaussian fits to Lα (top) and Lβ (bottom) peak. The dots represent the intensity corrected data, the dashed lines are the fitted Gaussians, and the solid line the sum of all fitted Gaussians.

2.6.2 Isolation of the gold K-XRF signal

Example measured spectra from the K-XRF bench-top system are displayed in Figure 16.

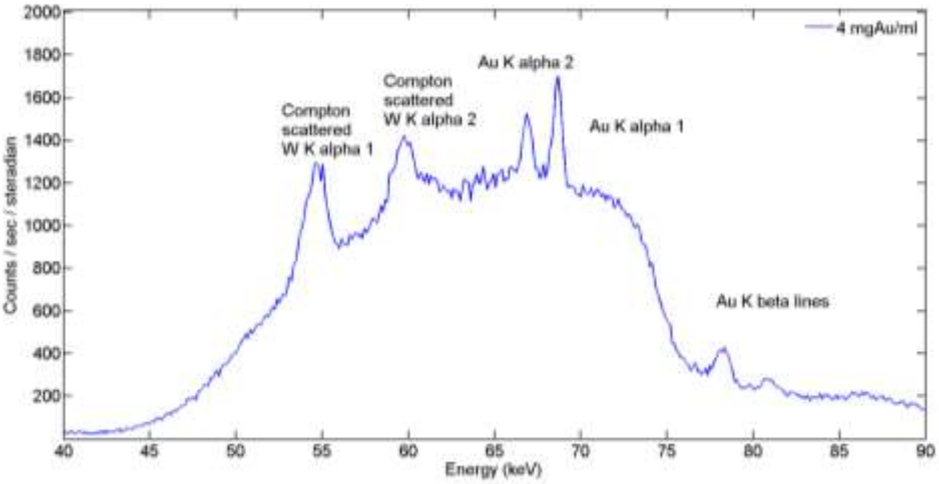

Figure 16 Measured K-XRF spectrum of a 4 mgAu/ml GNP sample.

A region covering the $K\alpha_1$ and $K\alpha_2$ peaks was selected for analysis (those lines being the strongest present in the range of concentrations measured). A 2-order polynomial least squares fit gave the best fit to the background non-peak regions, and was interpolated to give an estimate of the background signal under each gold XRF peak (an example background fit is displayed in Figure 17).

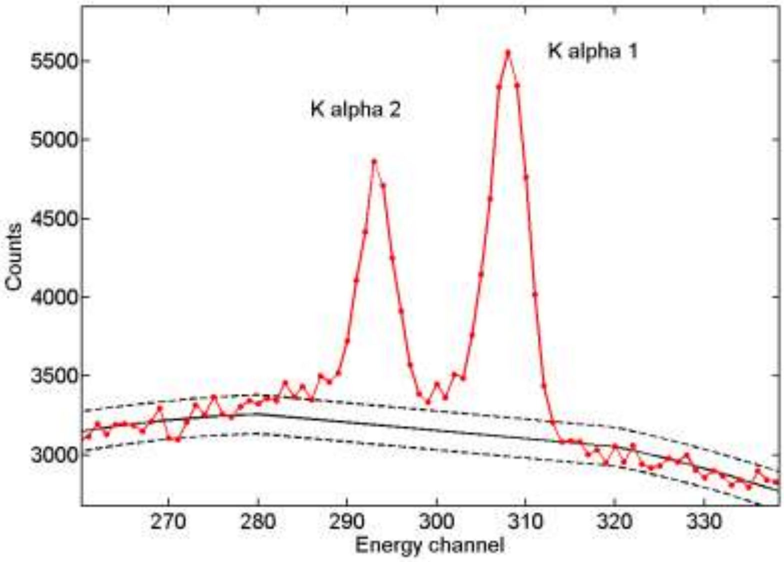

Figure 17 Data surrounding the gold Kα peaks. A background fit (solid line) gives the background beneath each gold fluorescence peak. The 95% confidence levels to the background fit are displayed as the dashed lines.

The background fit (B_i) was subtracted from the measured peak counts (P_i) to isolate the gold XRF signal (F_i). A Gaussian was fitted to each prominent gold K-line ($K\alpha_1$ and $K\alpha_2$). Gaussians were fitted without the peak-position constraint of the L-XRF technique, because the channel to energy calibration drifted between measurements; a shortcoming in using the nitrogen cooled HPGe detector.

2.6.3 Absorption correction technique

Quantitative measurement of GNP concentration is achievable due to the calibrated relationship between GNP concentration and number of gold XRF events in the measurement volume. However, the latter is not completely described by the number of x-rays reaching the detector, because some of the emitted fluorescence x-rays are absorbed by the elements present in the sample. Attenuation of (i) the incident beam and, (ii) the gold XRF x-rays by the sample both act to reduce the amplitude of the gold XRF peaks and thus distort the GNP concentration information held within the gold XRF peaks.

Previous studies have shown that radiation Compton scattered by the sample can be used as an internal standard to correct for the effects of self-absorption and geometrical variations on measured XRF signal [54], [55]. The detected Compton scatter intensity I_c can be described as:

$$I_c \propto \frac{S_c}{\mu_i + \mu_c} \qquad \text{Equation 5}$$

where μ_i is the attenuation coefficient at the incident x-ray wavelength, μ_c the attenuation coefficient at the Compton wavelength, and S_c is the Compton scatter intensity per atom.

The fluorescence intensity I_f can be described as:

$$I_f \propto \frac{t}{\mu_i + \mu_0} \qquad \text{Equation 6}$$

where t is the fluorescence emission coefficient and is proportional to $Z^{5 \text{ to } 6}$ for this range of Z, and μ_0 the attenuation coefficient for the observed radiation.

S_c is independent of Z at these energies; its intensity is due to the attenuation of incoming and outgoing radiation by the sample. In this way, normalising to the Compton scatter peak provides information on the attenuating properties of the sample, and so can be used to correct for absorption.

Scatter normalisation will also correct for any small changes in source-sample or sample-detector distance errors in sample positioning. For a fixed geometry, the magnitude of the measured gold XRF signal is proportional to the gold concentration. However, the size of the gold XRF peaks is affected by the solid angle of x-ray detection and by any changes in the source-sample-detector geometry. Both the Compton and coherent scatter background and the XRF signal are measured in the same source-sample-detector geometry, and so the ratio of XRF to scatter will remain approximately constant for a given sample (as long as the GNPs are uniformly distributed throughout the irradiated volume).

The Compton peak of the incident 15 keV beam and molybdenum Kα line was used to perform this correction for the L-XRF synchrotron and L-XRF bench-top system respectively. The Compton peak of the tungsten $K\alpha_1$ line was used to perform this correction for the K-XRF bench-top system. The resulting scatter corrected fluorescence signal I_{FS} is:

$$I_{FS} = \frac{I_{net}}{I_C} \qquad \text{Equation 7}$$

where I_{net} is the sum of the background-subtracted Gaussian-fitted XRF peak data, and I_C is the intensity of the Compton-scattered x-rays.

The scatter correction technique was tested by repositioning the same sample for five measurements. The standard deviation of the measured gold XRF signal over all measurements was 9.1% without the correction and 1.6% using a scatter correction.

2.6.4 Detection limit

The detection limit (DL) is a measure of the capability of the system to distinguish a true net peak intensity (taken as the peak height P of the Gaussian fit to the gold XRF peaks) from the random fluctuations of the background signal. The background noise (σ_b) was taken to be the standard deviation of the data points about the background least-squares fit. Signals below the threshold represented by the DL are indistinguishable from the background noise.

The magnitude of P must be at least 1.96 σ_b to be able to distinguish the net fluorescence signal from statistical fluctuations with a 95% confidence level. It follows that the DL can be determined by finding the concentration at which $P/\sigma_b = 1.96$.

2.6.5 Sensitivity

The sensitivity of an XRF system is indicated by the gradient of a plot of XRF signal against GNP concentration, plotted without any absorption corrections, in terms of counts per second per mgAu/ml [56].

2.6.6 Linearity and accuracy

The linearity between the scatter corrected gold XRF signal and GNP concentration was investigated. A weighted linear least-squares fit was applied to the XRF signal measured at each concentration. Data points below the detection limit were not included in this fit. A weighting w_i was applied to the ith measurement of magnitude

$$w_i = \frac{1}{E_i^{\,2}} \qquad \text{Equation 8}$$

where E_i is the error of the ith XRF signal measurement and was calculated by summing in quadrature the statistical error in the gold and scatter signals. The gradient of the linear fit is related to the sensitivity of the system in measuring GNP concentration, and the error in the gradient of the linear fit determines the accuracy with which the GNP concentration can be measured, as illustrated in Figure 18.

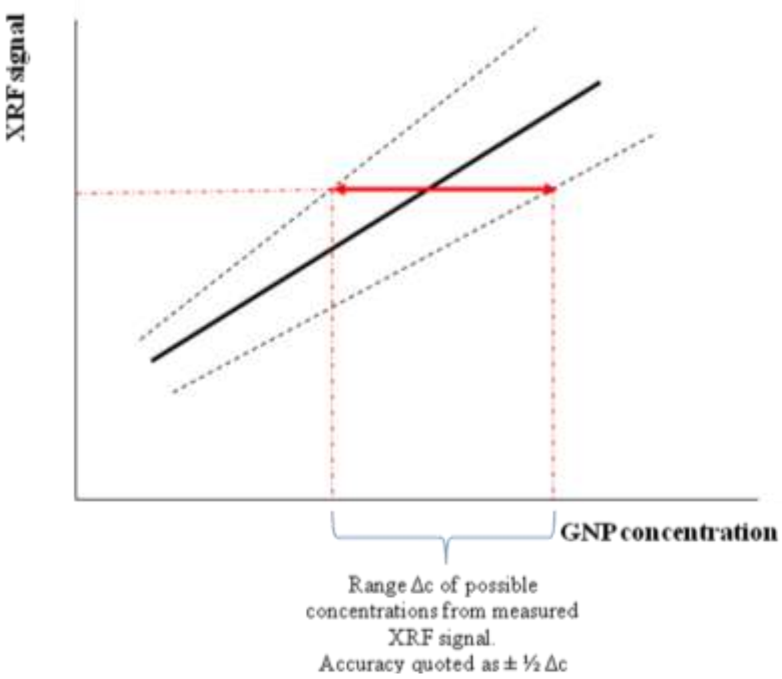

Figure 18 Illustration describing determination of accuracy of GNP concentration measurement. The solid line and black dashed lines represent linear fit and 95% confidence bounds of linear fit respectively. The accuracy is calculated by determining the range of GNP concentrations covered by a single XRF measurement.

2.7 Results

2.7.1 Measured spectra

Figures 13 and 16 display spectra obtained using each system for similar sample concentrations. It can be seen that the count rate of the gold XRF peaks of a 4 mgAu/ml GNP sample measured using the synchrotron L-XRF source is more than 15 times greater than for the L-XRF bench-top system. This is due to the greater incident x-ray intensity and larger beam area possible for a synchrotron source (the beam width of the bench top system is limited to 3.4 mm FWHM; widths greater than this degrade beam uniformity). The count rate of the gold peaks using the L-XRF bench-top system is approximately six times that of the K-XRF bench-top system for the 4 mgAu/ml sample. The background beneath the gold signal of the K-XRF system is much greater than for either of the L-XRF systems. This combined with the lower peak count rate makes the K-XRF system far less sensitive to low GNP concentrations.

2.7.2 Absorption correction techniques

The scatter normalisation technique resulted in a more accurate calibration line with more tightly constrained 95% confidence bounds. The accuracy of concentration measurement, taken to be the range of GNP concentrations covered by the 95% confidence lines for a single XRF signal value, was found to improve by 71% on performing the scatter correction. The difference in accuracy between the scatter corrected and non-scatter corrected data is illustrated in Figures 19 and 20.

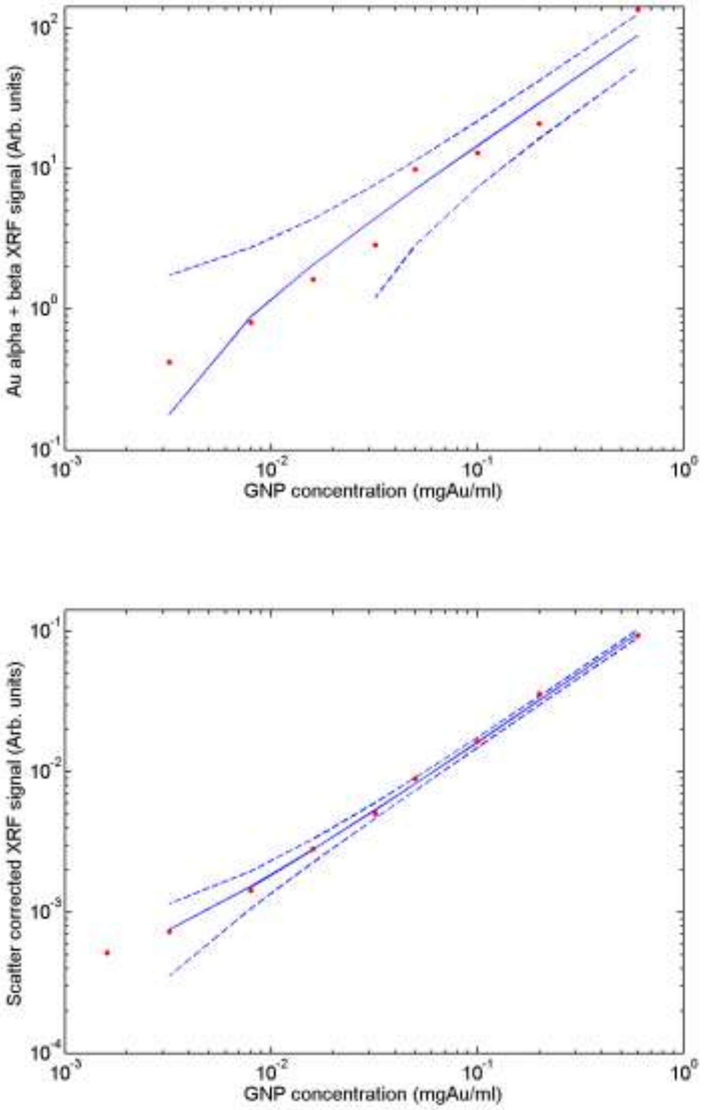

Figure 19 Weighted least squares linear fit (solid line) of XRF signal over a range of measured GNP concentrations using the L-XRF synchrotron source. The XRF signals are without (top) and with (bottom) a scatter correction. 95% confidence levels of the linear fit are displayed as dashed lines. Error bars are present but smaller than the size of the plotted data points.

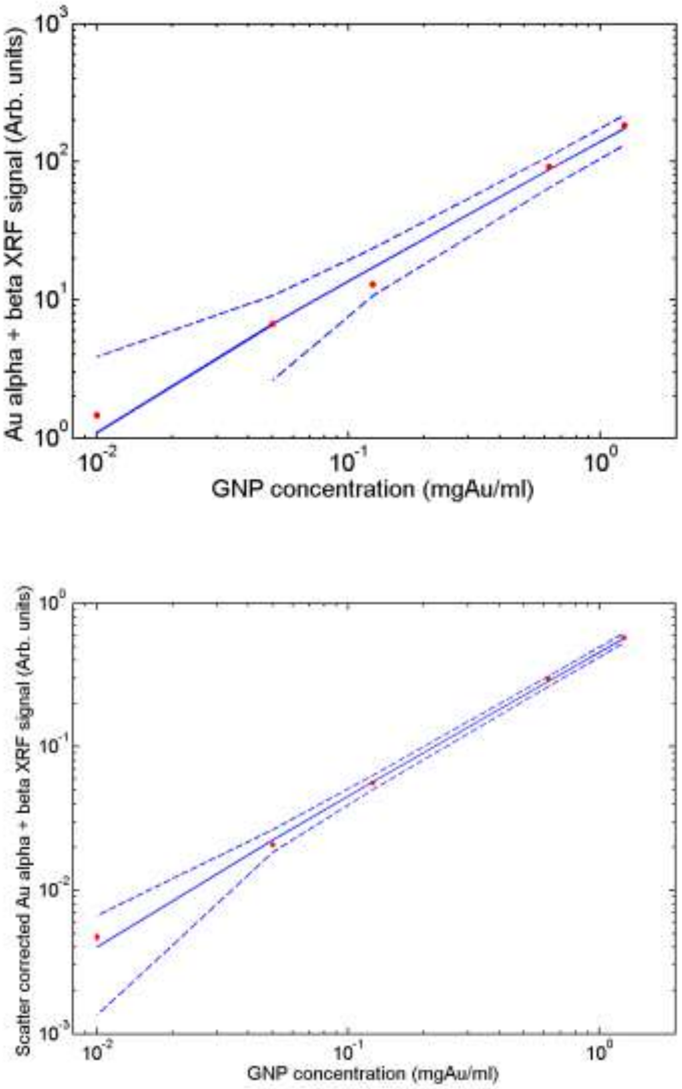

Figure 20 Weighted least squares linear fit (solid line) of XRF signal over a range of measured GNP concentrations using the L-XRF bench-top source. The XRF signals are without (top) and with (bottom) a scatter correction. 95% confidence levels of the linear fit are displayed as dashed lines. Error bars are present but smaller than the size of the plotted data points.

Figures 19 and 20 graphically display that the scatter correction technique acts to linearise the data points, which results in a more closely fitting 95% confidence level. All further analysis has therefore utilised the scatter correction technique.

2.7.3 Linearity of calibration line and accuracy of concentration measurement

Figure 21 displays the weighted least-squares linear fit and associated 95% confidence levels of the scatter-corrected XRF signal against GNP concentration for each XRF system. The magnitude of the scatter-corrected XRF signals of each system should not be directly compared as they are corrected by different scatter signals which vary in magnitude for each of the three systems.

It was found that the linearity between the gold XRF signal and GNP concentration did not degrade when translating between the synchrotron source and the bench-top source. The accuracy of GNP concentration measurement was found to be the same for both L-XRF systems; concentrations may be measured to within ± 0.005 mgAu/ml at low concentrations (between DL and 0.1 mgAu/ml). The K-XRF system could measure GNP concentration to within ± 0.02 mgAu/ml at concentrations between its DL and 2 mgAu/ml.

The relative merits of one- and two-peak analysis were compared; analysis using the $L\alpha$ peak and sum of the $L\alpha + L\beta$ peaks gives a similarly accurate fit with tighter 95 % confidence bounds. Sole use of the $L\beta$ peak reduces the accuracy by a factor of 2.

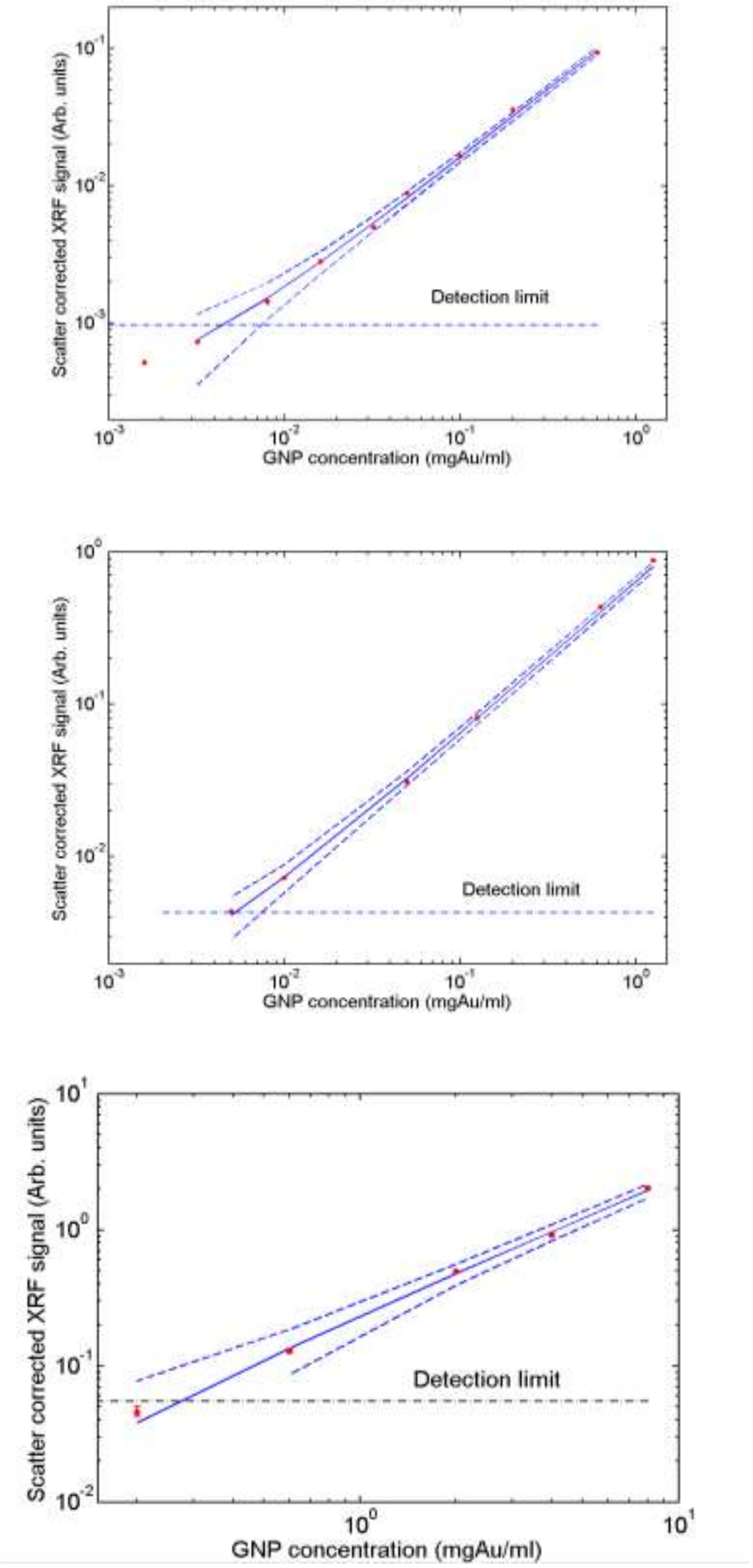

Figure 21 Weighted least squares linear fit (solid line) of XRF signal over a range of measured GNP concentrations using the L-XRF synchrotron source (top), L-XRF bench-top source (middle) and K-XRF bench-top source (bottom). 95% confidence levels of the linear fit are displayed as dashed lines, and the detection limit plotted.

2.7.4 Detection limit

The DL as defined in Section 2.6.4 was found for each XRF system and is displayed in Table 7. The $L\alpha$ peak analysis gives the lowest DL for each L-XRF system, as it has a greater yield than the $L\beta$ signal. Likewise, the $K\alpha_1$ peak analysis produced the lowest DL, having a greater yield than the $K\alpha_2$ line. It is worth noting that 0.008 mgAu/ml was the lowest GNP concentration ≥ 0.005 mgAu/ml (DL of bench-top system) measured using a synchrotron source, and so does not imply that the DL of the L-XRF bench-top system is lower.

Table 7 Detection limits of L-XRF systems (synchrotron and bench-top) and K-XRF bench-top system at a 95% confidence level. 0.008 mgAu/ml was the lowest GNP concentration ≥ 0.005 mgAu/ml (DL of bench-top system) measured using a synchrotron source, and so does not imply that the DL of the L-XRF bench-top system is lower.

	Detection limit (mgAu/ml)			
	L-XRF synchrotron	L-XRF bench-top		K-XRF bench-top
$L\alpha$	< 0.008	0.005	$K\alpha_1$	0.2 < DL < 0.6
$L\beta$	0.008	0.005 < DL < 0.01	$K\alpha_2$	0.6 < DL < 2.0

2.7.5 Sensitivity

The measured sensitivity to gold XRF signal is displayed in Table 8 for each system. The sensitivity was calculated by finding the gradient of a linear fit to the count rate per solid angle of each gold peak; no correction for beam intensity or self-attenuation was performed to enable direct comparison of the three systems.

Table 8 Measured sensitivity to XRF signal of GNPs for each measurement system

Sensitivity (XRF peak counts per mgAu/ml per second per solid angle)				
	L-XRF synchrotron	L-XRF bench-top		K-XRF bench-top
$L\alpha$	~95,200 ± 7%	~3700 ± 8%	$K\alpha_1$	~400 ± 20%
$L\beta$	~87,500 ± 8%	~3600 ± 9%	$K\alpha_2$	~700 ± 18%
$L\alpha + L\beta$	~182,700 ± 6%	~7300 ± 7%	$K\alpha_1 + K\alpha_2$	~1100 ± 15%

L-XRF synchrotron beam size = 13 mm wide x 2.7 mm deep

L-XRF bench-top beam size = 3.4 mm wide x 1.5 mm deep

K-XRF bench-top beam size = 10 mm wide x 8 mm deep

It is no surprise that two-peak analysis yielded a greater sensitivity than using either sole peak. This is due to the increase in signal intensity upon summing both peaks together. The synchrotron L-XRF system was approximately 25 times more sensitive than the bench-top L-XRF system. The L-XRF bench-top system was found to be between 5 - 9 times more sensitive than the K-XRF bench-top system (depending on which peaks were used for analysis).

2.7.6 XRF measurements at depth

The quantitative measurements of GNP concentration have been performed on small samples contained in thin plastic pots in order to minimise attenuation of the XRF signal. However, the eventual aim of the XRF technique is to measure GNP concentration *in vivo* or in thick *ex vivo* tumour biopsies; the GNPs will be distributed at depth and therefore the effect of overlying tissue must be considered. The extent of this effect will be different for L-XRF and K-XRF modes, the latter being of higher energy and therefore less attenuated by overlying thicknesses.

2.7.6.1 L-XRF measurements at depth

The L-XRF synchrotron system was used to perform a series of XRF measurements of an 8 mgAu/ml GNP sample with five different thicknesses of Perspex (0, 2, 4, 8 and 16 mm) placed between the sample and detector (see Figure 22). Perspex has similar attenuating properties to tissue at these energies. An acquisition time of 180 s was made for each measurement.

Figure 22 Depth measurement of 8 mgAu/ml GNP sample; a range of Perspex thicknesses were added above the sample to test the effect of depth of measurement on the L-XRF method.

The effect of adding Perspex thickness to the measured XRF spectra is displayed in Figure 23.

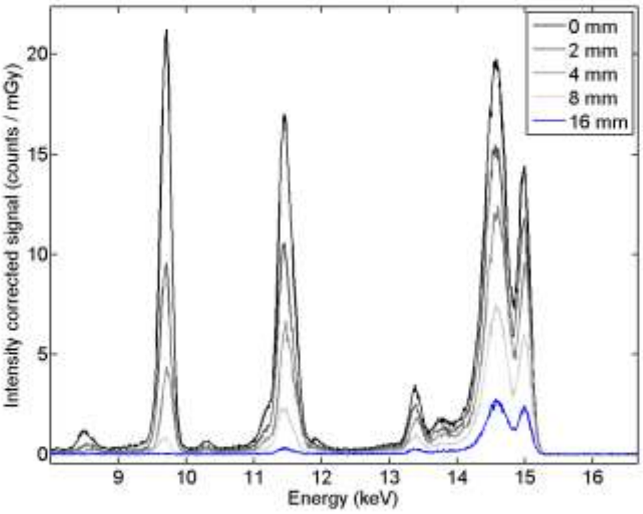

Figure 23 Measured L-XRF spectra of an 8 mgAu/ml sample acquired with a range of Perspex thicknesses above the sample.

Figure 23 displays only a slight difference in the background of the gold XRF signal with increasing Perspex thickness. This is because the source was monoenergetic, and so Compton scatter x-rays are all of a similar energy (the Compton scatter peak is found at 14.6 keV at 90° detection) and do not contribute to the background of the gold signal. Figure 23 demonstrates that the gold L-XRF lines decrease in size with increasing Perspex thickness due to attenuation by the Perspex. The XRF signals of the $L\alpha$ and $L\beta$ lines have been plotted against Perspex thickness to illustrate this (Figure 24).

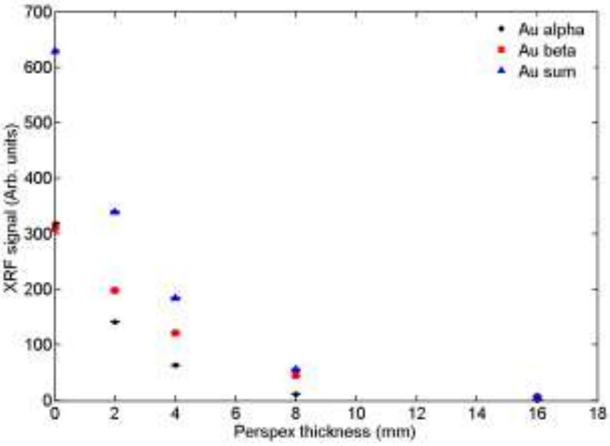

Figure 24 Effect of Perspex thickness above an 8 mgAu/ml sample on measured L-XRF signal.

All gold signals were found to be above the DL of the system. 16 mm Perspex gave a 99.2% and 88.8% reduction in the detectability of the $L\alpha$ and $L\beta$ signals respectively. Even though the $L\beta$ signal has a lower yield than the $L\alpha$ peak, it was found to be less affected by overlying thicknesses as it is a higher energy signal and therefore more penetrating. For this reason, it may be beneficial to use the $L\beta$ peak for analysis of measurements made at depth.

2.7.6.2 K-XRF measurements at depth

The K-XRF bench-top system was used to perform a series of XRF measurements of an 8 mgAu/ml GNP sample surrounded by four different thicknesses of Perspex (0, 6, 9 and 15 mm). The Perspex completely surrounded the sample rather than just being above the sample as for the L-XRF measurements. The effect of adding Perspex thickness to the measured K-XRF spectra is displayed in Figure 25.

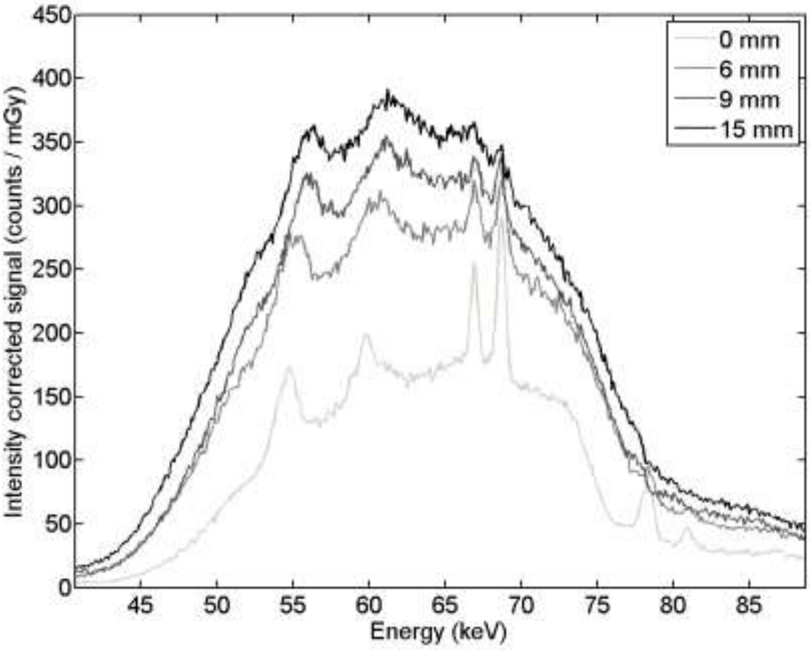

Figure 25 Measured K-XRF spectra of an 8 mgAu/ml GNP sample surrounded by a range of Perspex thicknesses. Each spectrum was normalized to the intensity measured by an ion chamber in the beam for each measurement.

Figure 25 displays an increase in the background scatter component with increasing Perspex thickness. This results from scatter interactions taking place in the Perspex both of the incident x-ray beam and of the x-rays exiting the sample; the thicker the Perspex, the greater the number of scatter interactions occurring. This increases the number of x-rays reaching the detector (as the detector is in a 90º geometry). A larger background component makes it more difficult to see the XRF signal from lower concentrations. An increase in unwanted background counts also acts to increase the detector dead time, which has a negative impact on the measurement by increasing required acquisition time and also can lead to distortion of the measured spectrum.

Figure 25 also demonstrates that the gold K-XRF lines decrease in size with increasing Perspex thickness due to attenuation by the Perspex. The XRF signals of the $K\alpha_1$ and $K\alpha_2$ have been plotted against Perspex thickness to illustrate this (Figure 26).

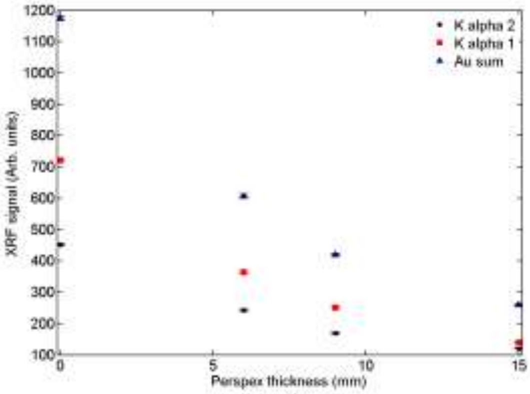

Figure 26 Effect of Perspex thickness surrounding 8 mgAu/ml sample on measured K-XRF signal.

All measurements were above the DL of the system. An 84% decrease in detectability of the 8mgAu/ml sample was found when adding 15 mm Perspex around the sample. A Perspex geometry similar to that used in the L-XRF measurements would bring about a much lower decrease, as the incident beam would not have been attenuated. It can be concluded that the K-XRF technique is less affected by overlying thickness than the L-XRF technique, as expected.

2.7.7 Summary of results

Three XRF systems have been compared in terms of sensitivity, accuracy of measurement and minimum detectable limit. The key results of all three systems are summarised in Table 9.

Table 9 Summary of key results in order to compare the performance of each XRF system.

	L-XRF synchrotron source	**L-XRF bench-top source**	**K-XRF bench-top source**
Detection limit (mgAu/ml)	< 0.008	0.005	0.2 < D.L. < 0.6
Sensitivity (XRF peak counts per mgAu/ml per second per solid angle)	~182,700 ± 6%	~7300 ± 7%	~1100 ± 15%
Uncertainty (mgAu/ml) **(for concentration range)**	± 0.005 (DL – 0.1 mgAu/ml)	± 0.005 (DL – 0.1 mgAu/ml)	± 0.02 (DL – 2 mgAu/ml)

2.8 Discussion

2.8.1 Sensitivity

The sensitivity defined as the measurable XRF signal per unit GNP concentration is affected by both the intensity and spectral shape of the x-ray source. The two translations made (from the L-XRF synchrotron system to the L-XRF bench-top system, and from the L-XRF to K-XRF bench-top system) will be treated in turn. The dominant factors contributing to the differences in performance between the systems will be identified.

2.8.1.1 L-XRF synchrotron to L-XRF bench-top translation

The synchrotron system was 25 times more sensitive than the bench-top system, with typical counting times of 120 s necessary to achieve a 1% statistical error of XRF peak counts for the 0.1 mgAu/ml sample. This difference in performance can be attributed to the following:

a) The intensity of the synchrotron source is approximately two orders of magnitude bigger than that of the bench-top source. The intensity difference is the major contributing factor to the difference in performance of the two systems. A more intense source will result in a greater sensitivity per unit time. The intensity of the laboratory source may be increased by an order of magnitude by using one of the many commercially available higher power x-ray generators. This will make laboratory measurement times of GNP concentrations more similar to when using a synchrotron source.

b) The sample measurement volume was four times greater for the synchrotron system than the bench-top system. This is due to the limitations on beam size posed by beam uniformity of the molybdenum source.

c) A smaller contributing factor is the difference in photoelectric interaction cross section between the main energies of each source; the synchrotron source set at 15 keV has a 1.5 times greater photoelectric cross section than the molybdenum $K\alpha_1$ line of the bench-top system (158.6 cm^2/g and 106.7 cm^2/g respectively).

2.8.1.2 L-XRF to K-XRF bench-top transition

The sensitivity of the L-XRF bench-top system was found to be 6.5 times greater than the K-XRF system. This difference in performance can be assigned to the following factors:

a) The main contributing factor to the difference in L-XRF and K-XRF sensitivity is the difference in photoelectric interaction cross section, which is 13 times greater for the main energy of the L-XRF source than for the K-edge energy of gold (taken to represent the greatest contribution to XRF for the polyenergetic K-XRF source). However, the fluorescence yields are also different for K and L fluorescence; the $K\alpha_1$ and $K\alpha_2$ emission rate is 2.15

times greater than for *Lα* and *Lβ* emission. These two factors together make L-XRF a factor of 6 more likely to occur than K-XRF.

b) The sample measurement area of the K-XRF system was twice that of the L-XRF system.

c) The intensity of the K-XRF source was greater than the L-XRF source; however this cannot be directly attributed to the difference in sensitivity because the spectral shape must also be considered (further discussed in the following section).

2.8.1.3 Effect of spectral shape on XRF signal

The incident x-ray spectral shape also affects sensitivity; use of an optimum source energy just above the absorption edge of gold increases the photoelectric cross section and so will increase the rate of emission of XRF x-rays. Increasing the source intensity increases both the background and the peak counts equally, whereas optimising the spectral shape can result in increasing the number of peak counts whilst reducing the background. Beam filtration may be used to optimise the spectral shape, but this involves a compromise with beam intensity and results in longer acquisition times to achieve the same counting statistics.

A comparison of spectral shape of the synchrotron source, and filtered and unfiltered molybdenum bench-top sources has been made to inform future work. Measured incident spectra using (i) no beam filtration, producing a more polyenergetic beam, and (ii) a 50 µm thick molybdenum filter, providing a quasi-monoenergetic beam, are displayed in Figure 27. The latter source-filter combination acts to reduce the component of the incident beam below the threshold energy required to induce fluorescence, which would add to unwanted background signal without contributing to gold XRF. The selected filter thickness is a compromise between removing the low energy x-rays and maintaining the intensity of x-rays above the gold L-edge.

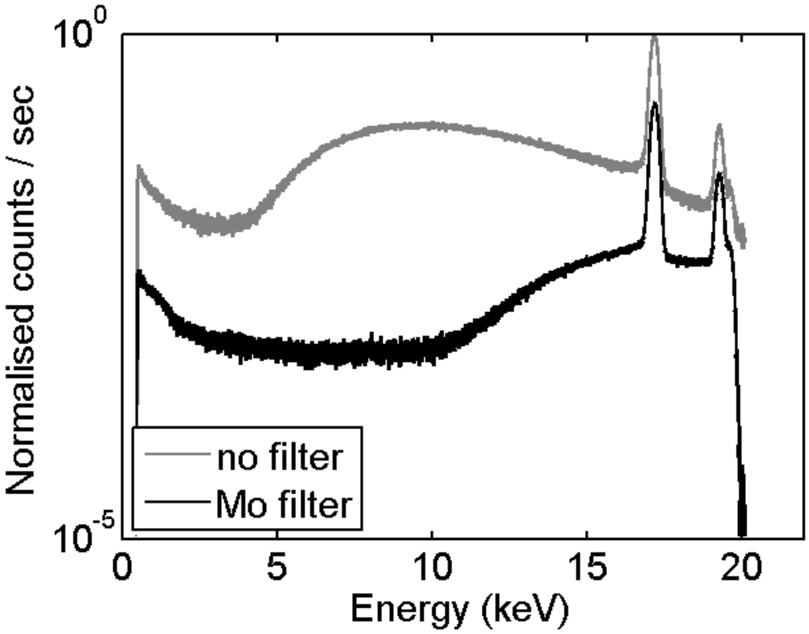

Figure 27 Incident spectra of a molybdenum bench-top source with and without 50 μm molybdenum filtration.

The number of incident x-rays that are involved in a photoelectric interaction (I_{PE}) and may therefore contribute to an XRF event has been theoretically determined for each XRF system:

$$I_{PE} = \sum_{E_{edge}}^{E\max} I_0(E)(1 - e^{-\sigma(E)\,x}) \qquad \text{Equation 9}$$

where $I_0(E)$ is the number of incident x-rays of energy E and $\sigma(E)$ is the photoelectric cross section at E. E_{edge} corresponds to the energy threshold for fluorescence (11.9 keV for L-XRF and 80.8 keV for K-XRF).

The 'useful' proportion of the total incident beam R_{XRF} was calculated as the ratio of the number of incident x-rays that contribute to a photoelectric interaction against the total number of incident x-rays (Equation 10):

$$R_{XRF} = \frac{I_{PE}}{\sum_{E=0}^{E_{\max}} I_0} \qquad \text{Equation 10}$$

R_{XRF} was calculated for the synchrotron L-XRF system using a simulated monoenergetic beam at 15 keV, the bench-top L-XRF system using the measured spectra in Figure 27, and the K-XRF system using an incident spectrum simulated with SpekCalc [53]. A power fit was used to interpolate values of gold attenuation coefficients [52]. A range of thicknesses of lead filtration were investigated for the K-XRF system. Results are displayed in Table 10.

Table 10 Characteristics of each source for gold XRF measurement (Cross sections interpolated from [52]*).*

	Main x-ray energy (keV)	**PE absorption cross section of gold (cm^2/g)**	**Coherent and incoherent scatter cross section of gold (cm^2/g)**	**R_{XRF} (calculated for x-rays passing through 0.1 mm gold)**
Synchrotron	15	158.6	3.259	79.4%
L-XRF bench-top	17.48 (Mo $K\alpha_1$ line)	106.7	2.742	33.8% (unfiltered) 60.1% (50 µm Mo)
K-XRF bench-top	Polyenergetic source	8.2842 (81 keV)	0.3722 (81 keV)	0.8% (no filtration) 2.0% (0.5 mm Pb) 3.0% (1 mm Pb) 4.6% (2 mm Pb)

Measurement found that the introduction of a 50 µm molybdenum filter acts to reduce the rate of L-XRF production almost by a factor of eight due to the decrease in intensity caused by attenuation by the filter. This reduction was confirmed by calculating the ratios of I_{PE} between the unfiltered and filtered molybdenum source; the unfiltered beam produced 7.2 times more photoelectric events than the filtered beam. However, the filtered source yields a greater useful proportion of the incident beam that can induce L-XRF (1.8 times greater when using the molybdenum filter), and so has a smaller ‘useless’ component that merely contributes background signal (values displayed in Table 10). In order to improve both the sensitivity and DL of the bench-top system, it is recommended that use of molybdenum filtration be further investigated, but using a higher intensity x-ray tube to compensate for the reduction in beam intensity introduced by a filter.

Simulations found that introduction of 0.5 mm Pb and 1 mm Pb filtration to the K-XRF system yielded a 2.6 and 3.8 times greater useful proportion of the incident beam respectively than when used without filtration. However, the rate of K-XRF production reduced by a factor of 6.2 and 21.6 when using these filter thicknesses due to the decrease in intensity. A filter thickness of 0.5 mm Pb was found to be a good compromise between lowering the background beneath the gold signal and keeping the rate of XRF production sufficiently high. Use of greater thicknesses of filter may be necessary in order to further reduce the background beneath the gold signal for measurement of lower GNP concentrations.

2.8.2 Detection limit

The detection limits of the L-XRF systems were found to be above the clinically required detectable concentration of ~0.01 mgAu/ml in the absence of overlying media (refer to Section 1.5.1). The K-XRF system was found to be unable to detect such low concentrations. However, it may have use in clinical techniques using higher concentrations of GNPs.

The high energy resolution of the SDD module is responsible for the good performance of each L-XRF system, not only in terms of being able to resolve the x-rays of each fluorescence peak but also in giving a low DL. To achieve a low DL, the XRF peak must be easily visible above the background upon which it sits. The energy deposited by an x-ray is represented by the area of the whole peak. If a sample containing a certain amount of gold is measured using two detectors of differing energy resolution R (where R = FWHM of the fluorescence peak), for the peak area to remain constant, a wider peak (poorer R) must be smaller, and a narrower peak (better R) must be taller. The DL also improves as detection time is increased, until the instrumental error (in this case the detector electronic noise) dominates above statistical noise. The electronic noise charge of the SDD is very low at 8.3 electrons for a 1 μs shaping time, enabling very low detection limits.

The DL is also smaller when the sample matrix (the material surrounding the GNPs) is less absorbing of both the incident and fluorescence x-rays, enabling higher measurement intensities for the lower concentrations. For this set of measurements the matrix was water, and is similarly absorbing to the clinical case of GNPs embedded in soft tissue. However, in the case of thicker samples where the gold is embedded more deeply, and also in regions of more highly absorbing anatomy such as bone, the DL will be degraded.

The DL is closely related to the system sensitivity; a poorer sensitivity will result in a lower number of XRF peak counts above the background, and hence a degradation in ability to detect lower concentrations over a fixed period of time.

2.8.3 Uncertainty in quantitative analysis

The overall uncertainty in quantitative XRF analysis is a contribution of the random and systematic errors introduced at each stage of the analysis process [57]. Random errors include the counting statistical errors involved in the measurement of B_i and P_i, and determine the precision of measurement (i.e. the repeatability of a result). Systematic errors are introduced if a poorly determined calibration line is used, mainly caused by errors in sample preparation, errors in the calculation of the calibration line gradient, and corrections for sample absorption. Systematic errors determine the accuracy of an XRF measurement (i.e. the closeness of the measured concentration to its true value).

Precision can be improved by:

- Increasing counting statistics. Longer counting times were required for the L-XRF bench-top source due to its lower intensity compared with the synchrotron source. It is suggested that a higher power bench top x-ray source be used for future measurements in order to attain measurements in similarly short times as for synchrotron measurements. Increasing counting statistics also improves accuracy of the calibration line.

- A repeatable sample positioning procedure. The scatter correction technique acts to correct for errors in sample repositioning.

The main factor that affects accuracy is the integrity of the calibration line. Each component of the XRF system has an effect on this:

- *X-ray source:* In order to achieve a good signal to noise ratio (SNR), a source must be used that provides an optimum spectral shape to encourage photoelectric events and minimise scatter events that will contribute to the background. A high SNR will produce a lower error on each data point and so a more accurate linear fit and more tightly constrained 95 % confidence bounds.
- *Sample collimator:* The peak to background ratio improved by 35% when using a collimator in the L-XRF bench-top system. Further improvements to collimator design may be made to improve the accuracy.
- *Detector:* As previously discussed, the detector energy resolution has a direct effect on SNR. The SDD and HPGe detectors used for this set of measurements have sufficient energy resolution.
- *Calibration samples:* error in GNP concentration was kept as low as possible during the sample making process. Atomic absorption spectrometry may be used to give a gold standard measure of the gold concentration present in each sample if the samples are not needed for future measurements.

2.9 Summary of key points learned

In summary, each system component affects the performance of the XRF technique in the following ways:

2.9.1 Effect of detector choice

- *Energy resolution:* a high energy resolution is required to increase the signal to noise ratio in order to observe the gold XRF peak above the background. This will improve the detection limit and increase sensitivity.

- *Efficiency of detection at relevant energies:* the detecting layer should be of sufficient thickness and made of an appropriate material to maximise efficiency of detection. This will increase the sensitivity of the system.

- *Maximum detectable count rate:* the detector should be able to operate at high count rates in order to reduce acquisition time, and thus improve sensitivity. Detectors that suffer from pulse pile up at high count rates degrade the measurement as the spectrum becomes warped due to dead time losses.

- *Peak drift:* A detector with minimum peak drift is preferable, so that the effect of summing does not act to spread the XRF peak out (thereby degrading the detection limit).

2.9.2 Effect of exciting source

- *Intensity:* the rate of XRF production, and therefore sensitivity, increases as source intensity increases (as long as the detector can measure at sufficient count rates).

- *Spectral energy and shape:* The energy should be optimised to increase the photoelectric interaction cross section (and therefore maximise gold XRF production). The spectral shape should be optimised to reduce useless low energy components of the beam that do not contribute at all to XRF production, and high energy components that do not contribute greatly to XRF production. An optimum spectral shape will improve both the sensitivity and lower the detection limit.

- *Divergence:* a divergent beam increases the background signal by (i) increasing the background scatter signal from other components in the system, and (ii) a less well defined 90° geometry is achievable, and so there is a greater Compton background component. This acts to worsen the detection limit.

- *Stability:* beam stability is not an issue as long as an ionisation chamber is used to correct for fluctuations in the beam.

- *Beam area:* a larger available beam size will increase sensitivity by increasing the rate of production of the XRF signal.

2.9.3 Effect of signal (K- vs. L-XRF)

- *Fluorescence yield:* the photoelectric cross section is greater at L-energies than K-energies. Even though the fluorescence yield per photoelectric interaction is greater for K-XRF, fewer photoelectric interactions occur for the K-XRF system. L-XRF is a factor of six times more likely to occur than K-XRF. Therefore, L-XRF systems are fundamentally more sensitive and have a greater signal to background ratio of the gold signal.

- *Depth measurements:* K-XRF systems use higher x-ray energies, and are therefore less affected by overlying thicknesses. K-XRF may be more useful than L-XRF in at-depth measurements.

2.10 Alternative method of quantitative measurement of GNP concentration: X-ray edge subtraction

2.10.1 Background

X-ray edge subtraction (XRES) techniques have proven beneficial for identifying high Z contrast agents. XRES makes use of the large difference in attenuation properties of high Z materials such as gold at energies either side of absorption edges (as illustrated in Figure 28), and can provide considerable enhancement in contrast over conventional x-ray imaging.

XRES, in this case, is being used to locate the presence of GNPs. XRES techniques involve acquisition of two images just above and below the L_3 edge of gold (11.92 keV).

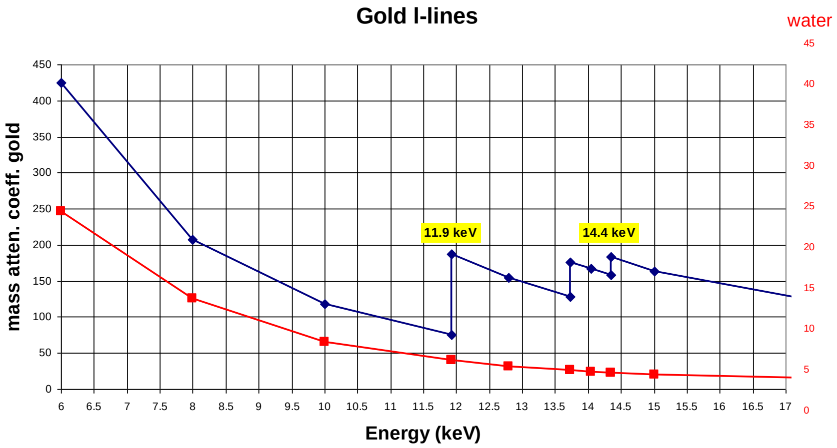

Figure 28 Attenuation coefficients of gold (blue) and water (red) illustrating the achievable contrast.

Figure 28 illustrates that the difference in attenuation coefficient value is much greater for gold than for water at the two image energies, and so a subtraction of the two images will enhance the gold contrast. A preliminary study has been undertaken to assess XRES for use in quantitative measurement of GNP concentrations in water.

2.10.2 Method

XRES images were taken of eleven GNP samples of concentrations ranging from 0.0005 - 4 mgAu/ml to investigate the relationship between concentration and subtracted pixel value, and to test the minimum detectable concentration. The experimental set-up is displayed in Figure 29.

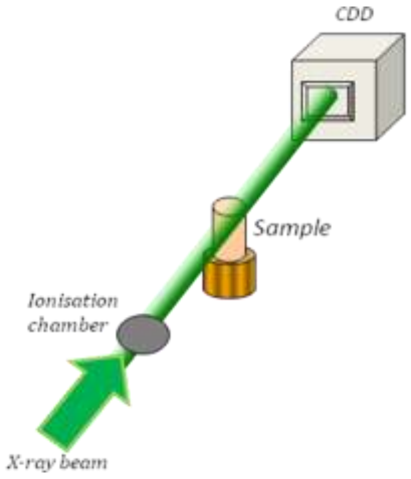

Figure 29 Schematic of the x-ray edge subtraction system.

Measurements were made at the SYRMEP beamline at the Elettra synchrotron source, Trieste, Italy. A Photonic Science X-ray Hystar 2048 CCD camera, with an equivalent pixel size of 9 µm, was used to acquire two x-ray transmission images of 40 acquisitions each, taken just above (12.07 keV) and just below (11.77 keV) the L_3 edge of gold (11.92 keV). An ionization chamber monitored the beam intensity in order to normalize the data.

2.10.2.1 Samples

The samples consisted of GNPs (Aurovist^{TM}, Nanoprobes Inc., USA) suspended in a 1 ml de-ionised water buffer (introduced in Section 2.2). The sample concentrations were selected to resemble possible tumour gold concentrations *in vivo* [24], and to test the minimum detectable concentration. A 1 ml DIW sample was measured for background data.

2.10.2.2 Image processing

Each image was corrected for beam intensity using an ionisation chamber. A dark field image (an image acquired with no x-ray beam) and a flat field image (taken with no sample at both x-ray energies) were additionally acquired to perform background and flat field corrections.

The images were then processed as follows. The dark field image ($I_{darkfield}$) was subtracted from each sample image (I_{sample}) and flat field image ($I_{flatfield}$), and each sample image was flat field corrected according to Equation 11.

$$I_{corr} = \frac{I_{sample} - I_{darkfield}}{I_{flatfield} - I_{darkfield}} \qquad \text{Equation 11}$$

The corrected sample images for the high and low energy acquisitions were then log-subtracted to give an image of the GNPs (Equation 12):

$$I_{sub} = \ln[I_{corr,high}] - \ln[I_{corr,low}] \qquad \text{Equation 12}$$

2.10.3 Results

Figure 30 displays the improvement in gold contrast using XRES over the gold L_3 edge. No gold detail is visible in either the low or high energy transmission images. However, when the log-subtraction of the two is taken to form the XRES image, gold contrast improves.

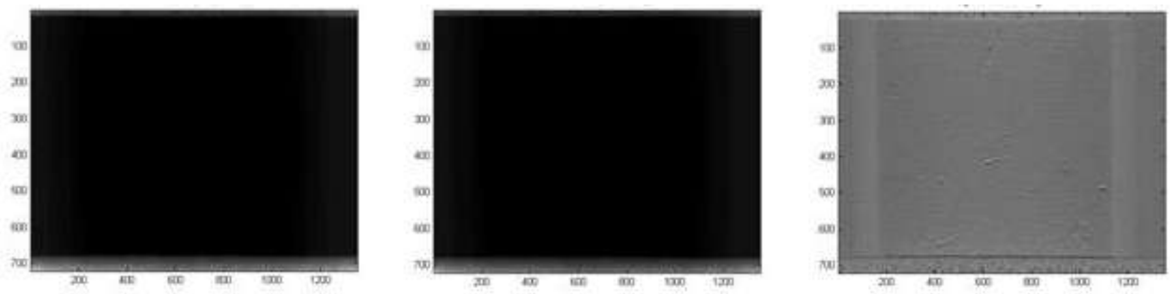

Figure 30 Transmission image of GNP sample at 12.07 keV (left), 11.77 keV (centre) and XRES image of same GNP sample (right). The XRES image on the right displays an image of the gold sample, with the sample holder detail present on the edges of the image.

A profile plot taken across the XRES image displays a shape associated with a cylindrical uniform sample; the central component of the profile is non-flat due to greater attenuation occurring medially rather than at the sample edges (Figure 31).

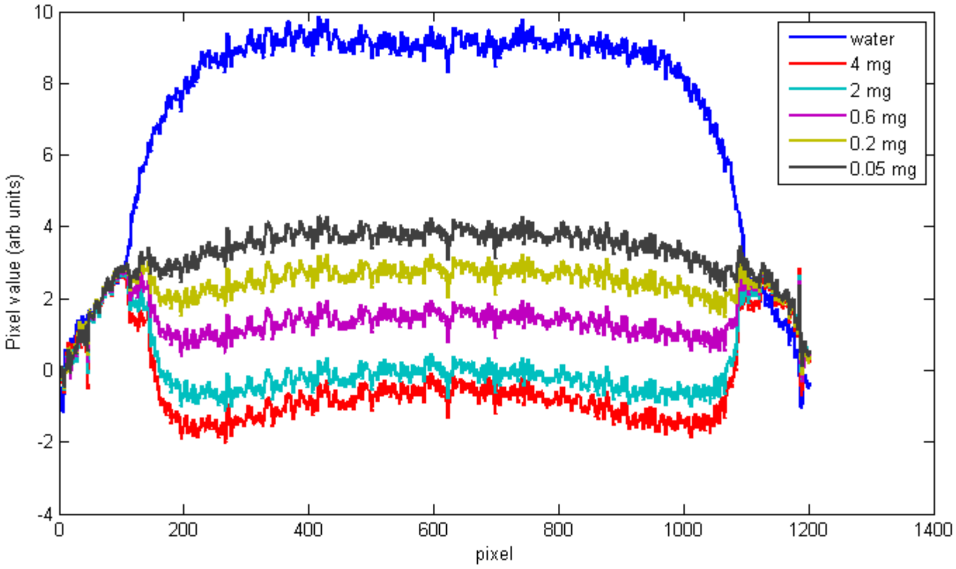

Figure 31 Profile plots across the XRES image.

As the samples were cylindrical, one would expect a greater amount of gold in the thicker central strip of the image than the peripheral regions. Figure 31 demonstrates that the XRES images show an increase in attenuation at the thicker, central portion of the sample, an effect that is more pronounced with increasing GNP concentration. Figure 31 also demonstrates that different GNP concentrations can be distinguished from each other.

The relative heights of the water and GNP solution profiles show that the edge subtraction technique can be sensitive to lower GNP concentrations. The detection limit of the system was not fully determined, and further measurements at lower concentrations are required to further investigate this.

The feasibility of the XRES technique to perform quantitative measurement of GNP concentration was assessed. The mean pixel value (MPV) over a region of interest covering the central portion of the sample was found for both the subtracted image set and the original high energy images. The MPV was plotted against sample GNP concentration, as illustrated in Figure 32.

The MPV plots in Figure 32 illustrate that both the conventional transmission imaging and the XRES imaging techniques can be used as a method to quantify the concentration of GNPs; there is a downward trend in MPV across the range of measured GNP concentrations.

The gradient of the plots in Figure 32 indicate sensitivity of the imaging technique to GNP concentration. The XRES imaging technique displays a steeper gradient at higher GNP concentrations than the conventional transmission imaging technique. The XRES imaging technique therefore improves senstivity to quantitative measurement of GNP concentration.

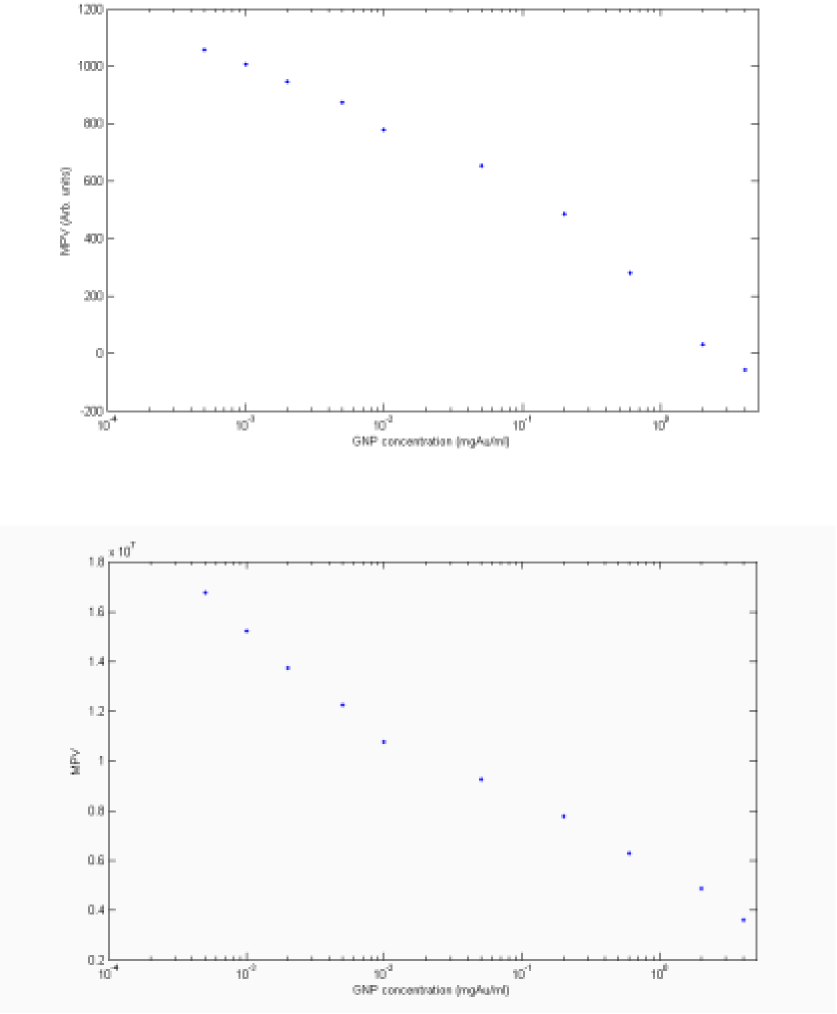

Figure 32 Log-subtracted (top) and high energy transmission (bottom) MPV over central ROI.

2.10.4 Discussion

An XRES system consisting of a CCD camera and synchrotron radiation source was used to acquire transmission images above and below the L_3 edge of gold over a range of GNP concentrations. This preliminary study of the XRES technique has demonstrated promising potential in measuring GNP concentrations expected to be found *in vivo*. Both the transmission and XRES image mean pixel values were found to be near-linear with gold nanoparticle concentration.

It is recommended that further investigation is required to establish the detection limit and sensitivity of this technique. This study has not included as full a treatment as that performed to characterise the XRF system, as its aim was to demonstrate the feasibility of the technique rather than fully assess it. It was decided that the XRF technique was the preferred technique to be developed for GNP concentration measurement *in vivo*. The reasons for this are as follows:

- A greater sensitivity is gained from using L-edge XRES due to the greater cross section of absorption than at K-edge energies. As XRES is a transmission imaging technique, there is a limit in sample thickness due to the poor penetration of low L-energies. XRF is not a transmission technique, and instead uses a 90^{o} geometry, enabling measurement of shallow sites in a thick sample.

- XRES requires a dual-energy source (tuned just above and just below the absorption edge), that is near-monoenergetic to gain good quantitative information of elemental concentration. A bench-top source with these properties was not available to us.

- The intensity of the XRF signal directly relates to the concentration of GNPs present, as a characteristic peak for gold is available. However, the mean pixel value of the XRES technique is a combination of the absorption of all elements present. The extent of the unwanted contribution of other elements present is related to the closeness in energy of the source used to acquire the two images.

- XRF can easily distinguish two or more elements, but this is not straight forward for the XRES technique.

It was therefore decided to leave assessment of the XRES technique at the preliminary stage, and pursue the use of the XRF technique to measure GNP concentrations in thick biological samples. However, the XRES technique will be returned to in the future if a fast imaging technique is required for thin samples.

2.11 Conclusions

X-ray based techniques can be used to analyse GNP-biomarker distribution and concentration at depth (unlike NPs tuned for optical techniques). A novel system has been constructed that has successfully obtained XRF spectra over a range of clinically relevant GNP concentrations. The results show promising potential in meeting our initial aims in being able to quantitatively measure GNP concentration, with a linear relationship between GNP concentration and XRF signal found. Concentrations can be measured up to an accuracy of ± 0.005 mgAu/ml for both the L-XRF systems (using a synchrotron and bench-top source). The linearity extends down to the detection limit of 0.005 mgAu/ml; a concentration that is lower than concentrations found *in vivo* as presented in the literature (~ 0.01 mgAu/ml) [25]. Our novel XRF system therefore meets the requirements set out at the design stage. Our system has a detection limit that surpasses the sensitivity of other x-ray based techniques found in the literature [24], [38], and could be used in the future to answer the clinical need for radiotherapy imaging of clusters of infiltrating cells. The measured DL was found to be the same for both the synchrotron and bench-top sources, showing potential for this technique to be used in the clinic. The sensitivity of the synchrotron system was 25 times more than the bench-top source, a difference that can be lessened through use of a higher power bench-top source. The main reasons for the novel system’s high sensitivity to low concentrations are the excellent energy resolution of the SDD, use of an optimal experimental geometry and source and choice of detecting L- rather than K-fluorescence. The XRF signal is low at small concentrations, and so it is suggested that a higher power bench-top source be used to gain sufficient counting statistics over shorter times.

A K-XRF technique was also assessed, and its performance was found to be worse than for the L-XRF system, having 6.5 times less sensitivity than the L-XRF bench-top system, and a detection limit of 0.2 mgAu/ml. This can be attributed to lower photoelectric interaction probabilities at higher K-edge energies, and a higher spectral background contribution. The K-XRF technique is however less affected by overlying thickness, and so may have a future use in looking at thick samples of high GNP concentration.

A preliminary investigation of an alternative x-ray method of measuring GNP concentration was considered. An x-ray edge subtraction (XRES) technique was used to measure a range of GNP concentrations and successfully produce XRES images with mean pixel values that were found to be near-linear with GNP concentration. It was decided that the XRF technique was more appropriate to meet the aims of an *in vivo* or thick *ex vivo* measurement technique; XRES is a transmission technique and will not perform well for thick samples. XRF was also preferred as it can be used to image more than two elements simultaneously, enabling the future possible use of imaging more than one biomarker.

Chapter Three

3 Development of tissue engineered bio-samples

3.1 Aims and objectives

An XRF system has been developed that is capable of quantitative measurement of GNP concentration. A range of GNP concentrations suspended in water have been successfully measured (Chapter Two) with a linear relationship between GNP concentration and gold XRF signal displayed down to a detection limit of 0.005 mgAu/ml. In order to meet the eventual aims of the project, there is a need to test the newly developed XRF technique on appropriate biological samples that better represent the clinical situation.

The aim investigated in this chapter is two-fold:

1. To produce a set of cellular bio-phantoms with GNP inclusions at concentrations expected to be found *in vivo*.
2. To produce a 3D *in vitro* cancer model which mimics the microarchitecture of solid cancers, with GNP inclusions, to provide a challenging test object to eventually assess the performance of 3D XRF imaging techniques.

In order to meet these aims, the following objectives were set:

1. Develop a protocol to achieve (i) cellular uptake of GNPs by (ii) a known amount.

2. Identify a method to construct reproducible 3D cellular phantoms suitable for XRF measurement techniques.

In order to achieve the above objectives, I worked at the UCL Division of Surgery and Interventional Science, Royal Free campus, to learn 2D *in vitro* tissue culture techniques and to develop a procedure for GNP uptake into cells. I also spent time at the UCL Division of Surgery and Interventional Science, Stanmore campus, to learn tissue engineering techniques used in developing 3D *in vitro* cultures.

3.2 Introduction to tissue culture and engineering

Many avenues of investigation in cancer research make use of tissue culture techniques to study the properties of cancers, their response to therapeutics and the effect of the immediate microenvironment on their behaviour (including conditions such as pH, oxygen concentration, and presence of other cell types). 2D *in vitro* cell culture provides reproducible, dependable and robust techniques and models that have contributed considerably to the relevant body of knowledge. The 2D approach typically consists of seeding established cancer cell lines into culture grade plasticware, e.g. flasks, micro well plates and Petri dishes. The cells attach to the bottom plastic surface and grow to form a confluent monolayer, in the presence of liquid nutrients (media comprising salt/sugar solutions, with amino acids and various growth factors). However, in the human body cells reside in 3D configurations and are often surrounded by ECM. Structure and positioning depends on cell type and function within the specific organs, e.g. hepatocytes are closely packed together in the liver in hexagonal-shaped lobules, lymphocytes are individually suspended in circulating blood or lymphatic vessels, and osteoblasts are located on the bone surface in a sheet-like arrangement of cuboidal cells. Phenotypes are not always retained in 2D cell culture conditions, where some *in vivo* characteristics can be lost: e.g. hepatocytes lose some liver-specific functions such as albumin production when in 2D, but retain these functions when maintained in 3D [58], [59]. Cell phenotype and biological activity can also be determined by cell-cell and cell-ECM interactions [60], [61] not always provided by 2D cultures. Cells present in a monolayer are generally exposed to uniform environmental conditions whereas cells in tissues (particularly solid malignant tumours) are exposed to gradients of nutrients, pH and waste products [62].

Animal models, most commonly using the laboratory mouse (*Mus musculus*), have been used to address the limitations of 2D culture systems. Human tumour xenografts consisting of implanting human cancer cells in organs / tissues of the mouse offer the potential to mimic *in vivo* human tumours and the associated microenvironment [63]. Mice used for xenografts are immunocompromised so they do not reject human cells. Mouse models present a more realistic 3D model of disease and so cancer cells are thought to be closer to the phenotype found in native human cancers. However the mouse as a tumour host does not necessarily respond in the same way as the human body. For example, a study investigating endostatin (an angiogenic inhibitor) gave different results between mouse model experiments and human trials. Endostatin was administered to three groups of mice growing different tumours (Lewis lung carcinoma, fibrosarcoma and melanoma) [64]. All tumours regressed significantly. However, phase 1 clinical trials showed that endostatin works differently in humans; no significant biological activity was reported [65]. Only three out of 15 patients showed therapeutic benefits; one patient tumour showed slow regression (17% over a year) and tumours in two patients remained stable.

More recently, the use of 3D *in vitro* models is gaining in popularity. 3D culture systems range in complexity from cancer cell spheroids to more complex tissue engineered models, and have been developed in an attempt to address the shortfalls of 2D culture. As such, they also aim to provide viable, but presently limited, alternatives to animal models. Multicellular spheroids (MCS) are formed by culturing cells in spinner flasks or agar coated culture plates; cells form spherical clusters up to several millimetres in size that can survive for weeks [66]. MCS offer a reproducible model that more closely resembles *in vivo* tissue including production of an ECM and similar patterns of protein production [60]. In the later stages of growth, MCS mimic regions found in solid tumours including an outer proliferating region and a central necrotic core which develops due to lack of nutrients and oxygen [67]. However, MCS do not fully emulate native tumour tissue in that they do not include a complex ECM, and do not contain cell types typically found in the tumour stroma (supporting tissue).

3D culture matrices, also known as scaffolds, are porous structures that can support cell growth, organisation and differentiation, and in some circumstances may be used as an animal-model replacement. They are engineered to mimic the ECM, which in human tissue is composed of proteins, proteoglycans and polysaccharides such as collagen, hyaluronic acid (HA) and laminin [68]. Each component can be individually used (collagen type I hydrogel [69], HA hydrogel [70] and laminin rich BD Matrigel [71] are found in the literature) or combined together to form the scaffold. Engineering the scaffold enables control of matrix characteristics such as density and porosity. Synthetic materials may also be used, e.g. PEG, a biocompatible material that has been widely used in tissue engineering. PEG was used in the synthesis of a 3D tumour model of human epithelial ovarian cancer [72]. This model proved more resistant to chemotherapeutics (paclitaxel and cisplatin) than the 2D model, once again highlighting the difference in cell response to therapy in 2D and 3D geometries.

This chapter presents work towards production of a novel 3D *in vitro* tumour model. A previously developed technique that embeds cells in a 3D collagen matrix [73] has been extended to create novel 3D phantoms consisting of cells incorporating GNPs. The cellular phantoms were designed with the ability to control parameters such as cell type, cell density, GNP concentration and GNP distribution. The capability to control the distribution and concentration of GNP-loaded cells provides a technique that can create challenging 3D imaging phantoms to test the performance of the developed novel XRF imaging techniques presented in Chapter Four. It should be noted that the phantoms were designed to incorporate 2D cultured cells into a 3D matrix with the purpose of measuring the cellular GNP concentration using the novel XRF technique. At this stage the aim is not to culture cells in 3D. However, this work will be extended in the future to 3D culture techniques in order to construct a more realistic tumour model consisting of dense artificial cancer masses (ACMs) that have taken up GNPs, nested into less dense ECM containing cell types which populate the tumour stroma (such as fibroblasts and macrophages). The eventual aim will be to mimic the tumour microenvironment to determine how cell-cell communication, cell-ECM interactions, ECM and cell density, and outside forces found physiologically such as mechanical stress and fluid flow, will affect uptake of NPs in cells.

3.3 Considerations involved in development of a 3D cellular model with nanoparticle inclusions

The model development has involved two main steps: (i) internalisation of GNPs into tumour and non-tumour stromal cells, (ii) the engineering of a 3D structural scaffold in which to embed cells.

3.3.1 Internalisation of GNPs into cells

An understanding of cell uptake processes is required in order to be able to control cell uptake of NPs. The cellular plasma membrane is a dynamic structure of lipid bilayers and proteins that segregates the cytoplasm from the external environment and regulates transport of substances into cells. Oxygen, carbon dioxide, water, and small hydrophobic or non-polar molecules can pass through the membrane through diffusion (driven by concentration gradients). Small molecules such as amino acids and ions enter cells through active transport through the membrane protein pumps or ion channels. Nano-sized hydrophilic bio-macromolecules are transported into the cell through endocytosis, which is a form of active transport. This process involves the cell taking in objects by enclosing them into invaginations which form at the cell membrane and which develop into vesicles, as illustrated in Figure 33. Common endocytotic processes that engulf particles in membrane vesicles are:

(i) Phagocytosis: this is mainly undertaken by monocytes, macrophages, and neutrophils, the purpose being to engulf particles such as bacteria with diameters > 750 nm.

(ii) Pinocytosis: smaller particles (a few to several hundred nm in size) are internalised by this process. The fluid surrounding the cell is internalised, implying that all substances in the fluid area of invagination are taken up simultaneously [74]. This process occurs in almost all cell types.

(iii) Clathrin-mediated endocytosis: this is the most studied endocytic pathway, and is a type of receptor mediated endocytosis (RME) [74]. When materials are < 100 nm in size, their dimensions approach the size of biomolecules; this provides an opportunity since NPs can mimic biomolecules and be treated by cells as such. Particles are deposited in small endocytotic vesicles (usual diameter < 100 nm) that fuse with early endosomes [75].

The processes leading to penetration of NPs through the cell membrane directly relates to cellular uptake; however, a systematic knowledge of these processes is still lacking from the literature [75].

Once particles are internalised and localised in vesicles, the vesicles degrade down to multivesicular bodies / late endosomes which then fuse with lysosomes. Lysosomes contain proteases and other enzymes that degrade most biological materials. Alternatively the particles may leave the cell surface directly through the early endosome or through recycling endosomes. This process is illustrated in Figure 33.

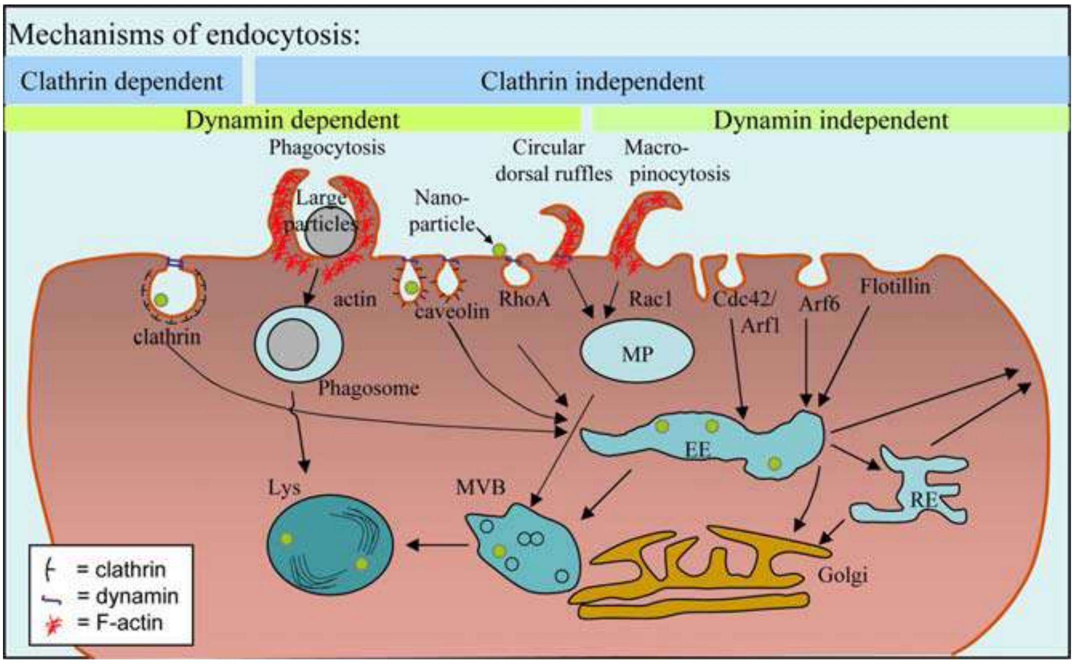

Figure 33 Model of endocytotic mechanisms and intracellular transport [74].

The rate of transport of NPs into cells is governed by factors that affect the interaction between the NP and the cell membrane, the key factors being (i) NP size, (ii) NP shape, (iii) NP surface chemistry, (iv) NP charge and (v) properties of the cell membrane dependent on cell type. In order to achieve uptake of GNPs into the cell lines used in this study, each of the major factors were considered.

3.3.1.1 Size

It was found that the uptake of GNPs in HeLa cells varies with their size [76], [77], with the most efficient uptake found for NP sizes 25 – 50 nm. It is proposed that this size gives good multivalent cross linking with membrane receptors and an optimum geometry for membrane wrapping involved in RME [78]. It is worth noting that most NPs used in medicine will have a size distribution that may result in a range of possible endocytotic routes into the cell.

3.3.1.2 Shape

Spherical GNPs enter cells more readily than gold nano-rods (GNRs), due to the longer membrane-wrapping time required for the rod-shaped particles [79]. Spherical GNPs were used in this study. Likewise, the aspect ratio of GNRs determines cell uptake efficiency; shorter GNRs are internalised more readily than longer GNRs with similar surface charges [80].

3.3.1.3 Surface chemistry

Surface chemistry is paramount in order to functionalise NPs for medical use, reduce surface reactivity and toxicity, and improve stability. Serum protein adsorption onto the NP surface occurring either *in vivo* (when in blood, plasma or interstitial fluid) or *in vitro* (when suspended in growth medium, as for this study) can mediate the cellular uptake process allowing NPs to be internalised by RME [81]. For example, the amount of serum proteins adsorbed on GNRs (particularly bovine serum albumin) showed a positive correlation with cell uptake [80]. Cell medium supplemented with 10% foetal calf serum was used in GNP incubation of cells in this study.

It has also been suggested that NPs may aggregate in electrolytic solutions, such as cell media, if they are not stabilised with serum proteins, the aggregation being caused by electrostatic interactions [81], [82]. NPs that have clumped together may potentially enter cells at a diminished rate due to the increased size of aggregates [77].

The proteins adsorbed to the NP surface will vary depending on the biological microenvironment the NP is in. Also, distortion of the protein structure may occur upon interaction with the NP, altering the way the protein interacts with the cell membrane [77]. Overall, effects on internalisation are not well understood.

NPs can be further functionalised by adding ligands onto their surface that preferentially attach to (target) specific proteins on the cell surface [83]. This will be implemented in future studies to develop more complex 3D biological phantoms, but has not been included at this stage.

3.3.1.4 Surface charge

Modification of the surface of NPs may also change the particle surface charge, a factor that relates to cellular uptake. The cell surface contains charged phospholipid head groups and proteins, which are generally negatively charged. Thus, positively charged NPs are more readily internalised than negatively charged or neutral particles. The surface charge of the NPs also affects the internalisation mechanism, with negatively charged NPs not undergoing RME, and positively charged NPs being rapidly internalised by RME [75].

3.3.1.5 Cell surface – protein interactions

Data regarding cell surface-protein interactions with NPs is limited, and the available data are from *in vitro* measurements; further knowledge of interaction processes occurring *in vivo* is needed. The relationship between cell type and NP properties is not yet well understood; evidence suggests that the cell type affects both the endocytotic pathway and intracellular response to NPs [75]. Cell-specific uptake mechanisms can lead to increased sensitivity or resistance to NP toxicity [84]. For example, modified GNRs can selectively kill cancer cells (A549) but not normal cells (normal human bronchiolar epithelial cell 16HBE and mesenchymal stem cells) due to differences in intracellular trafficking of the NPs for each cell line [85], [86]. This has potential in clinical translation.

3.3.1.6 Cytotoxicity of NPs

Evidence for the cytoxicity of GNPs is equivocal. GNPs were reported to induce DNA damage and oxidative damage in lung fibroblast cells [87]. It has been recently reported that the cytotoxicity can be attributed to the cetyltrimethylammonium bromide

(CTAB) coating used to functionalise GNPs rather than the GNPs themselves [77], [80]. CTAB can enter cells with or without NPs, damage mitochondria and then induce apoptosis [80]. On the other hand, no cellular toxicity was associated with uptake of GNPs stabilised by citric acid ligands by HeLa cells (98% viability shown using a trypan blue exclusion staining assay) [81].

No substantial changes in gene expression or cytotoxicity were found when incubating cells with gold nanorods (GNRs) alone [77]. This study proposed that as GNRs enter and leave cells in vesicles (as do GNPs), the GNRs are trapped in vesicles and are likely to experience little interaction with the nucleus and cytosol, and therefore have limited toxicity. The study conducted microarray experiments and examined gene expression profiles for HeLa cells incubated with GNRs. By studying gene expression, it is possible to map the direct effects that drive cell changes due to the presence of NPs. Some genes involved in apoptosis were found to be down-regulated, suggesting that GNRs cause changes in the apoptotic pathway. However, further investigation is needed before the relationship of NP and apoptotic genes is fully understood due to the complex involvement of many proteins and feedback loops in apoptosis [77]. Cytotoxicity may also depend on the cell line used, as the cellular uptake and removal of NPs differs for different cell types as previously noted [75].

A study of the effect of GNP size on cell toxicity was undertaken for GNP sizes 0.8 – 15 nm [88]. Connective tissue fibroblasts, epithelial cells, macrophages and melanoma cells (the four cell types tested) proved most sensitive to GNPs 1.4 nm in diameter. In contrast, 15 nm GNPs were found to be non-toxic at up to 60-fold higher concentrations than 1.4 nm GNPs. The cellular response was found to be size dependent; 1.4 nm GNPs caused mainly rapid cell death through necrosis within 12 hours, while closely similar sized 1.2 nm GNPs effected cell death by apoptosis. The reason for this is currently unknown, but it may be due to differences in subcellular distribution of NPs dependent on NP size, particularly in terms of where the NPs are localised within the cell.

A study using 3D tumour spheroids has shown that NP toxic effects are significantly reduced by up to a factor of five in 3D as opposed to 2D cultures [89]. It was proposed that two important aspects explain this reduction in toxicity to 3D cultures (which more closely resemble the *in vivo* toxicity response): (i) 3D culture is denser due to cell clusters and contains an ECM layer; this better mimics tissue mass transport, (ii) cell phenotype changes due to intensified cell-cell interactions [89]. The data obtained from 3D cultures correlate well with the data from animal models, showing future potential of the use of GNPs.

It has been proposed that GNPs can affect intracellular signalling by binding to cell surface receptors [90]. Cells control their function and state through signalling events triggered by binding of protein ligands with membrane receptors, and the extent of receptor-ligand binding and receptor cross-linking affects the intensity and duration of the signalling process. NPs coated with ligands could change the degree of surface receptor cross-linking by a controllable amount dependent on size, shape and coating of the NPs. It has been proposed to investigate this further to control subsequent cell responses and mediate biological effects to assist cancer treatment [90].

3.3.2 Engineering of a 3D scaffold

The second step of the phantom-making process involved constructing a 3D scaffold in which to embed the GNP-loaded cells. Choice of scaffold was influenced by available expertise but also by the scaffold having the desired characteristics for these studies and for future testing.

It was decided to use natural (ECM proteins) over synthetic scaffolds (such as ceramics currently used in the Stanmore campus) since the ultimate aim was to develop a 3D *in vitro* model of cancer with a microarchitecture mimicking that found in situ (comprising of foci of cancer cells surrounded by tumour stroma, i.e. ECM and supporting non-cancer cell types).

The ECM of tissue is composed of four major proteins: collagen, fibronectin, elastin and laminin. Collagens are the most abundant and are so the logical choice to construct a scaffold. There are at least 19 types of collagen in the body, with collagen type 1 being predominant, and so a collagen type 1 gel was selected to comprise the scaffold. Collagen type 1 is present in scar tissue, and found in structures including organic bone tissue and tendons. Collagen type 1 consists of three polypeptide α-chains arranged in a triple-helix forming sequence [91].

The ability to engineer scaffolds means that characteristics such as density and porosity can be manipulated. Collagen density can be controlled through methods such as plastic compression, which impacts on the porosity [92]. Cellular densities within foci of tumour cells in tissue and surrounding tissues are not well documented, but generally solid cancers are quite hard, dense tissues (with an estimated cell density of 10^7 cells/cm^3). This is rarely considered in cultured models. However the present 3D model made using collagen as the acellular component offers the opportunity to manipulate densities for sections of the phantom in further studies. Refer to Section 3.4.10 for a full discussion of this technique.

3.4 Development of bio-phantom construction protocol

3.4.1 Aims of production of bio-phantoms

A series of biological cellular phantoms were produced in order to demonstrate the use of the novel quantitative XRF technique developed in Chapter Two. The ability of the novel technique in sensitivity to GNP concentration and distribution needs to be assessed using samples that closely resemble the clinical situation. Two different types of cellular phantoms were constructed to achieve this:

1. A set of bio-phantoms to investigate effectiveness of quantitative measurement of GNP concentration using the bench-top L-XRF technique developed in Chapter Two. These phantoms will consist of GNP-loaded cells uniformly embedded in an uncompressed 3D collagen matrix. The design criteria for this set of phantoms are outlined in Section 3.4.2.
2. A range of more complex 3D ACM phantoms will be produced for future testing of the imaging capabilities of both the L-XRF technique and a combined diffraction / fluorescence imaging system (proposed in Chapter Four). These phantoms will consist of a dense GNP-loaded cancer mass

surrounded by a less dense collagen gel embedded with non-cancer cells. A discussion of this set of phantoms is found in Section 3.4.10.

3.4.2 Design criteria for a useful bio-phantom for XRF analysis

In order to test the ability of the novel XRF system to quantitatively measure GNP concentration in cells, the biological phantoms were designed to meet the following criteria:

a) A uniform distribution of GNP-filled cells in the scaffold was required; this is to relate the number of cells in the measurement volume to the total number of cells in the entire sample.

b) The sample holder must be thin and of a low attenuation coefficient to enable x-rays to penetrate the sample and avoid inclusion of scatter from the holder.

c) The cells must contain GNP concentrations similar to that found clinically. A literature search was performed to find typical *in vivo* GNP concentrations. The GNP concentrations found for a Her2+ breast cancer targeted GNP study using a mouse model have been presented in Chapter One (Table 3). The concentrations found ranged from 0.16 mgAu/ml (muscle uptake) to 3.48 mgAu/ml (periphery of Her2+ tumours) [24]. The authors explain that an unusually high GNP dose (22 mgAu) was injected into the mouse; our phantoms were designed to include even lower concentrations than those reported in Table 3 to represent a more realistic clinical situation.

d) The concentration of GNPs in the sample must be above the detection limit of the system. The detection limit measured in Chapter Two was lowered further through modification of the system, now enabling sensitivity down to 0.001 mgAu/ml (refer to Section 3.7.3.3 for details on the system modification).

3.4.3 Chronological steps towards a bio-phantom protocol

The following iterative steps were undertaken in order to meet the design criteria for XRF imaging:

1. Incubation of cells with NPs: This was first attempted by adding GNP containing-medium to a pre-prepared, live 3D culture of cells embedded in collagen gel. The sample was incubated for 48 hours. In this time, the peripheral ~1 mm layer of the gel darkened to a black colour (indicating GNP presence) with no colour change seen deeper into the sample, suggesting the GNPs did not penetrate through the collagen scaffold to reach cells deep in the sample. This mimics the *in vivo* situation of increased uptake in the periphery of tumours compared with the centre of tumours [24] and so could be useful in future studies of GNP transport throughout the ECM. However, this did not meet the design criteria of a known and controllable GNP distribution required for XRF measurement of GNP uptake (criteria (a) above)), and it was decided to incubate the cells with GNPs in 2D culture. This resulted in a more even exposure of cells to GNPs, resulting in a more even GNP uptake. The GNP-loaded cells were then transferred to the 3D collagen gel and set.

2. Uniformity of distribution of cells within the matrix: Iterative improvements in the sample-making process were made to achieve this; using a micro-pipette to evenly disperse the cells throughout the collagen gel just before the gel set is standard practice to achieve a uniform distribution.

3. Washing of cells: Dark spots of size ~ 2 μm were visible under a microscope in the first batch of samples, thought to be due to GNPs outside of the cells aggregating together. To ensure that all GNPs measured by the XRF technique were NPs taken up by cells, a rigorous washing procedure (with isotonic phosphate buffered saline (PBS)) was included in the protocol. It is evident from transmission electron microscopy (TEM) images (such as Figures 42 and 44) that washing the cells results in samples where the only detected GNPs are internalised by cells.

4. Sample size: Samples were initially set in a bijou sample holder of internal diameter 15 mm and height 50 mm. The size of the bijou was greater than the measurement volume, and so regions of the sample outside the measurement volume acted to attenuate the signal. Smaller sample pots of dimensions of inner diameter 8 mm and height 45 mm were used to reduce this effect. Another benefit of using a smaller pot is that less GNP solution is required to incubate the cells (as smaller flasks were used), to minimise experimental costs.

The main problem encountered with the sample making procedure was the collagen gel setting process. One group of samples did not set correctly; it is thought this was due to the collagen not being at a low enough temperature. It is advised to keep the collagen refrigerated when not in use. Also, the most common reason for gels failing to set is incorrect pH. The optimum pH for gel-setting is indicated by colour changes of the indicator dye (methyl red) included in the medium from yellow to pink, and judgement on correct change is operator dependent. A more vigorous system would include development of an optical spectrometer to measure when the correct colour is reached.

3.4.4 Cell Maintenance

The cell lines used were the human colon adenocarcinoma cell line HT29 (passage (p) 30-42) and the mouse embryonic fibroblast cell line 3T3 (p 28-32) (both from the European Collection of Cell Cultures, Sigma-Aldrich, Dorset UK). Colorectal cancer was chosen as the demonstrator cancer type because of the availability of a well characterised cell line (HT29). The cell lines represent tumour (HT29) and non-tumour (3T3) cellular components in the phantoms.

Standard cell maintenance protocol was implemented throughout. Cells were maintained under sterile conditions as 2D monolayers in 100% humidity, 5% CO_2 in air at 37 °C in an incubator. The cells were cultured in Dulbecco's Modified Eagle Medium (DMEM) with 1000 mg glucose/L, L-glutamine, NaHCO and pyridoxine HCl (Sigma-Aldrich) supplemented with 10% Foetal Calf Serum (FCS, 5129, First Link UK Ltd, Birmingham UK) and 1% Penicillin/Streptomycin (P/S, GIBCO, Invitrogen, Paisley

UK). The latter was added as a prophylactic antibiotic. The DMEM contains nutrients that the cells require to function and stay alive, and must be changed frequently (~twice weekly) to replace nutrient levels that have been depleted and remove cell wastes.

Once cells are seeded into a flask, they adhere on the bottom surface (this process takes less than 24 hours; usually up to 4 hours) and grow to form a monolayer. While populating the available space, cells continue to perform cellular functions. Optical microscope images of the cell lines used in this experiment are displayed in Figure 34.

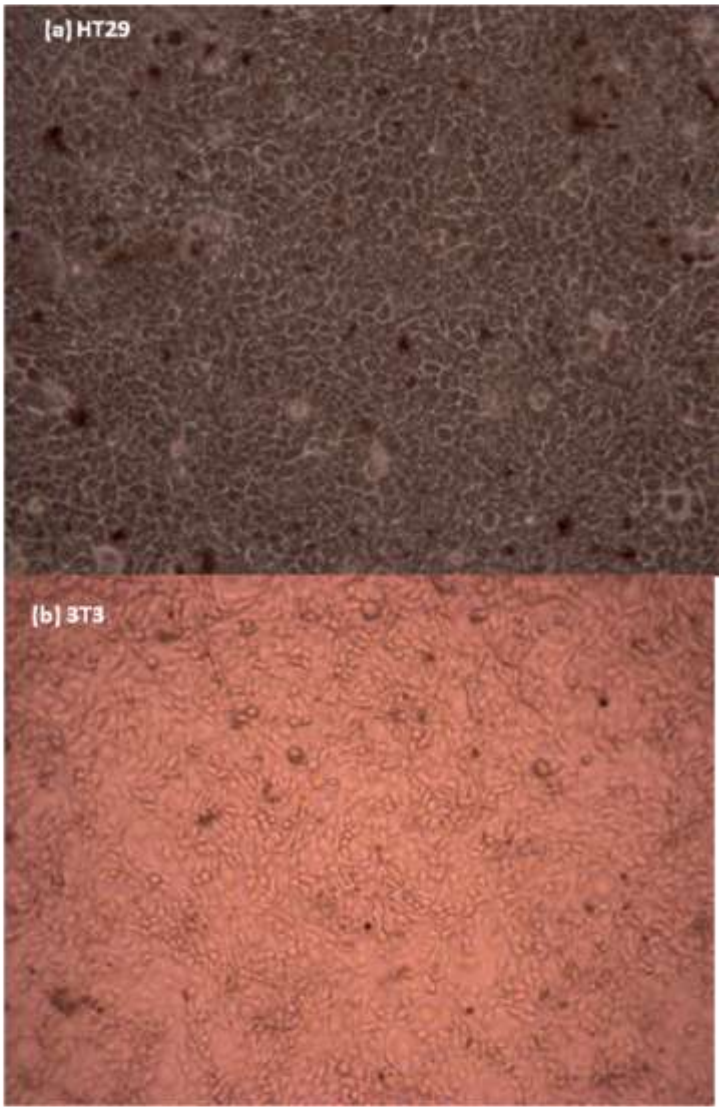

Figure 34 Optical microscope images of (a) HT29 and (b) 3T3 cells, at 100 X magnification. The cell lines have been incubated with 0.5 mgAu/ml GNPs. Black dots

within or on top of cells are thought to be GNP aggregates. The number of cells continuously increases as cells undergo mitosis. Biologists use the term ‘confluence’ to numerically describe this; 100% confluency describes a flask surface completely covered in cells, 50% confluency is when the cells cover half of the surface, and so on. Once the cells become 100% confluent, there is no more space to support normal growth, and as a result growth slows down and eventually stops. This is due to contact inhibition (cells arrest growth when they come into contact with each other), and also a lower availability of nutrients and build-up of waste.

To avoid overcrowding and maintain healthy cells in culture, cultures are propagated usually before they reach 100% confluence – at between 85-95% confluence. This is achieved by a process called passaging, which involves trypsinising (enzymatically detaching) cells from their adherent plastic surface, and adding a fraction of those cells to a new flask for seeding (not less than 10% of the original detached population). The process is as follows:

1. Cell medium is removed from the flask, and the cells washed with PBS, followed by PBS-EDTA (ethylenediaminetetraacetic acid). Washing removes the medium and associated proteins which are able to bind trypsin and neutralize its action. EDTA chelates proteins present on the cell membranes that contain calcium, and so begins the process of breaking protein-protein links between cells.
2. Trypsin (1 mg/ml trypsin in PBS-EDTA, Gibco) is added to the flask and incubated for approximately 30 seconds, along with mechanical disruption of the flask to mechanically encourage the cells to fully detach from the plastic, as determined using an optical microscope. The amount of trypsin added depends on the size of the flask used; 1.5 ml was used for the 75 cm^2 flasks routinely used for cell maintenance, and 0.5 ml for the 25 cm^2 flasks used in the nanoparticle incubation studies.
3. Cell medium is then added to the detached cells in order to neutralise the effect of the trypsin (12 ml or 5 ml medium for the 75 cm^2 or 25 cm^2 flasks respectively). If trypsin remains in the solution for too long it starts breaking

up cell membranes and killing cells. 10% of the cell / medium suspension is then transferred (passaged) into a clean flask, and the total volume made up to 10 – 15 ml or 3 – 5 ml using cell medium for the 75 cm^2 or 25 cm^2 flasks respectively. The two step addition of medium ensures that the trypsin is fully neutralized (this requires a 1:1 ratio of FCS:trypsin; or 10:1 ratio of FCS-supplemented medium:trypsin). The flask is then placed level inside the incubator and the process repeated once the cells have grown to near 100 % confluence.

3.4.5 Incubation of cells with gold nanoparticles

The GNP-PBS suspension was prepared as outlined in Section 2.2 under aseptic conditions, using PBS instead of DIW. Each pot of Aurovist^{TM} 1.9 nm GNPs contains 40 mg GNPs; the content of the pot was suspended in 4 ml PBS to give a final concentration of 10 mgAu/ml PBS. One of the smallest available culture flasks (25 cm^2) was used in order to minimise the amount of GNPs required for each study but at the same time provide a few million cells for experimentation. This meant that 4 ml of the required GNP concentration was sufficient for incubation. Figure 35 displays the appearance of the flasks at the time of incubation.

Figure 35 Cell culture flasks containing HT29 cells being incubated with GNPs (right) and without GNPs (left)

An example of the volumes of GNP-PBS solution and cell medium required to give the correct concentration is demonstrated in Table 11.

Table 11 Quantities of GNP-PBS suspension and cell medium required for nanoparticle incubation of cells.

GNP concentration (mgAu/ml)	**GNP mass in 4 ml to give this concentration (mg)**	**Volume of GNP-PBS solution (10 mgAu/ml) needed (ml)**	**Volume of medium added (ml)**
4	16	1.6	2.4
2	8	0.8	3.2
1	4	0.4	3.6
0.5	2	0.2	3.8
0	0	0	4

Once cells were 75% confluent, the cell medium was removed and replaced with 4 ml of the GNP-containing medium and incubated for the required time at conditions outlined in Section 3.4.4. This procedure was based on the *in vitro* GNP incubation studies reported in the literature [88], [93]. A time of uptake study (described in Section 3.6) found that the optimum incubation time was 24 hours for the 1.9 nm GNPs.

After the incubation period, the cells were thoroughly washed with PBS followed by PBS-EDTA to remove GNPs not taken up by cells, trypsinised according to standard protocol, with 0.5 ml trypsin (procedure outlined in Section 3.4.4), re-suspended in fully supplemented medium and a small amount (up to 50 µl) was removed to count cell numbers using a haemocytometer (under an optical microscope). The cell suspension was made into a final volume of 5 ml and spun at 400g for 5 min in a centrifuge in order to separate out the cells from the liquid medium, and retrieve the cells in the form of a cell pellet. Figure 36 displays a photograph of an example cell pellet. The cells are then ready to be resuspended in very small volumes (100 µl) and be included in a 3D collagen gel model, as described in Section 3.4.7.

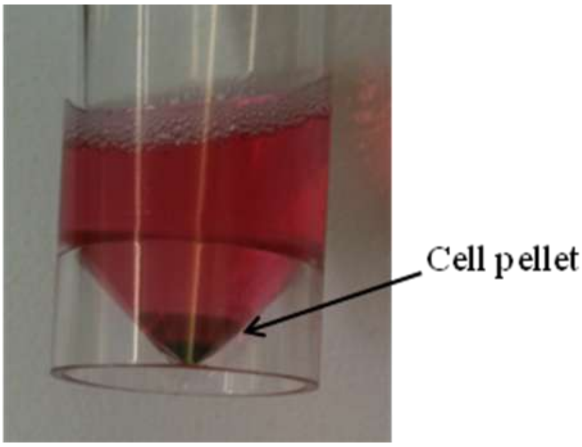

Figure 36 Photograph of cell pellet formed after centrifuging a cell suspension. The black colour of the cell pellet is due to the GNP inclusions in the cells (1.9 nm GNPs are black in colour).

3.4.6 Cell counting

It is important to know the number of cells included in a 3D collagen gel model in order to perform gold XRF signal corrections. Standard cell counting protocol was used. A haemocytometer is a device used to count cells; it consists of a thick glass slide with an indentation that creates a chamber when a thinner glass coverslip is in contact with it (Figure 37).

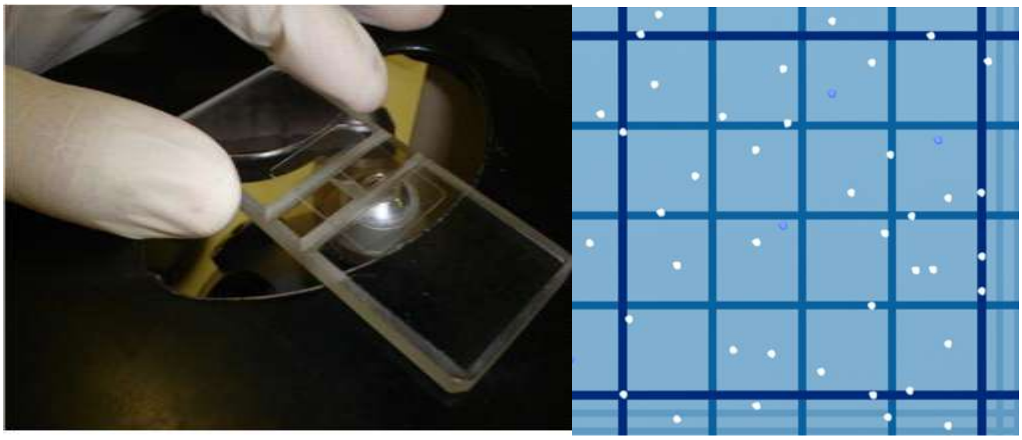

Figure 37 Haemocytometer with glass coverslip being viewed with an optical microscope. The right hand side image displays cells (white spots) contained within the etched haemocytometer grid as viewed under a microscope.

A small volume of the cell suspension is applied to the edge of the coverslip using a micro-pipette, and is sucked into the chamber by capillary action, completely filling the chamber. The chamber is engraved with a laser-etched grid of lines that are visible under a microscope (illustrated in Figure 37). The area bound by the lines and the chamber depth is known, and so it is possible to count the number of cells per unit volume of fluid through a microscope. An appropriate dilution of the cell suspension should be used in order to reach a compromise between achieving a large enough sample size and avoiding overcrowding making it difficult to count (not less than 100 cells per central chamber; empirically no more than 300).

The accuracy in the cell counting technique is ± 10% [94]; this was achieved through the counting of over 100 cells per sample. Between 3 – 5 readings from separate chambers were carried out for each cell population to average numbers and reduce errors due to pipetting or dispersal. In practice, this error is driven by operator practice; the same operator was used for each sample thereby inducing the same error in all readings. Flow cytometry provides an alternative method of cell counting, which could be implemented as a faster and more accurate cell counting technique in future work.

3.4.7 Preparation of a 3D collagen model

Collagen lattices are formed by allowing fibrillogenesis to occur; this is a thermodynamically driven aggregation of fibrils following neutralisation of native collagen solution (implemented in our procedure). The collagen lattice is made of narrow fibrils at extremely low density (0.2 – 0.4% collagen in > 99% fluid) [73]. Cells within such reconstituted lattices are thought to bundle fibrils together over time [95]; however, our collagen gels were fixed one hour after the collagen set and so the fibrillar architecture did not have time to be remodelled.

A standard protocol was followed to produce the cell-embedded collagen phantoms [73]. 1 ml of cell populated collagen gel was produced for each sample using 0.8 ml collagen type I (rat-tail collagen type I, protein concentration 2.035 mg/ml in 0.6% acetic acid, First Link UK Ltd.), 0.1 ml of Minimum Essential Medium (MEM, 10X with Earle's Salts, without L-glutamine, sodium bicarbonate, GIBCO 21430, Invitrogen) and 0.1 ml of cell suspension.

Collagen type I was mixed with MEM and its pH was neutralised by the addition of 1 M sodium hydroxide in a dropwise fashion until a colour change from yellow to cirrus pink was observed (pink indicating the pH required for the gel to set (7 – 7.7) [96]. The cell suspension was immediately added and the mixture micro-pipetted to ensure a uniform suspension of the cells in the collagen, taking care to prevent the formation of air bubbles which would affect the required cell density uniformity. The mixture was then transferred to a plastic container of inner (outer) diameter 8 mm (9 mm), height 45 mm, and the gel set in a humidified incubator with 5% CO_2 at 37 °C for 30 minutes. An example of the appearance of the collagen embedded samples is displayed in Figure 38.

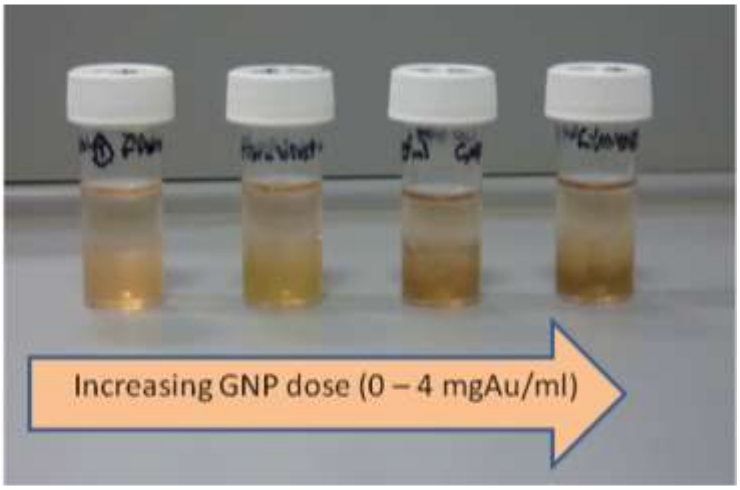

Figure 38 3T3-embedded collagen samples over a range of initial GNP concentrations.

3.4.8 Fixation of samples

Gel samples were fixed one hour after setting up the collagen gel. 0.8 ml of gluteraldehyde fixative (10% gluteraldehyde, 90% PBS) was added to the gel pot and left at room temperature for 24 hours until the gel fully fixed (this is indicated by a progressive lightening in colour of the pink gel). The gluteraldehyde solution was then removed, the gel washed with 0.8 ml PBS, and then finally covered in 0.8 ml PBS. The samples were then stored at 5 °C in order to minimise the risk of infection or bacteria formation.

3.4.9 TEM imaging protocol

TEM imaging is a widely used technique to determine NP distribution within cells. The TEM imaging for this study was performed by the Electron Microscopy service at the Royal Free Hospital, London, using the following procedure.

Following fixation in gluteraldehyde, the samples were cut into cubes < 2 mm in thickness which were washed with several changes of PBS and postfixed using 1% osmium tetroxide / 1.5% potassium ferricyanide (BDH, Leicester, UK) for 1.5 hours. The samples were then washed using distilled water and dehydrated using graded alcohols from 30% to 100%. They were then placed in 50% alcohol / 50% Lemix (TAAB Laboratories Equipment Ltd, Reading, UK) epoxy resin mixture overnight, and the following day infiltrated with 100% Lemix resin for two days (Lemix epoxy resin consists of 25 ml Lemix A, 55 ml Lemix B, 20 ml Lemix D and 2 ml benzyldimethylamine). They were finally embedded in fresh Lemix resin and polymerised at 70 °C overnight.

Ultrathin sections were cut using a diamond knife (Diatome) and collected on 300HS, 3.05 mm copper grids (Gilder). The ultrathin sections were stained with saturated uranyl acetate in 50% ethanol (TAAB) for four minutes followed by Reynold’s lead citrate for five minutes (Reynold’s lead citrate: dissolve 1.33 g lead nitrate (BDH, Leics UK) in 15 ml distilled water, and 1.76 g sodium citrate (BDH) in 15 ml distilled water). Solutions were mixed together and the resulting precipitate dissolved with 8 ml 1M sodium hydroxide (BDH, Leics UK) making up to a final volume of 50 ml.

The ultrathin sections were viewed using a Philips CM120 TEM and photographed with an AMT Digital Camera (Deben UK).

3.4.10 Development of a novel 3D artificial cancer mass with GNP inclusions

The collagen hydrogels described in Section 3.4.7 consist mainly (> 99%) of water and are therefore of a much lower density than that found *in vivo*. Advances have been made to increase the density in a controlled way to more closely resemble native tissue. Simple engineering principles can be used to squeeze out excess fluid and so increase collagen density. Techniques include use of a load to plastically compress the hydrogel, capillary suction of fluid into porous layers and also self autocompression under the gel’s own weight [92]. Plastic compression technology can be applied to increase matrix density by up to 30% (similar to solid cancer densities) [97]. Cell viability is retained in cells embedded in the scaffold during compression; the standard compression method results in only a 10% reduction in viability [92].

The compression process was found to produce structuring consisting of compacted lamellae of collagen fibrils parallel to the fluid-leaving surfaces [92]. This was proposed to be a consequence of the directional flow of fluid from a single surface. It was found that collagen fibrils and cells were retained at the leaving interface, increasing the density at the surfaces of the compressed gels. Structuring can be further controlled by applying uniaxial strain to the hydrogels to generate alignment of cells [98]. Greater control of the mechanical properties and dimensions of the compressed gel may be achieved through selection of the compaction technique used and the extent and speed that the interstitial fluid is expelled [92]. For example, slowing the process down and having greater control of fluid removal through use of blotting paper rather than a load will enable more control over compacted gel dimensions.

Previous work by the UCL Division of Surgery & Interventional Science enabled the construction of samples that closely mimic colorectal cancer. The samples were composed of a dense ACM embedded in a less dense collagen gel containing sparse fibroblasts and endothelial cells [99]. The constructed 3D model had the advantages of controllable matrix density and spatial position of different cell types. The compressed ACM showed a major feature of *in vivo* cancer masses, namely hypoxia was confirmed in the cells in the central core, and release of VEGF (vascular endothelial growth factor, a proangiogenic factor relating to hypoxia and tumour growth) was detected in cancer cells present at the tumour mass edges [63], [100]. Work in similar 3D non-cancer models by the same group has demonstrated that increasing collagen density in cell-seeded scaffolds results in the formation of oxygen gradients, where cells on the surface are exposed to higher oxygen levels compared to the core. The level of hypoxia is controllable and dependent on the cell and matrix density. Reversal of angiogenic up-regulation is also possible through simple perfusion features that mimic vasculature [101]. We hope to make use of such tissue engineering strategies in the near future to create 3D tumour models with hypoxic cores to investigate the effectiveness of GNPs targeted for hypoxia.

This project has aimed to extend the 3D ACM technique [99] to incorporate cells with GNP inclusions with the aim of providing a novel 3D GNP imaging phantom of similar cell type and density found *in vivo*. The produced samples will act as complex imaging phantoms to test the XRF imaging system (and enable 3D XRF images to be acquired) and also to enable future testing of the combined fluorescence / diffraction imaging system proposed in Chapter Four.

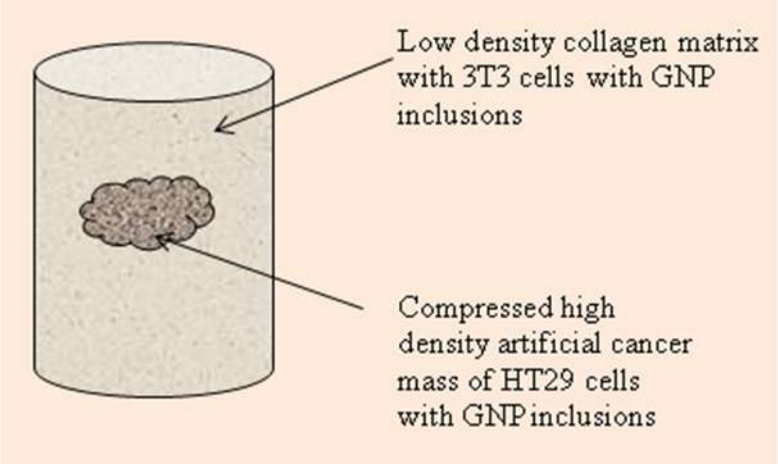

Figure 39 Illustration of the novel 3D tumour model with GNP inclusions.

The procedure used to produce the 3D GNP-loaded imaging phantom is as follows:

1. All cells were incubated with GNPs of required concentration in 2D culture, according to the procedure described in Section 3.4.5. This step brings novelty to the previous ACM technique through incorporation of GNPs.
2. A collagen gel was created by populating collagen with HT29 cells.
3. The unset gel was poured into a cuboidal mould and allowed to set at room temperature for 30 minutes.
4. The gel-containing mould was placed onto a nylon mesh which was in turn placed on top of a 165 µm stainless steel mesh resting on absorbent paper [73]. The gel was compacted using a standard plastic compression protocol modified from [92] (compression under a load (73.55 g) for five minutes). This process was repeated on the other side of the gel to reduce cell concentration gradients resulting from directional fluid flow. It has been previously demonstrated that this compression technique brings approximately a 16 – fold increase in collagen density from the uncompressed gel, giving a final collagen density of 6.7% [99].

The mould and load are displayed in Figure 40.

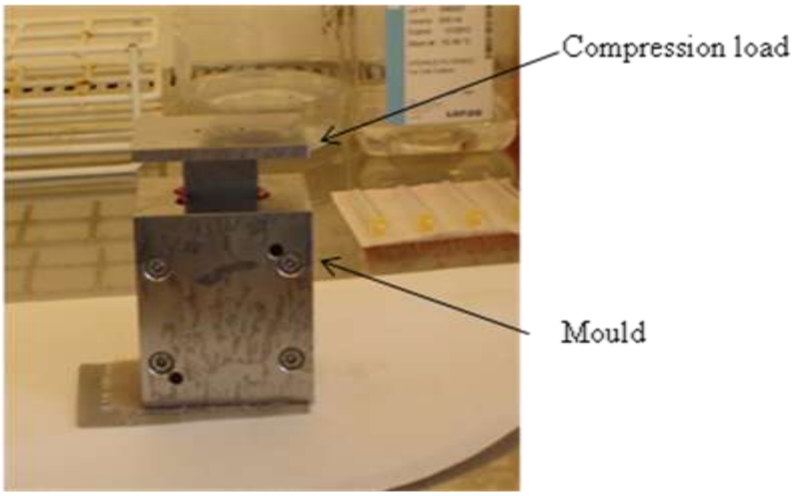

Figure 40 Mould and compression load used to compress the gel to form an ACM.

5. A portion of the dense ACM was cut from the bulk cuboid gel using a surgical knife (Figure 41), and placed in a non-dense surrounding collagen gel which was populated by 3T3 fibroblasts.

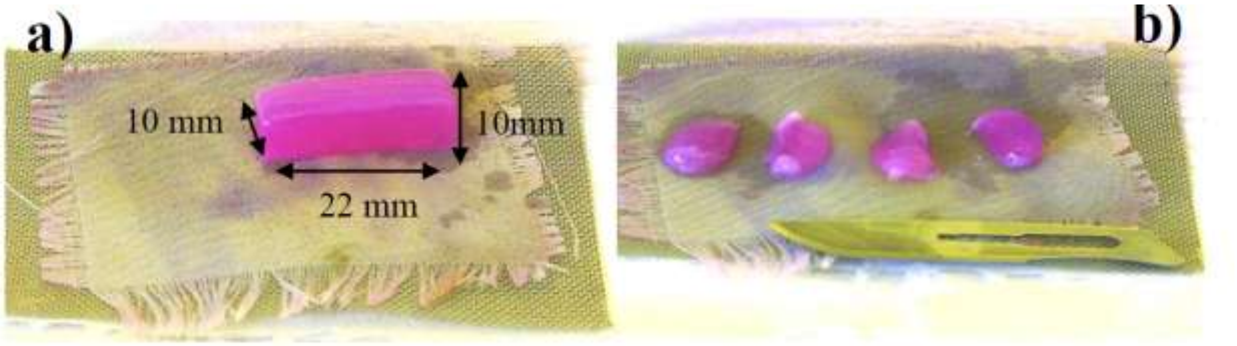

Figure 41 (a) Cuboidal ACM once removed from mould, (b) ACM components to be inserted into a low density collagen gel seeded with 3T3 cells (image taken from [99]*).*

6. The finished sample was incubated for 30 minutes, and the sample fixed according to the procedure outlined in Section 3.4.8.

3.4.11 Discussion

The initial aim of producing a set of 3D GNP-loaded cellular phantoms in order to test the L-XRF measurement system was met. We achieved GNP uptake in both cell lines used, confirmed with TEM analysis, as will be shown in Section 3.5.3. We also successfully adopted a standard collagen construction procedure in order to uniformly embed the GNP-loaded cells in a 3D matrix. Further discussion of the optimisation process of the phantom making procedure is found in Section 3.5 (comparing the uptake of two GNP sizes) and Section 3.6 (assessing appropriate incubation times to use). This set of phantoms was successfully used to demonstrate the ability of the L-XRF technique in measuring GNP concentration in cells (refer to Section 3.7).

A range of ACM imaging samples were produced and taken to the Elettra synchrotron source, Trieste in order to test a novel XRF imaging technique (details of the system can be found in Section 4.4). The cells were incubated with 15 nm GNPs, which were subsequently shown to be not taken up by the cells in Section 3.5. The decision to make this set of samples using 15 nm GNPs was based on results reported in the literature saying that they were less cytotoxic than the smaller GNPs [88]. However, results discussed later in the thesis indicate that 15 nm GNPs are not taken up by cells in sufficient numbers; this result was confirmed when no gold XRF signal was detected from the ACM set of samples. This meant that on this occasion no XRF images were possible as there were very few GNP inclusions in the phantoms. However, the phantom production technique in terms of the tissue engineering procedure involved worked well; the produced set of samples successfully consisted of a dense ACM of HT29 cells surrounded by a less dense collagen matrix with 3T3 cells embedded at a lower density.

3.5 GNP cell uptake of two different GNP sizes

3.5.1 Aim of investigation

GNPs of two different diameter sizes were available for this work, 1.9 nm and 15 nm, both commercially available from Aurovist^{TM}, Nanoprobes Inc., USA. The uptake of the two NPs was compared in order to select the NP size to use for subsequent experiments.

3.5.2 Method

HT29 and 3T3 cell cultures were incubated with both NP sizes at a GNP dose of 2 mgAu/ml (as outlined above). The 1.9 nm GNPs were incubated for 24 hours, whereas the 15 nm GNPs were incubated for 48 hours (the 15 nm measurement being performed prior to knowing the optimum time of uptake of GNPs). The difference in incubation time still enables a broad comparison to be made of uptake of different GNP sizes, as it is demonstrated in Section 3.6 that uptake still occurs at 48 hours.

3.5.3 Results

TEM images of 3T3 and HT29 cells are displayed in Figures 42 - 45. Figures 46 and 47 display TEM images of a greater magnification to illustrate the distribution of GNPs within each cell type.

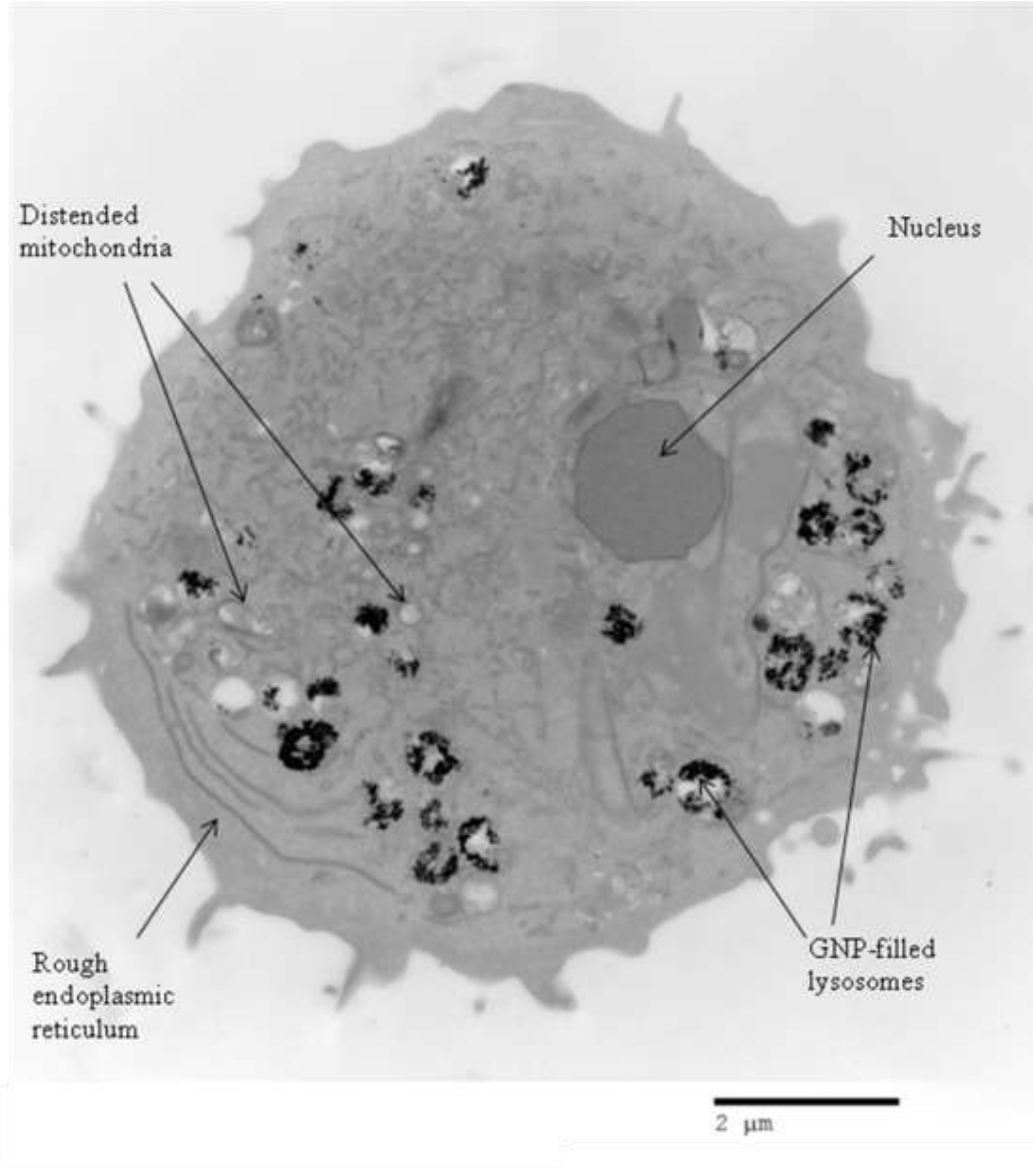

Figure 42 TEM image of a 3T3 cell incubated with 1.9 nm GNPs.

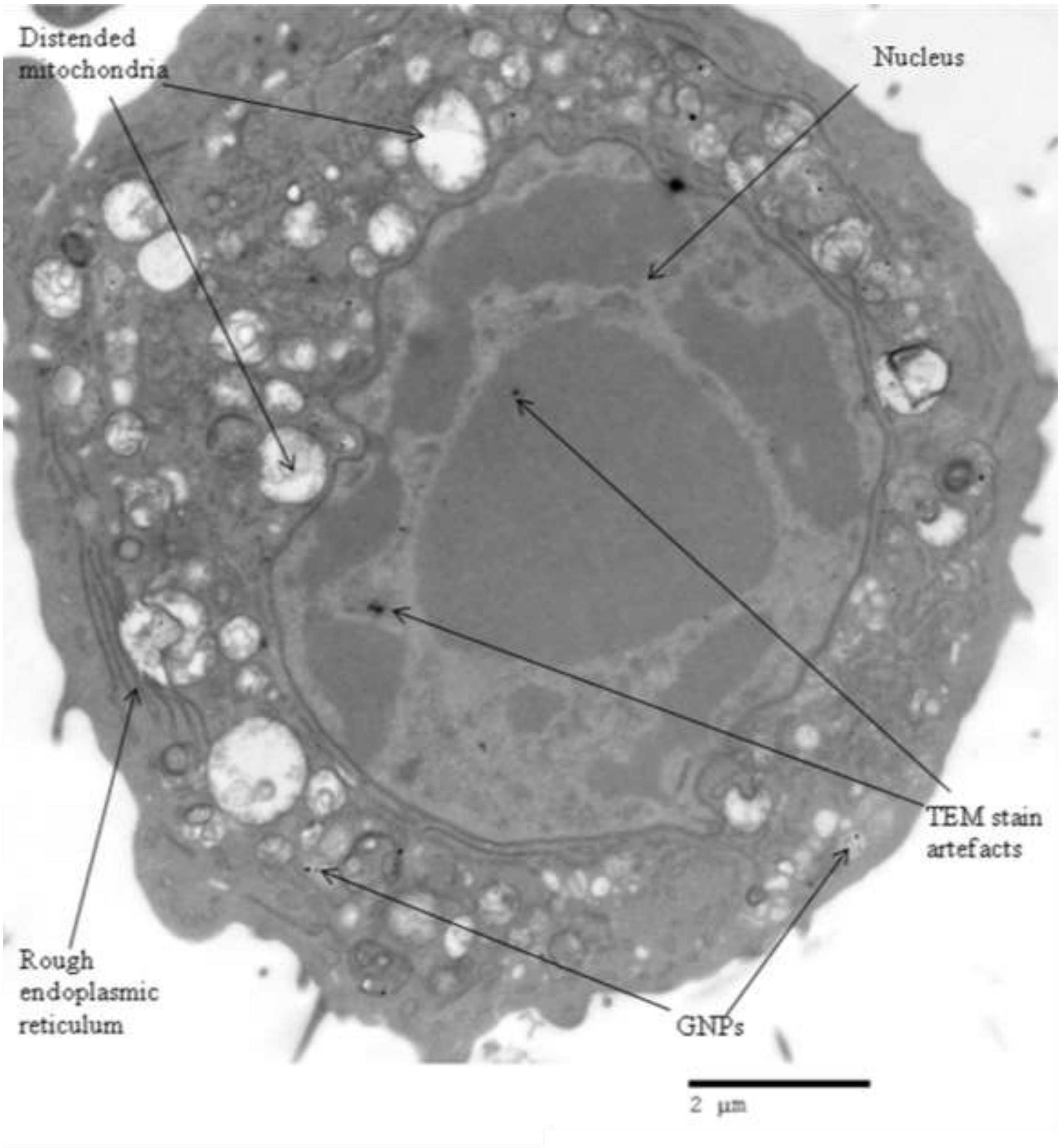

Figure 43 TEM image of a 3T3 cell incubated with 15 nm GNPs.

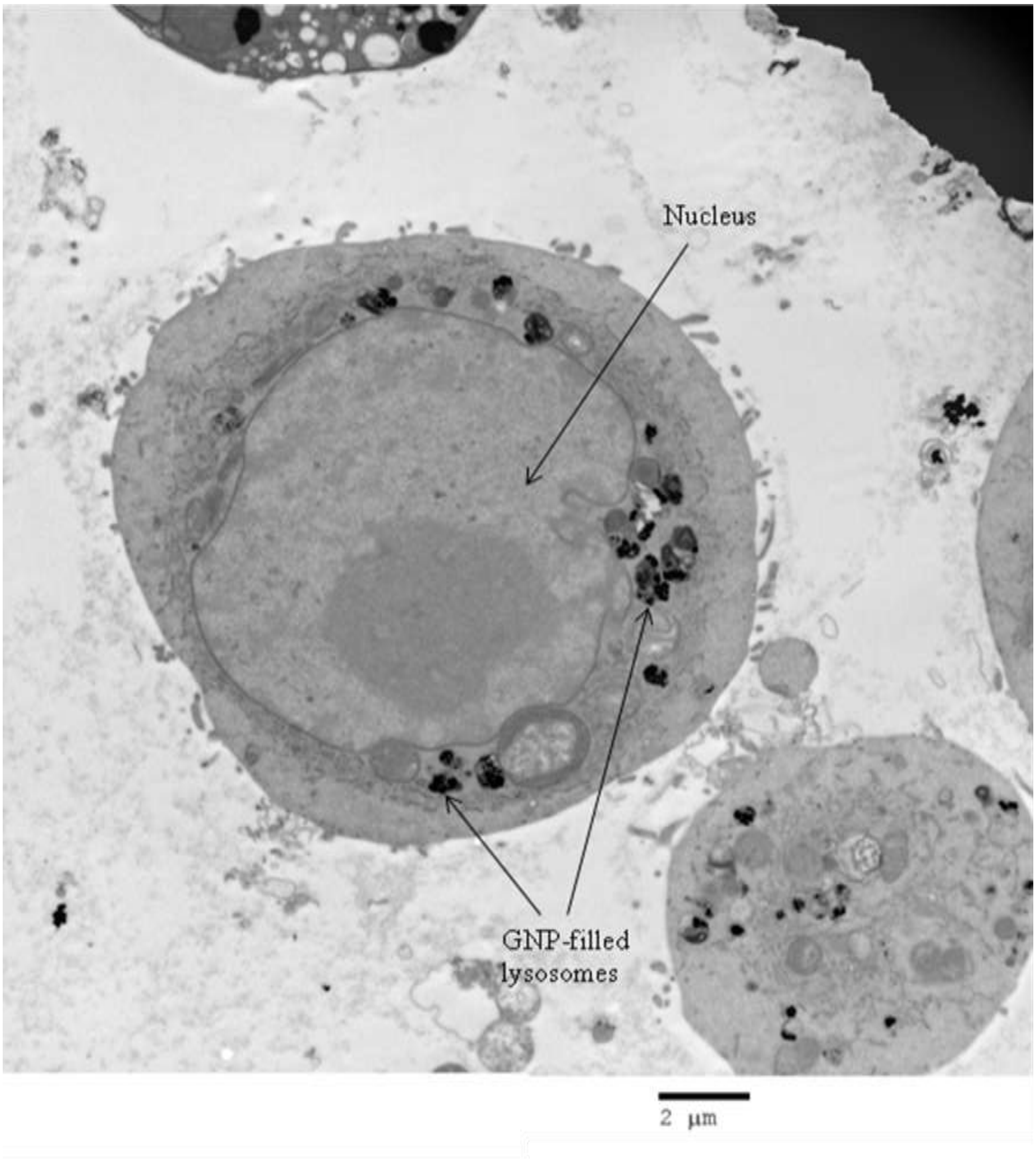

Figure 44 TEM image of HT29 cells incubated with 1.9 nm GNPs.

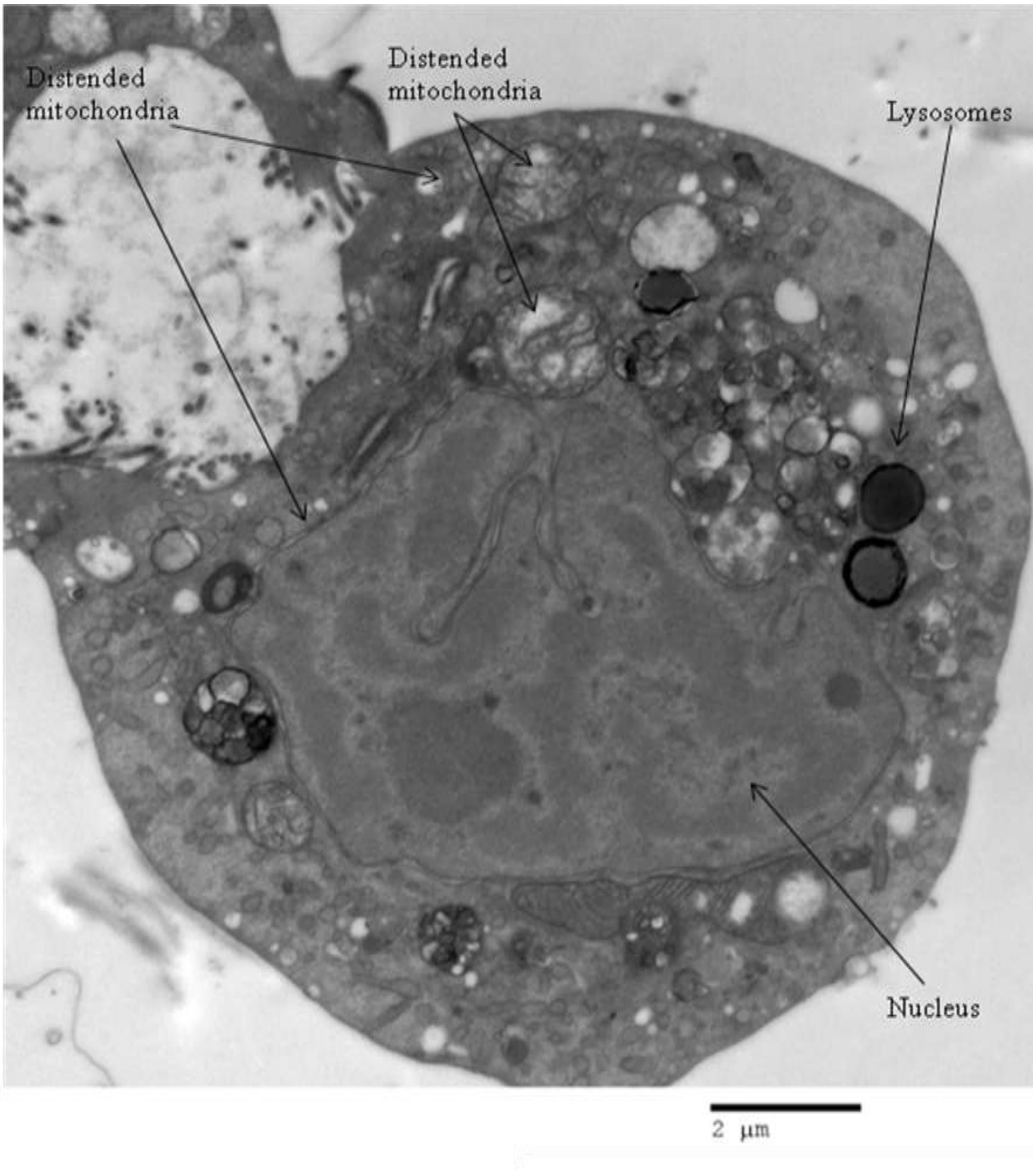

Figure 45 TEM image of a HT29 cell incubated with 15 nm GNPs.

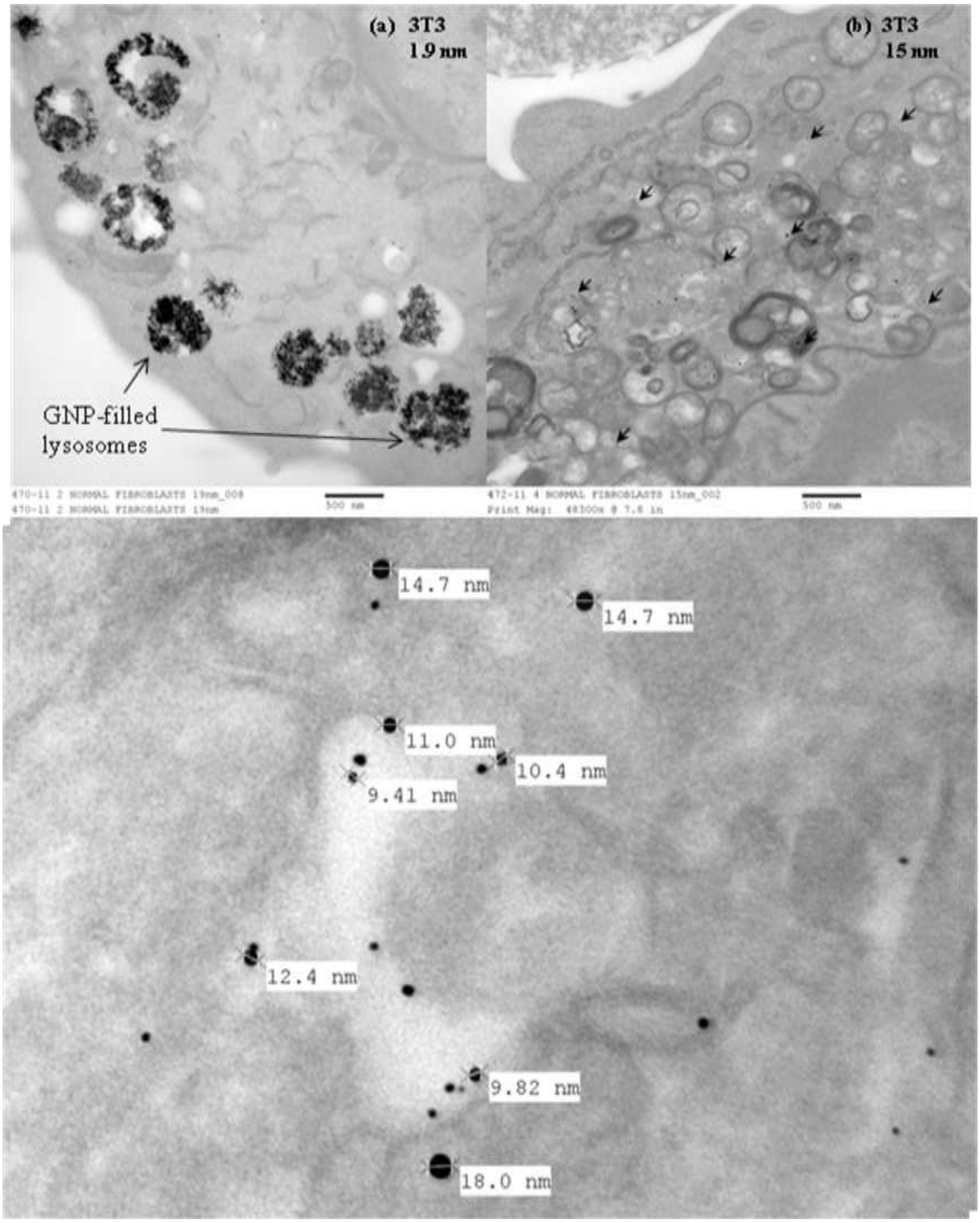

Figure 46 High magnification TEM images of 3T3 cells incubated with (a) 1.9 nm. Images (b) and (c) both show 3T3 incubation with 15 nm NPs. No size measurements could be made of the 1.9 nm as the GNPs were too densely packed within the endosomes. The range of GNP sizes found for the 15 nm nominal size was 9.41 nm – 18.0 nm (image (c)).

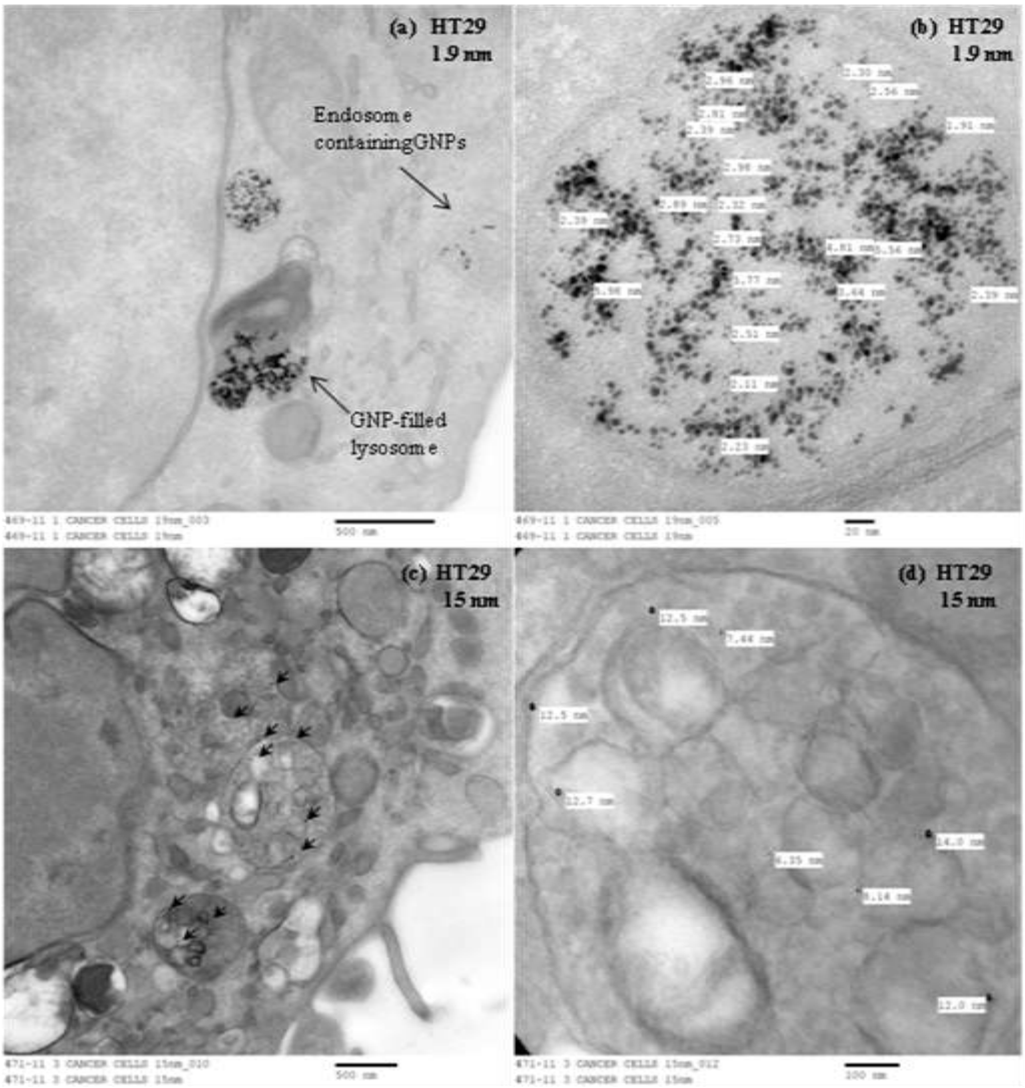

Figure 47 High magnification TEM images of HT29 cells incubated with (a) and (b) 1.9 nm and (c) and (d) 15 nm. The size of GNPs found within the cells ranged between 1.91 nm – 5.98 nm for the 1.9 nm nominal size, and between 6.35 nm – 14.0 nm for the 15 nm nominal size.

TEM analysis of the cells showed that the 1.9 nm variety was more avidly taken up by cells than the 15 nm GNPs for both cell lines and so it was decided to use 1.9 nm GNPs in subsequent experiments. X-ray microanalysis was performed to confirm gold presence within the cells; this involved a TEM technique that bombards the sample with electrons and detects the emitted x-rays (the energy of the emissions being characteristic to elements present).

3.5.4 Discussion

The TEM images demonstrate uptake of the GNPs into the cells; as ultramicrotome sections are approximately 100 nm thick, and one can visualise cell organelles in the slices, we can conclude that the GNPs are inside cellular/intracellular vesicles as opposed to just on the surface of cells. The cells in the TEM images appear viable; the darkness of the cytoplasm indicates presence of ground substances and health of the cytoplasm, and organelles required for healthy cell functioning are present (such as the nucleus, endoplasmic reticulum and mitochondria).

This study showed a greater cellular uptake of 1.9 nm GNPs than 15 nm GNPs for both HT29 and 3T3 cells lines, and so 1.9 nm GNPs were used in subsequent experiments. This result conflicts with the limited literature available, which suggests the optimum size of GNPs for cell uptake is 25 – 50 nm [76], [93]. However, the reported study was undertaken using transferrin-coated NPs, whereas our study was performed using NPs coated in serum proteins adsorbed from the growth medium and this may lead to different cell uptake. Extensive investigation of other protein coatings is required to completely understand the effect of GNP size on cellular uptake [76].

It is interesting to note that literature reports that large GNPs (~ 50 nm) can enter cells as a single NP, whereas interaction of NPs smaller than 50 nm with the cell membrane does not produce enough membrane bending energy to completely wrap the NPs on the surface of the cell membrane; at least six 14 nm GNPs must cluster together to enable uptake [76]. Other literature contradicts this; endosomes containing single 10 nm NPs were observed [102]. We have observed that 1.9 nm GNPs are visibly clustered / aggregated together inside vesicles (as demonstrated in Figures 42 and 44) but single 15 nm GNPs were found within vesicles in the cytosol, with no clustering evident over the incubation time period. The conflicting results in the literature may be explained by differences in functionalisation of the NPs (transferrin vs. peptide for the first and second studies mentioned respectively, and a possible difference in protein coating between the 1.9 nm and 15 nm GNPs in our study) and its effect on uptake mechanism. Real-time single particle imaging is necessary to understand the effect of clustering and protein coating on cellular uptake.

The TEM images of the 1.9 nm uptake (Figures 42 and 44) shows that the GNPs are localised within vesicles located in the cell cytoplasm. It is thought that GNPs are initially contained in endosomes after undergoing endocytosis, and then travel through the cytoplasm within the endosomes to fuse with lysosomes (the larger densely filled vesicles present in Figures 42 and 44). Figure 47 (a) demonstrates an example of both a GNP-containing endosome and a GNP-filled lysosome. This observation is consistent with NP uptake theory described in Section 3.3.1, and provides evidence that the GNPs were internalised through the cellular process of endocytosis. This contradicts a previously reported study using 2 nm GNPs coated with Herceptin which showed no uptake into human breast cancer cells (compared with 40 nm GNPs which were taken up by RME [90]). This study reports that the 2 nm GNPs only fix to the surface of the cell, and do not penetrate the membrane. However, this study uses a different protein coating and cell type, which may explain the difference in result to our findings.

Figure 48 shows further evidence of endocytosis; this TEM image has captured the steps of endocytosis, including GNP-cell membrane interaction, membrane invagination and endosome formation, and travel of endosome towards GNP-filled lysosomes.

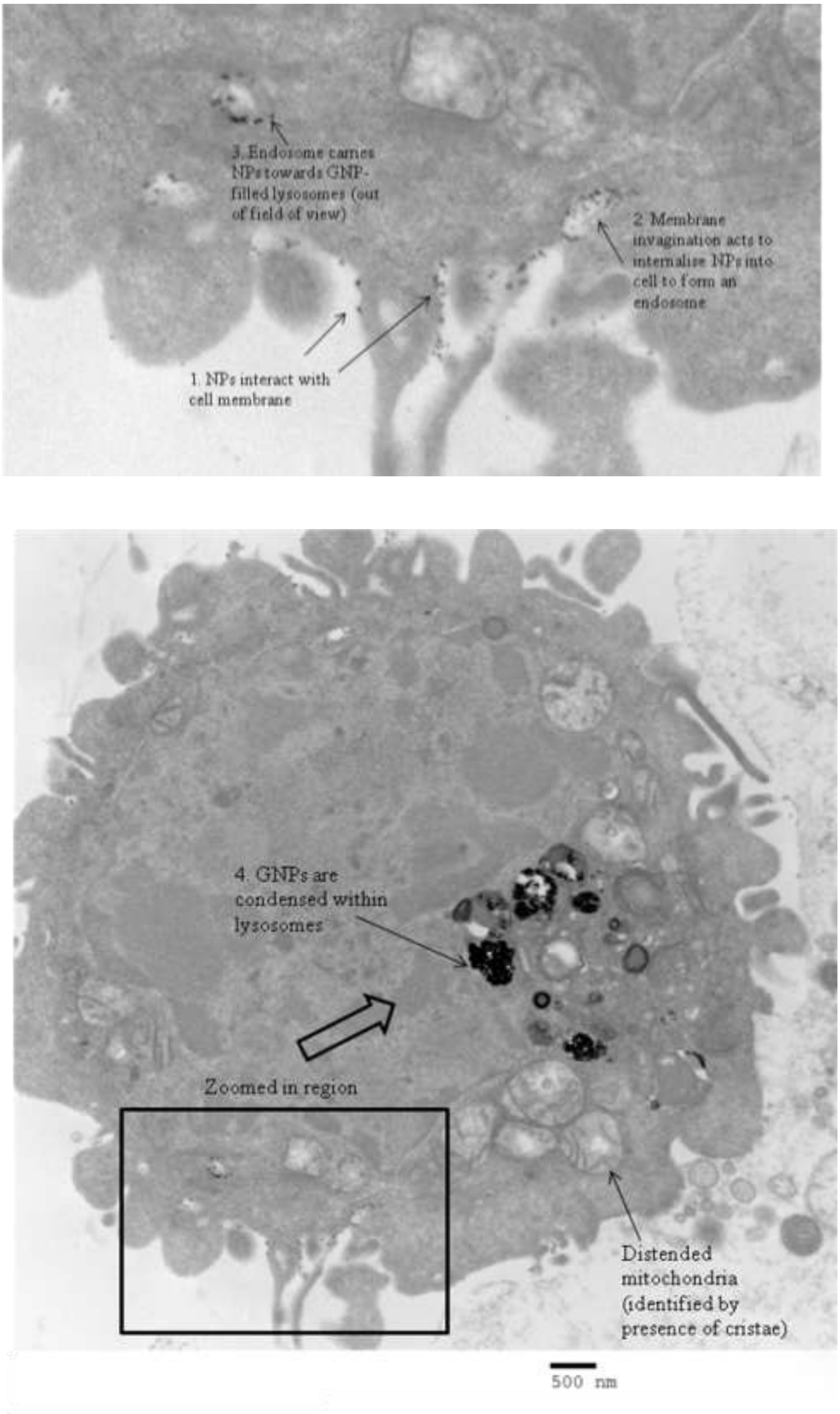

Figure 48 TEM image of cell membrane surface of HT29 cell incubated with 1.9 nm GNPs. The image has captured each step of endocytosis: (1) NP-membrane interaction, (2) membrane invagination to take up GNPs into cell, and (3) resulting endosome carries GNPs towards lysosomes.

Figures 43 and 45 demonstrate the lack of presence of GNP-filled lysosomes in cells incubated with 15 nm GNPs. The few 15 nm GNPs that were internalised are located in vesicular structures. The comparatively poor uptake of the 15 nm GNPs may be due to differences in serum protein adsorption depending on NP size but investigation as to the possible reasons why the proteins preferentially bound to the smaller GNP size is required. There is currently insufficient information to draw conclusions about this, but some initial ideas include the possibility of a bad batch of 15 nm NPs with problems with the surface coating.

The effect of GNP size on cellular removal of GNPs (exocytosis) must also be considered. Literature proposes that the rate of exocytosis decreases linearly with increasing GNP size; the rate of exocytosis of 14 nm GNPs was found to be five times higher than 100 nm GNPs [76]. Our result also appears to conflict with this postulation, in that there were more 1.9 nm NPs present in the cell than 15 nm. However, it appears that the reason there are so little 15 nm GNPs present in the cells is due to ineffective cellular uptake (endocytosis) of 15 nm NPs rather than an increased rate of exocytosis. This can be inferred since exocytosis was not observed over similar timescales and conditions in a case which should be more likely (i.e. during 1.9 nm NP incubation).

Referring to the incubation time study reported in Section 3.6, we can infer that the marked difference in uptake between 15 nm and 1.9 nm GNPs is not due to the difference in incubation time (48 hours and 24 hours respectively for these experiments); there was an increase and not decrease in uptake between 24 and 48 hours incubation (refer to Figure 49). However, this was tested for 1.9 nm GNPs and may be different for 15 nm GNPs; further investigation is required if future work requires the use of 15 nm GNPs.

The final possible reason for the result may be explained by the health of the cells in the 2D culture; the cells in the TEM images of the 1.9 nm GNP study appear healthier than those exposed to 15 nm GNPs. The latter showed particularly distended mitochondria (Figures 43 and 45), indicating that the cells are undergoing the first steps of necrosis [103]. Mitochondria were correctly identified through the presence of double membrane features characteristic to these structures. The 15 nm and 1.9 nm studies were performed on different days. It may be possible that the cells involved in the 15 nm GNP study were not healthy, and under sub-optimum incubation conditions which affected their ability to take up GNPs. Another alternative explanation is that the 15 nm GNPs may have been cytotoxic to both cell lines and induced poor health in the cells. This postulation is contradicted by literature which reports that GNPs 15 nm in size were found to be non-toxic up to 60-fold higher concentrations than 1.4 nm GNPs [88]; refer to Section 3.3.1.6 for further discussion. Cells were incubated with the 15 nm GNPs for double the incubation time than with 1.9 nm GNPs; this may have increased cytoxicity as they were exposed to NPs for a longer period of time. It was recommended in Section 3.6 that 24 hours rather than 48 hours is sufficient to achieve GNP uptake without obvious signs of cytotoxicity.

Further investigation is necessary to establish the difference in uptake between the two GNP sizes. There is insufficient information in the literature to enable a full explanation of the results of this study. However, within the scope of this project the conclusion was that 1.9 nm GNPs were to be used for producing the cellular phantoms as they had proved to be readily taken up by cells.

3.6 Selection of GNP incubation time

3.6.1 Aim of investigation

The aim of this study is to determine an appropriate GNP incubation time that achieves sufficient GNP uptake without impacting on cell health. The findings of this study will be fed into the cellular phantom making procedure. GNP incubation times quoted in the literature range from six hours [77] to 48 hours [88], and a recommended time was not reported in the literature for the cell lines and NP size used in our study.

3.6.2 Method

Samples were prepared as outlined in Section 3.4. Five flasks were plated with 1 M HT29 cells. On reaching 70% confluence the cells were incubated with 4 ml GNP-medium suspension at a concentration of 2 mgAu/ml over a period of 4, 10, 24 and 48 hours (covering the time intervals mentioned in the literature). A control flask did not receive GNPs. The samples were fixed according to the above protocol (Section 3.4.8), and TEM images obtained according to the protocol outlined in Section 3.4.9.

3.6.3 Results

TEM images of samples incubated with GNPs over 4, 10, 24 and 48 hours were taken. The resulting images are displayed in Figure 49.

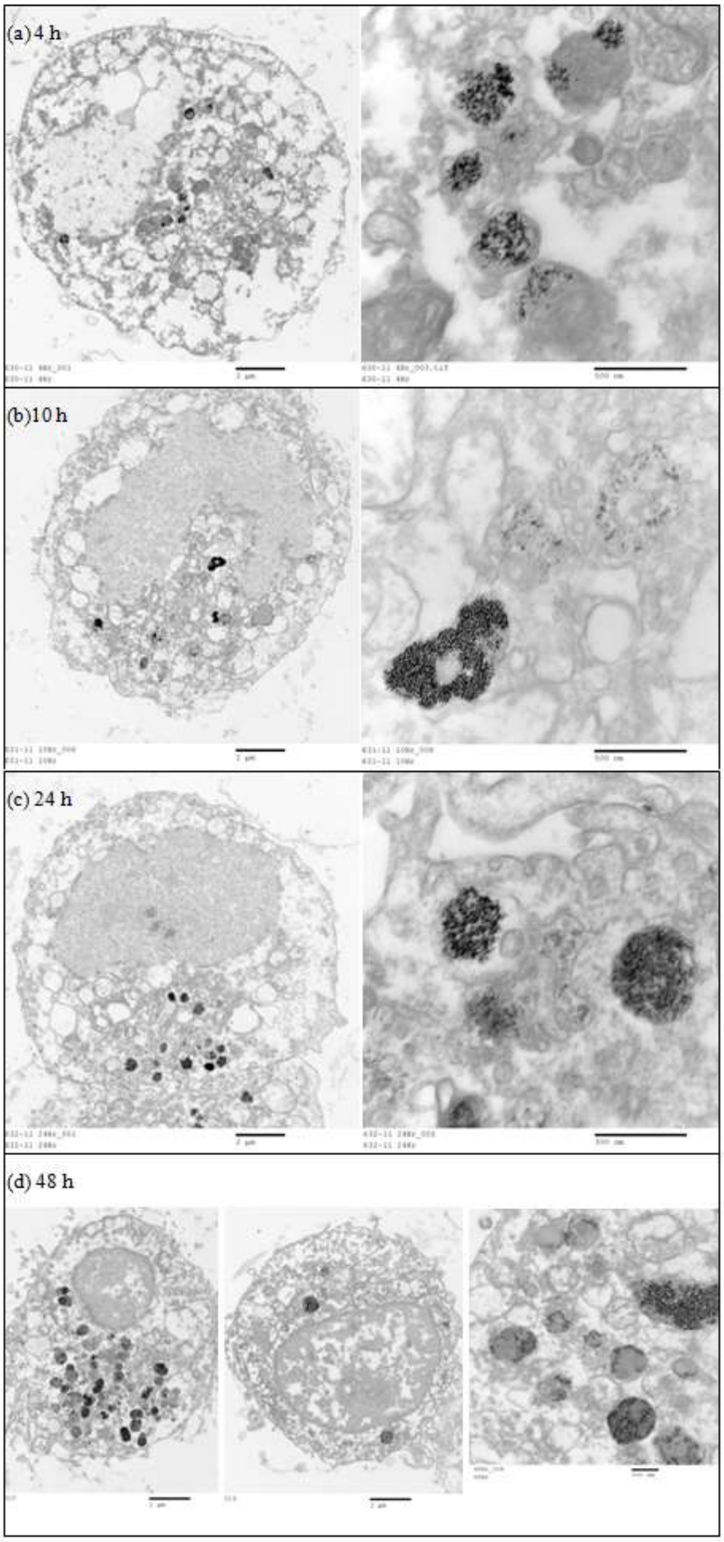

Figure 49 TEM images of HT29 cells exposed to 1.9 nm GNPs over a range of incubation times: (a) 4 h, (b) 10 h, (c) 24 h and (d) 48 h. Magnifications of 7100 x and 53000 x were used for the cell (right) and endosome (left) images respectively. Two cell images of the 48 h incubation time are displayed to illustrate the wider variation in the number of GNP-containing endosomes per cell.

3.6.4 Discussion

The NP uptake appeared to increase with incubation time as displayed in Figure 49. This is in agreement with the literature [78]. There was no great difference in the number of vesicles containing GNPs for the 4 and 10 hour incubation time sample, but an increase in GNP internalisation is seen at 24 hours incubation. The 48 hour incubation time sample displays the greatest number of GNP-filled endosomes inside one cell. However, it was decided that 24 hours was an appropriate incubation time to use for the biological phantom making technique because the cells in the 2D culture looked stressed and became over confluent at 48 hours and started to detach from the culture plastic.

Typical HT29 cell diameters were measured to be ~ 10 μm but each TEM image in Figure 49 is of a tissue section ~ 100 nm thick, and so each TEM section only represents a small portion of the cell that can be from anywhere across the cell. Therefore TEM images can only give a qualitative comparison of GNP uptake at different incubation times unless hundreds of sections are analysed. The 48 hour TEM images present two different cell sections: one that contains a high amount of cytoplasm (left hand side image), and the other that contains less cytoplasm and more nucleus (central image). The images show a factor of two increase in densely filled lysosomes present in moving from 24 hours to 48 hours incubation, but there is also twice the area of cytoplasm in the 48 hour image and so a firm conclusion cannot be made. However, the 10 hour and 24 hour TEMs have a more similar area of cytoplasm, and so a better comparison can be made with the number of densely filled lysosomes doubling between 10 and 24 hours incubation.

The cells present in Figure 49 appear to be undergoing necrosis, characterised by the breaking up of membranes and degradation of cytoplasm and nuclear material. Necrosis occurs rapidly in response to sudden stress of the cell, and results in the rupturing of cellular membranes and release of the cell contents to extracellular space. The gel preparation for this batch of cells may explain the poor state of the cells. Cell death can be induced by cells being present in a sub-optimum pH. The production of the gels involves a pH neutralisation process, and the gels can successfully set over a pH range of 7 – 7.7 [104]. However, cells require a pH of 7.3 – 7.4. The under- or over-neutralisation of the gel may have provoked cell death. Apoptosis on the other hand is slower acting; cells undergo a pre-programmed sequence of events, resulting in fragmentation of nuclei and cytoplasmic organelles into small apoptotic bodies that can be cleared by phagocytes. Membrane blebbing and vesicle formation is typical of apoptosis [88]. Figure 49 displays more signs of necrosis than apoptosis. However, the conclusion that there was uptake of GNPs can still be drawn, and it is evident that the amount of uptake is incubation time dependent.

As in the previous study, and in agreement with the literature, the TEM images show that the GNPs are all localised inside vesicles within the cell cytoplasm. This once again provides evidence for the uptake mechanism of endocytosis, suggesting that the cells were behaving as normal at the incubation stage of the experiment.

Further work could investigate the time taken to internalise and externalise GNPs for each cell line and GNP size / coating (this level of detail was not necessary to meet the aims of this study). Literature reports that 50 nm GNPs reside in lysosomes in cells within 40 minutes of incubation [93]; this should be slower for smaller NPs as the rate of uptake is less. The time of uptake should also vary with protein coating and cell type, as discussed in Section 3.3.1. Chitrani showed that once deposited inside vesicles, the vesicles diffuse through the cytoplasm at a speed of 10.2 ± 1.8 µm/hr [93]. Chitrani’s group reported that nanovesicles were found to move toward the cell interior, followed by upward motion toward the cell periphery. The cytoplasm is a densely entangled network of actin bundles interpenetrated by a fluid phase that is crowded with globular macromolecules; the cytoplasm components differ between cell lines, and so the speed of nanovesicles is cell-type dependent [93].

The results of this study were fed into the cellular phantom making procedure, and an incubation time of 24 hours was used at the GNP incubation stage.

3.7 GNP dose uptake measurement

3.7.1 Aim of investigation

The aim of this study was to establish a technique to attain a known GNP uptake in the cell lines used by altering the incubation GNP dose. The phantoms created were used to demonstrate the ability of the XRF system in quantifying GNP concentration in the bio-phantoms. XRF measurement of GNP concentration may be used to infer typical numbers of NPs per cell in order to assess the potential of the technique in meeting the clinical aims outlined in Section 1.2. TEM images of each sample were also made to demonstrate GNP uptake to corroborate with XRF measurement. The results of this study will be used to create ACMs with known concentrations of GNP inclusions in the different phantom components. Cells were incubated with a range of GNP concentrations, and measurements of the internalised GNP concentration performed using (i) the developed XRF technique, and (ii) TEM analysis.

3.7.2 Production of samples

1 M cells were seeded of each cell line: five flasks each of HT29 cells and 3T3 cells. Once 70% confluent, the cells were incubated with 4 ml of GNP concentrations ranging from 0.5 – 4 mgAu/ml to investigate the effect of initial incubation GNP concentration on cellular GNP uptake. The GNP incubation time was selected to be 24 hours; this was found to be an appropriate time interval (refer to Section 3.6). The number of cells embedded into the collagen gel is displayed in Table 12.

Table 12 Number of HT29 and 3T3 cells embedded into collagen scaffold for each sample.

3T3 cells		**HT29 cells**	
Initial GNP concentration (mgAu/ml)	No. cells in sample (million)	Initial GNP concentration (mgAu/ml)	No. cells in sample (million)
4	3.30 ± 0.33	4	3.90± 0.39
2	1.50 ± 0.15	4A	2.73± 0.27
1	4.95 ± 0.50	2	4.20± 0.42
0.5	3.06 ± 0.31	1	5.25± 0.53
0 (Control)	1.05 ± 0.11	0 (Control)	3.10± 0.31

No relationship was evident between the number of cells counted in each flask and GNP dose. A variation in cell growth between different flasks is expected (even when seeded and incubated concurrently). Variation in the number of cells in each flask can be attributed to the following factors:

- Conditions within the multiuser incubator may be non-uniform: e.g. CO_2 and H_2O droplets may not circulate equally to all flasks, and there may be temperature gradients within the incubator. Flasks were stacked on top of each other for this set of experiments, which may further increase non-uniformity of conditions. It is recommended to place flasks side by side to reduce this effect. This is thought to be the most significant effect on cell number variation.

- A tilted incubator shelf results in a non-uniform coverage of the cells by growth medium. This may result in preferential cell death at the edges of the flasks. This effect is heightened as only 4 ml medium covered the cells.

- Pipetting errors in the seeding phase.

Once fixed, the GNP concentration of each sample was measured using the novel XRF analysis technique of Chapter 2.

3.7.3 X-ray fluorescence analysis of samples

3.7.3.1 Purpose of XRF measurement

The ability of the bench-top L-XRF system (described in Section 2.4) in measuring GNP concentration within bio-phantoms was assessed in order to determine the system’s potential in sample analysis in future work, and also to assess the system’s role for *in vivo* use. Quantitative XRF measurement of GNP concentration will be used to determine cellular uptake of GNPs, required to inform the manufacture of ACMs with components of known GNP concentration.

Chapter Two demonstrated that L-XRF techniques can be used to quantify GNP concentration down to a detection limit of 0.005 mgAu/ml. A great advantage of the

XRF technique in measuring GNP concentration is that the sample does not have to be destroyed, and so further analysis using other techniques such as TEM may be performed. Also, as XRF measurement does not destroy the sample, there is future potential in performing real-time monitoring of NP motion through biological phantoms.

A technique widely used in the literature to measure NP concentration is inductively coupled plasma atomic emission spectroscopy (ICP-AES). ICP-AES digests the cell pellet in nitric acid at 110 °C to perform the analysis, and so the cells cannot be further analysed [77]. XRF provides a much better alternative with potential to measure live 3D cultures.

3.7.3.2 Method

A bench-top molybdenum x-ray source operating at 50 kV and 1 mA was used to induce XRF in the GNPs, with a beam size of 3.7 mm (horizontal) x 2.1 mm (vertical). An iterative improvement was made to decrease the detection limit of the system by adding a 20 μm molybdenum filter. This acted to filter out lower energy components of the incident spectra which would not contribute to XRF of gold, but would increase the background beneath the XRF signal. The filter thickness was a compromise between minimising the unwanted background beneath the XRF peaks and attaining a high enough incident x-ray intensity. This modification led to an improvement in the sensitivity of the system to lower concentrations, with a minimum detection limit of 0.001 mgAu/ml now being detectable (a factor of five lower than the previous system).

3.7.3.3 Assessment of optimum filter thickness

A range of filter thicknesses were tested to see the effect on the emitted x-ray spectrum. Results are displayed in Figure 50.

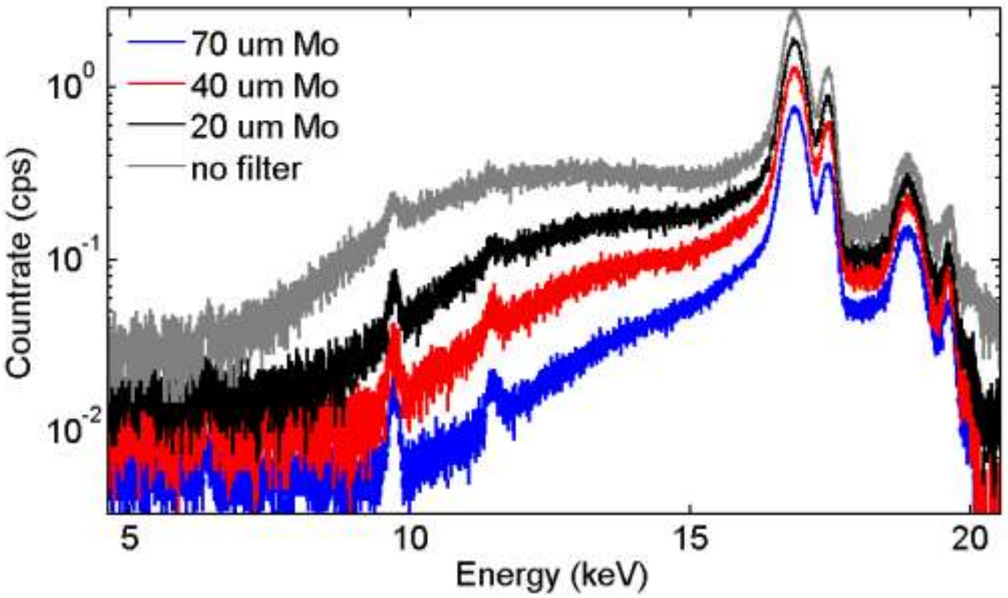

Figure 50 X-ray spectra measured in L-XRF mode of a 0.04 mgAu/ml calibration sample using a range of molybdenum filter thicknesses (0, 20, 40 and 70 µm thickness measured over 600 s, 1200 s, 1500 s and 4000 s respectively).

A 6-order least-squares polynomial fit was made to the background data either side of the gold XRF peaks, and the standard deviation of the data points about this fit (σ_{fit}) was found. The ratio of the height of the gold $L\alpha$ signal to σ_{fit} was used to indicate the signal to noise ratio for each filter thickness used. Results are displayed in Table 13.

Table 13 SNR of a range of molybdenum filter thicknesses of XRF spectra acquired of a 0.04 mgAu/ml GNP calibration sample.

Filter thickness (µm)	**Signal to noise ratio (SNR = $L\alpha$ peak height / σ_{fit})**	**Acquisition time (min)**	**SNR per minute (min^{-1})**
0	2.6	10	0.26
20	3.8	20	0.19
40	4.3	25	0.17
70	7.1	66.7	0.11

The 20 µm molybdenum filter was selected as it provided a good compromise between gold XRF signal to noise ratio and attenuation of the incident beam which would reduce the rate of XRF.

3.7.3.4 Results

A. Measured spectra

Figure 51 displays spectra obtained using each system for two initial GNP concentrations (4 mgAu/ml and the control (0 mgAu/ml)). Typical measurement times ranged from 40 minutes for high concentration samples to 400 minutes for the lowest concentration.

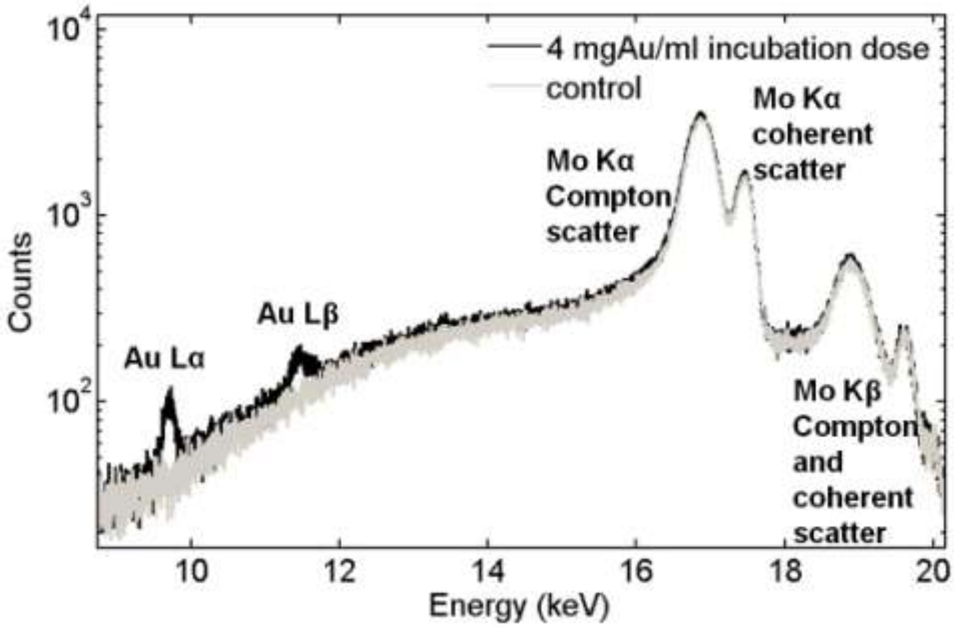

Figure 51 Measured spectra of 4 mgAu/ml GNP incubation dose sample and 0 mgAu/ml (control sample) acquired over 2400 s.

The cell samples that have been incubated with gold present a spectrum with the characteristic gold fluorescence lines, compared with the control samples which showed no gold presence (Figure 51).

B. Calibration curve

XRF analysis was performed on a range of known GNP concentration solutions in order to determine the actual GNP concentration present in the biological phantoms. The calibration curve is displayed in Figure 52.

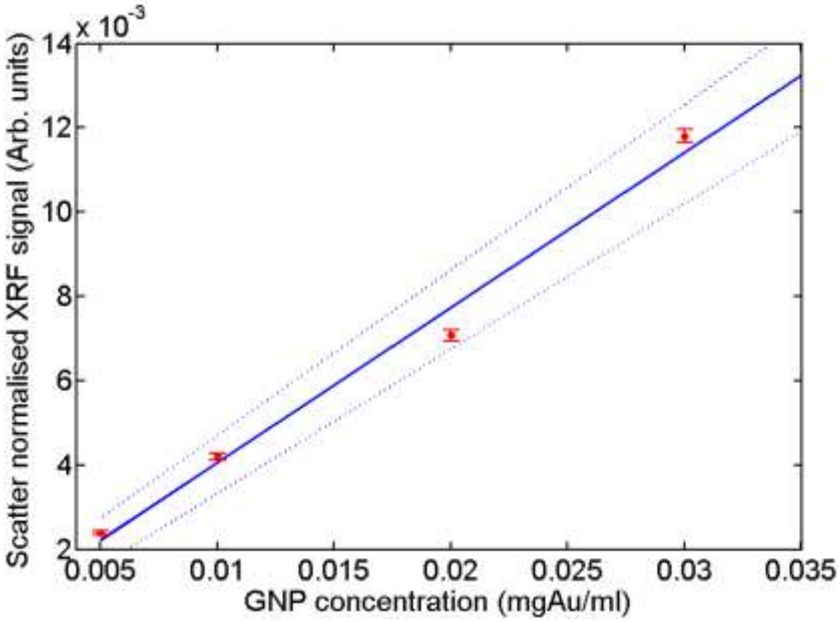

Figure 52 Calibration curve relating scatter-normalised XRF signal to GNP concentration. The XRF signal has been normalised to the Compton peak and acquisition time. A weighted linear fit (solid line) and boundary levels (dashed lines) are shown. The boundary levels were fit to fully include 100% of the data points and their error bars. Measurements were made over a range of known GNP concentration solutions.

C. Gold concentration per sample

XRF measurements were acquired for each sample, and the XRF signal was converted to GNP concentration using the calibration curve (Figure 52). The boundary levels of the calibration linear fit were used to determine the error on each sample GNP concentration measurement (refer to Section 2.6.6 for a description of this), which was then added in quadrature to the error in the XRF measurement resulting from statistical fluctuations. All gold concentrations were measured to be above the detection limit of the system (0.001 mgAu/ml). Figure 53 displays the measured GNP concentration found for the 3T3 and HT29 samples.

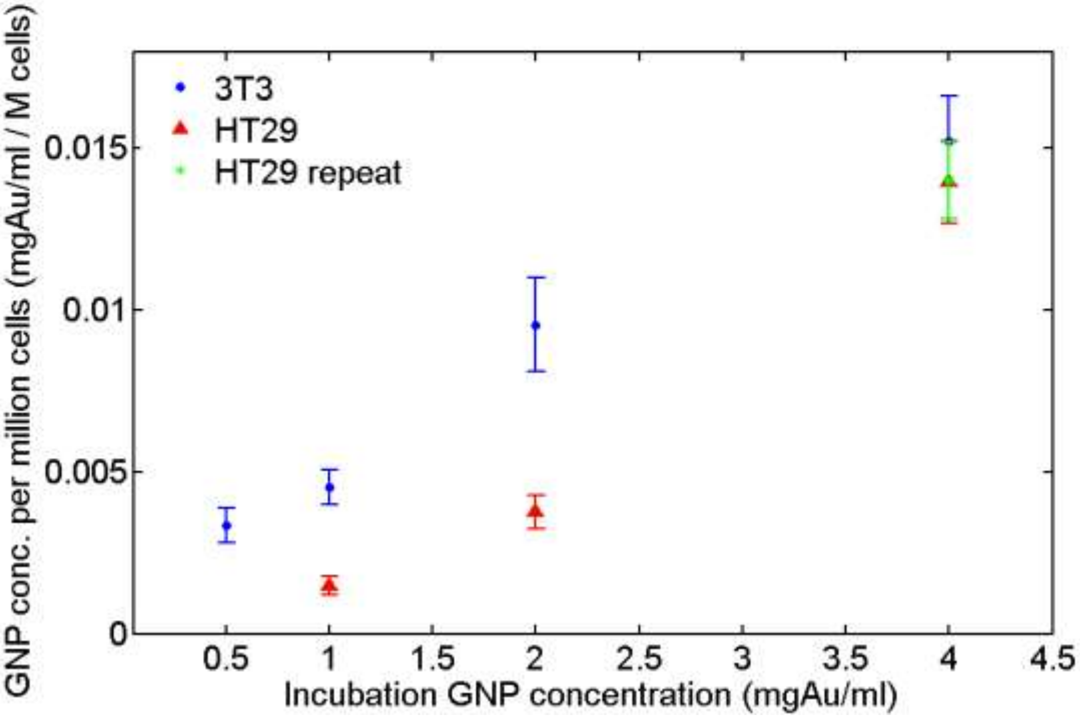

Figure 53 Measured GNP concentrations found in 3T3 and HT29 samples over a range of four and three initial incubation doses respectively. A repeat sample of HT29 cells given an initial dose of 4 mgAu/ml was made to test repeatability in the sample making process.

An order of magnitude estimate of the number of GNPs taken up per cell has been undertaken for the highest measured GNP uptake (the 3T3 sample given an incubation dose of 4 mgAu/ml), in the following way:

- *The mass of gold per cell was estimated:* A GNP concentration of ~ 0.015 mgAu/ml was measured for this sample using XRF analysis (Figure 53) in a sample that was normalised to 1 million cells per ml. This corresponds to **0.015 ngAu per cell**.
- *The mass of one 1.9 nm GNP was estimated:* Each NP was assumed to be a solid sphere of gold of calculated volume 4.2 nm^3. The volume was multiplied by the known density of gold (19.32 g/cm^3) to give an **estimated mass of 7 x 10^{-11} ng per NP.**
- The XRF signal from the sample incubated with 1 mgAu/ml is measured to be four times lower than that incubated at 4 mgAu/ml. Therefore, it can be

estimated that the number of NPs per cell for this particular incubation dose is **5 x 10^7 NPs per cell.**

This number of NPs per cell is in agreement with literature; one study reports a value of NP uptake per cell four orders of magnitude lower (3000 per cell) than the estimated value above for HeLa cells given an incubation dose four orders of magnitude lower (0.14 µgAu/ml) with 14 nm GNPs [81]. A different NP size, GNP coating (stabilised with citric acid in the literature) and different cell line means the results are not directly comparable, but indicates that our estimate of number of GNPs per cell is sensible.

In order to determine the minimum number of GNP-filled cells that the developed XRF technique is sensitive to, the number of GNP-filled cells corresponding to the detection limit (0.001 mgAu/ml) has been estimated in the following way:

- Assuming we set an incubation dose of 4 mgAu/ml, Figure 53 shows a bulk measured concentration of ~ 0.015 mgAu/ml per million cells. Extrapolating down to the measured detection limit of 0.001 mgAu/ml indicates that the current system is sensitive to ~ 70,000 cells per cm^3 in a sample that has been given the same incubation dose. Based upon the above assumptions this equates to a minimum number of detectable NPs 70,000 cells x 2 x 10^8 NPs which is **1.4 x 10^{13} NPs per cm^3**.

3.7.4 TEM analysis of samples

The group of HT29 samples were measured using TEM analysis; resulting images can be found in Figure 54.

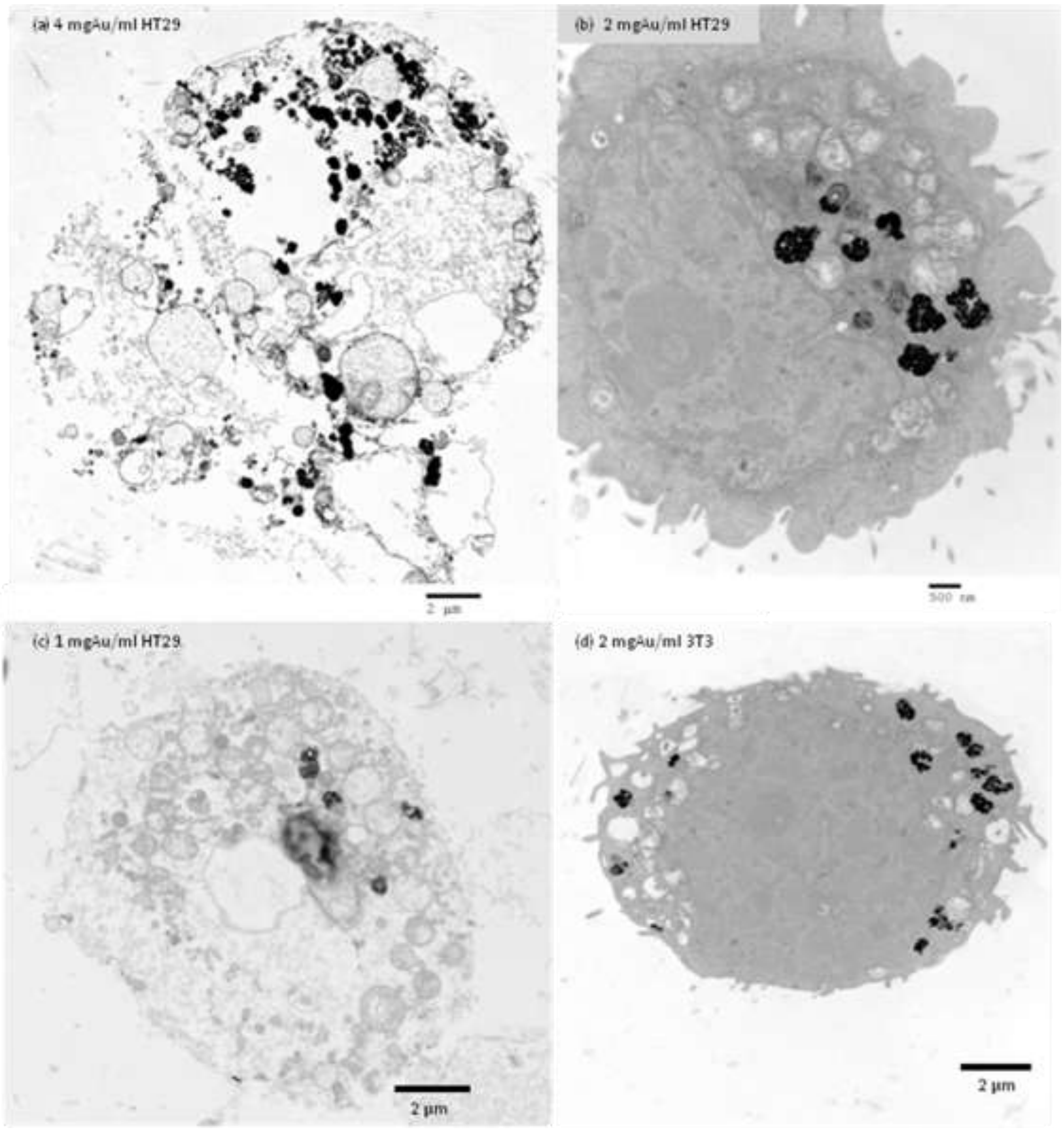

Figure 54 TEM images of HT29 cells incubated with three different GNP doses: (a) 4 mgAu/ml, (b) 2 mgAu/ml, (c) 1 mgAu/ml. An image (d) is displayed of 3T3 cells incubated with 2 mgAu/ml as a comparison to (b).

It can be seen that the GNPs have been internalised into the cells and are contained within vesicles (lysosomes) located in the cell cytoplasm.

The number of nanoparticle-containing vesicles was found to increase with GNP incubation dose in the cell sections displayed in Figure 54. The visible density of GNPs per vesicle was also found to increase between GNP incubation doses 2 and 4 mgAu/ml, with no great difference found between 1 and 2 mgAu/ml (Figure 55). It was also found that the density of GNPs per vesicle varied within one cell as illustrated in Figure 55 (d). The vesicles were too densely packed to quantify the number of GNPs per vesicle.

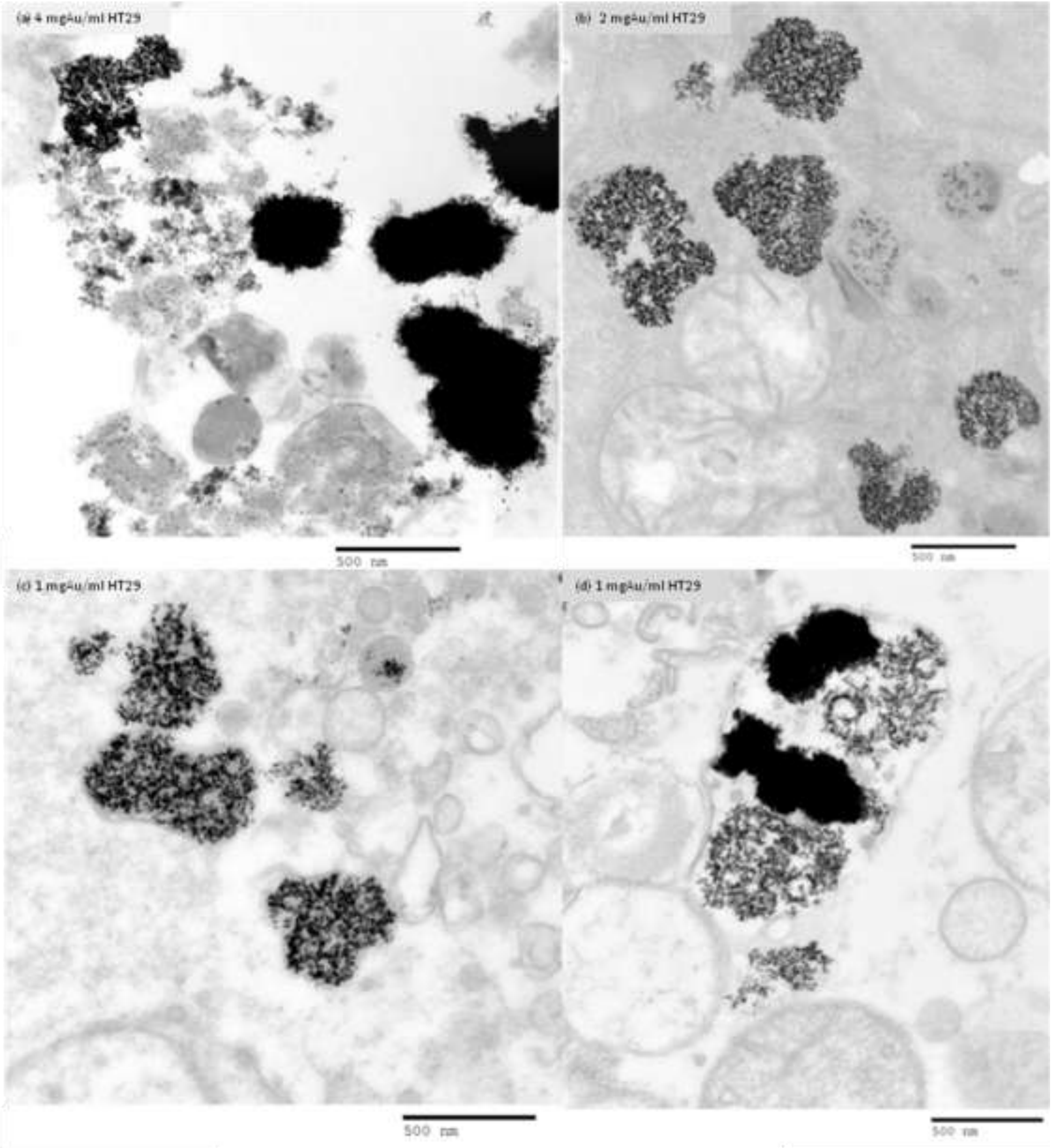

Figure 55 TEM images of GNP-filled vesicles within HT29 cells incubated over a range of GNP concentrations: (a) 4 mgAu/ml, (b) 2 mgAu/ml and (c) 1 mgAu/ml. Image (d) displays that vesicles within one cell are filled at different densities.

3.7.5 Discussion

Figure 53 demonstrates that the measured sample GNP concentrations display a positive correlation with incubation GNP dose for both cells lines, as expected. The XRF signal from the sample incubated with 1 mgAu/ml is measured to be four times lower than that incubated at 4 mgAu/ml. This is supported by the TEM images in Figure 54, which shows an increase in GNP presence within cells with incubation dose (and an increase in the number of GNP-filled lysosomes). This result is in agreement with the literature; a study that exposed HeLa cells with GNRs over a range of incubation doses found a positive correlation of uptake with incubation dose [77]. Our study showed no saturation (i.e. no further increase in GNP uptake once a certain number of GNPs per cell were reached) at the incubation GNP concentrations tested. Saturation of cell uptake is reported in the literature; HeLa cells were found to take a maximum number of 3000 citrate-stabilised 14 nm GNPs per cell, corresponding to an incubation dose of 0.14 µgAu/ml [81].

Both of the repeat HT29 samples of incubation dose 4 mgAu/ml gave the same final GNP concentration within measurement error, demonstrating the repeatability of the sample making process.

The percentage uptake of initial incubation GNP dose per million cells was found to range between 0.3 – 0.5% and 0.1 – 0.3% for the 3T3 and HT29 cell samples respectively. The efficiency of uptake could be improved in the future by actively targeting the cells using a protein coating on the cell that is more likely to selectively interact with the cell membrane. It has been reported that GNPs stabilised by citric acid ligands had three times the cell uptake than transferrin coated GNPs (transferrin is one of the many proteins in serum) [81]. Serum proteins contain a diverse set of proteins, and so the surface of the citrate-stabilised GNPs may contain a variety of serum proteins on its surface (including α- and β-globulin known to be taken up by cells). The diversity of the proteins will enable entrance into cells via multiple receptors as compared with transferrin which only has two corresponding receptors [81]. It should be noted that the rate of uptake may also depend on the number of available proteins present in the DMEM and serum not absorbed onto the GNPs; these unbound proteins can compete for receptor sites on the cell membrane. It is the aim of future work to identify an antigen that is expressed by the HT29 cells that can be used to inform the choice of protein coating/conjugated antibody on the GNPs. We also aim to look at GNP size in greater detail in future work to optimise the efficiency of uptake.

3T3 cells showed a marginally greater uptake of GNPs than HT29 cells in this study. The dependence of cell type on GNP uptake is little understood in the literature, and further investigation in the field is required. NP uptake through RME occurs when a NP-ligand binds onto a receptor on the cell's surface and enters the cell when the membrane invaginates. Cells have a maximum receptor density dependent on cell type for a specific protein (the number of receptors per cell surface area), and available receptors determine whether the NP enters the cell via RME. However, it is understood in the literature that the receptor recycles itself back to the membrane after releasing the ligand into the cell, and so it is not a straight forward relationship between number of receptor sites and GNP uptake [81]. However, for the aims of this project in using GNPs to target cancer *in vivo*, it can be inferred that tumour masses *in vivo* will passively take up a greater amount than healthy tissues/cells. This is due to a combination of leaky vasculature and poor lymphatic drainage around tumour sites, an effect referred to as EPR (a concept introduced in Section 1.5.1). Results presented in the literature show enhanced uptake by tumour cells than healthy cells due to this effect [24]. Preferential tumour uptake can be further improved through functionalising the NPs with ligands that are actively taken up by proteins present on tumour cell membranes. This will enhance GNP uptake by increasing the probability of a GNP – cell membrane interaction, resulting in membrane wrapping and endocytosis of the GNP into the cell.

We have demonstrated that the bench-top L-XRF technique developed in Chapter Two can be used to measure GNP uptake in cellular phantoms. The XRF technique was used to perform an order of magnitude estimate of the number of GNPs per cell (at the highest given GNP dose of 4 mgAu/ml); it is estimated that ~ 5×10^{7} GNPs are present per cell. It was found that the detection limit of the system (0.001 mgAu/ml) is capable of measuring ~ 1.4×10^{13} GNPs per cm^{3}, i.e. 70,000 cells in a 1 cm^{3} volume (of cells incubated with a dose of 4 mgAu/ml). The amount of uptake can be increased through active targeting of the GNPs, and so the system could be sensitive to even less than this cell density.

3.8 Conclusions

An XRF system capable of quantitative measurement of GNPs has been developed and tested on GNP-water samples in Chapter Two. The aim of the sample development in this chapter was to produce a range of biological phantoms with GNP inclusions at concentrations that represented the clinical situation in order to demonstrate the XRF measurement technique in a more realistic case. Production of the phantoms involved two stages: (i) effecting GNP uptake in cells, and (ii) embedding the cells in a 3D scaffold. The former stage was successfully achieved; it was found that using 1.9 nm GNPs and an incubation time of 24 hours gave sufficient GNP uptake. It is thought that GNP uptake was facilitated by protein adsorption onto the GNP surface of proteins found in the growth medium. TEM analysis confirmed that GNP uptake was achieved in both cell lines, through the mechanism of endocytosis. A second size GNP of nominal size 15 nm was found to be taken up much less readily by cells. The toxicity of 15 nm GNPs was brought into question and a further study to measure the toxic effects of the 15 nm GNP is required. The latter stage built on previous work in 3D cell culture that provides a technique to embed cells uniformly in a collagen type I matrix [73]. The 3D phantoms were successfully made according to the design criteria outlined in Section 3.4.2 in order to ensure that the XRF technique could be used as a tool for GNP uptake measurement. In summary:

- Samples contained a GNP concentration above the minimum detection limit of the XRF system (> 0.001 mgAu/ml)
- Cells were thoroughly mixed into the collagen gel to give a uniform distribution of cells
- A thin sample holder was used to minimise x-ray signal loss and reduce scatter from the holder

It was found that GNP uptake increases with incubation dose. Attaining a known GNP uptake was shown to be repeatable within measurement error. The XRF technique (a technique that doesn’t destroy samples) successfully measured GNP concentration in the cellular samples; concentration measurement could be used to determine the efficiency of uptake. The percentage uptake of initial incubation GNP dose per million cells was found to range between 0.3 – 0.5% and 0.1 – 0.3% for the 3T3 and HT29 cell samples respectively. TEM images qualitatively corroborated the XRF technique's findings that uptake was proportional to initial GNP dose. The passive GNP uptake demonstrated here may be extended through functionalisation to meet the overall eventual aim of this project in using GNPs as a contrast agent to image the distribution of bio-parameters of a tumour. The measured uptake efficiency could be increased in the future by coating the GNPs in a protein taken up by the specific target cells. In an *in vivo* situation tumour cells will take up more GNPs than healthy cells due to leaky tumour vasculature and poor lymphatic drainage at tumour sites. It was estimated that a 4 mgAu/ml incubation dose resulted in ~ 5 x 10^7 GNPs taken up per 3T3 cell. It was also estimated that the measured detection limit of the XRF system (0.001 mgAu/ml) enables ~ 1.4 x 10^{13} GNPs to be detected per cm^3. The number of cells that this corresponds to is dependent on incubation dose, and other factors that affect NP uptake such as surface properties and size of GNPs.

A set of artificial cancer mass phantoms were successfully constructed, building on the work previously undertaken [99]. This work was extended to produce a set of novel phantoms with GNP inclusions for XRF imaging. A new batch of 3D artificial cancer mass samples will be made in 2012. Our previous studies demonstrate that we have developed a GNP uptake procedure whereby cells were proven to take up known concentrations of 1.9 nm GNPs. We will use 1.9 nm GNPs at the cell incubation stage instead of 15 nm GNPs, and so we can infer that will be able to successfully produce the ACM phantoms with no issue. A repeat set of XRF imaging experiments are due to take place shortly at the Diamond synchrotron source, Oxford, with results to be published in 2012.

The 3D cellular phantoms with GNP inclusions are planned to be used in future work investigating the dose enhancement effect of GNPs. Radiobiological studies will be performed on GNP-filled cells to determine the extent of the dose enhancement effect.

Chapter Four

4 Towards a real system

Chapter Two has demonstrated the sensitivity of XRF techniques in quantitative measurement of GNP concentration. Spectroscopic measurements were found to show a linear behaviour down to the lowest measured concentration of 0.001 mgAu/ml. Chapter Three has shown that cell uptake of GNPs can also be measured and quantified by XRF techniques. This Chapter presents a feasibility study looking at key aspects towards a real imaging system. The XRF spectrometer has been developed with the ability to be coupled to mechanical collimators or polycapillary lenses in order to form pixellated images. The scope of this work was to demonstrate the feasibility of performing energy resolved imaging of GNP distribution at concentrations relevant for *in vivo* and *in vitro* studies. Preliminary XRF images of GNP concentration will be presented. The scope of this chapter is also to assess the feasibility of a proposed combined system that can measure both XRF and XRD signals. Some key design elements of a novel combined XRF/XRD technique have been investigated to inform future development of the multi-modality system. A series of diffraction measurements have been performed to assist in assessing the feasibility of the combined technique in tissue discrimination. The diffraction measurements presented in this chapter act as exploratory work, and are not the main focus of the project.

4.1 Requirements for biomarker imaging

Chapter One introduced the idea that GNPs may be used as a contrast agent to identify tumours and attached to antibodies to provide information about tumour characteristics, particularly radiosensitivity for radiotherapy applications. The case study of hypoxia was presented in Section 1.1.2 as a potential use of GNP measurement. Section 1.5.1 introduced the clinical need for imaging GNP distribution, particularly for GNPs located (i) *in vivo*, and (ii) in *ex vivo* samples or *in vitro* research samples. The key imaging requirements are outlined for each potential use, in order to inform the design of a GNP imaging system.

4.1.1 Sensitivity to NP concentration

Chapter 2 demonstrated that the L-XRF spectroscopic systems were more sensitive to measurement of GNP concentration than the K-XRF system, and could achieve sensitivity in quantitative measurement down to the detection limit of 0.005 mgAu/ml. Further improvements made to the bench-top XRF system in Chapter 3 (through the use of a molybdenum filter) showed that the system can be sensitive to even lower GNP concentrations (0.001 mgAu/ml).

When translating the 1D spectroscopic system to a 2D or 3D imaging system, the GNP concentration inside each pixel must be considered, as does the partial volume effect (discussed in Section 4.1.3). The measurement time must be increased to compensate for a decrease in measurement volume (i.e. when forming a pixellated image). Higher intensity sources can be used to minimise acquisition times, and focussing polycapillary optics may be implemented to focus x-rays to a point on the sample.

4.1.2 Spatial resolution

The spatial resolution requirements depend upon the application of the imaging system. Radiotherapy techniques clinically treat to within 1 mm of the defined treatment volume; therefore an imaging system that can image to at least this resolution is required. The margins of treatment volumes are extended beyond the visible tumour in order to incorporate sub-clinical disease. As already mentioned in Chapter One, small clusters of proliferating cancer cells on the periphery of the bulk tumour mass are not easily imaged using current techniques. A technique that is sensitive to the presence of such small clusters of cells would have a great impact on treatment volume delineation. The partial volume effect in imaging modalities has an impact on achievable spatial resolution; refer to Section 4.1.3 for a further discussion of this.

The demands of imaging research samples are different, as the technique will be used to provide maps of different tumour characteristics. Hypoxia is an example tumour characteristic that will be mapped. An example of the distribution of hypoxic cells found in a sample is displayed in Figure 56. The image is of a slice of tissue taken from a hypoxic mouse model, and was produced using optical fluorescence imaging techniques (with hypoxia tracer pimonidazole shown in green) that can view details on the level of ~10 μm. Being an optical fluorescence technique, the sample had to be sufficiently thin to allow transmission of the optical signals.

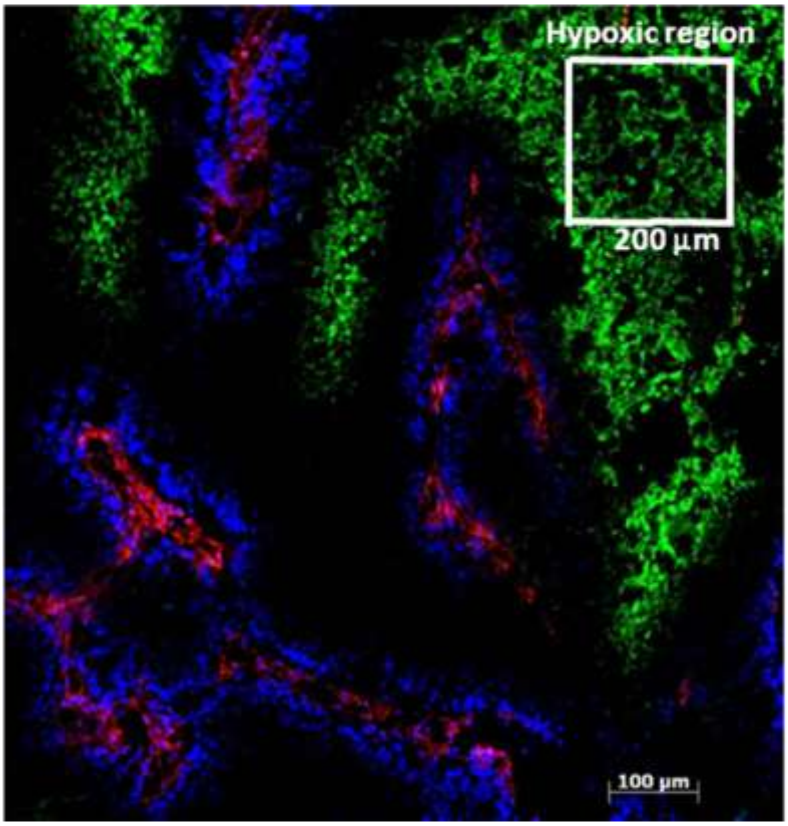

Figure 56 An optical fluorescence image of murine carcinoma, labeled with hypoxia marker pimonidazole (green), acquired by Dr A Ammar, UCL Cancer Institute. The red indicates functioning blood vessels, and blue indicates oxygenated cells.

Figure 56 shows that typical regions over which tumour characteristics change are of the order of 100 – 200 µm in size. A useful GNP imaging system would be able to image sample regions at this size scale.

4.1.3 Partial volume effect

The partial volume effect occurs when a single voxel contains a mixture of different tissue types. For example, if a group of GNP-filled cells take up 50% of the voxel volume, then the apparent GNP concentration measured in that voxel will by half of what is actually present in the cells, and the apparent tissue volume will appear more than the actual cell cluster size. This is illustrated in Figure 57.

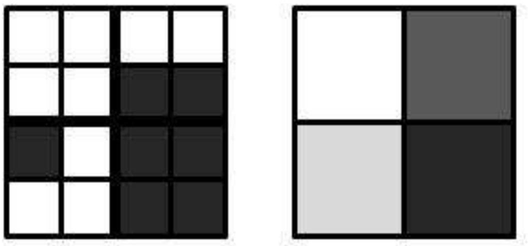

Figure 57 Illustration of the partial volume effect

The partial volume effect is decreased when the voxel size is decreased, as the tissue is better resolved. Therefore this effect will be greater for radiotherapy applications than for research sample measurement, the latter technique requiring a better spatial resolution.

4.2 Development of nanoparticle imaging phantoms

A range of GNP imaging phantoms were designed to test the performance of different XRF imaging systems.

4.2.1 Sensitivity

It is important to be able to test the ability of the XRF imaging system to quantitatively measure GNP concentration. A phantom was designed, composed of a series of holes of diameter 9 mm drilled into a Perspex block of thickness 10 mm. The distance of the hole periphery from the x-ray entrance side is 1 mm (Figure 58).

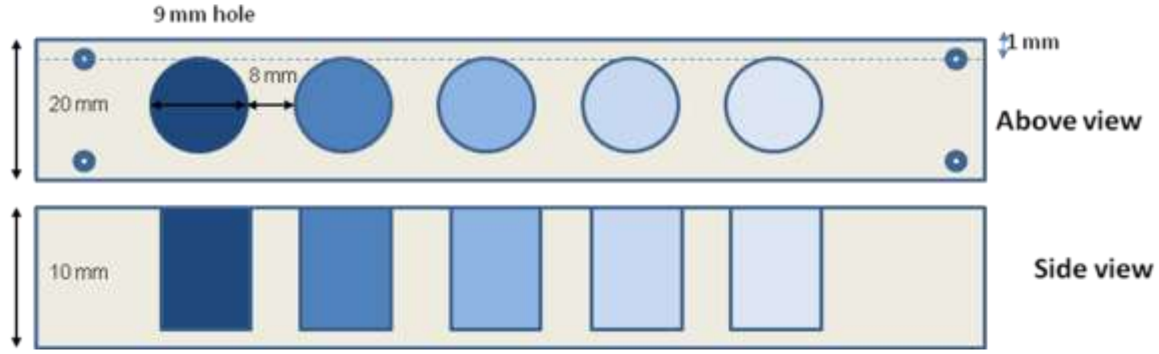

Figure 58 Sensitivity phantom consisting of 9 mm holes drilled into a 10 mm thick Perspex slab. The holes can be filled with GNP solutions of varying concentrations.

Each hole can be filled with a different GNP concentration, and a profile scan taken across to assess the XRF measurement technique. Two methods of filling the holes were attempted:

a) Suspending the GNPs in a low temperature agar gel (Agarose A2576, Sigma Aldrich, Dorset UK). This was considered to enable the sample to be more easily transportable, and to see if the agar gel suffered less from evaporation over time, as longer measurement times were envisaged for imaging mode. The procedure involved dissolving agar crystals in water at 80°C. The required GNP concentration was added and thoroughly mixed in the solute. A fine needle syringe was used to transfer the liquid agar solution into the phantom, taking care not to form air bubbles. The filled phantom was refrigerated at 5°C and left to set for 1 hour.

b) Filling the holes with GNPs suspended in DIW. This technique involved the same preparation as in Section 2.2. The filling process was carefully achieved using a fine needle syringe to smoothly fill the hole without creating air bubbles.

The agar gel technique was not successful, and the gel volume was found to shrink over the measurement time. This affected the XRF measurement too much and so it was decided to use the water-suspension technique, with the sample resting on a cooling plate to minimise evaporation. No evaporation was noticed throughout the course of measurement.

4.2.2 Contrast resolution

A phantom was designed in order to assess the ability of the XRF imaging system to resolve different GNP concentrations. A donut configuration was selected, enabling one GNP concentration to be surrounded by a GNP solution of different concentration. The phantom consisted of a series of 9 mm holes drilled into a 10 mm thick Perspex slab; an inner hole of diameter 5mm was drilled in the centre of the 9 mm hole to contain a straw of 5 mm diameter. This straw acted as a barrier between the two GNP concentration solutions.

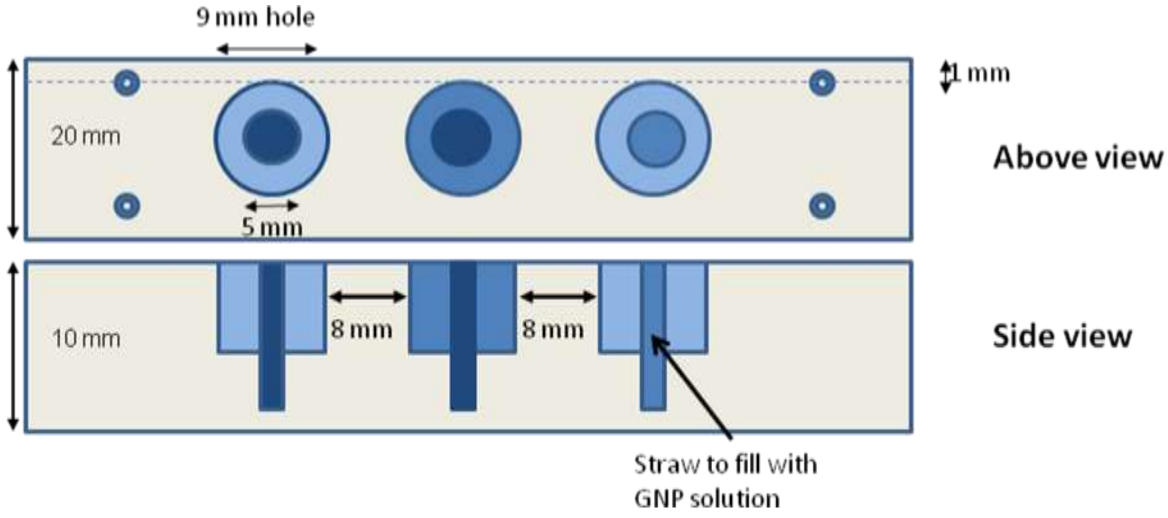

Figure 59 Contrast phantom; 9 mm hole including a straw located centrally to provide a barrier between two different GNP concentration solutions.

The difference in the concentration can be made large (high contrast phantom) or small (low contrast phantom). The outer concentration was selected to be lower than the inner concentration in each case to mimic the *in vivo* situation of greater uptake in the tumour with lower uptake in surrounding tissues.

In order to test the performance of the XRF imaging technique the literature was searched for typical GNP concentrations found in tumours and the tumour stroma, and the phantoms constructed in order to mimic the reported GNP concentrations. The typical GNP concentrations taken found from a mouse study investigating GNP uptake [24] are displayed in Section 1.5.1 (Table 3).

Figure 60 displays a photograph of the phantom filled with GNP solutions.

Figure 60 High contrast phantom filled with GNP solutions 4 mgAu/ml (central) and 0.2 mgAu/ml (outer ring)

4.3 Imaging system 1: SDD step and scan with mechanical collimator

In order to test the imaging capability of the XRF technique, the synchrotron L-XRF system characterised in Section 2.3 was used to perform a 1D profile scan of the sensitivity phantom. Measurements were made at the B16 beamline at the Diamond synchrotron source, Didcot, UK. A profile scan was thought sufficient as a first indicator of the usefulness of the imaging system.

4.3.1 Experimental arrangement

Figure 61 displays the sample and detector arrangement, and illustrates the spatial coordinates used in this section.

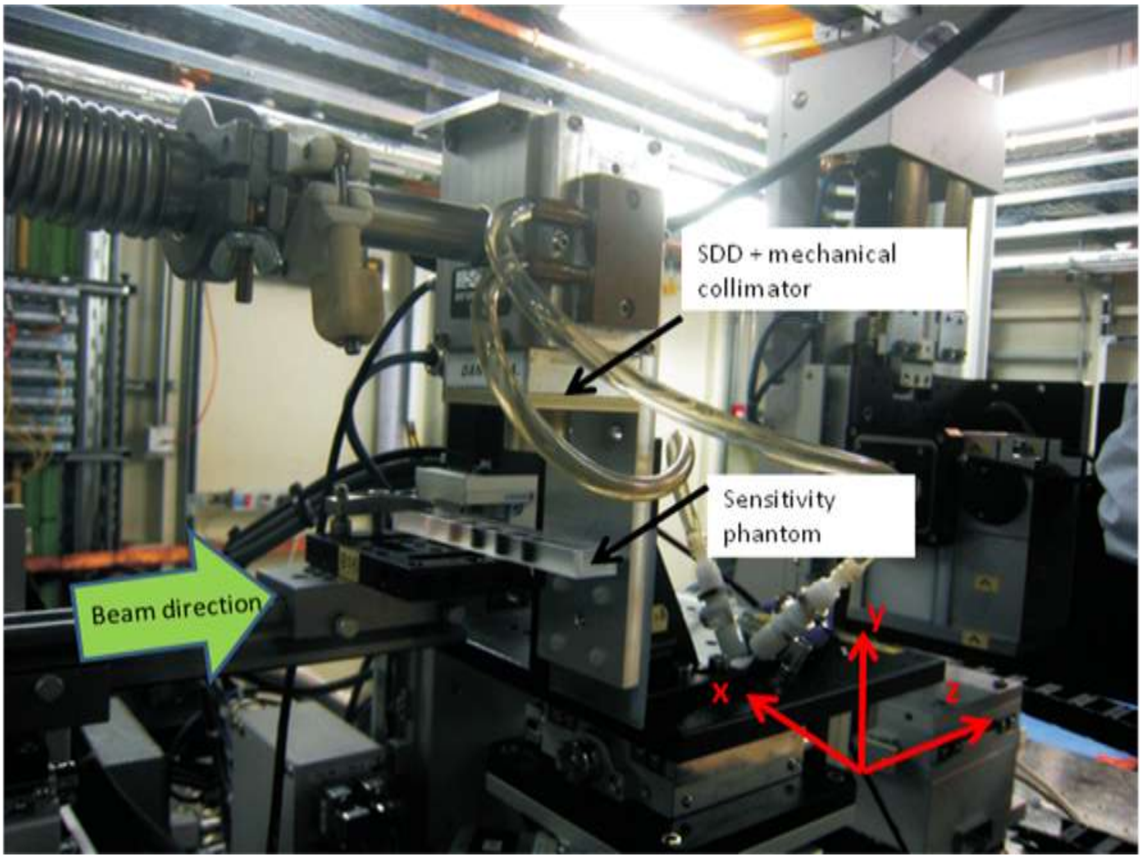

Figure 61 Experimental set-up of scanning imager

A CCD camera behind the sample was used to monitor the beam-sample alignment and make conventional transmission images. An ionization chamber was used to monitor beam intensity.

4.3.2 X-ray source

The synchrotron source was set to 15 keV with a beam size of 0.8 mm (x) x 4 mm (y) with 1 mm aluminium filtration in the beam. The aluminium filtration acted to reduce the intensity of the beam to levels that the SDD can operate at without count rate problems.

4.3.3 Nanoparticle phantom

The sensitivity phantom was filled with GNP solutions of concentrations 0.016, 0.1, 0.5, 2 and 8 mgAu/ml.

4.3.4 X-ray detector

The SDD detection module (first introduced in Chapter 2) was mounted with a 90° geometry in order to minimize the Compton background, and positioned on the z-axis in line with the centre of the GNP inclusions of the phantom. The SDD was operated at a shaping time constant of 1 μs for the whole measurement for reasons explained in Section 2.3.3.

4.3.5 Collimation

The mechanical collimator described in Section 2.3.4 was attached to the SDD for reasons outlined in Section 2.3.4.

4.3.6 Measurement volume

The voxel size of each profile scan measurement is defined by the beam size in the x- and y-direction (0.8 mm x 4 mm), and the sample thickness in the z-direction (10 mm). Refer to Figure 61 for spatial coordinate definitions. The detector-sample distance was sufficiently great that the detection solid angle covered the whole sample in the z-direction. The voxel size in the x-direction, being set by the 0.8 mm beam width, was not affected by the detector collimator hole size; this meant that a mechanical collimator could be used instead of an optic, in order to increase the count rate of the gold XRF signal.

4.3.7 Imaging procedure

The GNP-filled hole was automatically scanned at a 1 mm step interval in the x-direction, setting the resolution of the profile scan, and the energy spectrum was acquired at each point with a measurement time of 60 s per point for the highest two concentrations, and 120 s per point for the remaining concentrations. The sample scan procedure is illustrated in Figure 62.

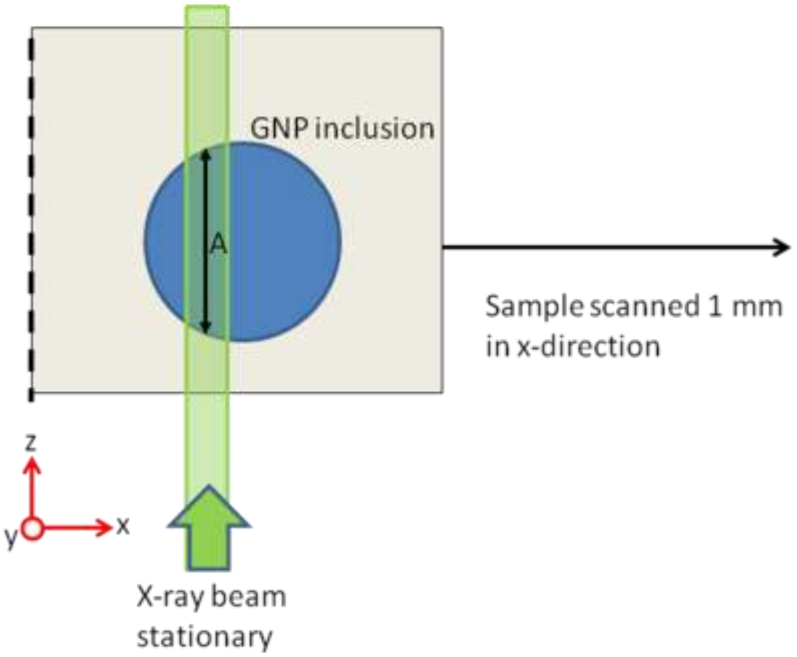

Figure 62 Illustration of 1D profile scan procedure. A represents the chord of the circle of 9 mm diameter, representing the GNP inclusion.

4.3.8 Results of 1D scan of sensitivity phantom

Figure 63 shows the recorded spectra as a function of the x-scanning coordinate for the 8 mgAu/ml hole. The attenuation of the elastic and Compton scattering peaks in the hole region and the build up of the gold XRF lines is clearly visible.

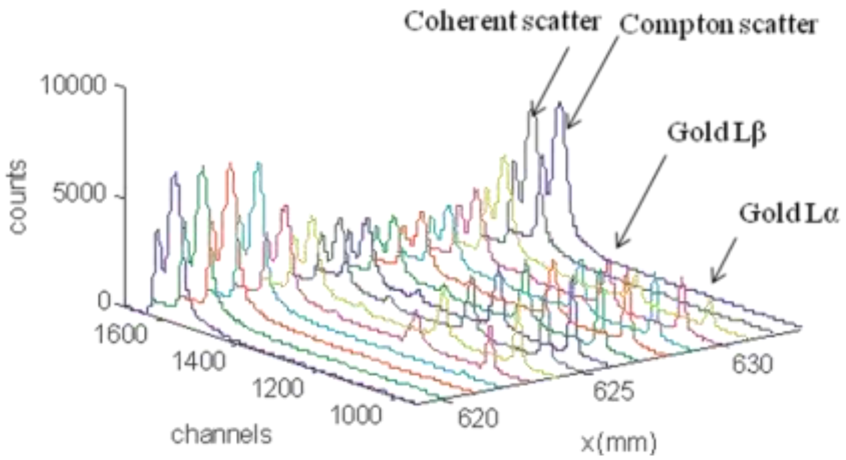

Figure 63 Recorded spectra as a function of the x-scanning coordinate in the case of the highest probed concentration hole (8 mgAu/ml). The attenuation of the coherent and Compton scattering peaks in the hole region and the build-up of the gold fluorescence lines is clearly visible.

The integral of the counts under the gold $L\alpha$ and $L\beta$ peaks were plotted against the scan coordinate. Normalising to the beam intensity was not necessary as the beam was found to be stable to within 1% during all measurements.

The experimental data points were fitted according to Equation 13, derived to describe the fluorescence yield (*FY*) as being proportional to the chord length of the GNP inclusion circle (found by a simple application of Pythagoras' theorem), expressed as a function of the scanning coordinate x_{sample}:

$$FY(x) = k \cdot 2 \cdot \sqrt{R^2 - \left(x_{sample} - x_o\right)^2} \qquad \text{Equation 13}$$

where R is the hole radius, x_0 is the centre of the hole and k is the constant of proportionality representing the fluorescence yield in the given solid angle. Figure 64 displays the gold XRF signal plotted against scan coordinate. The purple line shows the best fit of the experimental data according to Equation 13.

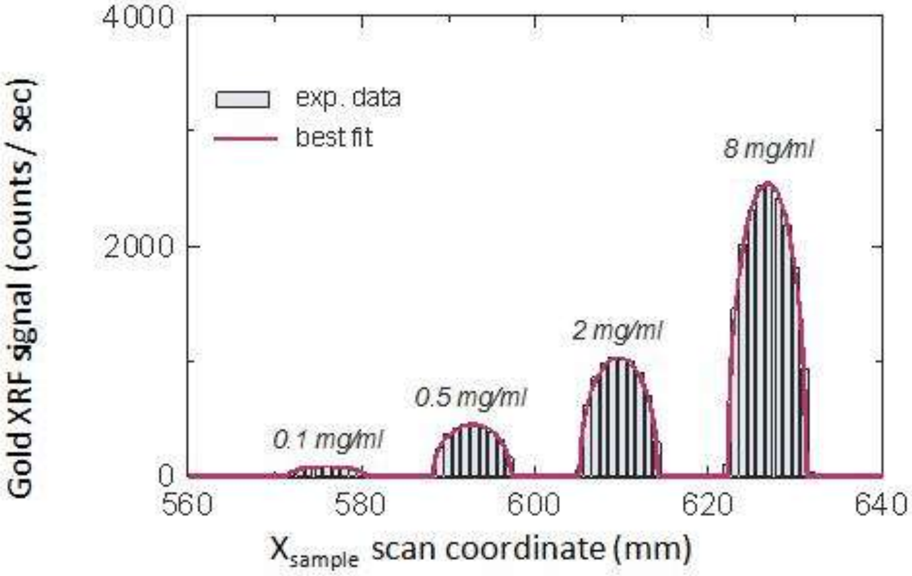

Figure 64 Gold XRF signal vs. scan coordinate. The GNP concentration is indicated over each hole. The purple line shows the best fit of the experimental data according to Equation 13.

The 0.015 mgAu/ml detail is not plotted, as the system was not sensitive to its presence over the measurement time of 120 s.

4.3.9 Discussion

It can be seen that the measured XRF signal was found to be proportional to the chord length of the GNP inclusion at each x_{sample} position, with Equation 13 found to describe the measured data (Figure 64). The width of the holes was measured to be 9 mm, in agreement with the phantom geometry.

Chapter Two has already demonstrated the ability of the synchrotron L-XRF technique used here in quantitative measurement of GNP concentration. The ability to quantify GNP concentration is equally applicable in this profile scan study, but has not been reported in this case because the purpose of this study was to demonstrate imaging feasibility of the technique. This aim has been met, as discussed in the previous paragraph. In order for the profile scan measurement performed here to give quantitative information on GNP concentration, a more full analysis would be required, including attenuation corrections and treatment of the partial volume effect. Analysis of the relative heights of the measured XRF signals for each concentration was not performed, and quantitative information about GNP concentration cannot be directly found at present as the system was not calibrated for absolute concentration measurement.

This series of measurements indicate that the XRF technique is able to perform 1D profile scans of GNP distribution. This result was then translated to a 2D imaging technique to assess the role of the XRF system in acquiring 2D images.

4.4 Imaging system 2: SDD step and scan with a focussing polycapillary optic

2D images of two contrast phantom details were performed using the same set up as in the previous system, replacing the mechanical collimator with a focussing polycapillary optic. The optic enables smaller voxel sizes in both the x and z directions than when using a mechanical collimator.

4.4.1 Translating from a mechanical collimator to focussing polycapillary optic

Focussing polycapillary optics are generally used to capture x-rays emitted from a source and focus them to a small spot area to increase the intensity over small areas of a sample to enable high intensity XRF measurement. Focussing optics are designed to have gently bending hollow capillaries of curvature smaller than the critical angle that propagate x-rays through them to focus them to a point. According to the physics of x-ray optics smaller focal spot sizes are expected with increasing x-ray energy [47].

The XRF imaging system described here has utilised a focussing polycapillary optic to collect the x-rays emitted from the sample after XRF excitement, and to transport the collected x-rays to the detector chip. The lens enables an increased distance between the sample and detector without a decrease in effective collection angle of the XRF x-rays. Their use can potentially increase the spatial resolution of the image by allowing measurement of small areas of the sample, with particular improvements made compared with the mechanical collimator system in the z-direction. The lens used in this system was measured to have a nominal focussing spot size of ~ 300 μm FWHM in the energy range 5 – 10 keV [47]. The mechanical collimator system could spatially resolve the sample in one direction (along the x-axis) by an amount dictated by the beam width set (0.8 mm), and in the z-direction an amount governed by the solid angle of collection (dictated by the sample-detector distance and collimator hole size). The focussing lens also enables the detector to focus measurement at a specific depth in the sample (along the y-axis) according to the focal point of the lens.

4.4.2 Experimental arrangement

The experimental set-up of the 2D scanning system making use of a focussing polycapillary optic is displayed in Figure 65.

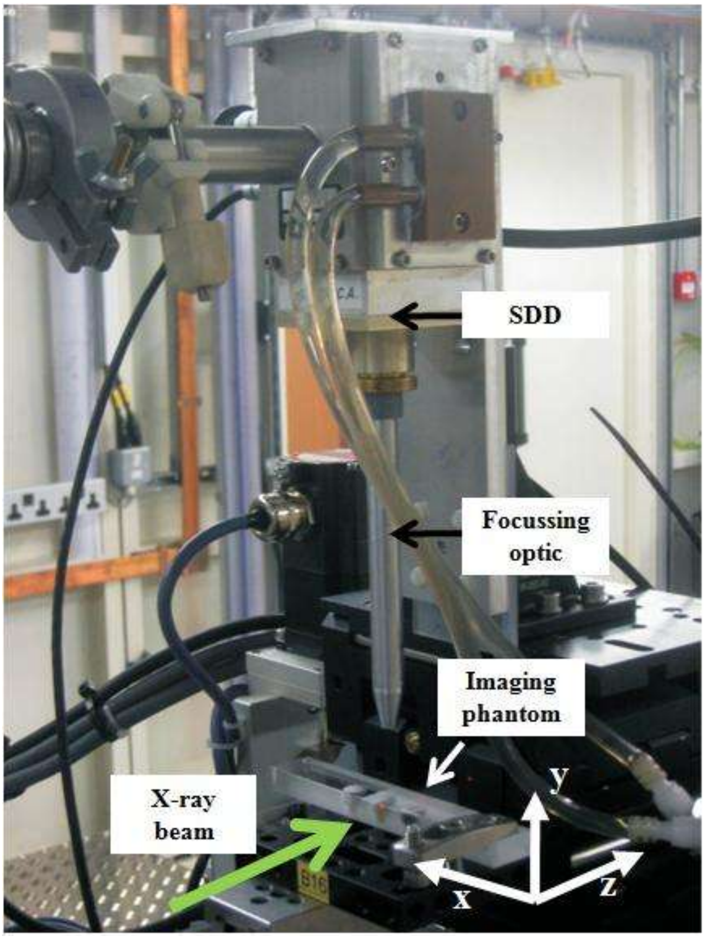

Figure 65 Experimental set-up for 2D scanning system.

4.4.3 X-ray source

The primary beam was set to 4 mm (x) x 4 mm (y) with no filtration.

4.4.4 Nanoparticle phantom

The contrast phantom displayed in Figure 59 was filled with the following GNP solution concentrations: (i) high contrast phantom: 4 mgAu/ml (inner) and 0.2 mgAu/ml (outer), a factor of 20 different, and (ii) low contrast phantom: 0.125 mgAu/ml (inner) and 0.025 mgAu/ml (outer), a factor of five different.

4.4.5 Polycapillary x-ray optics

An 84MLS11 polycapillary optic lens (Institute for Scientific Instruments GmbH, Berlin, Germany) was coupled to the SDD for 2D step and scan imaging. The lens is slightly focussing, measured to have a nominal focal spot size of ~ 300 µm FWHM in the energy range 5 – 10 keV [47].

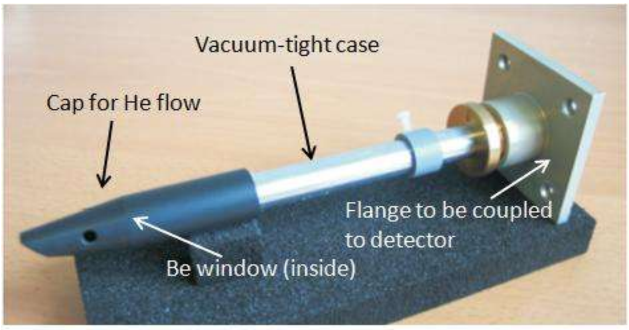

Figure 66 84MLS11 polycapillary optic lens (Institute for Scientific Instruments GmbH, Berlin, Germany) in its vacuum tight case.

The detector is sealed in a custom compact case, vacuum-tight down to 10^{-4} mbar. The housing is sealed with an 8 µm thick beryllium entrance window [105].

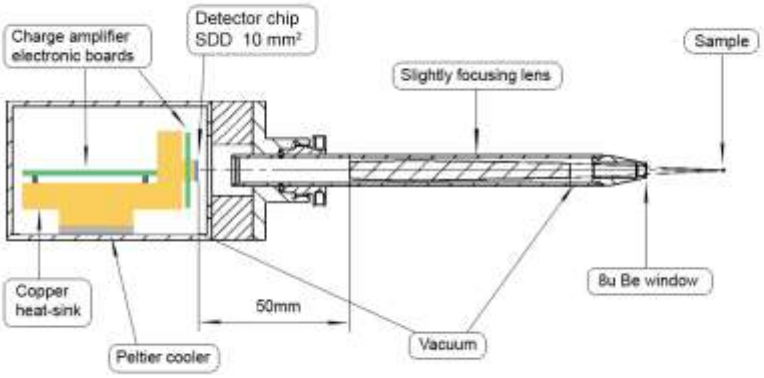

Figure 67 Designed vacuum tight detection module with the polycapillary lens [105].

Lens parameters given by the manufacturer are displayed in Table 14:

Table 14 Geometrical parameters of the 84MLS11 x-ray polycapillary optic lens [47].

Parameter	**Value**
Capture angle	0.095 rad
Capillary diameter	30 μm
Focal distance – sample side	60 mm
Focal distance – detector side	100 mm
Lens length	85 mm
Lens curvature radius	1050 mm

4.4.6 Gold nanoparticle imaging procedure

The beam, sample and SDD were aligned as follows. A transmission CCD image of the sample was used to align the inner high GNP concentration component in the beam. The beam size was collimated down to 4 mm x 4 mm to cover the centre of the sample. The SDD was then scanned across in the x-direction in 0.5 mm steps; the profile of gold XRF counts was plotted, with the centre of the profile corresponding to the position of alignment of the SDD with the beam. The SDD scan was repeated in the z-direction. At this point, the centre of the sample, the beam and the SDD are aligned. The sample was then scanned in both the x- and z- directions with a 600 μm x 600 μm pitch to build up a pixellated image. The scanned area was 12 mm x 7.2 mm. An X-Y-Z micrometric stage system was responsible for sample movement and remote control management by the DAQ enabled automatic X-Y scans. An acquisition time of 40 s per point was taken and the full energy spectrum obtained at each point.

4.4.7 Image reconstruction

The images were reconstructed by collaborators in Politecnico di Milano, Italy, with results published in [105]. The GNP images were reconstructed off-line by computing the integral counts under the gold $L\alpha$ and $L\beta$ peaks. Figure 68 displays example energy spectra within the Perspex component of the phantom, and within the 4 mgAu/ml GNP solution volume. It can be seen that the background was negligible beneath the gold peaks, and so no background subtraction was made when integrating the gold peak counts. The tails of the elastic scattering peak and of the Compton scattering peaks show an overlap that has been neglected in this analysis.

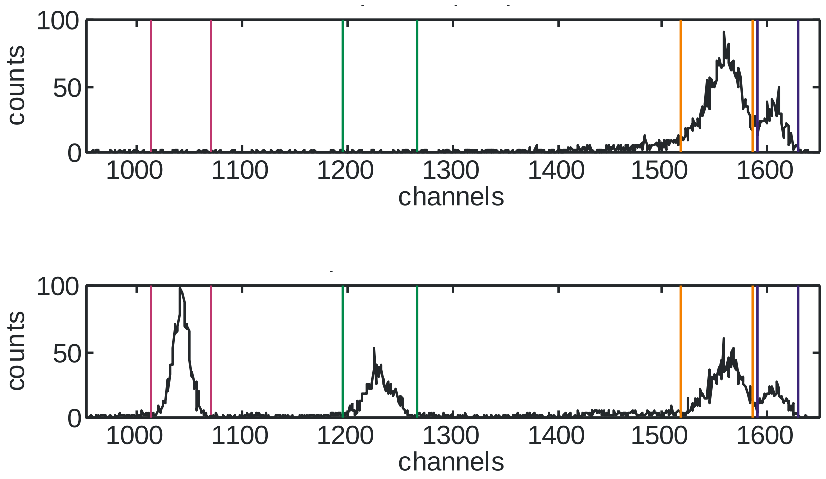

Figure 68 Sample energy spectra collected in two different points of the scan in pure Perspex (top) and within the hole filled with 4 mgAu/ml GNP solution (bottom). Coloured lines show the ROIs used for the computation of the integral counts- from left to right: gold $L\alpha$ line (pink), gold $L\beta$ line (green), Compton scattering peak (orange) and elastic scattering peak (blue).

The image reconstruction protocol did not attempt to quantify GNP concentration in each pixel, and was undertaken to demonstrate the feasibility of forming an image of GNP distribution. GNP concentration sensitivity has previously been demonstrated in Chapter Two. This approach provides the same information but from a smaller volume. Therefore sensitivity is expected to be lower than reported in Chapter Two.

4.4.8 Results

Figure 69 displays the 2D pixellated images obtained by plotting the logarithm of the gold $L\alpha$ and $L\beta$ peak ROIs as a function of scan position for the high contrast phantom (with and without normalising to the coherent scatter peak), and also the scatter normalised low concentration phantom. The primary beam is incident on the right side of the images in Figure 69.

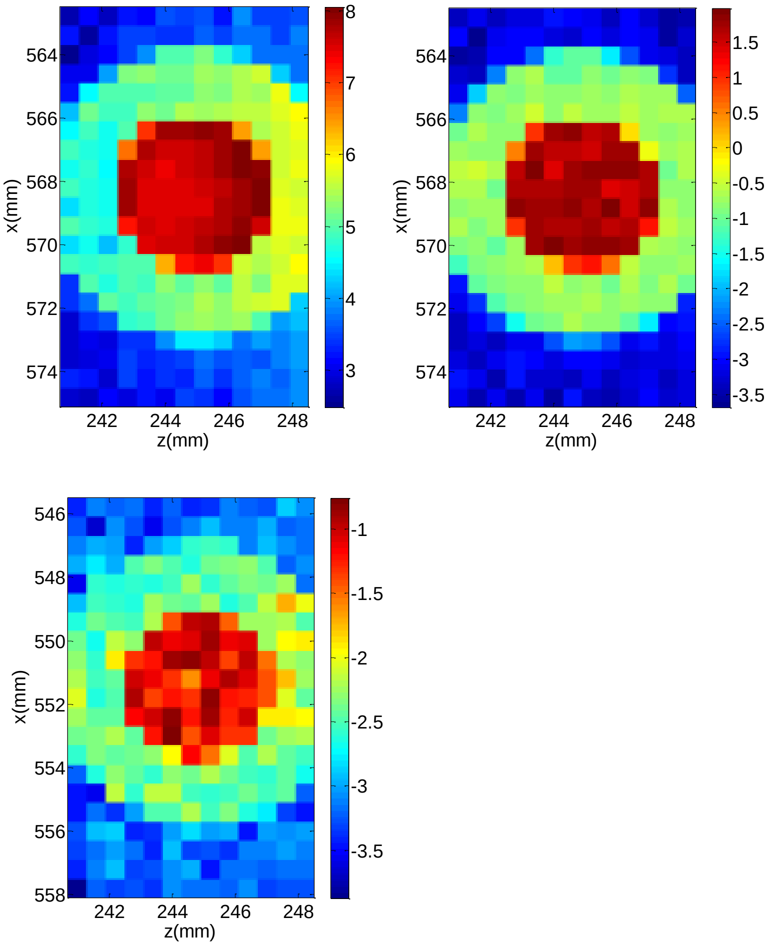

Figure 69 2D gold XRF images in log scale of GNP contrast phantoms acquired using an SDD coupled to a focusing polycapillary optic. (Top left) un-normalized high contrast phantom, (top right) coherent scatter normalized high contrast phantom, and (bottom) coherent scatter normalized low concentration phantom.

4.4.9 Discussion

Figure 69 demonstrates that the developed XRF imaging system can be used to image GNP concentrations as low as 0.025 mgAu/ml. Lower concentrations were not tested in this study due to restrictions on acquisition time at the synchrotron source. It can be inferred from the detection limit measurements in Chapter Two that the system will have sensitivity to even lower concentrations. The results also demonstrate that GNP concentrations differing by factors of twenty and five can both be distinguished by the novel imaging system. This achieves the aim of the project in distinguishing tumour cells from surrounding healthy cells; *in vivo* uptake between the tumour periphery and surrounding tissue are reported to be a factor of 22 and 14 different for functionalised and unfunctionalised GNPs (refer to Table 3) [24].

The crescent shape seen in the right of the left hand image is due to attenuation of the primary beam in penetrating the sample. In order to account for beam absorption a scatter normalisation technique was implemented (refer to Section 2.7.2 for a discussion of why scatter normalisation is effective in correcting for absorption). This was achieved in this case by normalising to the image obtained using the integral counts of an ROI covering the coherent scatter peak of each spectrum. The image of the resulting normalised image in log scale is also displayed in Figure 69, and shows the effectiveness in correcting for attenuation effects.

At this stage, the imaging system does not provide absolute quantitative information of GNP concentration. In order to achieve this in future system development, the following must be considered:

- Partial volume effect and correction methods to account for this.
- The system must be fully calibrated so that the gold XRF signal at a known beam thickness and solid angle is known.
- Further methods of attenuation correction should be investigated. One possibility is the use of transmission images to measure the attenuation coefficient of each pixel in order to perform the absorption correction.

4.5 Imaging system 3: Use of an energy resolving pixellated detector

In order to avoid step and scan XRF imaging techniques which potentially require long measurement times, the feasibility of excitation of the whole sample with a wide beam and detection of the XRF x-rays with a 2-D energy resolving pixellated detector has been investigated. Use of a collimating polycapillary optic coupled to the detector preserves the positional information from where fluorescence was emitted.

4.5.1 Controlled drift detector

A Controlled Drift Detector (CDD) (Politecnico di Milano, INFN Milano and MPI Munich) of pixel size 180 µm x 180 µm, and 24 drift channels each with 34 pixels was used to form the XRF images. The CDD was coupled to a collimating polycapillary optic angular filter (IfG Berlin), of channel size 30 µm.

The CDD is a fully depleted silicon detector that operates in single-photon counting integrate-readout mode and allows detection of position and energy of each photon in the range 0.5-30 keV. High frame rates (up to 100 kHz) are achievable [106]. The chip thickness was 300 µm allowing absorption efficiency of 93% for the gold $L\alpha$ line.

Equally spaced potential wells are generated along the length of the detector; the charge generated by the interacting photon is collected in these wells. The potential barriers are then removed and the charge collected drifts towards the readout located at the end of each column. One positional coordinate is given by drift time, the other by knowing which drift column the event occurred. The amplitude of the signal pulse provides the energy information.

Use of the CDD / parallel optic system improves the achievable resolution of XRF imaging by a factor of 1.6 compared to using the SDD / focussing optic system. There are no differences in efficiency of detection of the gold signal, or achievable count rate between the CDD and SDD. The ~1 keV energy resolution of the CDD can distinguish the gold $L\alpha$ and $L\beta$ peaks, and can also easily distinguish the scatter peaks from the gold XRF signal. The only effect the degradation in energy resolution will have compared to the SDD is that the detection limit of the system will worsen (refer to Section 2.8.2 for a discussion of this effect). A more detailed study in the future is required to quantify the achievable detection limit of the CDD system. Use of the CDD also enables quicker acquisition times, as it is used to simultaneously collect the XRF spectra for 816 pixels; in order to acquire data for an image with the same number of pixels, the SDD system would have to perform 816 individual scans leading to acquisition times nearly three orders of magnitude greater. In order to calculate the actual difference in acquisition time, the sensitivity to the gold XRF signal of each system must be considered.

The characteristics of both the CDD and SDD systems have been compared in Table 15.

Table 15 Characteristics of the SDD and CDD systems for use in XRF imaging. The image pixel size of the CDD was calculated as a quadrature sum of CDD pixel size and polycapillary optic channel size.

Parameter	**SDD + focussing optic**	**CDD + parallel optic**
Energy resolution	350 eV at 20 keV	1 keV average at 20 keV
Max count rate	100 kHz	100 kHz
Substrate thickness	450 μm Si	300 – 450 μm Si
Efficiency at Lα	97%	93 – 97%
Image pixel size	300 μm (focus spot size)	182 μm

4.5.2 Selection of detector collimator

In order to acquire a 2D XRF image of the sample on the detector in one shot, a detector collimator is required. The spatial resolution of an XRF image is a summation in quadrature of the detector pixel size and the collimator hole size. A multi-hole mechanical collimator (typically with hole dimensions limited to ~0.5 mm) may be used (refer to Figure 81 for illustration of such a collimator). The hole size therefore dominates the spatial resolution. To overcome the practical limitations of mechanical collimator hole size polycapillary optic technology may be used. A parallel polycapillary optic acts as a fine angular selector with a divergence of collection of the order of a few millirads. Optic channel sizes of the order of a few tens of micrometers means that the detector pixel size (180 μm for the CDD) sets the limiting factor for the spatial resolution. Use of a parallel optic improves the spatial resolution by a factor of ~2.5 compared with using a typical multi-hole collimator (each collimator giving pixel values of ~180 μm and ~500 μm respectively).

Use of the parallel polycapillary optic acts to greatly reduce the collection angle of x-rays emitted from the sample; this acts to decrease the scatter component of the measured spectrum. However, this also acts to reduce the count rate of the gold XRF signal, which will have a negative impact on the sensitivity of the system. The system sensitivity is also decreased due to transmission losses in the optic. The transmission efficiency of optics is a function of x-ray energy (due to the dependence on the critical angle on energy). Further discussion of parallel polycapillary optics and a demonstration of the angular acceptance of a parallel polycapillary optic are presented in the following section.

4.5.3 Demonstration of angular acceptance of parallel polycapillary optics

This section presents results that indicate the superior angular acceptance capabilities of parallel polycapillary optics, a characteristic that makes the optics useful as a fine angle collimator. Polycapillary lenses are monolithic structures of bundles of hollow glass capillaries. X-rays are guided along the capillaries by total external reflection (TER), and only accepted into the optic channels if the incident angle of the x-ray is below the critical angle for TER at that energy ($\theta_c(E)$). The proposed system will use an optic made of borosilicate glass, for which $\theta_c(E)$ is:

$$\theta_c(E) = \frac{30}{E}\ mrad \qquad \text{Equation 14}$$

where E is the photon energy in keV [107].

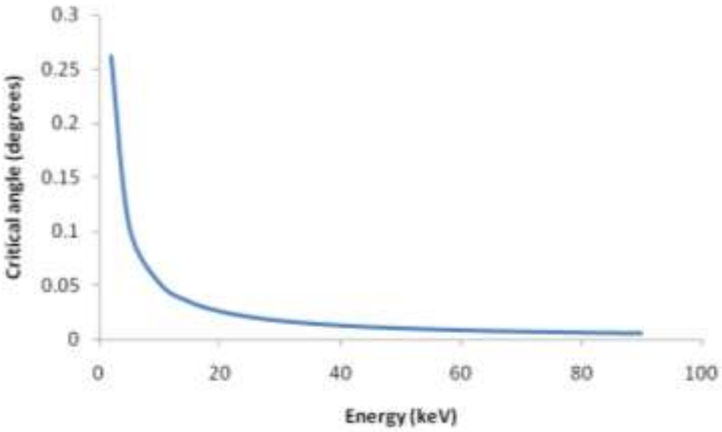

Figure 70 Relationship between critical acceptance angle of the polycapillary optic and x-ray energy.

$\theta_c(E)$ is larger for lower x-ray energies than higher energies. $\theta_c(E)$ is of the order of a few mrad for x-rays in the 5-30 keV energy range, and the fibres therefore act as fine angular collimators, filtering through x-rays at the selected scatter angle and rejecting x-rays incident at all other angles. This allows formation of a 2D image (across the area of the optic) of the x-rays emitted in the solid angle of collection of the optic, and therefore enables faster image acquisition than point-by-point scanning.

A parallel polycapillary optic angular filter (XOS, New York) was characterised in order to investigate its use as a collimator in imaging systems. It is made from parallel borosilicate glass capillaries each of diameter 5.0 µm forming a monolithic structure of outer diameter (flat-to-flat) 11.0 mm. The capillaries are 20 mm in length. The x-ray transmission efficiency is quoted as 47% at 17.4 keV by the manufacturer.

Polycapillary optics require a careful performance qualification (particularly for beams with broad spectral properties). The angular / energy dependence of the optic was measured using a CMOS pixellated sensor.

A motorised linear translation stage (Newport, USA) of movement resolution 0.1 µm was used to scan the CMOS sensor across an uncollimated x-ray beam to locate the area of maximum x-ray intensity; this area corresponds to the central axis of the beam. The central axis refers to the central component of the x-ray beam that describes the direction of the beam, and is the area of greatest x-ray intensity. At each position an average image was taken over 100 frames, and the mean pixel value (MPV) from a region of interest 170 x 170 pixels central to the image was measured. Figure 71 displays the location of maximum intensity.

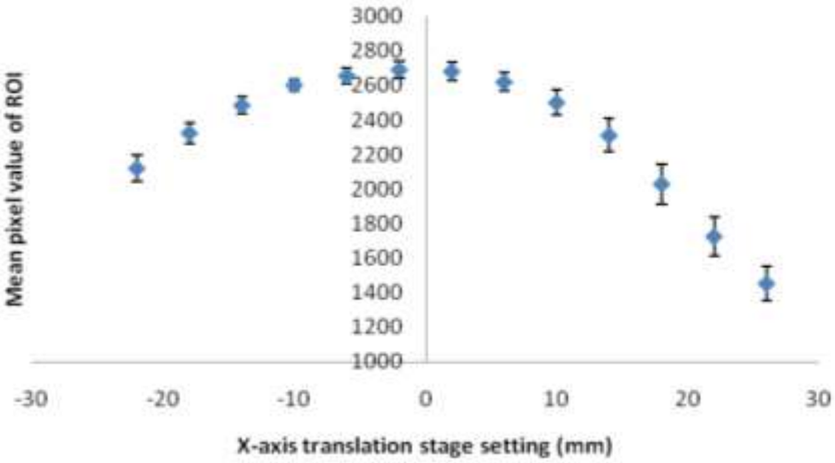

Figure 71 Position of maximum intensity measured across the face of the beam.

The angular position of maximum x-ray intensity was then found. With the CMOS sensor in the location of maximum intensity, a fine cross wire was used to visualise the centre of the beam. The cross wire was mounted on an x-y linear translation stage in front of the sensor and positioned so that its image lay at the centre of the CMOS sensor. A tungsten target x-ray source was used in fine focus setting giving a focal spot size of 0.4 x 0.4 mm; fine focus was selected in order to produce a sharp image of the fine cross wire and collimator edges. The beam was collimated around the cross wire to 1 mm at the detector face.

With the CMOS sensor in this position, the optic was placed into a purpose built holder that was mounted in front of the sensor. The detector-collimator system was rotated around the direction parallel to the central axis of the x-ray beam using a rotary stage with an angular precision of 5 minutes. At each rotation angle, 100 frames were acquired to produce an average image of the beam. Measurements were made at 30, 40 and 50 kV. The mean pixel value of a region of interest 200 x 200 pixels at the centre of the beam cross section was plotted as a function of optic angle (rocking angle) for each x-ray energy. As the centre of the collimator face was not perfectly on the centre of rotation, each rotation produced a slight beam translation. The data was fitted with a Gaussian distribution and the corresponding FWHM of the rocking curves were found (refer to Figure 72).

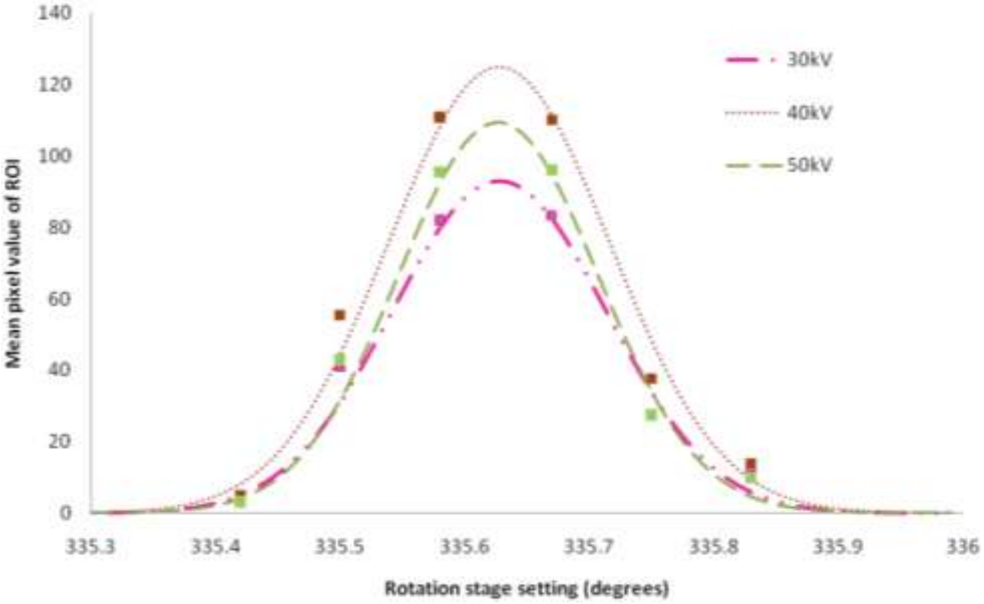

Figure 72 Energy and angular dependence of x-ray acceptance of polycapillary optic

This measurement has demonstrated the potential use of a parallel polycapillary optic in acting as a fine diffraction collimator; the angular acceptance of the optic was found to be independent of energy over the range 30 - 50 kV_p, with an average FWHM of 0.2°, as displayed in Figure 72. The angle of peak transmission was found to be at the same rotation stage setting for each energy.

It should be noted that the optic cannot be employed at high x-ray energies (such as for K-XRF techniques) due to penetration of x-rays through the glass fibres; a collimator with different glass composition could be designed with high Z components for use at high energies. The use of the current optic is limited to application in L-XRF techniques.

4.5.4 Experimental arrangement

Measurements were made at the SYRMEP beamline at the Elettra synchrotron source, Trieste, Italy. The CDD module was mounted with a 90° geometry and coupled with a parallel polycapillary optic to ascertain the position of emission of gold fluorescence. A CCD camera behind the sample monitored the beam-sample alignment and made conventional transmission images to assist beam-sample-detector alignment.

An ionization chamber was used to monitor beam intensity. The experimental set up is displayed in Figure 73.

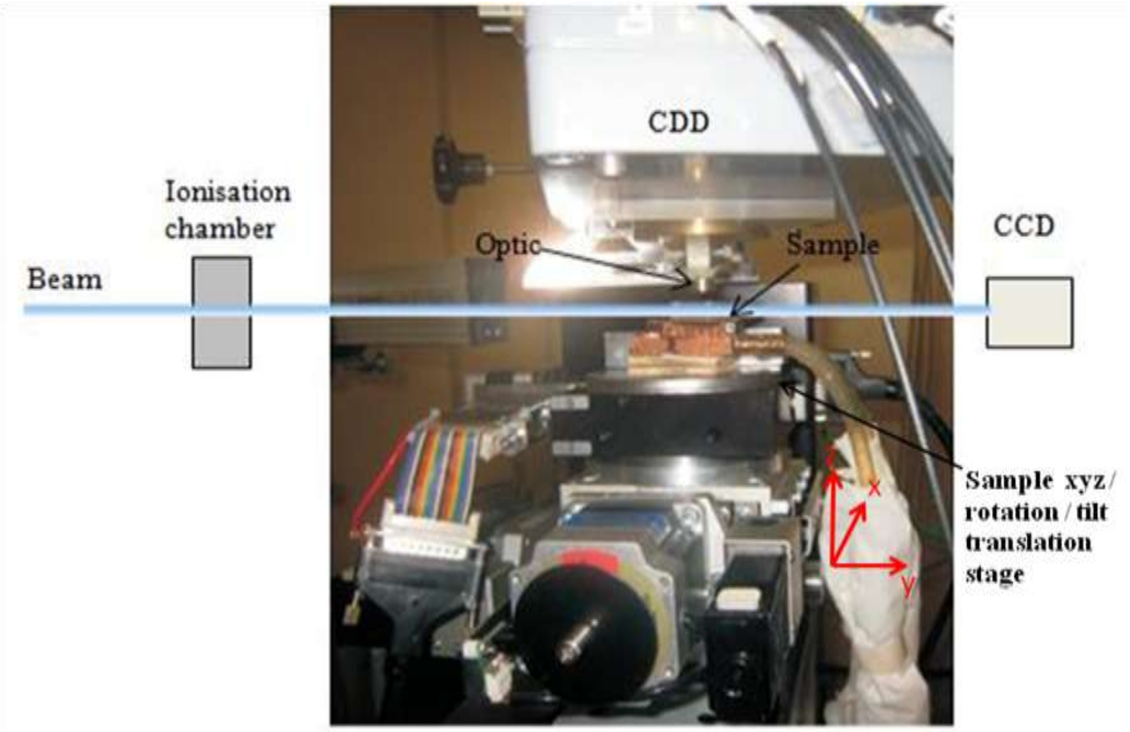

Figure 73 Experimental set up of CDD XRF imaging system.

4.5.5 X-ray source

The synchrotron source energy was set to 15 keV. A beam size was set to completely cover the detection area of the sample (detector dimensions 4.3 mm x 6.1 mm). The sample thickness measured was 3.8 mm, and the view area limited to the field of view of the polycapillary optic lens and the detector area.

4.5.6 Nanoparticle phantom

The contrast resolution phantom was filled with different concentrations of GNPs (4 mgAu/ml (central) and 0.25 mgAu/ml (peripheral) for the high-contrast phantom, and 1.6 mgAu/ml (central) and 0.5mgAu/ml (peripheral) for the low-contrast one). The high contrast detail had concentrations different by a factor of 16, and the low contrast a factor of 3.2 different.

4.5.7 Detector collimator

A parallel polycapillary optic (model 72MLS) made available by IfG GmbH, was used with glass capillary channel diameter 30 µm ± 1 µm, bunched together to form a monolithic structure of total diameter 8 mm. The capillaries are 40 mm in length. The capillaries are encased in a metal cylinder of outer diameter 12 mm and total length 44 mm.

4.5.8 X-ray detector

A description of the CDD module used can be found in [106]. In summary, the CDD had a silicon substrate thickness of 300 µm and measured energy resolution of 320 eV at the manganese $K\alpha$ line (5.9 keV). During measurement at Elettra, the energy resolution was found to degrade to 460 eV FWHM measured at the copper $K\alpha$ line (8 keV), due to the noisy environment of a synchrotron beam. The parallel collimating optic was coupled to the CDD.

4.5.9 Gold nanoparticle imaging procedure

An iron slab was placed beside the phantom hole detail to facilitate sample-beam alignment, and the detector scanned to align the detector with the beam (iron – beam – detector alignment was achieved when iron XRF lines were detected), using the same procedure as outlined in Section 4.4.6. The sample image area was fully illuminated by the synchrotron beam, and the CDD set to acquire for 6500 s for the high contrast phantom and 11,000 s for the low contrast phantom.

4.5.10 Image reconstruction

Reconstruction was performed by collaborators in Politecnico di Milano, Italy, with results published in [105]. ROIs were set over the gold $L\alpha$, gold $L\beta$ and coherent scatter peaks for each detector pixel spectrum. The latter ROI was set to perform a scatter normalisation to the XRF image to correct for sample absorption.

4.5.11 Results

Two XRF images of a high contrast and low contrast phantom are displayed in Figure 74.

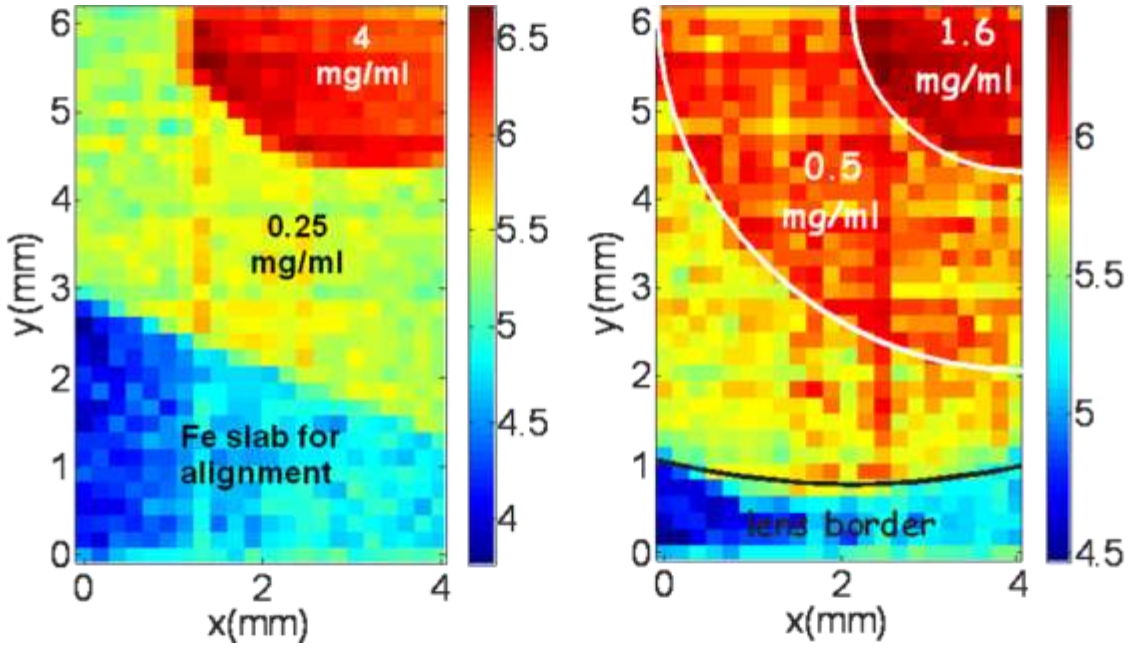

Figure 74 XRF images (log scale) of GNP contrast resolution phantom using the CDD – polycapillary optic XRF system. The images are of high contrast (left) and low contrast (right) details. GNP concentrations are labeled on the images.

4.5.12 Discussion

The novel CDD-parallel optic XRF imaging technique demonstrated sensitivity to GNP concentrations as low as 0.25 mgAu/ml (the lowest measured concentration). The technique was able to distinguish GNP concentrations that were different by a factor of 16 (high contrast phantom) and 3.2 (low contrast phantom). The system therefore achieves the requirement needed to distinguish tumour from surrounding healthy tissue (refer to Table 3). The images in Figure 74 achieve the purpose of this study, which was to demonstrate the ability of the one-shot system to image GNP distribution. These images do not provide absolute quantitative information of GNP concentration at this stage. In order to achieve quantitative images in future work, a complete calibration of the CDD to gold XRF signatures is required, and this information is not available at present. Refer to Section 4.5.2 for a discussion of how the CDD specifications (energy resolution and efficiency) will affect this system's performance compared with L-XRF systems using the SDD.

The high contrast image in Figure 74 displays presence of the iron slab alignment tool as a cold spot on the image (i.e. very few x-rays were detected in the gold ROI at the position of the iron). A cold spot is also present on the bottom of the low contrast image due to the location of the lens border.

4.6 Summary of key results of XRF imaging of GNPs

An XRF spectrometer (SDD) has been developed with the ability to be coupled to mechanical collimators and polycapillary lenses which define measurement volumes in order to build up pixellated images. The feasibility of performing energy resolved imaging of GNP distribution at concentrations relevant for *in vivo* and *in vitro* studies has been demonstrated. GNP concentrations different by a factor of 20 down to a factor of 3.2 have been shown to be easily resolvable, making this system capable of distinguishing tumour from non-tumour (refer to Section 1.5.1). Further work is required to test the contrast resolution capability of the system further. Details of phantoms with concentrations as low as 0.025 mgAu/ml (the lowest concentration present in the phantom) have been successfully imaged in this study. It can be inferred from the detection limit measurements in Chapter Two that the system will have sensitivity to even lower concentrations.

In order to avoid step and scan XRF imaging techniques (potentially requiring long measuring times) the feasibility of excitation of the whole specimen with a wide beam and detection of the fluorescent x-rays with a 2-D energy resolving detector without scanning has been investigated. A parallel polycapillary optic coupled with the detector has been successfully used to ascertain the position where fluorescence is emitted.

Further work is required to investigate methods to perform absolute quantitative imaging. This is not an easily solved problem, and will involve development of correction procedures for sample attenuation, partial volume effect and calibration techniques to gain absolute concentration information.

4.7 Development of a combined XRF/XRD system

Both XRD and XRF techniques have proven beneficial for identifying and characterising biological tissues. Section 1.5.5 introduced the concept of using XRD analysis to discriminate between tissue types based on differences in structural composition of tissues. XRD techniques can provide a considerable enhancement in contrast over conventional x-ray imaging [46]. XRF was also introduced in Section 1.5.4 as a potential method to locate the presence of nanoparticles, such as gold, which are embedded into tissues as biomarkers to map the disease state. The sensitivity of the XRF technique to GNP concentrations in water and in cells has been demonstrated in Chapters Two and Three respectively, and extension of the technique as a GNP imaging modality has been displayed in this Chapter.

The final part of this thesis proposes to determine the feasibility of combining these techniques to both locate tumours and provide information on tumour conditions, using GNPs as a contrast agent labelled to biomarkers. The following sections will detail ideas to develop a high resolution, combined imaging system, and will present a key set of preliminary measurements in order to determine the potential of the proposed combined imaging technique.

In order to assess the feasibility of a combined XRF/XRD system as a technique that meets the aims detailed in Chapter One (Section 1.3), the following questions will be answered in the final sections of this thesis:

1. *Does XRD have a role in identifying tissue type to distinguish tumour from healthy tissue?* Refer to Section 4.7.2 for a discussion of the potential use of XRD in tissue discrimination.

2. *Can XRD discriminate between tissue types used in the bio-phantoms developed in this project?* Section 4.7.3 displays measurements performed to determine differences (if any) between XRD signals from different phantom components.
3. *Do GNPs have an XRD signature of their own that could add to that of the tissues being measured? Do GNPs have an XRD signature that may interfere with the signature of the measured tissues?* Section 4.7.4 reports results of measured GNP XRD signals and draws conclusions based on these findings.

Each subsequent section will aim to answer the above questions in turn. All XRD measurements reported in the following sections are preliminary results, and are not the main focus of the project.

4.7.1 X-ray diffraction techniques

Coherent scatter contains useful information about the structure and elemental composition of the scattering material, as introduced in Section 1.5.5. XRD techniques measure coherent scatter to determine molecular structure, chemical bonds and bond lengths, and can identify protein types. The momentum transfer value (Equation 3) of diffraction peaks relates to the elemental composition and structure of the material, while the peak widths relate to the order of the material (more crystalline structures have narrower peaks). Soft tissue has short range order producing broader diffraction peaks at lower scattering angles than crystalline materials. In terms of imaging different tissue types, the combination of position and intensities of all peaks provides a unique diffraction signature for each tissue type.

As the momentum transfer is related to x-ray energy and scatter angle (Equation 3), there are two ways to extract the diffraction signature from a material: (i) angular dispersive x-ray diffraction (ADXRD) and (ii) energy dispersive x-ray diffraction (EDXRD). EDXRD uses a polyenergetic source (a conventional x-ray tube) and an energy resolving detector, such as the SDD, set at a fixed angle. The incident polyenergetic beam is collimated to a pencil beam, and further collimated before arriving at the energy resolving detector to define the scatter angle (as displayed in Figure 75). The scatter signature is measured as a function of energy by the detector.

ADXRD uses a monoenergetic source and measures the scatter intensity as a function of angle. Synchrotrons are commonly used to produce the monoenergetic beam. Standard laboratory x-ray diffractometers use a copper target and nickel filter to produce monoenergetic copper *Kα* characteristic x-rays of energy 8 keV. This low energy is not suitable for imaging of thick samples due to its small penetration depth. Alternatively, filters may be chosen to filter a standard tungsten x-ray tube to create a narrower spectral width, though not completely monoenergetic (as demonstrated by [108]); however Bragg law interference conditions will be met by a range of scatter angles leading to a blurring out of the diffraction peaks. A compromise must be made between the increase in x-ray fluence and the degradation of momentum transfer resolution this will produce.

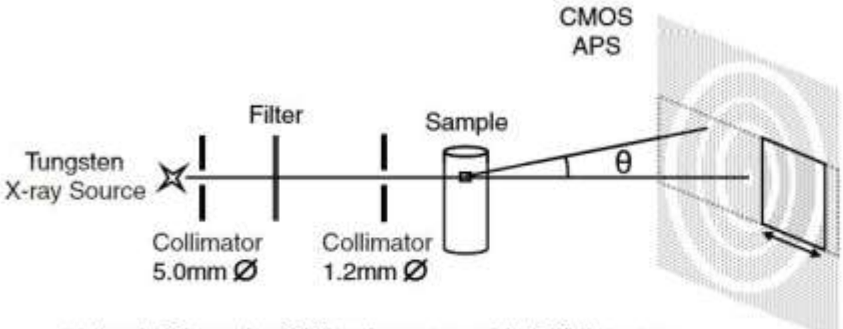

(a) Angle Dispersive Diffraction setup with APS detector

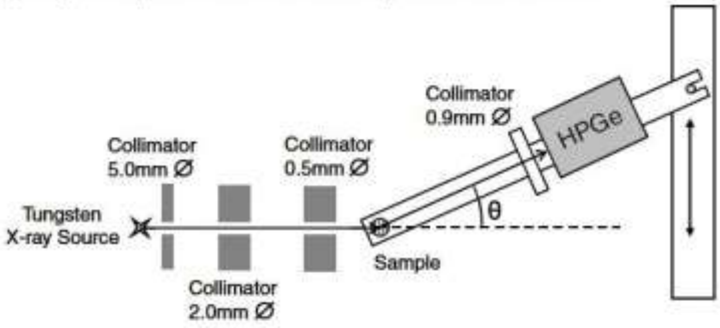

(b) Energy and Angle Dispersive Diffraction setup with HPGe detector

Figure 75 EDXRD and ADXRD experimental set-up using a HPGe detector and CMOS sensor respectively [108].

4.7.2 The role of x-ray diffraction in tissue discrimination

Knowledge of scatter cross sections and momentum transfer values of scatter peaks assists in the design of diffraction systems in terms of optimising x-ray energy and scatter angle. The literature contains measured form factors and coherent scatter coefficients for a range of materials relevant to this project.

Kidane et al. (1999) examined 100 breast tissue samples (including adipose, fibrosis, fibroglandular, benign, fibrocystic change, fibroadenoma and carcinoma) using the EDXRD technique [41]. Figure 76 presents the linear differential scatter coefficients of normal breast tissue and breast carcinoma as measured by Kidane *et al*.

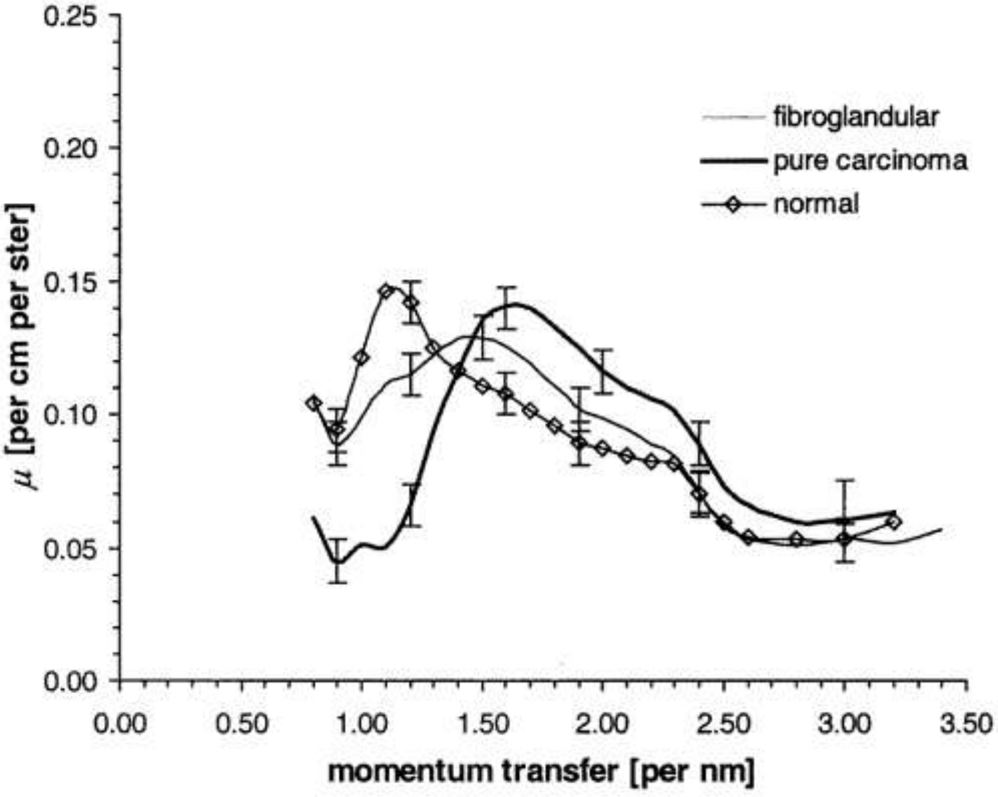

Figure 76 Comparison of the scatter signatures for the 'pure' carcinoma sample with that of both normal *breast tissue (50:50 fat/fibrous mixture) and a pure fibroglandular sample* [41].

Poletti *et al* (2002) used ADXRD and examined both healthy (glandular and adipose) and cancerous breast tissue [109]. Both studies agreed that x-ray signatures of adipose show a relatively sharp peak at momentum transfer 1.1 nm^{-1}, whereas carcinoma showed a broader peak at a higher momentum transfer value of 1.6 nm^{-1} with a lower intensity due to the reduction of structural order in cancerous tissue.

4.7.2.1 Role of XRD techniques in collagen measurement

Collagen is the main protein of connective tissue in the human body with more than 20 different collagen types identified so far [91]. Collagen molecules are rod-shaped approximately 300 nm long and 1.5 nm wide. Fibrils (collagen molecules packed into an organised overlapping bundle) have a characteristic periodicity of 65 nm (referred to as the d-spacing) [91].

It is known that the extracellular matrix (ECM) components of the breast degrade in the presence of malignancy, with collagen undergoing significant structural alterations on the nano-scale [110], [111], [112]. Collagen may also have a significant role in both metastasis [113] and cancer invasion. Cancer invasion is associated with the destruction as well as synthesis of collagen matrix proteins. Invasive carcinoma cells migrate along collagen strands and the invasive tumour front is rich in loose newly formed fibrils [114].

Small angle x-ray diffraction (SAXS) has been used as a contrast mechanism showing the structural differences in collagen between normal and cancerous tissue [114], [112]. This technique uses synchrotron radiation and much lower scattering angles than used in the measurements performed throughout this project. The scattering pattern results from the size, shape and ordering of large structures with typical distances 100 to 10,000 times the distances between neighbouring atoms (length scales from 10 to 1000 nm). The SAXS patterns were analysed in terms of intensity and position of reflections resulting from the axial period, orientation and diameter of fibrils. Ordered collagens were found in benign tumours and far away from malignant regions, whilst poorly ordered collagens were found in invaded tissue. Scattering intensity was greater for areas invaded by cancer indicating that the supra-molecular structure breaks down into smaller structures which have a larger specific surface area. Small but distinctive differences in axial period (d-spacing) was found; where the collagen was embedded in invaded adipose tissue or near a necrotic region the axial period was found to be 65.3 ± 0.2 nm, whereas the period in benign tumours or healthy connective tissue was 65.0 ± 0.1 nm. Necrotic areas were found to have no trace of ordered collagen, but do contain molecular coils [114].

Round et al. (2005) used a laboratory-based diffractometer instead of synchrotron radiation to collect SAXS data from cancerous and non-cancerous breast tissue [115]. The data were analysed using multivariate analysis (MVA), a statistical technique applied to complex systems (e.g. a biological system) for which each measurement holds many aspects of the object.

It can be inferred from the literature that XRD does have a role in identifying tumour from healthy disease, and that there is a role for small angle XRD in measuring collagen structure as an indicator of tumour state. Therefore it is proposed that a combined XRF/XRD system could be useful.

4.7.3 The role of x-ray diffraction in distinguishing bio-phantom tissue

The role of XRD techniques in distinguishing components of the bio-phantoms developed in Chapter Three has been considered.

4.7.3.1 Measurement of diffraction signals from bio-phantoms

In order to determine if there is a diffraction signature difference between the biological components of the research samples, a series of diffraction measurements were made using the diffractometer at the B16 beamline at the Diamond Light Source, UK.

The beam was set to 15 keV (to meet the requirements of an XRF system) and a beam size 0.8 mm high and 4.0 mm wide was set to fully illuminate the sample. The samples were contained in a 5 ml bijou pot made of low scattering plastic. The samples consisted of: (i) set collagen type I hydrogel, (ii) 3T3 cells embedded in collagen and (iii) water. The samples were made using a standard 3D cell culture technique [92]; refer to Section 3.4 for further details of the samples.

Measurements were made between scatter angles 3.5° – 35° in 0.5° steps to cover the momentum value range of interest for soft tissue. Each scatter angle was measured over 20 s. Momentum transfer calibration was performed by scanning a water sample of known diffraction peak at 1.6 nm^{-1}.

The measured diffraction signatures are displayed in Figure 77. The diffraction signatures were measured to a level of accuracy needed to provide the necessary information required at this stage (i.e. to determine if there is a diffraction signal for the phantom components, and if there is any difference in this signal between the components). No attenuation correction has been applied to account for different x-ray path lengths over the range of scatter angles.

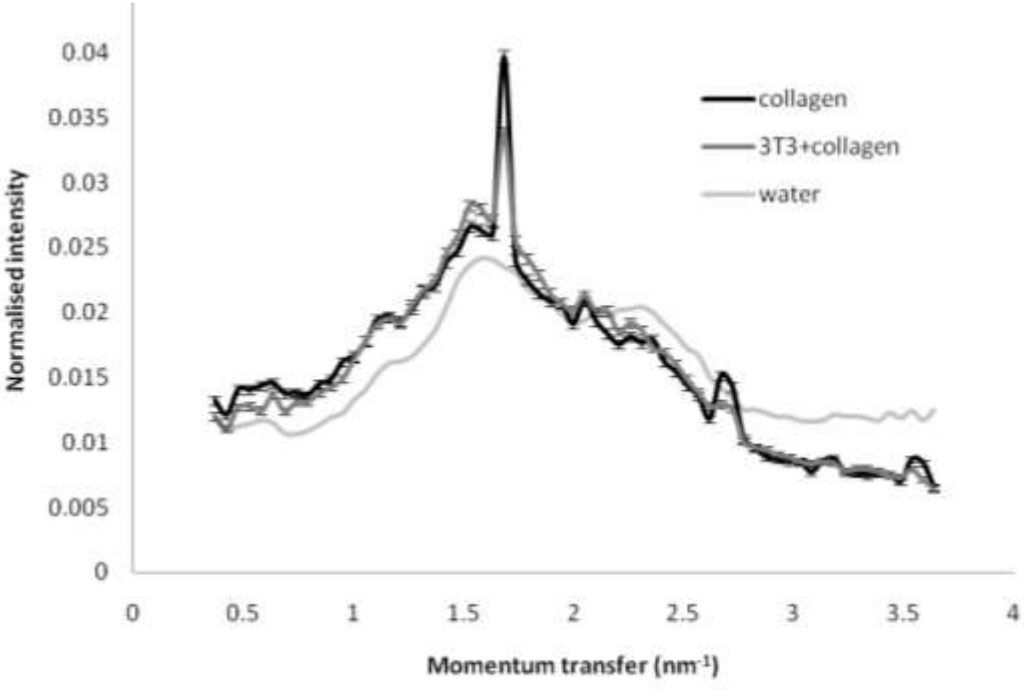

Figure 77 Measured diffraction signatures of the collagen type I hydrogel, with and without 3T3 presence, and a water sample. Detected counts were normalized to the total sum of all counts in the spectrum. No attenuation correction for x-ray path length through the sample has been made.

Figure 77 illustrates a strong diffraction peak at 1.68 nm^{-1} for the two collagen samples (both with and without 3T3 cells). This peak is not present in the water sample. Therefore, it is thought that this peak may be due to collagen type 1 presence, and its sharpness indicates a non-amorphous, well structured material. There is a difference in this peak intensity between the two collagen samples; it is proposed that this intensity difference is due to different collagen densities in the measurement volume. Further measurement is required to confirm this. It can be seen that each sample measurement shows a contribution from water; water is a main constituent of the collagen gel and so this result is expected.

A second set of diffraction measurements was performed at the Elettra synchrotron source, Italy, in order to compare the diffraction signals of HT29 cells and 3T3 cells. The cells in each sample were embedded in a collagen type I hydrogel, using the procedure outlined in Section 3.4.7. The cell phantoms are not completely representative of tissue found *in vivo*. They form a simplified model of human tissue in which only one cell type is present in the measurement volume. A major difference between the bio-phantoms and real tissue is the ordering and distribution of the cells; cells in human tissue are distributed according to the function of the cell, e.g. endothelial cells line up to form sheets. This structure is not present in the bio-phantoms, and cells are uniformly embedded into the pores of the collagen type I gel. However, the elemental composition of the cells should be representative of *in vivo* tissue. This set of phantoms has a low collagen density, being composed of ~ 0.4% collagen (by percentage weight), not having undergone the plastic compression as outlined in Section 3.4.10, which is more than an order of magnitude lower collagen density than typically found in tissue. The water content (> 99% by percentage weight) is therefore much greater than that expected *in vivo*. The cell density is also a lot less than that found *in vivo* and so will result in a weaker diffraction signal from the cells, with a greater contribution from water than if an *ex vivo* sample was being investigated.

A parallel polycapillary optic (model 72MLS of channel size 30 μm) was coupled to the SDD to provide a high angular resolution in the measurement system. This optic has previously been characterised to have an angular acceptance of 0.14° at 16.5 – 18.5 keV [45]. The SDD was mounted on a swinging arm that rotated about the sample, defining the scatter angle. An angular range of 11 – 26° was covered in 1° steps; this covered the momentum transfer range of interest at the incident x-ray energy setting of 15 keV.

The data was corrected as follows: (i) an ionisation chamber reading corrected for fluctuations in beam intensity at each scatter angle, (ii) each signature was normalised to the total number of counts in each spectrum. No attenuation correction was applied, nor sample holder subtraction performed. It was decided not to perform the latter as no attenuation correction has been applied and so the measured contribution from the pot could not be directly stripped from each sample signal. Furthermore, a thin walled low Z container was used and so the contribution from the pot was small. The results are displayed in Figure 78.

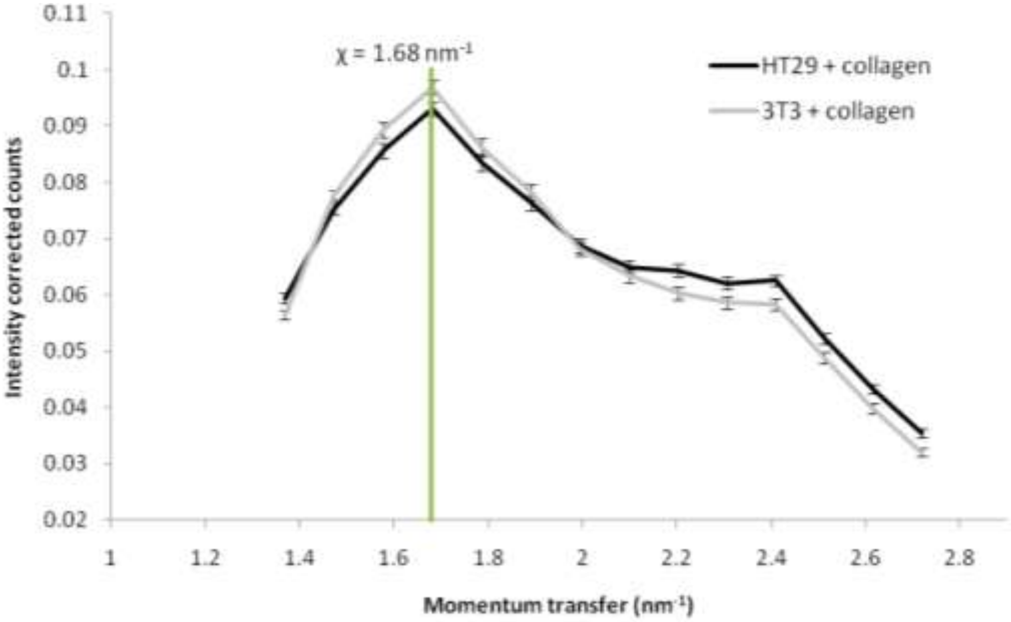

Figure 78 Measured diffraction signatures of biological phantoms composed of HT29 and 3T3 cells embedded in a collagen matrix. Each data point was normalized to incident beam intensity measured using an ionization chamber, and each profile normalized to the integral sum of counts for each spectrum. No attenuation corrections or empty pot subtraction were performed.

Both samples show a diffraction peak at momentum transfer value 1.68 nm^{-1} corresponding to the collagen peak. The measurements suggest there is a measurable difference between the signatures of 3T3 and HT29 cells, with the HT29 sample being more scattering between 2.1 – 2.4 nm^{-1}, and less scattering at lower momentum transfer values. It can be inferred from this result that the diffraction signature can be used to distinguish the different cell type components in future research samples.

4.7.3.2 Discussion

A literature review of clinical uses of XRD has presented a clear answer to Question 1: XRD does indeed have a role in tissue discrimination. Literature reports that the XRD signatures of healthy and tumour tissue are sufficiently different to enable the tissues to be distinguished. The XRD measurement performed in Section 4.7.3.1 highlights the potential use of the diffraction signal thought to be from collagen (at x = 1.68 nm^{-1}) for clinical applications. It can be inferred from the literature discussed in Section 4.7.2.1 that there is a role for XRD in measuring collagen as an indicator of tumour state. It is recommended that further work is undertaken to develop bio-phantoms that mimic collagen structural differences found between tumour and healthy tissue through use of tissue engineering techniques and 3D live cultures (refer to Section 3.4.10 for a discussion of such tissue engineering techniques). XRD measurement of the phantoms will investigate the sensitivity of our XRD technique in measuring collagen structural changes.

In answer to Question 2 asked in Section 4.7, no firm conclusions can be made at this stage as to whether XRD can be used to distinguish bio-phantom components under imaging conditions; the differences between XRD signatures are measurable but small. Further work should be undertaken in order to quantify the difference in XRD signals between the sample components. It would be beneficial to measure the diffraction signatures of cultured cells before being embedded in collagen in order to understand the contribution from each sample component.

4.7.4 XRD measurement of GNP samples

There are many XRD measurements covering a range of sizes of GNPs (between 0.8 – 20 nm in diameter) present in the literature, all measured using the copper $K\alpha$ line (8 keV) [116], [117], [118]. All groups are in agreement with a main GNP diffraction peak at 38°, i.e. a momentum transfer value of 2.1 nm^{-1}. This peak corresponds to the (111) d-spacing of gold [116].

The diffraction signature of a high concentration 1.9 nm GNP-DIW solution (8 mgAu/ml) was measured at the Elettra Synchrotron source, Italy, and compared to the XRD signature from water. An incident x-ray energy of 15 keV was selected to assess the XRD signal that is induced at the energy used in the XRF system. The same measurement procedure as described in Section 4.7.3.1 was used. An angular range of 11 – 25° was measured in 1° steps; this covered the momentum transfer range of interest. Figure 79 displays the measured diffraction signals.

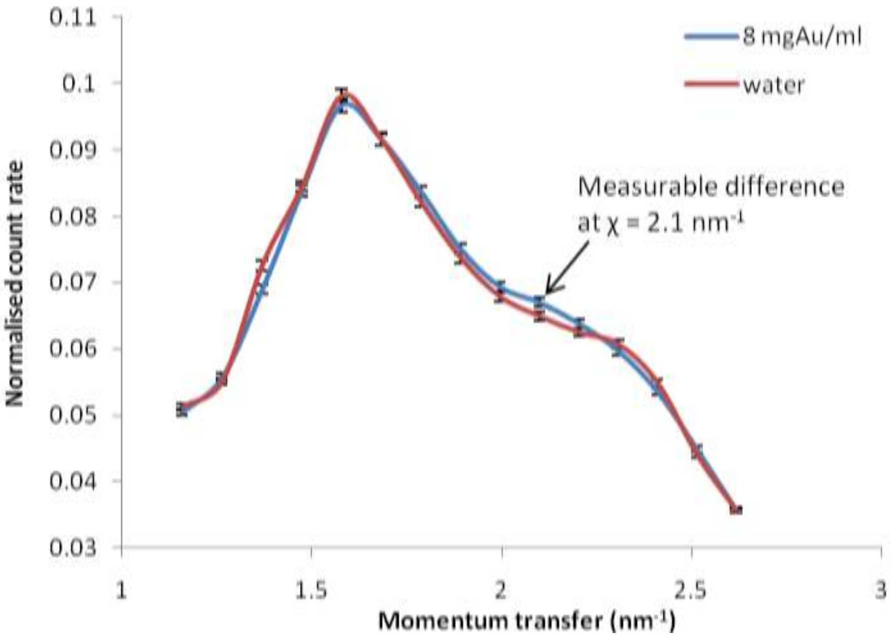

Figure 79 Measured diffraction signature of an 8 mgAu/ml GNP sample and water. The measured count rate was normalized to the integral sum of the whole spectrum.

Figure 79 displays a peak at 1.6 nm^{-1}; this corresponds to the known momentum transfer of water. There is a slight but measurable difference of 3.1% (greater than the percentage error of < 1%) between the diffraction signals of water and GNP solution at the expected GNP momentum transfer value of 2.1 nm^{-1}.

4.7.4.1 Discussion

We have demonstrated a small (but still measurable) difference of 3.1% between the diffraction signals of water and GNP solution at the expected GNP momentum transfer value of 2.1 nm^{-1}. This indicates that there is a diffraction signal from the 1.9 nm GNPs, but it is very slight and will lessen at lower GNP concentrations. The literature reports that the strength of the XRD signal is proportional to the size of the NP, with larger NPs having a higher degree of crystallinity and therefore a stronger

XRD signal [119], [120]. Smaller NPs have a larger surface area / volume ratio, and atoms at the particle's surface are not as densely packed as those in the core of the particle [119]. Figure 80 displays the broadening of the gold XRD peaks due to the loss of structural order at lower GNP sizes.

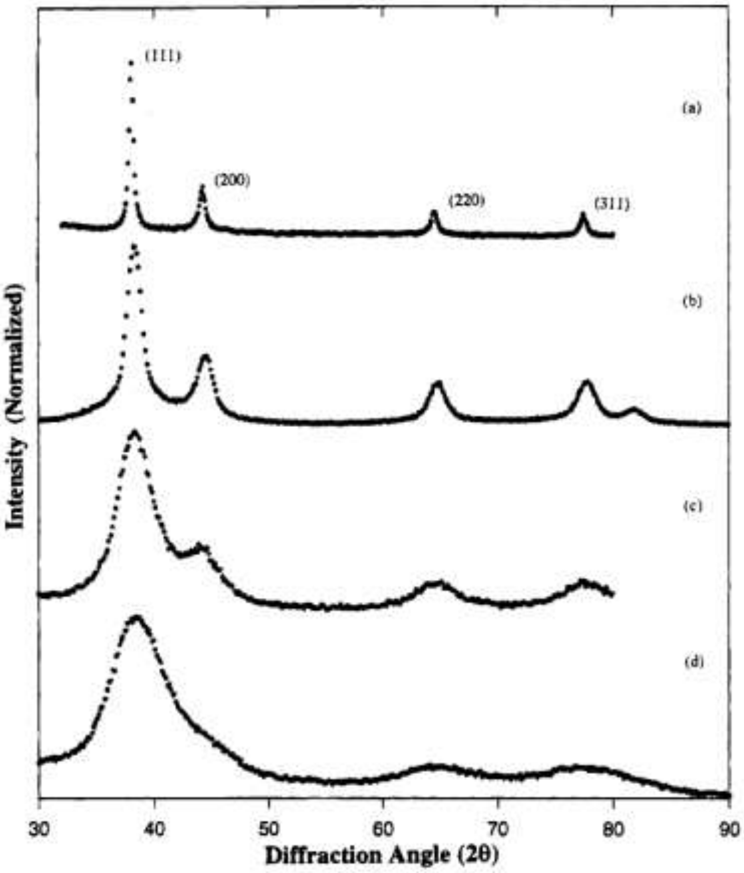

Figure 80 XRD spectra for four different GNP sizes: (a) 20.2 nm, (b) 6.8 nm, (c) 3.0 nm and (d) 1.6 nm. Spectra were measured using the copper Kα line. The main GNP peak occurs at x = 2.1 nm^{-1}*. Figure taken from* [120].

Literature suggests that GNPs of a size less than 2 nm are structurally disordered and their atomic arrangements exhibit amorphous-like rather than crystallographic features [120]. This explains why the measured XRD signal from 1.9 nm GNPs is so small.

In answer to Question 3 posed in Section 4.7, two useful conclusions may be made from these measurements:

- The XRD signal from GNPs is small and will not contribute much information to imaging GNP concentrations in a combined XRF/XRD system.
- The XRD signal from the GNPs is at a momentum transfer value that is significantly different to those of interest in the biological tissue components, and so will not interfere with XRD measurement of tissue.

If larger GNPs were used in future work, the first conclusion may not apply; it is expected that the XRD signal increases with GNP size, and may then contribute a useful signal to the combined technique.

4.7.5 Towards the design of a combined XRF/XRD system

A multi-modality XRF/XRD system has been proposed to acquire images sensitive to GNP concentration and distribution and tissue type The system requirements for measuring XRF and XRD signatures of tissues embedded with GNPs will be outlined, proceeding to a discussion of feasibility of the combined system.

4.7.5.1 Limitations of previous systems

Current fixed angle scattering systems produce 2D images by raster scanning a narrow pencil beam across the sample. This limits the speed of image acquisition. The speed has been increased by using a multiple parallel holed mechanical collimator, displayed in Figure 81 [121].

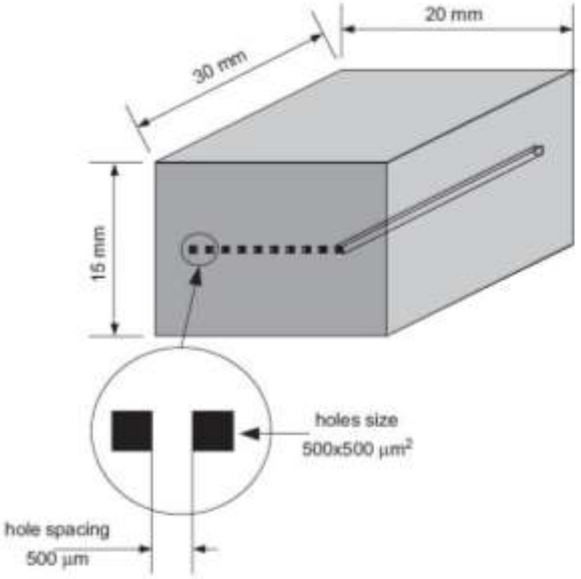

Figure 81 Schematic diagram of a multi-hole mechanical collimator [121].

The achievable spatial resolution is governed by the size of the pencil beam incident on the sample and the size of the scatter collection area, which in turn is dictated by the collimator hole size (of the order of 500 µm). Systems using mechanical collimators therefore do not benefit from the smaller pixel sizes of currently available imaging detectors (~10 µm). An XRD system design consisting of polycapillary optic technology overcomes these limitations.

Two novel fixed-angle x-ray scatter imaging systems with multi-momentum transfer capability were developed by Politecnico di Milano (our collaborators on this project) making use of the SDD and CDD module coupled to a parallel polycapillary optic [46], [122]. The systems featured improved spatial resolution through use of the optic, and spatial resolution was limited by the detector pixel size and not collimator hole size. The CDD, having spectroscopic resolution, enables use with both monoenergetic and polyenergetic sources, making the system translatable from synchrotron sources to a bench-top source. Simultaneous acquisition of images at multiple momentum transfer value is also possible enabling images of different tissue types to be acquired concurrently to assist tissue identification.

4.7.5.2 Spatial resolution of the system

The dimensions of the scatter volume are related to the incident collimated beam size Δx, the detector-collimator resolution Δd (the sum in quadrature of the hole size of the scatter collection collimator Δc and the detector pixel size Δp (Equation 16)), and the scatter angle θ as illustrated in Figure 82:

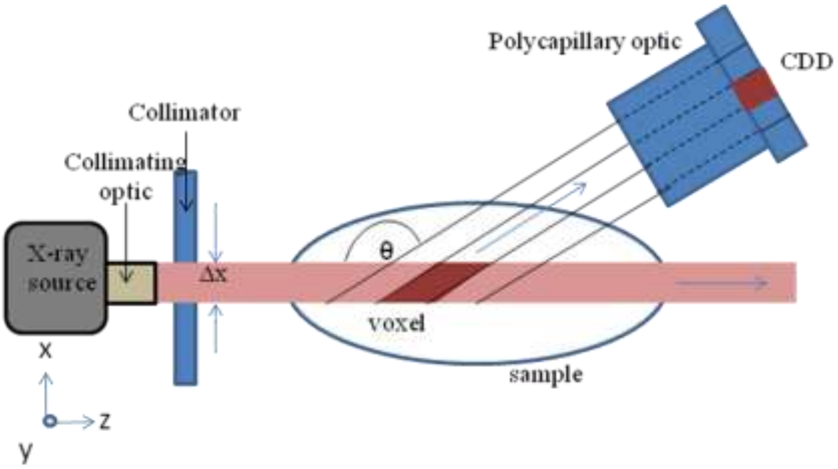

Figure 82 Voxel size of image produced by polycapillary optic system. The sample may be scanned in the x-direction to produce data required for a 3-D image.

The red beam indicates an image slice of the system. The voxel size in the y direction is Δd, in the x direction is Δx, and in the z direction (describing the voxel depth in the direction of the beam) is:

$$\Delta z = \frac{\Delta d}{\sin\theta} + \frac{\Delta x}{\tan\theta} \qquad \text{Equation 15}$$

where

$$\Delta d = \sqrt{\Delta c^2 + \Delta p^2} \qquad \text{Equation 16}$$

The improvement in spatial resolution resulting from the use of a polycapillary optic rather than a mechanical collimator has been calculated. For example, a collimator with 500 μm hole size collecting at scatter angle 6° and a beam size of 500 μm, using the CDD module of pixel size 182 μm results in a voxel size of 500 μm x 532 μm x

9847 μm. Replacing the scatter collection collimator with a polycapillary optic of channel size 5 μm improves the spatial resolution to 500 μm x 182 μm x 6498 μm; an improvement of 66% in the y direction and 34% in the z-direction. In order to reduce the voxel size even more, the incident beam size may be reduced to shrink the voxel depth along the length of the beam. This will also lessen the partial volume effect (the impact of the partial volume effect on tissue discrimination was discussed in Section 4.1.3).

4.7.5.3 Momentum transfer resolution

Tissue discrimination depends on momentum transfer resolution. The resolution is a combination of the x-ray source spectral width (or energy resolution of the detector) ΔE for an ADXRD (or EDXRD) system respectively, and the angular resolution of the system:

$$\frac{\Delta\chi}{\chi} = \sqrt{\left(\frac{\Delta\theta}{\theta}\right)^2 + \left(\frac{\Delta E}{E}\right)^2} \qquad \text{Equation 17}$$

The angular resolution of the system is given by the Equation 18:

$$\frac{\Delta\theta}{\theta} = \frac{\theta_{\max} - \theta_{\min}}{\theta} \qquad \text{Equation 18}$$

where θ is the nominal scatter angle, and θ_{max} and θ_{min} are the maximum and minimum scatter angle respectively through which a photon can be scattered and still reach the detector (Figure 83). The angular resolution can be greatly improved by replacing a mechanical collimator with a polycapillary optic angular filter. To illustrate this, θ_{max} and θ_{min} have been calculated geometrically for a mechanical collimator set up:

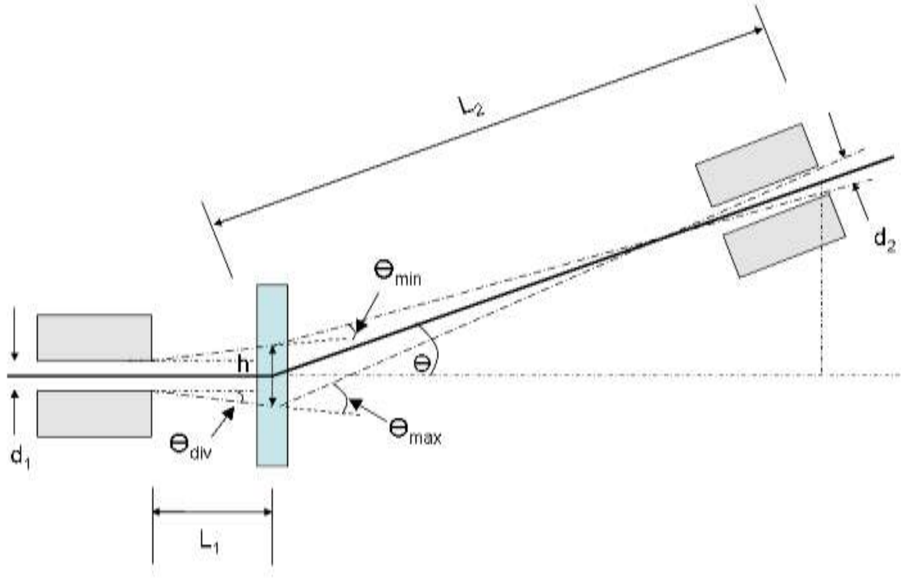

Figure 83 Schematic of general XRD system, used to calculate the momentum transfer resolution components [123].

$$\theta_{\max} = \tan^{-1}\left[\frac{[L_2 - \frac{d_2}{2}\tan\theta]\sin\theta + \frac{h}{2} + \frac{\frac{d_2}{2}}{\cos\theta}}{L_2\cos\theta - \frac{d_2}{2}\sin\theta}\right] + \theta_{div} \qquad \text{Equation 19}$$

$$\theta_{\min} = \tan^{-1}\left[\frac{[L_2 + \frac{d_2}{2}\tan\theta]\sin\theta - \frac{h}{2} - \frac{\frac{d_2}{2}}{\cos\theta}}{L_2\cos\theta + \frac{d_2}{2}\sin\theta}\right] - \theta_{div} \qquad \text{Equation 20}$$

where $h = 2L_1 \tan\theta_{div} + d_1$ Equation 21

d_1 and d_2 are the primary and secondary collimator diameters

l_1 is the primary collimator exit to sample distance

l_2 is the sample to secondary collimator exit surface

The effect of each system parameter has been theoretically calculated, and the results shown in Figure 84. In summary:

1. Doubling d_1 increases (worsens) angular resolution by a factor of ~ 1.04 - 1.1
2. The same is true for d_2
3. Doubling the angle of divergence increases (worsens) angular resolution by a factor of ~ 1.8
4. Doubling L_1 increases (worsens) angular resolution by a factor of ~ 1.05 – 1.1
5. Doubling L_2 decreases (improves) angular resolution by a factor of ~ 0.8

The angular acceptance of the mechanical collimator shown in Figure 81 has been calculated to be 1.9°, whereas the angular acceptance of a polycapillary optic has been measured as 0.2° (see Section 4.5.4); this corresponds to a 9.5 times improvement in angular acceptance on using the optic.

The achievable momentum transfer resolution values have been estimated for each XRD system using Equation 17 at the momentum transfer value of breast carcinoma (1.6 nm^{-1}): (i) optic coupled to CDD (Δx = 0.1 nm^{-1}), (ii) optic coupled to SDD (Δx = 0.06 nm^{-1}).

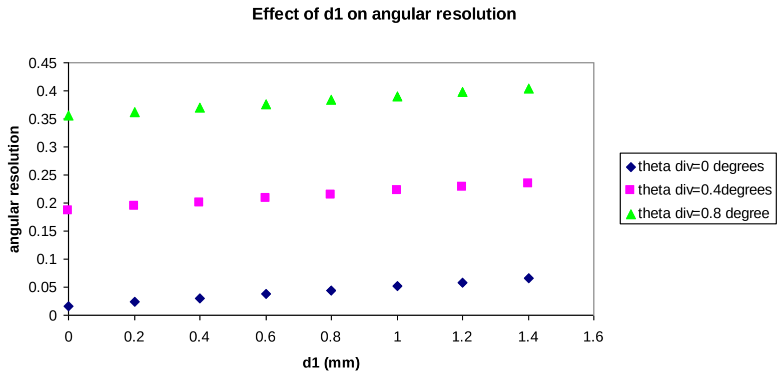
Effect of d1 on angular resolution

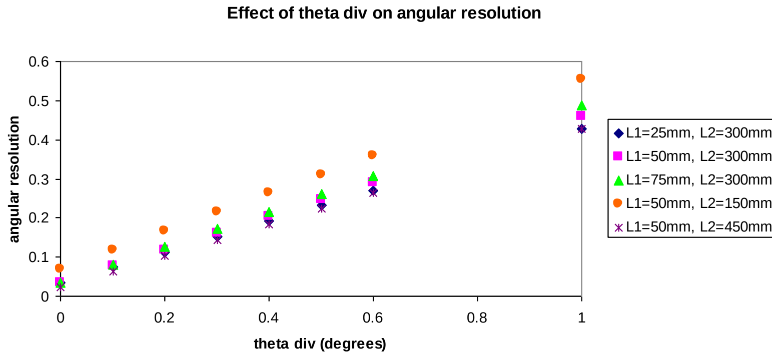
Effect of theta div on angular resolution

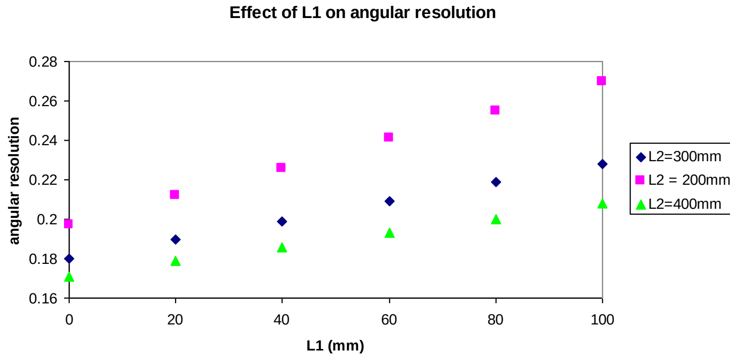
Effect of L1 on angular resolution

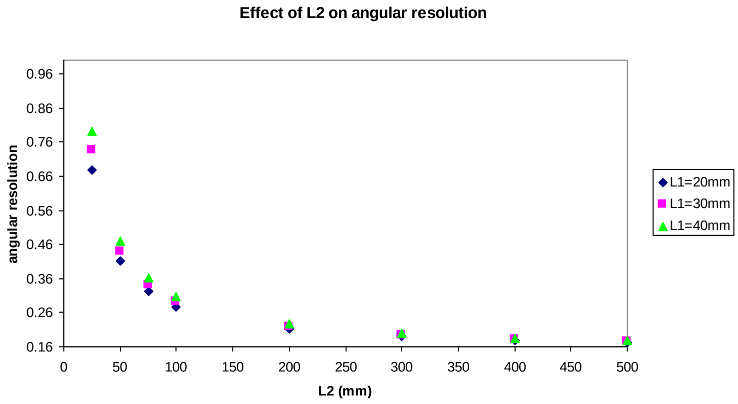
Effect of L2 on angular resolution

Figure 84 Effect of collimator width (d1 and d2), angle of divergence, L1 and L2 on angular resolution.

4.7.5.4 Discussion

The previous sections have outlined some thoughts towards the design of a novel XRF/XRD system. The combined system will enable imaging of GNP distribution and discrimination of tissue type using XRF and XRD techniques respectively. The clinical need for a system that is sensitive to sub-clinical disease with the ability to distinguish cancer from healthy tissue and measure GNP concentration was introduced in Section 1.3. The novel system was designed in answer to this clinical need; the estimated resolution capabilities are better than those of systems present in the literature. A high spatial resolution will act to reduce the partial volume effect to enable discrimination of tissue type and GNP concentration over smaller volumes. Preliminary calculations and measurements have demonstrated that use of a polycapillary optic can improve spatial resolution by up to 66% compared with use of a mechanical collimator. The achievable spatial resolution is a function of scatter angle, incident beam thickness and collimator – detector pixel area. Further work is needed to select the optimum scatter angle. This will involve:

(i) Consideration of voxel size (which reduces with angle).

(ii) Reduction of the Compton background beneath the XRF signal. XRF is isotropic whereas Compton scatter is at a minimum at 90º. This is achieved at high scatter angles.

(iii) Increasing the detection of coherent compared with Compton scatter. Coherent scatter is forward peaked whereas Compton scatter can be considered more uniformly distributed at low angles. This is achieved at low angles.

Use of a polycapillary optic also improves the momentum transfer resolution by a factor of ten compared with a mechanical collimator system. The momentum transfer resolution of two systems has been calculated to be 0.1 nm^{-1} and 0.06 nm^{-1} for the optic coupled to the CDD and SDD respectively. Using breast tissue as an example, the main coherent scatter peaks of healthy and carcinoma are found at momentum transfer values of 1.1 nm^{-1} and 1.6 nm^{-1} respectively. It can be concluded that the peak *position* of these tissues can be discriminated using either proposed XRD system. Even if the actual peak positions of tissue to be discriminated have a momentum transfer difference less than the momentum transfer resolution of the system it may still be possible to differentiate them providing the spectral shape differs. Spectral shape can potentially be used as a measured parameter in this system by virtue of the fact that it has both energy and position information.

The peak positions of an artificial cancer mass (x = 1.6 nm^{-1} from [41]) and collagen type I gel (thought to be x = 1.68 nm^{-1} from measurement) have a peak separation of 0.08 nm^{-1}. The CDD cannot achieve this, even when used with the polycapillary optic, whereas the superior energy resolution of the SDD may be able to achieve this. However, the spectral shape parameter could mean that differentiation is possible with both systems.

The incident x-ray spectrum (considering both energy and intensity) affects the scatter signature in the following ways: (i) the position of the peak (energy dependence of scatter), (ii) peak height (intensity of scatter) and (iii) peak width (spectral shape). Section 2.5.5 introduced the concept of using filters to shape the beam produced by an x-ray tube.

As discussed in Section 2.4.1.1 the ideal beam for XRF measurements would have a narrow spectral width and high intensity. The spectral width required for XRD measurements is different for each diffraction mode:

1. ADXRD requires a near-monoenergetic beam, such as a synchrotron or molybdenum filtered bench-top source.
2. EDXRD requires a spectral width wide enough to cover the momentum range of interest (i.e. the momentum range where there is a maximum difference in scatter intensity between gold and carcinoma). It is beneficial to select as narrow a spectral width as possible to (i) reduce the number of low energy x-rays not contributing to the useful scatter information but contributing to dead time losses of the detector, (ii) reduce the number of higher energy x-rays not providing useful scatter information but

contributing to the Compton scatter background that degrades the useful signal.

In choosing the ideal incident spectrum for a combined system, the coherent scatter peak positions and intensities of tissue types to be distinguished must be considered, in addition to XRF excitation energies of gold. For ADXRD measurements, an energy giving the greatest difference in scatter angle between the materials being measured should be selected. For EDXRD, a fixed scatter angle should be used that brings about the greatest difference in scatter energy (to increase the separation of the scatter peaks on an energy-axis with a separation greater than the energy resolution of the detector).

In order to find the mean energy giving the greatest difference in scatter angle between healthy breast (x=1.1 nm^{-1}) and carcinoma (x=1.6 nm^{-1}), calculations of energy and scatter angle at these values of x have been performed. The result is illustrated in Figure 85, and shows that the largest scatter angle distinction between healthy tissue and carcinoma can be found at mean energies below 30 keV. For EDXRD measurements, it can be seen that a fixed scatter collection angle below 5° brings about the greatest difference in scatter peak energy between healthy tissue and carcinoma. To excite the gold L-lines (requiring a beam energy above 13.7 keV) a fixed scatter angle of 15° and a filtered beam ranging from ~ 10 - 16 keV x-rays will produce healthy tissue and carcinoma peaks separated by 4.7 keV, which is easily resolvable by the CDD and SDD.

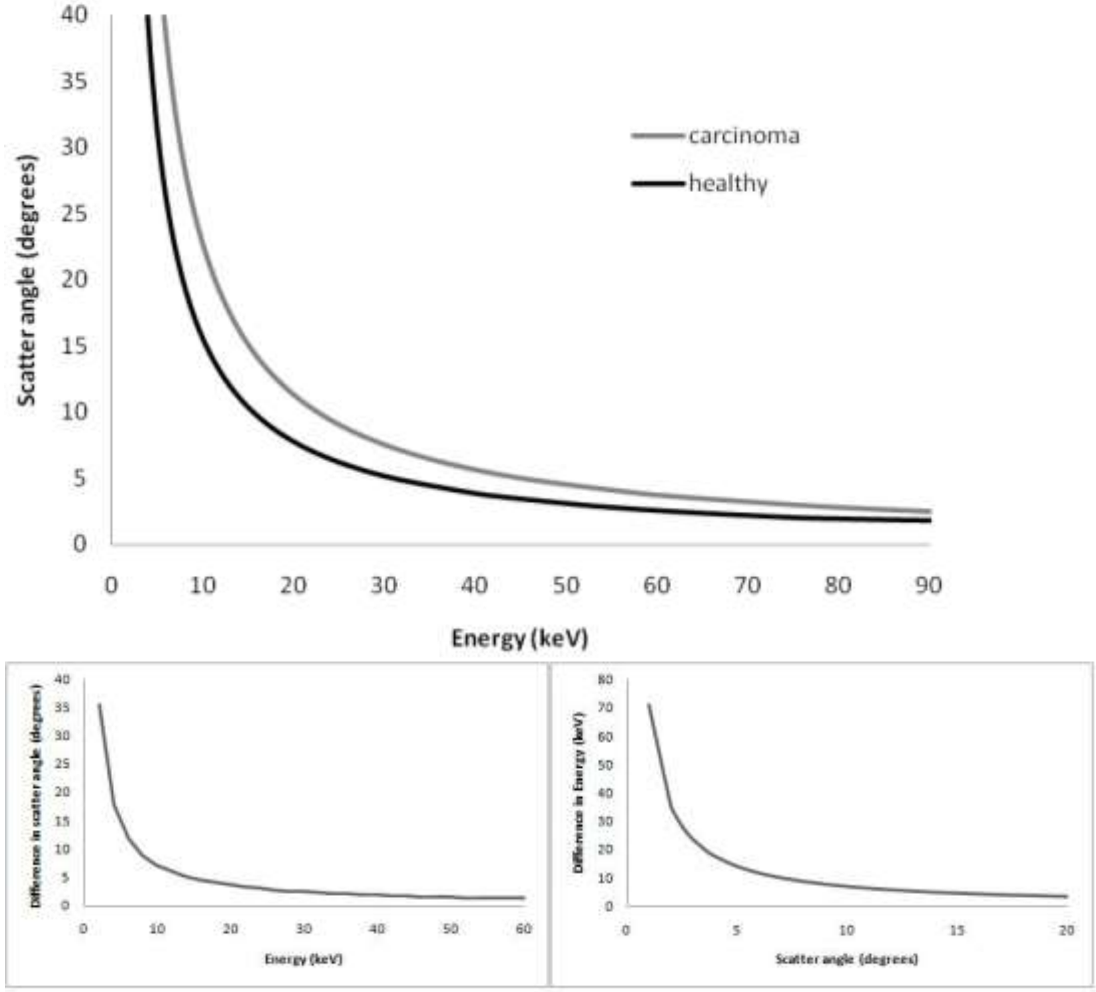

Figure 85 Top: Calculated values of constant momentum transfer for healthy breast (x=1.1 nm^{-1}) and breast carcinoma (x =1.6 nm^{-1}): the plot illustrates that the greatest difference between healthy tissue and carcinoma occurs at low energies (below 30 keV). Bottom left: Calculated scatter angle difference between healthy breast and carcinoma over a range of energies. Bottom right: Calculated energy difference of healthy breast and carcinoma coherent scatter peaks over a range of scatter angles.

There are two proposed possibilities for the format that a combined system could take:

(i) *Using two separate spectrometer arms to simultaneously measure XRF and XRD:* One arm optimised for XRF measurement will be set at 90º (using one of the imaging modules demonstrated in Section 4.4 and 4.5). The other arm will be set at an optimum scatter angle for XRD detection, using either the CDD or SDD coupled to a parallel polycapillary optic.

(ii) *Using one spectrometer arm to simultaneously measure XRF and XRD:* This will involve either the SDD or CDD coupled to a parallel polycapillary optic to gain both XRF and XRD signal from the same spectra. An optimum scatter angle should be selected to gain sufficient XRF and XRD signal as discussed above. Placing the spectrometer at angles less than 90º will act to reduce the XRF signal to background ratio, and use of the optic will result in signal loss due to losses in transmission. To demonstrate this effect, preliminary measurements were made of an 8 mgAu/ml sample in typical XRF (90º, no optic) and XRD (11º, with parallel optic) geometries. Figure 86 displays the measured spectra for each geometry.

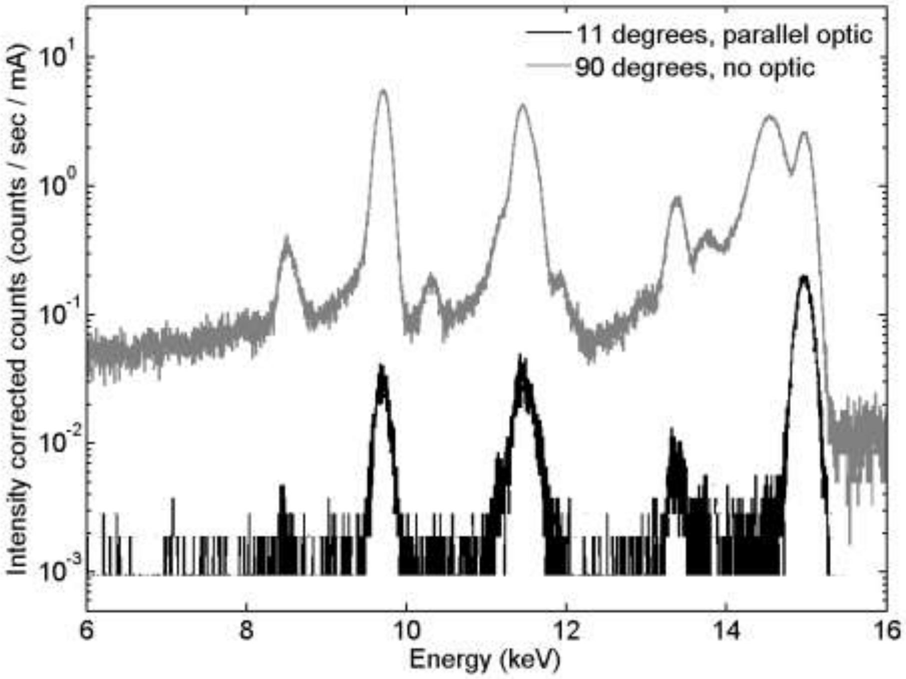

Figure 86 Emitted x-ray spectra of an 8 mgAu/ml sample measured in two different geometries: (i) in optimum XRF geometry (90º with no optic) acquired over 60 s, and (ii) in a typical XRD geometry (11º with a parallel optic) acquired over 240 s. Both spectra have been corrected for acquisition time and measured incident beam intensity to enable comparison.

It can be seen that measurement in typical XRD geometries reduces the gold XRF signal by over two orders of magnitude. It can be inferred that the sensitivity and detection limit of GNP concentration measurement will be worsened using XRD geometries, and so the two-arm system would be a better technique. However, further work is required to investigate methods to fully optimise a one-arm system in terms of detection angle.

4.7.6 Summary of key ideas

The latter half of this chapter has introduced the potential role of diffraction in a combined XRF/XRD system in order to image GNP concentration and distinguish tissue type simultaneously. Design aspects of the system have been considered, and capabilities of the proposed system have been estimated through preliminary measurements. In summary:

- There is a strong role for XRD in tissue discrimination (in particular between healthy and cancerous tissue as reported in the literature), enabling potential application for our purpose.

- GNP presence does not provide a strong XRD signal, and will not interfere with XRD measurement of tissue. If larger GNP sizes are used in further work, this conclusion may not apply as larger GNPs give stronger XRD signals.

- Use of a parallel polycapillary optic can improve spatial resolution and momentum transfer resolution (both key in sensitivity to sub-clinical clusters of proliferating cells) by factors of 1.6 and 10 respectively (dependent on detection geometry). The estimated resolution capabilities are better than those of systems present in the literature.

- Calculations have demonstrated that the proposed systems will be able to discriminate between healthy and cancerous tissue. Further work is needed to determine if the systems can distinguish between components found in the bio-phantoms produced in Chapter Three.

- Two possible systems have been proposed consisting of (i) a one-arm spectrometer to simultaneously measure XRD and XRF from the same spectrum, and (ii) a two-arm system consisting of two spectrometers to separately measure the signals. The one arm system poses potential issues in reducing sensitivity to the XRF signal when in diffraction set-ups, and further work is recommended to fully optimise the set up to be sensitive to both signals.

4.8 Conclusions

Just as Chapter Two demonstrated the ability of the XRF technique to quantify GNP concentration, this Chapter has met its aim in showing that XRF can be used to acquire images of GNP distribution. An XRF spectrometer coupled to a polycapillary lens has been developed and used to prove the feasibility of performing energy-resolving imaging of GNP distributions at concentrations relevant for *in vitro* imaging of bio-phantoms and *in vivo* imaging for radiotherapy applications. Details of phantoms with concentrations as low as 0.025 mgAu/ml have been successfully imaged, with potential to image lower concentrations: Chapter Two demonstrated that the technique is sensitive to quantitative measurement of GNPs down to the detection limit of 0.005 mgAu/ml (further improvements to the detection limit were made in Chapter Three to a limit of 0.001 mgAu/ml). The feasibility of excitation of the whole specimen with a wide beam and detection of XRF x-rays with a 2D pixellated energy dispersive detector without scanning was shown. This system avoids step and scan techniques and so reduces the required measurement times. Through the results of both this chapter and Chapter Two, it can be inferred that quantitative imaging of GNP concentration is feasible providing the imaging system has been calibrated for GNP concentration measurement.

A novel combined XRF/XRD system was proposed to image both GNP concentration and discriminate tissue type (with sufficient evidence in the literature that XRD can discriminate between tissue types). The system proposed is a high performance XRD system, with excellent momentum transfer resolution (due to the angular resolution improvements through use of the parallel polycapillary optic compared with other systems reported in the literature using mechanical collimators). One can therefore infer its potential clinical use, but cannot quantify its ability to distinguish tissue without further work.

5 Conclusions

This thesis has made a contribution in terms of a research effort aimed at identifying suitable techniques to image bio-markers to provide a map of radiosensitivity in order to guide radiotherapy treatment dose prescription. In answer to the aims of this project, GNPs have been identified as a suitable bio-marker imaging contrast agent; they can be functionalised to be taken up by less radiosensitive cells, and then imaged using x-ray techniques. A novel L-XRF system (consisting of an SDD module) has been conceived and developed that is capable of quantitative detection of GNPs, with a linear relationship between GNP concentration and L-XRF signal found. Concentrations can be measured up to an accuracy of ± 0.005 mgAu/ml for systems using either synchrotron radiation or a bench-top x-ray tube as the exciting source. The linearity extends down to the detection limit of 0.001 mgAu/ml; a concentration that is an order of magnitude lower than concentrations found *in vivo* as presented in the literature (~ 0.01 mgAu/ml) [25]. Our novel L-XRF system therefore meets the requirements set out at the design stage. Our system has a detection limit that surpasses the sensitivity of other x-ray based techniques found in the literature [24], [38], and could be used in the future to answer the clinical need for radiotherapy imaging of clusters of infiltrating cells. The measured DL was found to be the same for both the synchrotron and bench-top sources, showing potential for this technique to be used in the clinic.

A K-XRF technique was also assessed, and its performance was found to be worse than for the L-XRF system, having 6.5 times less sensitivity than the L-XRF bench-top system, and a detection limit of 0.2 mgAu/ml. This can be attributed to lower photoelectric interaction probabilities at higher K-edge energies, and a higher spectral background contribution. The K-XRF technique is however less affected by overlying thickness, and so may have a future application in measuring thick samples containing high GNP concentrations.

Translation from 1D spectroscopic measurement to 2D imaging was achieved. An L-XRF spectrometer coupled to a polycapillary lens has been developed, and demonstrated feasibility in performing energy-resolving imaging of GNP distributions at concentrations relevant for *in vitro* imaging of bio-phantoms and *in vivo* imaging for radiotherapy applications. Details of phantoms with concentrations as low as 0.025 mgAu/ml have been successfully imaged, with potential to image lower concentrations (the L-XRF technique having a DL of 0.001 mgAu/ml). The feasibility of excitation of the whole specimen with a wide beam and detection of XRF x-rays with a 2D pixellated energy dispersive detector without scanning was shown. This system avoids step and scan techniques and so reduces the required measurement times. Both systems can achieve spatial resolution capabilities better than 1 mm (thus meeting the requirements for use in radiotherapy). It can be inferred that quantitative imaging of GNP concentration is feasible providing the imaging system has been calibrated for GNP concentration measurement. Further work is required to investigate methods to perform absolute quantitative imaging. This is not an easily solved problem, and will involve development of correction procedures for sample attenuation, consideration of partial volume effect and calibration techniques to gain absolute concentration information.

Novel bio-phantoms were engineered with GNP inclusions at concentrations that represent the clinical situation in order to demonstrate the XRF measurement technique in a more realistic case. GNP uptake in 3T3 and HT29 cells was demonstrated; it was found that using 1.9 nm GNPs and an incubation time of 24 hours gave sufficient GNP uptake. A second size GNP of nominal size 15 nm was found to barely be taken up by cells. TEM analysis confirmed that GNP uptake was achieved in both cell lines, through the mechanism of endocytosis. The L-XRF technique was then used to measure GNP concentration in the cells. The cells were embedded in a 3D scaffold (collagen type I matrix) using a standard technique [73]. Each sample contained a GNP concentration above the DL of the XRF system (> 0.001 mgAu/ml). GNP uptake was shown to be repeatable within measurement error. The XRF technique (a technique that doesn’t destroy samples) successfully measured GNP concentration in the cellular samples; it was found that GNP uptake increases with incubation dose. The percentage uptake of initial incubation GNP dose per million cells measured by the XRF system was found to range between 0.3 – 0.5% and 0.1 – 0.3% for the 3T3 and HT29 cell samples respectively. In an *in vivo* situation tumour cells will take up more GNPs than healthy cells due to leaky tumour vasculature and poor lymphatic drainage at tumour sites. TEM images qualitatively corroborated the XRF technique’s findings that uptake was proportional to initial GNP dose. The passive GNP uptake demonstrated here may be extended through functionalisation to meet the overall eventual aim of this project in using GNPs as a contrast agent to image the distribution of bio-parameters of a tumour. Uptake efficiency could be increased in the future by coating the GNPs in a protein taken up by the specific target cells. It was estimated that a 4 mgAu/ml incubation dose resulted in ~ 5 x 10^7 GNPs taken up per 3T3 cell. It was also estimated that the measured detection limit of the XRF system (0.001 mgAu/ml) enables ~ 1.4 x 10^{13} GNPs to be detected per cm^3. The number of cells that this corresponds to is dependent on incubation dose, and other factors that affect NP uptake such as surface properties and size of GNPs.

A set of artificial cancer mass phantoms were successfully constructed, building on the work previously undertaken [99]. This work was extended to produce a set of novel phantoms with GNP inclusions for XRF imaging. The samples will be imaged at the Diamond Synchrotron in the near future. The 3D cellular phantoms with GNP inclusions are planned to be used in future work investigating the dose enhancement effect of GNPs. Radiobiological studies will be performed on GNP-filled cells to determine the extent of the dose enhancement effect.

An extension study aimed at developing a novel combined XRF/XRD system to perform quantitative measurement of GNP concentrations and enable tissue discrimination will be undertaken in the near future. There is sufficient evidence in the literature that XRD can discriminate between tissue types. The system proposed is a high performance XRD system, with excellent momentum transfer resolution (due to the angular resolution improvements through use of the parallel polycapillary optic compared with other systems reported in the literature using mechanical collimators). One can therefore infer its potential clinical use, but cannot quantify its ability to distinguish tissue without further work.

6 Bibliography

[1] E. Hall, *Radiobiology for the radiologist, Lippincott Williams and Wilkins, Fifth Edition*. 2000.

[2] P. Vaupel, S. Briest, and M. Hockel, “Hypoxia in Breast Cancer: Pathogenesis, Characterization and Biological/Therapeutic Implications,” *Wiener Medizinische Wochenschrift*, vol. 152, no. 13-14, pp. 334-342, Jul. 2002.

[3] A. R. Padhani, K. A. Krohn, J. S. Lewis, and M. Alber, “Imaging oxygenation of human tumours.,” *European radiology*, vol. 17, no. 4, pp. 861-72, Apr. 2007.

[4] G. L. Semenza, “Targeting HIF-1 for cancer therapy.,” *Nature reviews. Cancer*, vol. 3, no. 10, pp. 721-32, Oct. 2003.

[5] K. A. Krohn, J. M. Link, and R. P. Mason, “Molecular imaging of hypoxia.,” *Journal of nuclear medicine : official publication, Society of Nuclear Medicine*, vol. 49 Suppl 2, p. 129S-48S, Jun. 2008.

[6] C. V. Dang and G. L. Semenza, “Oncogenic alterations of metabolism.,” *Trends in biochemical sciences*, vol. 24, no. 2, pp. 68-72, Feb. 1999.

[7] D. Lukashev, A. Ohta, and M. Sitkovsky, “Hypoxia-dependent anti-inflammatory pathways in protection of cancerous tissues.,” *Cancer metastasis reviews*, vol. 26, no. 2, pp. 273-9, Jun. 2007.

[8] M. Höckel and P. Vaupel, “Tumor hypoxia: definitions and current clinical, biologic, and molecular aspects.,” *Journal of the National Cancer Institute*, vol. 93, no. 4, pp. 266-76, Feb. 2001.

[9] H. L. Janssen, K. M. Haustermans, A. J. Balm, and A. C. Begg, “Hypoxia in head and neck cancer: how much, how important?" *Society*, no. July, pp. 622-638, 2005.

[10] P. Vaupel and A. Mayer, “Hypoxia in cancer: significance and impact on clinical outcome.,” *Cancer metastasis reviews*, vol. 26, no. 2, pp. 225-39, Jun. 2007.

[11] J. Bussink, “Tumor hypoxia at the micro-regional level: clinical relevance and predictive value of exogenous and endogenous hypoxic cell markers,” *Radiotherapy and Oncology*, vol. 67, no. 1, pp. 3-15, Apr. 2003.

[12] P. F. Rijken, H. J. Bernsen, J. P. Peters, R. J. Hodgkiss, J. a Raleigh, and a J. van der Kogel, “Spatial relationship between hypoxia and the (perfused) vascular network in a human glioma xenograft: a quantitative multi-parameter analysis.,” *International journal of radiation oncology, biology, physics*, vol. 48, no. 2, pp. 571-82, Sep. 2000.

[13] M. Piert, H. J. Machulla, G. Becker, P. Aldinger, E. Winter, and R. Bares, “Dependency of the [18F]fluoromisonidazole uptake on oxygen delivery and tissue oxygenation in the porcine liver.,” *Nuclear medicine and biology*, vol. 27, no. 8, pp. 693-700, Nov. 2000.

[14] L. C. Enfield et al., “Three-dimensional time-resolved optical mammography of the uncompressed breast.,” *Applied optics*, vol. 46, no. 17, pp. 3628-38, Jun. 2007.

[15] J. F. Hainfeld, D. N. Slatkin, T. M. Focella, and H. M. Smilowitz, “Gold nanoparticles: a new X-ray contrast agent.,” *The British journal of radiology*, vol. 79, no. 939, pp. 248-53, Mar. 2006.

[16] S. Unezaki, “Direct measurement of the extravasation of polyethyleneglycol-coated liposomes into solid tumor tissue by in vivo fluorescence microscopy,” *International Journal of Pharmaceutics*, vol. 144, no. 1, pp. 11-17, Nov. 1996.

[17] R. Popovtzer et al., “Targeted Gold Nanoparticles Enable Molecular CT Imaging of Cancer,” *Nano Letters*, vol. 8, no. 12, pp. 4593-4596, Dec. 2008.

[18] D. A. Giljohann, D. S. Seferos, W. L. Daniel, M. D. Massich, P. C. Patel, and C. a Mirkin, “Gold nanoparticles for biology and medicine.,” *Angewandte Chemie (International ed. in English)*, vol. 49, no. 19, pp. 3280-94, Apr. 2010.

[19] M. M. Kemp and R. J. Linhardt, “Heparin-based nanoparticles,” vol. 1, pp. 77-87, 2010.

[20] X.-D. Zhang et al., “Irradiation stability and cytotoxicity of gold nanoparticles for radiotherapy.,” *International journal of nanomedicine*, vol. 4, pp. 165-73, Jan. 2009.

[21] J. F. Hainfeld, F. A. Dilmanian, Z. Zhong, D. N. Slatkin, J. A. Kalef-Ezra, and H. M. Smilowitz, “Gold nanoparticles enhance the radiation therapy of a murine squamous cell carcinoma.,” *Physics in medicine and biology*, vol. 55, no. 11, pp. 3045-59, Jun. 2010.

[22] S. Jain et al., “Cell-specific radiosensitization by gold nanoparticles at megavoltage radiation energies.,” *International journal of radiation oncology, biology, physics*, vol. 79, no. 2, pp. 531-9, Feb. 2011.

[23] J.-K. Kim et al., “Therapeutic application of metallic nanoparticles combined with particle-induced x-ray emission effect.,” *Nanotechnology*, vol. 21, no. 42, p. 425102, Oct. 2010.

[24] J. F. Hainfeld, M. J. O’Connor, F. a Dilmanian, D. N. Slatkin, D. J. Adams, and H. M. Smilowitz, “Micro-CT enables microlocalisation and quantification of Her2-targeted gold nanoparticles within tumour regions.,” *The British journal of radiology*, vol. 84, no. 1002, pp. 526-33, Jun. 2011.

[25] N. Khlebtsov and L. Dykman, "Biodistribution and toxicity of engineered gold nanoparticles: a review of in vitro and in vivo studies.," *Chemical Society reviews*, vol. 40, no. 3, pp. 1647-71, Mar. 2011.

[26] F. A. Dilmanian et al., "Single-and dual-energy CT with monochromatic synchrotron x-rays.," *Physics in medicine and biology*, vol. 42, no. 2, pp. 371-87, Feb. 1997.

[27] R. T. Zaman et al., "In Vivo Detection of Gold Nanoshells in Tumors Using Diffuse Optical Spectroscopy," *Quantum*, vol. 13, no. 6, pp. 1715-1720, 2007.

[28] X. Qian et al., "In vivo tumor targeting and spectroscopic detection with surface-enhanced Raman nanoparticle tags.," *Nature biotechnology*, vol. 26, no. 1, pp. 83-90, Jan. 2008.

[29] X. Yang, E. W. Stein, S. Ashkenazi, and L. V. Wang, "Nanoparticles for photoacoustic imaging," no. 2, 2009.

[30] S. Keren, C. Zavaleta, Z. Cheng, A. de la Zerda, O. Gheysens, and S. S. Gambhir, "Noninvasive molecular imaging of small living subjects using Raman spectroscopy.," *Proceedings of the National Academy of Sciences of the United States of America*, vol. 105, no. 15, pp. 5844-9, Apr. 2008.

[31] A. Thompson, "X-ray data booklet, Centre for x-ray optics and advanced light source," vol. Third Edit, 2009.

[32] L. Ahlgren, K. Lidén, S. Mattsson, and S. Tejning, "X-ray fluorescence analysis of lead in human skeleton in vivo.," *Scandinavian Journal of Work, Environment & Health*, vol. 2, no. 2, pp. 82-86, Jun. 1976.

[33] J. Shakeshaft and S. C. Lillicrap, "Technical note: an X-ray fluorescence system for the determination of gold in vivo following chrysotherapy.," *The British journal of radiology*, vol. 66, no. 788, pp. 714-7, Aug. 1993.

[34] J. Scott and S. Lillicrap, "133Xe for the x-ray fluorescence assessment of gold in vivo.," *Physics in medicine and biology,* vol. 33, no. 7, pp. 859-64, Jul. 1988.

[35] J. Borjesson, "Medical applications of x-ray fluorescence for trace element research," *Powder Diffraction*, vol. 22, no. 2, pp. 130-138, 2007.

[36] D. R. Chettle, M. C. Scott, and L. J. Somervaille, "Lead in bone: sampling and quantitation using K X-rays excited by 109Cd.," *Environmental health perspectives*, vol. 91, pp. 49-55, Feb. 1991.

[37] H. von Busch, "Investigation of externally activated x-ray fluorescence tomography for use in medical diagnostics," *Proceedings of SPIE*, vol. 5745, pp. 90-101, 2005.

[38] S.-K. Cheong, B. L. Jones, A. K. Siddiqi, F. Liu, N. Manohar, and S. H. Cho, “X-ray fluorescence computed tomography (XFCT) imaging of gold nanoparticle-loaded objects using 110 kVp x-rays.,” *Physics in medicine and biology*, vol. 55, no. 3, pp. 647-62, Feb. 2010.

[39] G. Harding and J. Kosanetzky, “X-ray diffraction computed tomography,” *Medical physics*, vol. 14, no. 4, pp. 515-525, 1987.

[40] H. Johns and J. Cunningham, *The Physics of Radiology. Springfield, Ill., USA*. 1983.

[41] G. Kidane, R. D. Speller, G. J. Royle, and A. M. Hanby, “X-ray scatter signatures for normal and neoplastic breast tissues.,” *Physics in medicine and biology*, vol. 44, no. 7, pp. 1791-802, Jul. 1999.

[42] A. Castoldi et al., “Application of Controlled-Drift Detectors in Diffraction Enhanced Imaging of Tissues,” *IEEE Transactions on Nuclear Science*, vol. 54, no. 5, pp. 1474-1480, Oct. 2007.

[43] J. A. Griffiths, G. J. Royle, J. A. Horrocks, A. M. Hanby, and R. D. Speller, “Correlation of Diffraction MicroCT Images of Breast Tissue with Pathological Analysis,” *2006 IEEE Nuclear Science Symposium Conference Record*, pp. 2936-2939, Oct. 2006.

[44] G. Royle, “Applications of X-ray diffraction analysis in crystalline and amorphous body tissues,” *Radiation Physics and Chemistry*, vol. 56, no. 1-2, pp. 247-258, Aug. 1999.

[45] C. Ozkan, “A novel x-ray scatter imaging system with multi-momentum transfer capability, PhD thesis,” 2009.

[46] C. Ozkan et al., “Performance assessment of a high resolution X-ray scatter imaging system with multi-momentum transfer capability,” *2009 IEEE Nuclear Science Symposium Conference Record (NSS/MIC)*, pp. 2342-2346, Oct. 2009.

[47] N. Grassi, C. Guazzoni, R. Alberti, T. Klatka, and A. Bjeoumikhov, “External scanning micro-PIXE for the characterization of a polycapillary lens: Measurement of the collected X-ray intensity distribution,” *Nuclear Instruments and Methods in Physics Research Section B: Beam Interactions with Materials and Atoms*, vol. 268, no. 11-12, pp. 1945-1948, Jun. 2010.

[48] E. Gatti and P. Rehak, “Semiconductor drift chamber - an application of a novel charge transport scheme,” *Nuclear Instruments and Methods in Physics Research*, vol. 225, pp. 608-614, 1984.

[49] P. Lechner et al., “Silicon drift detectors for high count rate X-ray spectroscopy at room temperature,” *Nuclear Instruments and Methods in Physics Research Section A: Accelerators, Spectrometers, Detectors and Associated Equipment*, vol. 458, no. 1-2, pp. 281-287, Feb. 2001.

[50] R. Alberti, N. Grassi, C. Guazzoni, and T. Klatka, “Optimized readout configuration for PIXE spectrometers based on Silicon Drift Detectors: Architecture and performance,” *Nuclear Instruments and Methods in Physics Research Section A: Accelerators, Spectrometers, Detectors and Associated Equipment*, vol. 607, no. 2, pp. 458-462, Aug. 2009.

[51] “http://www.shimadzu.com/an/elemental/xrd/use2.html.” accessed 25/8/2011

[52] C. Chantler et al., “X-Ray Form Factor, Attenuation and Scattering Tables (version 2.1),” *[Online] Available: http://physics.nist.gov/ffast. National Institute of Standards and Technology, Gaithersburg, MD*, 2005.

[53] G. Poludniowski, G. Landry, F. DeBlois, P. M. Evans, and F. Verhaegen, “SpekCalc: a program to calculate photon spectra from tungsten anode x-ray tubes.,” *Physics in medicine and biology*, vol. 54, no. 19, pp. N433-8, Oct. 2009.

[54] G. Andermann and J. W. Kemp, “Scattered X-Rays as Internal Standards in X-Ray Emission Spectroscopy,” *Analytical Chemistry*, vol. 30, no. 8, pp. 1306-1309, 1958.

[55] C. Bui, L. Confalonieri, and M. Milazzo, “Use of compton scattering in quantitative XRF analysis of stained glass,” *International Journal of Radiation Applications and Instrumentation. Part A. Applied Radiation and Isotopes*, vol. 40, no. 5, pp. 375-380, 1989.

[56] R. Van Grieken and M. AA, “Handbook for x-ray spectrometry, 2nd edition, Marcel Dekker, Inc.,” 2002.

[57] R. M. Rousseau, “Detection limit and estimate of uncertainty of analytical XRF results," vol. 18, no. 2, pp. 33-47, 2001.

[58] L. Sivaraman et al., “A microscale in vitro physiological model of the liver: Predictive screens for drug metabolism and enzyme induction,” *Current Drug Metabolism*, vol. 6, pp. 569-591, 2005.

[59] S. Ostrovidov, J. Jiang, Y. Sakai, and T. Fujii, “Membrane-based PDMS microbioreactor for perfused 3D primary rat hepatocyte cultures.,” *Biomedical microdevices*, vol. 6, no. 4, pp. 279-87, Dec. 2004.

[60] T. Goodman, N. C, and P. S, “3-D tissue culture systems for the evaluation and optimization of nanoparticle-based drug carriers,” *October*, vol. 19, no. 10, pp. 1951-1959, 2009.

[61] D. Albrecht, G. Underhill, and T. Wassermann, “Probing the role of multicellular organization in three-dimensional microenvironments,” *Nature methods*, vol. 3, no. 5, pp. 369-375, 2006.

[62] C.-H. Heldin, K. Rubin, K. Pietras, and A. Ostman, “High interstitial fluid pressure - an obstacle in cancer therapy.,” *Nature reviews. Cancer*, vol. 4, no. 10, pp. 806-13, Oct. 2004.

[63] A. Nyga, U. Cheema, and M. Loizidou, “3D tumour models: novel in vitro approaches to cancer studies.,” *Journal of cell communication and signaling*, Apr. 2011.

[64] T. Boehm, J. Folkman, T. Browder, and M. S. O’Reilly, “Antiangiogenic therapy of experimental cancer does not induce acquired drug resistance.,” *Nature*, vol. 390, no. 6658, pp. 404-7, Nov. 1997.

[65] J. P. Eder, “Phase I Clinical Trial of Recombinant Human Endostatin Administered as a Short Intravenous Infusion Repeated Daily,” *Journal of Clinical Oncology*, vol. 20, no. 18, pp. 3772-3784, Jun. 2002.

[66] T. Nederman and P. Twentyman, “Spheroids for studies of drug effects.,” *Cancer Research*, vol. 95, p. 84 102, 1984.

[67] N. S. Waleh, J. Gallo, T. D. Grant, B. J. Murphy, R. H. Kramer, and R. M. Sutherland, “Selective Down-Regulation of Integrin Receptors in Spheroids of Squamous Cell Carcinoma Selective Down-Regulation of Integrin Receptors in Spheroids of Squamous Cell Carcinoma ’,” *Cancer*, pp. 838-843, 1994.

[68] E. Cukierman, R. Pankov, D. R. Stevens, and K. M. Yamada, “Taking cell-matrix adhesions to the third dimension.,” *Science (New York, N.Y.)*, vol. 294, no. 5547, pp. 1708-12, Nov. 2001.

[69] B. Niggemann et al., “Tumor cell locomotion: differential dynamics of spontaneous and induced migration in a 3D collagen matrix.,” *Experimental cell research*, vol. 298, no. 1, pp. 178-87, Aug. 2004.

[70] L. A. Gurski, A. K. Jha, C. Zhang, X. Jia, and M. C. Farach-Carson, “Hyaluronic acid-based hydrogels as 3D matrices for in vitro evaluation of chemotherapeutic drugs using poorly adherent prostate cancer cells.,” *Biomaterials*, vol. 30, no. 30, pp. 6076-85, Oct. 2009.

[71] R. Hurst, C. Kamat, K. Kyker, D. Green, and M. Ihnat, “A novel mutlidrug resistance phenotype of bladder tumor cells grown on Matrigel or SIS gel,” *Cancer Lett*, vol. 217, no. 2, pp. 171-180, 2005.

[72] D. Loessner, K. S. Stok, M. P. Lutolf, D. W. Hutmacher, J. a Clements, and S. C. Rizzi, “Bioengineered 3D platform to explore cell-ECM interactions and drug resistance of epithelial ovarian cancer cells.,” *Biomaterials*, vol. 31, no. 32, pp. 8494-506, Nov. 2010.

[73] U. Cheema, C.-B. Chuo, P. Sarathchandra, S. N. Nazhat, and R. A. Brown, “Engineering Functional Collagen Scaffolds: Cyclical Loading Increases

Material Strength and Fibril Aggregation," *Advanced Functional Materials*, vol. 17, no. 14, pp. 2426-2431, Sep. 2007.

[74] T.-G. Iversen, T. Skotland, and K. Sandvig, "Endocytosis and intracellular transport of nanoparticles: Present knowledge and need for future studies," *Nano Today*, vol. 6, no. 2, pp. 176-185, Apr. 2011.

[75] F. Zhao, Y. Zhao, Y. Liu, X. Chang, C. Chen, and Y. Zhao, "Cellular uptake, intracellular trafficking, and cytotoxicity of nanomaterials.," *Small (Weinheim an der Bergstrasse, Germany)*, vol. 7, no. 10, pp. 1322-37, May. 2011.

[76] B. D. Chithrani and W. C. W. Chan, "Elucidating the mechanism of cellular uptake and removal of protein-coated gold nanoparticles of different sizes and shapes.," *Nano letters*, vol. 7, no. 6, pp. 1542-50, Jun. 2007.

[77] T. S. Hauck, A. A. Ghazani, and W. C. W. Chan, "Assessing the effect of surface chemistry on gold nanorod uptake, toxicity, and gene expression in mammalian cells.," *Small (Weinheim an der Bergstrasse, Germany)*, vol. 4, no. 1, pp. 153-9, Jan. 2008.

[78] D. B. Chithrani, "Intracellular uptake, transport, and processing of gold nanostructures.," *Molecular membrane biology*, vol. 27, no. 7, pp. 299-311, Oct. 2010.

[79] A. Verma and F. Stellacci, "Effect of surface properties on nanoparticle-cell interactions.," *Small (Weinheim an der Bergstrasse, Germany)*, vol. 6, no. 1, pp. 12-21, Jan. 2010.

[80] Y. Qiu et al., "Surface chemistry and aspect ratio mediated cellular uptake of Au nanorods.," *Biomaterials*, vol. 31, no. 30, pp. 7606-19, Oct. 2010.

[81] B. D. Chithrani, A. A. Ghazani, and W. C. W. Chan, "Determining the size and shape dependence of gold nanoparticle uptake into mammalian cells.," *Nano letters*, vol. 6, no. 4, pp. 662-8, Apr. 2006.

[82] S. H. Brewer, W. R. Glomm, M. C. Johnson, M. K. Knag, and S. Franzen, "Probing BSA binding to citrate-coated gold nanoparticles and surfaces.," *Langmuir : the ACS journal of surfaces and colloids*, vol. 21, no. 20, pp. 9303-7, Sep. 2005.

[83] P. Nativo, I. A. Prior, and M. Brust, "Uptake and intracellular fate of surface-modified gold nanoparticles.," *ACS nano*, vol. 2, no. 8, pp. 1639-44, Aug. 2008.

[84] H. Meng, T. Xia, S. George, and A. E. Nel, "A predictive toxicological paradigm for the safety assessment of nanomaterials," *ACS nano*, vol. 3, no. 7, pp. 1620–1627, 2009.

[85] L. Wang, Y.-feng Li, and L. Zhou, “Characterization of gold nanorods in vivo by integrated analytical techniques : their uptake , retention , and chemical forms,” *Analytical and Bioanalytical Chemistry,* vol. 396, no. 3, pp. 1105-1114, 2010.

[86] L. Wang et al., “Selective Targeting of Gold Nanorods at the Mitochondria of Cancer Cells : Implications for Cancer Therapy,” *Cell*, vol. 11, pp. 772-780, 2011.

[87] J. J. Li, D. Hartono, C.-nam Ong, B.-huat Bay, and L.-yue L. Yung, “Biomaterials Autophagy and oxidative stress associated with gold nanoparticles,” *Biomaterials*, vol. 31, no. 23, pp. 5996-6003, 2010.

[88] Y. Pan et al., “Size-dependent cytotoxicity of gold nanoparticles.,” *Small (Weinheim an der Bergstrasse, Germany)*, vol. 3, no. 11, pp. 1941-9, Nov. 2007.

[89] J. Lee, G. D. Lilly, R. C. Doty, P. Podsiadlo, and N. A. Kotov, “In vitro toxicity testing of nanoparticles in 3D cell culture.,” *Small (Weinheim an der Bergstrasse, Germany)*, vol. 5, no. 10, pp. 1213-21, May. 2009.

[90] W. Jiang, B. Y. S. Kim, J. T. Rutka, and W. C. W. Chan, “Nanoparticle-mediated cellular response is size-dependent.,” *Nature nanotechnology*, vol. 3, no. 3, pp. 145-50, Mar. 2008.

[91] K. Gelse, “Collagens—structure, function, and biosynthesis,” *Advanced Drug Delivery Reviews*, vol. 55, no. 12, pp. 1531-1546, Nov. 2003.

[92] R. A. Brown, M. Wiseman, C.-B. Chuo, U. Cheema, and S. N. Nazhat, “Ultrarapid Engineering of Biomimetic Materials and Tissues: Fabrication of Nano- and Microstructures by Plastic Compression,” *Advanced Functional Materials*, vol. 15, no. 11, pp. 1762-1770, Nov. 2005.

[93] B. D. Chithrani, J. Stewart, C. Allen, and D. A. Jaffray, “Intracellular uptake, transport, and processing of nanostructures in cancer cells,” *Nanomedicine: Nanotechnology, Biology and Medicine*, vol. 5, no. 2, pp. 118-127, Jun. 2009.

[94] M. Loizidou, Personal communication, 2011.

[95] F. Grinnell, C. H. Ho, Y. C. Lin, and G. Skuta, “Differences in the regulation of fibroblast contraction of floating versus stressed collagen matrices.,” *The Journal of biological chemistry*, vol. 274, no. 2, pp. 918-23, Jan. 1999.

[96] M. Eastwood, V. C. Mudera, D. A. McGrouther, and R. a Brown, “Effect of precise mechanical loading on fibroblast populated collagen lattices: morphological changes.,” *Cell motility and the cytoskeleton*, vol. 40, no. 1, pp. 13-21, Jan. 1998.

[97] E. Abou Neel, U. Cheema, J. Knowles, R. Brown, and S. Nazhat, “Use of multiple unconfined compression for control of collagen gel scaffold density and mechanical properties,” *Soft Matter*, vol. 2, no. 11, p. 986, 2006.

[98] U. Cheema, S.-Y. Yang, V. Mudera, G. G. Goldspink, and R. A. Brown, “3-D in vitro model of early skeletal muscle development.,” *Cell motility and the cytoskeleton*, vol. 54, no. 3, pp. 226-36, Mar. 2003.

[99] A. Nyga, “Tissue engineering for cancer therapy: In vitro modelling of tumour invasion, MSc Thesis,” 2011.

[100] U. Cheema, R. A. Brown, B. Alp, and A. J. MacRobert, “Spatially defined oxygen gradients and vascular endothelial growth factor expression in an engineered 3D cell model.,” *Cellular and molecular life sciences : CMLS*, vol. 65, no. 1, pp. 177-86, Jan. 2008.

[101] U. Cheema, T. Alekseeva, E. A. Abou-Neel, and R. a Brown, “Switching off angiogenic signalling: creating channelled constructs for adequate oxygen delivery in tissue engineered constructs.,” *European cells & materials*, vol. 20, pp. 274-80; discussion 280-1, Jan. 2010.

[102] R. Lévy, U. Shaheen, Y. Cesbron, and V. Sée, “Gold nanoparticles delivery in mammalian live cells: a critical review,” *Nano Reviews*, vol. 1, pp. 1-18, Feb. 2010.

[103] J. Lewin, TEM Servicess, Royal Free Hospital, Personal communication, 2011.

[104] U. Cheema, UCL Division of Surgical Science, Stanmore Campus, Personal communication, 2011.

[105] A. Castoldi, C. Guazzoni, K. Ricketts, A. Gibson, J. Griffiths, G. Royle, & A. Bjeoumikhov, “2-D Energy-Resolved Imaging of Gold Nanoparticle Distribution at Concentrations Relevant for In-Vitro Studies,” *IEEE Transactions on Nuclear Science*, 2011.

[106] A. Castoldi, C. Guazzoni, R. Hartmann, and L. Struder, “Principle and applications of Controlled-Drift Detectors,” *Nuclear Instruments and Methods in Physics Research Section A: Accelerators, Spectrometers, Detectors and Associated Equipment*, vol. 579, no. 1, pp. 79-82, Aug. 2007.

[107] L. Wang, B. K. Rath, W. M. Gibson, J. C. Kimball, and C. A. MacDonald, “Performance study of polycapillary optics for hard x rays,” *Journal of Applied Physics*, vol. 80, no. 7, p. 3628, 1996.

[108] S. E. Bohndiek et al., “A CMOS active pixel sensor system for laboratory- based x-ray diffraction studies of biological tissue.,” *Physics in medicine and biology*, vol. 53, no. 3, pp. 655-72, Feb. 2008.

[109] M. E. Poletti, D. Gonçalves, and I. Mazzaro, “X-ray scattering from human breast tissues and breast-equivalent materials.,” *Physics in medicine and biology*, vol. 47, no. 1, pp. 47-63, Jan. 2002.

[110] G. Falzon et al., “Wavelet-based feature extraction applied to small-angle x-ray scattering patterns from breast tissue: a tool for differentiating between tissue types.,” *Physics in medicine and biology*, vol. 51, no. 10, pp. 2465-77, May. 2006.

[111] M. Fernández et al., “Human breast cancer in vitro: matching histo-pathology with small-angle x-ray scattering and diffraction enhanced x-ray imaging.,” *Physics in medicine and biology*, vol. 50, no. 13, pp. 2991-3006, Jul. 2005.

[112] R. A. Lewis et al., “Breast cancer diagnosis using scattered X-rays.,” *Journal of synchrotron radiation*, vol. 7, no. 5, pp. 348-52, Sep. 2000.

[113] X. Xu, Y. Wang, Z. Chen, M. D. Sternlicht, M. Hidalgo, and B. Steffensen, “Matrix Metalloproteinase-2 Contributes to Cancer Cell Migration on Collagen,” *Cancer Research*, no. 25, pp. 130-136, 2005.

[114] M. Fernández et al., “Small-angle x-ray scattering studies of human breast tissue samples.,” *Physics in medicine and biology*, vol. 47, no. 4, pp. 577-92, Feb. 2002.

[115] A. R. Round et al., “A preliminary study of breast cancer diagnosis using laboratory based small angle x-ray scattering.,” *Physics in medicine and biology*, vol. 50, no. 17, pp. 4159-68, Sep. 2005.

[116] P. Singh, K. Kumari, A. Katyal, R. Kalra, and R. Chandra, “Synthesis and characterization of silver and gold nanoparticles in ionic liquid.,” *Spectrochimica acta. Part A, Molecular and biomolecular spectroscopy*, vol. 73, no. 1, pp. 218-20, Jul. 2009.

[117] F. Vitale et al., “Synthesis and characterization of gold nanoparticles stabilized by palladium(II) phosphine thiol,” *Journal of Organometallic Chemistry*, vol. 693, no. 6, pp. 1043-1048, Mar. 2008.

[118] W. Yan, V. Petkov, S. Mahurin, S. Overbury, and S. Dai, “Powder XRD analysis and catalysis characterization of ultra-small gold nanoparticles deposited on titania-modified SBA-15,” *Catalysis Communications*, vol. 6, no. 6, pp. 404-408, Jun. 2005.

[119] V. Petkov, Y. Peng, G. Williams, B. Huang, D. Tomalia, and Y. Ren, “Structure of gold nanoparticles suspended in water studied by x-ray diffraction and computer simulations,” *Physical Review B*, vol. 72, no. 19, pp. 1-8, Nov. 2005.

[120] D. V. Leff, P. C. Ohara, J. R. Heath, and W. M. Gelbart, “Thermodynamic Control of Gold Nanocrystal Size: Experiment and Theory,” pp. 7036-7041, 1995.

[121] S. Pani, G. Royle, R. Speller, A. Castoldi, A. Galimberti, and C. Guazzoni, “Use of a novel controlled drift detector for diffraction enhanced breast imaging,” *Nuclear Instruments and Methods in Physics Research Section A: Accelerators,*

Spectrometers, Detectors and Associated Equipment, vol. 573, no. 1-2, pp. 133-136, Apr. 2007.

[122] C. Ozkan, C. Guazzoni, A. Castoldi, and A. Bjeoumikhov, “Improved Energy-Dispersive X-ray Scattering System Based on Polycapillary Collimation and a Silicon Drift Detector,” pp. 1056-1061, 2010.

[123] E. Cook, “Analysis of energy dispersive x-ray diffraction profiles for material identification, imaging and system control,” *PhD Thesis*, 2008.